

## Durham E-Theses

---

### *Marine geophysical investigation of the Hatton bank volcanic passive continental margin*

Prescott, Clifford Neill

#### How to cite:

---

Prescott, Clifford Neill (1988) *Marine geophysical investigation of the Hatton bank volcanic passive continental margin*, Durham theses, Durham University. Available at Durham E-Theses Online:  
<http://etheses.dur.ac.uk/6660/>

#### Use policy

---

The full-text may be used and/or reproduced, and given to third parties in any format or medium, without prior permission or charge, for personal research or study, educational, or not-for-profit purposes provided that:

- a full bibliographic reference is made to the original source
- a [link](#) is made to the metadata record in Durham E-Theses
- the full-text is not changed in any way

The full-text must not be sold in any format or medium without the formal permission of the copyright holders.

Please consult the [full Durham E-Theses policy](#) for further details.

---

Academic Support Office, Durham University, University Office, Old Elvet, Durham DH1 3HP  
e-mail: [e-theses.admin@dur.ac.uk](mailto:e-theses.admin@dur.ac.uk) Tel: +44 0191 334 6107  
<http://etheses.dur.ac.uk>

Marine Geophysical Investigation of the Hatton Bank  
Volcanic Passive Continental Margin

by

Clifford Neill Prescott

The copyright of this thesis rests with the author.  
No quotation from it should be published without  
his prior written consent and information derived  
from it should be acknowledged.

A thesis submitted for the degree of  
Doctor of Philosophy at the University of Durham

Graduate Society

February, 1988



10 MAY 1988

## Abstract

The Durham/Cambridge/Birmingham Universities two-ship marine geophysical cruise to the Hatton Bank continental margin took place in May/June 1985, during which single- and two-ship seismic reflection/refraction data, together with under-way gravity and magnetic anomaly, and bathymetric data were collected within a 200 km by 150 km area straddling the continent-ocean transition. The processing, modelling and interpretation of four two-ship synthetic aperture profiles (SAP) and the gravity and magnetic anomaly data is presented.

Gravity models show that a density model based on the crustal velocity structure defined by synthetic seismogram modelling of the two-ship expanding spread profiles is insufficient to reproduce the observed gravity profile across the margin. This requires additional contributions in the form of density gradients in the underlying sub-crustal part of the lithosphere and asthenosphere, and this is investigated by thermal modelling.

Analysis of the magnetic anomaly data shows that oceanic magnetic anomalies 21 and 22 are developed in the north-west of the 1985 survey area. Anomalies 23 and 24 cannot be recognised due to post-rift igneous activity and/or subaerial seafloor spreading. The positions of anomalies 23 and 24B are reconstructed within the survey area, and the theoretical anomaly 24B position is used to determine the position of the continent-ocean boundary. Analysis of the anomalies recorded on the upper continental slope shows that the acoustic basement in this area is volcanic.

Interpretation of the SAP profiles shows that the margin can be described in terms of three distinct volcanic sequences. The continental sequence is composed of lavas extruded onto continental crust during a period of continental volcanism which occurred before the onset of seafloor spreading just prior to anomaly 24B. The sequence thickens to the north-west, to form a set of seaward-dipping reflectors. The oceanic sequence comprises oceanic crust within which structurally different seaward-dipping dipping reflectors are developed. This sequence is associated with the reconstructed positions of anomalies 23 and 24B, and is interpreted as having formed during a period of subaerial seafloor spreading. The late sequence separates, and in part overlies the continental and oceanic sequences. Magnetic anomalies associated with the late sequence are arcuate, and have high amplitudes, implying an origin other than simple seafloor spreading. The late sequence is interpreted as originating from post-rift igneous activity in the Eocene.



## Contents

Abstract.	
Contents.	
List of figures.	
Acknowledgements.	
	Page
Chapter 1 Introduction.	1
1.1 Regional geology.	2
1.1.1 Rockall Plateau.	2
1.1.2 East Greenland continental margin.	4
1.2 Plate tectonic evolution of the north Atlantic.	5
1.3 Dipping reflectors.	9
1.3.1 General structure.	9
1.3.2 Mutter's model "subaerial seafloor spreading".	10
1.3.3 Hinz's model.	11
1.3.4 The Voring Plateau.	13
1.3.5 The Rockall Plateau.	16
1.4 The 1985 survey and its objectives	19
1.5 Outline of the present survey.	21
Chapter 2 Data acquisition and preliminary processing.	23
2.1 Navigation.	23
2.2 Bathymetry.	24
2.3 Magnetics.	25
2.4 Gravity.	26
2.5 Seismic data.	29
2.5.1 Synthetic aperture profiles.	29
2.5.2 Expanding spread profiles.	32
Chapter 3 Processing of SAP data.	34
3.1 Introduction.	34
3.2 The processing system.	35
3.2.1 Hardware.	35
3.2.2 Software.	35

3.3 Seismic data processing.	36
3.3.1 Demultiplex.	36
3.3.2 CMP sort.	36
3.3.3 Velocity analysis and CMP stack.	37
Chapter 4 Gravity models of the Hatton Bank continental margin.	51
4.1 Introduction.	51
4.2 Past work.	52
4.3 Initial models.	54
4.3.1 The data.	54
4.3.2 The crustal model.	54
4.3.3 Assumed crustal structure and densities.	56
4.3.4 The sediments.	57
4.3.5 Dipping reflectors and lavas.	57
4.3.6 Oceanic crustal structure.	58
4.3.7 Continental crustal structure.	60
4.3.8 Continental densities.	61
4.3.9 Underplated lens density.	62
4.3.10 Upper mantle density.	63
4.4 Gravity models.	64
4.4.1 ESP control.	64
4.4.2 ESP control and upper mantle density gradient.	67
4.5 Model implications.	69
4.6 Thermal models.	72
4.6.1 Program tests.	74
4.6.2 Thermal models	75
4.7 Deep compensation.	77
4.8 Discussion.	79
Chapter 5 Magnetic anomaly interpretation.	82
5.1 Introduction.	82
5.2 Magnetic anomalies in the north-east Atlantic.	83
5.3 Anomalies 20 to 24 in the Iceland Basin.	84
5.4 Timing of the split between Greenland and Eurasia.	86
5.5 Interpretation of the 1985 survey magnetic anomaly data.	88
5.5.1 Magnetic anomaly contour map.	88

5.5.2 Identification and correlation of anomalies.	90
5.5.3 Anomaly 23 and 24 reconstructions.	91
5.5.4 Comparison of observed and reconstructed anomaly 23 and 24 positions.	94
5.6 Nature of continental basement.	97
5.7 Conclusion.	99
 Chapter 6 Interpretation of synthetic aperture profiles (SAP).	100
6.1 Introduction.	100
6.2 The Hatton Bank continental margin.	101
6.2.1 Sediment structure, and acoustic basement morphology.	102
6.2.2 Basement reflectors.	106
6.3 Basement velocity structure.	119
6.4 Interpretation.	122
6.4.1 Continental sequence.	122
6.4.2 Oceanic sequence.	123
6.4.3 Late sequence.	126
 Chapter 7 Conclusions and discussion.	128
7.1 Introduction.	128
7.2 Conclusions and general discussion.	128
7.2.1 Gravity modelling.	128
7.2.2 ESP velocity structure and lateral variations in the upper crust.	130
7.2.3 Magnetic anomalies.	130
7.2.4 The Hatton Bank volcanic margin.	132
7.3 Dipping reflectors and the continent-ocean boundary.	136
7.4 Concluding comments.	138
 References	140
 Appendix A. Listings of computer programs.	149
 Appendix B. Details of data available on magnetic tape at Durham.	193

## List of figures.

Figure	Following Page
1.1 Rockall Plateau bathymetry.	1
1.2 Gravity model across Rockall Plateau (reproduced from Scruton, 1972).	2
1.3 Bathymetry, magnetic anomaly lineations, and dipping reflectors on the East Greenland continental margin.	5
1.4 Fracture zones, magnetic anomaly lineations, and flow lines in the north Atlantic and Labrador Sea.	5
1.5 Subaerial seafloor spreading model of Mutter <i>et al.</i> , (1982).	10
1.6 Hinz's (1981) rift stage volcanic model.	11
1.7a Bathymetry, magnetic anomaly lineations, DSDP holes, and MCS lines on the Outer Voring Plateau.	13
1.7b Line drawing interpretation of MCS line 162, Outer Voring Plateau.	13
1.8 Schematic illustration of early Tertiary evolution of the Voring Plateau continental margin (reproduced from Skogsied & Eldholm, 1987).	15
1.9 Bathymetry, anomaly 24, DSDP holes, and MCS lines on Rockall Plateau.	16
1.10 Sequence of evolution of the south west Rockall Plateau continental margin (after Roberts <i>et al.</i> , 1984).	18
1.11 ESP and Variable offset lines shot on the Hatton Bank margin during 1985 survey.	20
1.12 Normal incidence seismic lines shot on the Hatton Bank margin during the 1985 survey.	20
1.13 Location of SAP profiles in 1985 survey area.	20
1.14 Ships tracks during the 1985 survey of the Hatton Bank continental margin.	21
2.1 Magnetic anomaly data recorded on the Hatton Bank continental margin during the 1985 survey.	26
2.2 Smoothed and unsmoothed gravity profile along SAP 2.	29

2.3 Gravity anomaly data recorded on the Hatton Bank continental margin during the 1985 survey.	29
2.4 SAP acquisition geometry.	30
2.5 ESP acquisition geometry.	32
3.1 Seismic reflection processing system configuration.	35
3.2 SAP1, CMP 510 : Raw CMP-sorted gather.	37
3.3 SAP1, CMP 510 : Velocity analysis of band-pass filtered and range corrected gather.	40
3.4 SAP1, CMP 510 : Band-pass filtered and range-corrected gather.	43
3.5 SAP1, CMP 510 : Trace autocorrelation function.	44
3.6 SAP1, CMP 510 : Deconvolved gather.	44
3.7 SAP1, CMP 510 : Trace autocorrelation of deconvolved gather.	45
3.8 SAP1, CMP 510 : Velocity analysis of deconvolved gather.	45
3.9 SAP1, CMP 510 : Velocity analysis of deconvolved and velocity filtered gather.	46
3.10 SAP1, CMP 510 : Muted gather.	46
3.11 SAP1, CMP 510 : Velocity analysis of deconvolved, muted, and velocity filtered gather.	46
3.12 SAP1, CMP 510 : Moved-out gather.	48
3.13 SAP2, CMP 1779 : Gather contaminated by excessive multiple energy.	49
4.1 Velocity structure of the Hatton Bank continental margin.	55
4.2 Density model based on figure 4.1.	64
4.3 Gravity model using the density model of figure 4.2.	64
4.4 Illustration of degree of compensation of figure 4.2.	64
4.5 Airy Isostatic gravity model.	65
4.6 Model 4.3 with upper mantle density gradient.	67
4.7 Model 4.6 with upper crustal intrusive.	68
4.8 Windowed gravity data.	69
4.9 Stacked, binned, and smoothed gravity profile.	69
4.10 Extended ESP-based gravity model.	69
4.11 Extended ESP-based gravity model with upper mantle density gradient.	69

4.12	Extended ESP-based gravity model with upper mantle density gradient, and upper crustal intrusive.	69
4.13	Comparison of observed oceanic crustal depths corrected for effects of sediment load, abnormal thickness, and anomalous density upper mantle, with theoretically expected depths.	71
4.14	Lithosphere thermal model.	73
4.15	Finite-difference representation of temperature nodes used in thermal modelling.	page 73
4.16	Comparison of theoretical and numerical solution of heat flow equation - case 1.	74
4.17	Comparison of theoretical and numerical solution of heat flow equation - case 2.	75
4.18	Thermal model results and density gradient for 20 km rift zone.	76
4.19	Thermal model results and density gradient for 60 km rift zone.	76
4.20	Thermal model results and density gradient for 120 km rift zone.	76
4.21	ESP based gravity model plus modelled upper mantle density gradient.	77
4.22	Degree of compensation of model of figure 4.21.	77
4.23	Comparison of observed oceanic crustal depths corrected for effects of sediment load, abnormal thickness, and anomalous density upper mantle, with theoretically expected depths.	77
4.24	Asthenosphere density gradient required to maintain model of figure 4.21 in isostatic equilibrium.	78
4.25	Gravity model of figure 4.21 with asthenosphere density gradient.	79
4.26	Gravity model of figure 4.25 with upper crustal intrusive.	79
4.27	Degree of compensation of model of figure 4.26.	79
4.28	Comparison of observed oceanic crustal depths corrected for effects of sediment load, abnormal thickness, and anomalous density upper mantle, with theoretically expected depths.	79
5.1	Synthetic anomaly profile for north-east Atlantic.	83
5.2	Magnetic anomalies east of the Reykjanes ridge and adjacent to the south west Rockall Plateau.	84

5.3 Magnetic anomalies north of Hatton Bank.	85
5.4 Magnetic anomalies adjacent to the east Greenland continental margin.	85
5.5 Magnetic anomaly contour map (in back pocket).	
5.6 Magnetic anomaly data available on the Hatton Bank.	90
5.7 Finite-difference reconstruction of anomaly 24B position.	92
5.8 Finite-difference reconstruction of anomaly 23 position.	93
5.9 Anomaly 24B, east Greenland, reconstructed to anomaly 24B time.	93
5.10 As figure 5.9, using adjusted angle of opening.	94
5.11 Composite figure of all reconstructions of anomaly 24B position.	94
5.12 Reduction of contour map of figure 5.5, with reconstructed anomaly positions marked.	94
5.13 Contour map of Roberts & Jones (1975), with proposed anomaly 23 continuation.	94
5.14 Magnetic anomaly profiles recorded along SAPs 1-4.	95
5.15 Closure of Reykjanes Basin to anomaly 24B time.	96
6.1 Distribution of dipping reflectors in the north Atlantic.	101
6.2 Map of Rockall Plateau showing bathymetry, DSDP sites, MCS lines, and anomaly 24 lineation.	101
6.3 Interpreted SAP 1 seismic section (in back pocket).	
6.4 Interpreted SAP 2 seismic section (in back pocket).	
6.5 Interpreted SAP 3 seismic section (in back pocket).	
6.6 Interpreted SAP 4 seismic section (in back pocket).	
6.7 Bottom circulation, sediment drifts and DSDP sites in the north Atlantic.	102
6.8 Isovelocity contour section across the Hatton Bank continental margin.	108
6.9 SAP interval velocity structure.	119
6.10 Generalised ESP velocity/depth structure.	119
6.11 Example plot of program CMPENV output.	120
6.12 Cross-strike comparison of dipping reflector velocity structure, SAPs 1 & 2.	120
6.13 Cross-strike comparison of dipping reflector velocity structure, SAPs 3 & 4.	120

6.14 Along-strike comparison of dipping reflector velocity structure.	120
6.15 Line drawing interpretation of normal incidence line NI3.	120
6.16 Along-strike comparison of late sequence velocity structure.	121
7.1 Schematic illustration of proposed sequence of evolution of the Hatton Bank continental margin.	133

### **List of tables.**

<b>Table</b>	<b>Following Page</b>
2.1(a) Details of RRS Charles Darwin gravimeter tie-ins.	28
2.1(b) Details of RRS Discovery gravimeter tie-ins.	28
3.1 SAP 1, CMP 510 : velocity function.	48
5.1 Magnetic anomaly amplitudes.	98



## Acknowledgements

Firstly I would like to thank Professor M. H. P. Bott for his provision of departmental facilities, and for his considerable advice whilst jointly supervising my work with Professor G. K. Westbrook. Thanks also go to Professor Westbrook and Dr. R. S. White who acted as principal scientists aboard the R.R.S. Charles Darwin and R.R.S. Discovery respectively during the 1985 survey, and to whose efforts the success of the cruise is due.

The officers and crew of both ships are thanked for their efficient and competent handling of the ships. The technical support of the R.V.S. personnel during the cruise is gratefully acknowledged. In particular, my thanks go to Ken Robertson, Stan Smith, Doriel Jones, and Ed Cooper for their hard work and dedication aboard the R.R.S. Charles Darwin.

The valuable advice and friendship of various fellow students and members of staff, including Dave Stevenson, Pete Brabham, and Richard Hobbs is appreciated. Mike Smith is thanked for his friendship, and for allowing me access to numerous of his computer programs and subroutines. In particular, Dr. Adrian Bowen is thanked for his companionship, conscientious hard work, and considerable expertise in the field of digital seismic signal processing. L. Parson, R. White, M. Bott, A. Bowen, R. Hyndman, S. Fowler, G. Spence, and J. Mutter are thanked for providing me with reprints and preprints of scientific papers.

My love and thanks go to my parents for their patience and unwavering loyalty and support over the last twenty-six years!

Special thanks and love go to Linda, without whose uncomplaining support and encouragement this thesis would not have been written.

This work was carried out whilst in receipt of a Natural Environment Research Council Studentship, and their support is greatly acknowledged.

## CHAPTER (1)

### Introduction.

The Rockall Plateau forms an extensive shallow water region of the north Atlantic east of the Reykjanes ridge (figure 1.1). Its major bathymetric expression consists of the relatively shallow Rockall, George-Bligh, and Hatton Banks which almost completely surround the Hatton-Rockall basin. Edoras, Fanghorn, and Lorient Banks form less extensive shoal areas to the south-west. The north-western continental margin of Rockall Plateau extends from  $60^{\circ}$  N to  $55.5^{\circ}$  N. Its principle morphology consists of a series of shallow north-east south-west trending basement ridges, which are the Hatton and Edoras Banks, with a relatively steep continental slope to the north-west into the Reykjanes Basin, the base of which is approximately defined by the 2500 m contour.

In May/June 1985, the margin west of Hatton Bank was the subject of a collaborative geophysical study between the Universities of Durham, Cambridge, and Birmingham, in which two-ship seismic techniques were employed to investigate the crustal structure within a 200 km by 150 km box straddling the margin (figure 1.1). Together with a dense grid of conventional single-ship multichannel seismic reflection profiles, and gravity and magnetic anomaly profiles recorded continuously along both ships tracks, these data provided an extremely comprehensive data set with which to study the nature of the continent-ocean transition of the Hatton Bank passive continental margin. This thesis describes the processing and interpretation of the gravity, magnetic, and two-ship synthetic aperture profile seismic reflection data acquired during the 1985 survey.



# Rockall Plateau, Bathymetry.

61°00'N  
13°00'W

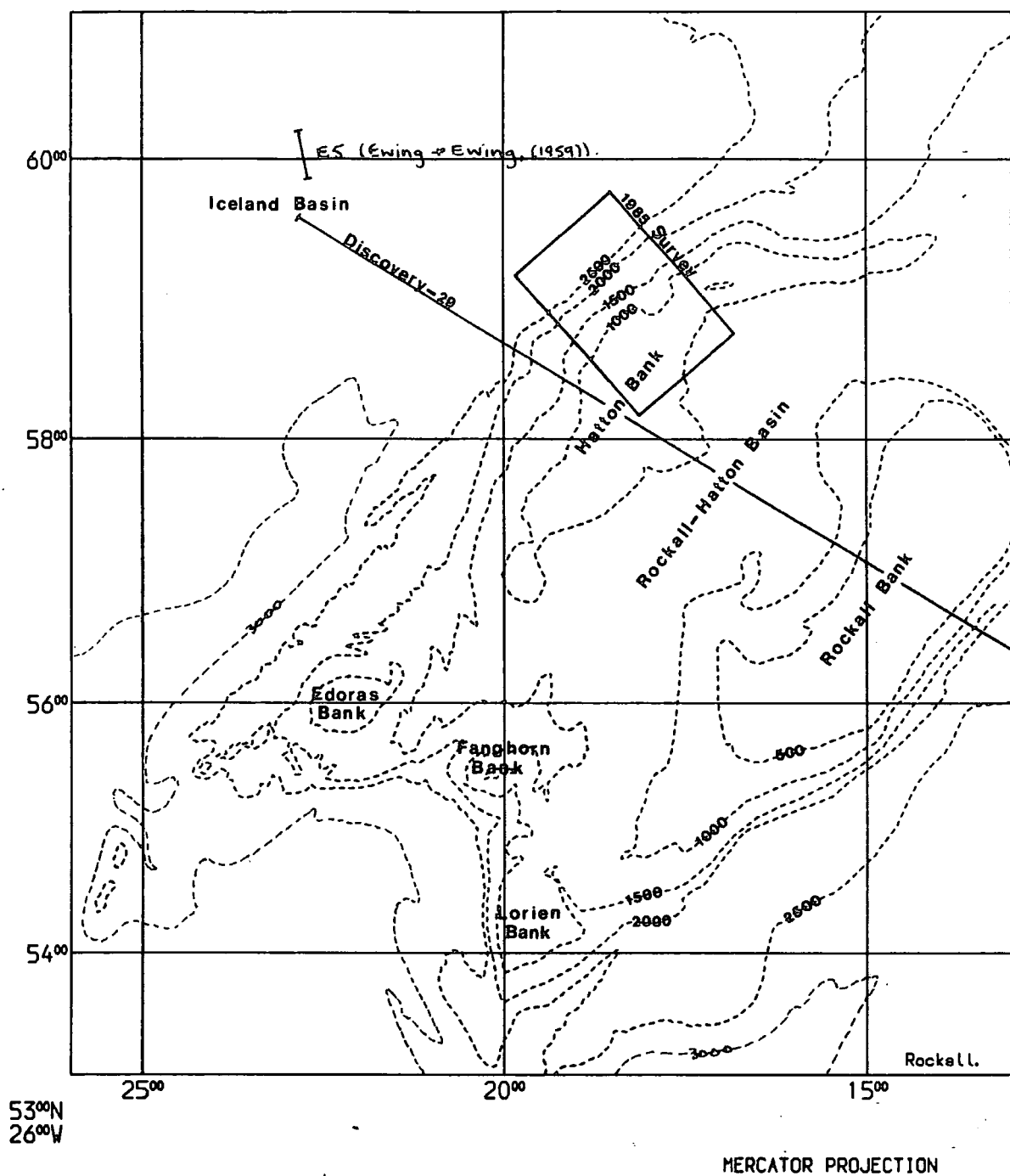


Figure 1.1 Map showing the major bathymetric features of Rockall Plateau. Depths are given in meters.

## 1.1 Regional Geology.

### 1.1.1 Rockall Plateau.

The suggestion that Rockall Plateau might form a microcontinental region was first made by Bullard *et al.* (1965), on the basis that it filled a conspicuous gap in reconstructions of the pre-drift configuration of the north Atlantic. Subsequently, seismic refraction experiments on Rockall Plateau and in the Hatton-Rockall Basin revealed seismic velocities and crustal thicknesses (of 33 and 22 km respectively), consistent with a continental crustal structure (Scrutton, 1970 ; 1972 ; Scrutton & Roberts, 1971). Gravity modelling, using the results of the refraction experiments as control on crustal structure and densities, confirm the continental affinity of the Rockall Plateau, and imply a Moho depth of 28 km underlying Hatton Bank (Scrutton, 1972) (figure 1.2). To the west and south-west of Rockall Plateau, clearly developed oceanic seafloor spreading magnetic anomalies abut the foot of the continental slope (Vogt & Avery, 1974), with the oldest oceanic anomaly corresponding to anomaly 24B (Paleocene/Eocene boundary ; Ness *et al.*, 1980) . North of Hatton Bank, Voppel *et al.* (1979) have demonstrated the presence of a similar sequence of magnetic anomaly lineations, although these are complicated by possible ridge jumps. Together with the typically oceanic velocity structure obtained at station E5 by Ewing & Ewing (1959), these data clearly imply the presence of oceanic crust underlying the ocean basins west and south-west of Rockall Plateau.

Geological evidence concerning the nature of Rockall Plateau adds conclusive support to the geophysical conclusions. Lead and strontium isotope analysis of the aegirine granite comprising Rockall islet imply continental contamination. Dredging and drilling operations on Rockall Bank resulted in the recovery of Laxfordian and

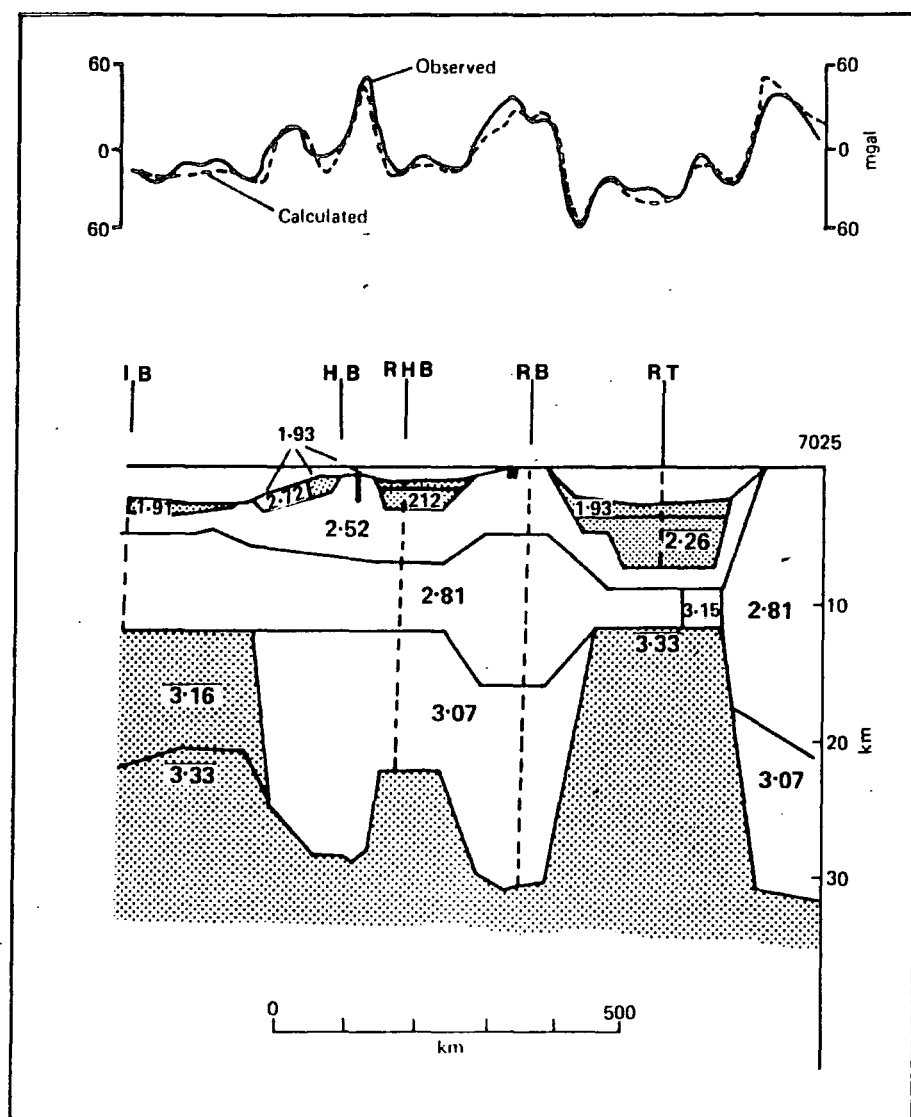


**Figure 1.2** Gravity model across the Rockall Plateau. RT=Rockall Trough, RB=Rockall Bank, RHB=Rockall-Hatton Basin, HB=Hatton Bank, IB=Iceland Basin. Densities are in  $\text{g cm}^{-3}$ . Location of line shown in figure 1.1. (Reproduced from Scrutton, 1972).

Grenvillian granulites (Miller *et al.*, 1973 ; Roberts *et al.*, 1972 ; 1973), confirming the continental affinity of the basement of Rockall Bank.

Seismic velocities within the Rockall Trough (Ewing & Ewing, 1959 ; Scrutton, 1972) are consistent with an oceanic crustal structure, although the presence of stretched continental crust has also been suggested (Talwani & Eldholm, 1977). The gravity model of Scrutton (1972) (figure 1.2), required a Moho depth of 12 km below sea level within the Rockall Trough, which was interpreted as evidence in favour of an oceanic crustal structure. Subsequently, Roberts *et al.* (1981) concluded from earlier geometrical considerations and magnetic anomaly models, that up to 120 km of oceanic crust accreted about a seafloor spreading axis in the mouth of the Rockall Trough during post-Albian, pre-Maestrichtian time, favouring the oceanic origin of Rockall Trough.

The shallow seismic structure of the Rockall Plateau and surrounding areas was described by Roberts (1975a) in terms of three seismic units; these consist of "basement", overlain by a "pre-R4 series" and a "post-R4 series" separated by a regional unconformity, R4. West of Rockall Plateau, horizon R4 (horizon R of Ruddiman, 1972) corresponds to the boundary between the overlying, well-layered turbidites of the Maury Fan, and the underlying relatively transparent pre-R4 series. R4 pinches out on the flank of the Reykjanes Ridge against oceanic basement of 37 ma age (Ruddiman, 1972). Continentwards, R4 wedges out against the continental basement of Hatton Bank (Roberts, 1975b). The unconformity was penetrated at DSDP Leg 12, sites 116, 117, where it was found to represent the transition from an underlying, pre-R4 series of Eocene age, to an overlying post-R4 series of Oligocene age. At DSDP Leg 48, site 403, R4 was found to correspond to a tuff bed of early-Eocene age, underlying two closely spaced unconformities between mid-Eocene and

Oligocene, and Oligocene and upper-Miocene sediments (Roberts *et al.*, 1979).

Seismic reflection profiles across the continent-ocean transition of the southwest Rockall Plateau have revealed the apparent absence of subsided and rotated fault blocks which characterise other rifted continental margins such as the northern Bay of Biscay margin (Whitmarsh *et al.*, 1986), and the presence of an extended westward-prograding sequence of seaward-dipping reflectors, which were originally interpreted as consisting of interbedded clastics and extrusives (Roberts *et al.*, 1979). Similar seaward-dipping sequences have been observed on other continental margins world-wide (Hinz, 1981), and subsequent drilling has shown these to be volcanic in origin.

#### 1.1.2 East Greenland Continental Margin.

The continental margin of East Greenland is conjugate to the Hatton Bank margin, and a brief description is given here based on the work of Featherstone *et al.* (1977). The margin is broadly divisible into morphological regions corresponding to the continental shelf, slope, and rise, and the adjacent ocean basin. The continental shelf widens north of 63.5° N, and is bound to the east by an unusually sharp shelf break, and steep continental slope. Seafloor depths increase from 315 m at the shelf break, to 1300 m at the foot of the continental slope. Oceanwards from the base of the slope, the seafloor of the continental rise is rough and devoid of recent sediments. This zone passes eastwards into the region of smoother seafloor corresponding to the ocean basin. South of 62° N, the inner, rough area of seafloor is absent. The transition between the two areas corresponds to a change in surface outcrop from underlying late Paleocene/Eocene marginal sediments, to late Oligocene oceanic sediments. The sedimentary successions are separated by a distinct unconformity

which abruptly cuts across the underlying marginal sediments, and is overlapped to the west by the younger oceanic sediments. The unconformity was referred to as horizon "U" by Featherstone *et al.* (1977).

Beneath the sediments, the basement landward of anomaly 24B exhibits an extensive sequence of seaward-dipping reflectors overlain by smooth acoustic basement (figure 1.3). These were interpreted as sediments overlying continental crust. These have been observed on other continental margins and have been shown by drilling to be volcanic in origin. A closely comparable sequence has been described by Roberts *et al.* (1979) on the conjugate south-west Rockall Plateau continental margin. This sequence passes oceanward into a region of diffractive acoustic basement associated with clear seafloor spreading magnetic anomalies, interpreted as oceanic crust. Anomaly 24B is the oldest clearly developed magnetic anomaly adjacent to the continental margin. Northwards, anomalies 24 and 23 successively cut out against the continental slope (figure 1.3). Featherstone *et al.* (1977) suggested that the missing anomalies were isolated on the conjugate margin following a westward jump of the ridge axis after anomaly 23 time (chapter 5).

## **1.2 Plate Tectonic Evolution of the North Atlantic.**

In this section the plate tectonic evolution of the north Atlantic between the Azores-Gibraltar and Greenland-Scotland ridges is presented, based principally on the synthesis given by Srivastava & Tapscott (1986). Figure 1.4 shows the principal magnetic anomaly lineations and fracture zones in the north Atlantic Ocean, the Labrador sea, and the Norwegian-Greenland seas reproduced from Srivastava & Tapscott (1986).

Seafloor spreading in the north Atlantic between Iberia and north America



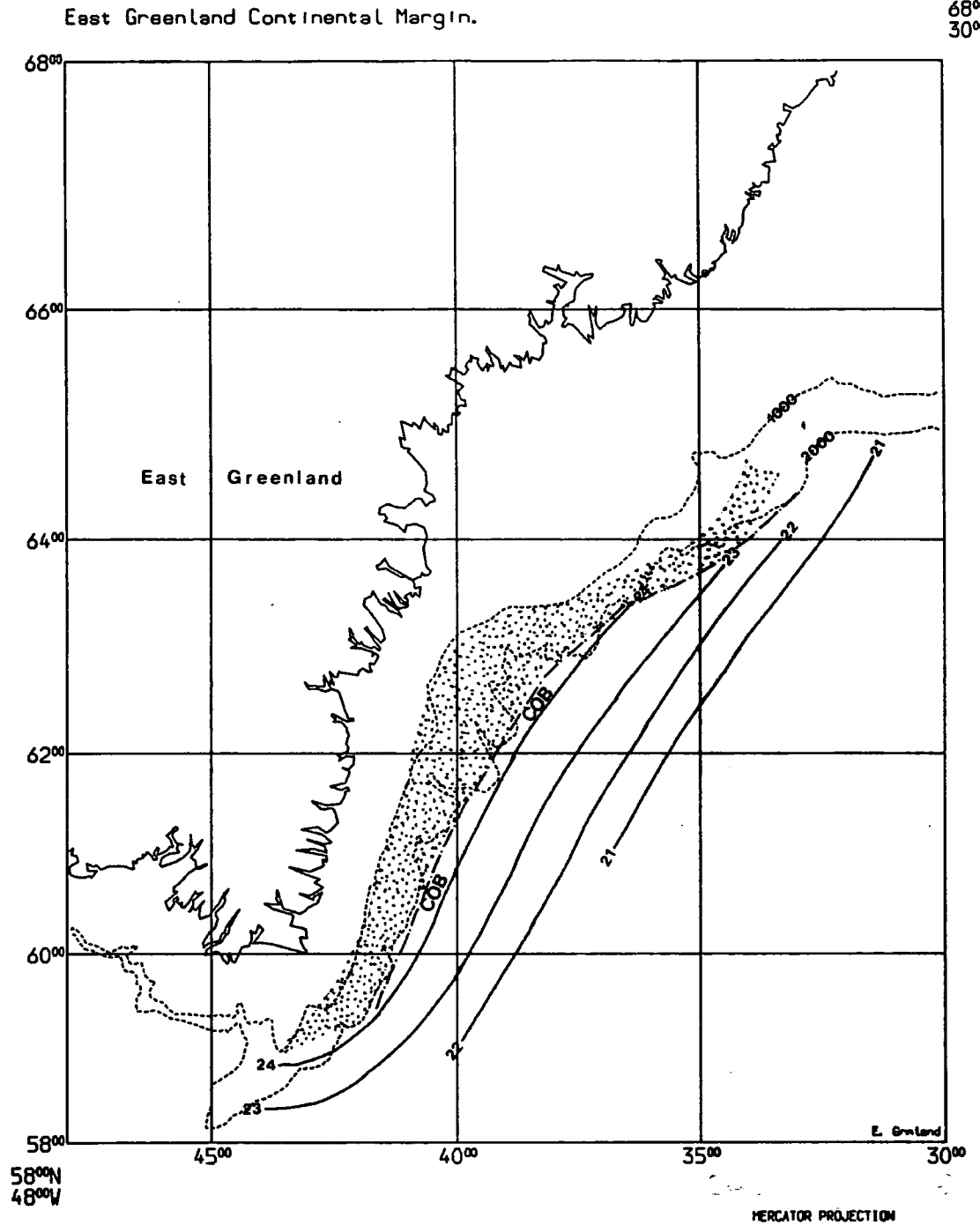


**Figure 1.3** Map of the East-Greenland continental margin. 1000 m and 2000 m contours, continent-ocean boundary, and anomaly lineations 21-24 shown. Shaded area corresponds to region exhibiting basement seaward-dipping reflectors (Based on Featherstone *et al.*, 1977).



began during anomaly M-4 time, although rifting may have been initiated as early as anomaly M-11 time. With the transition from rifting to spreading, Iberia began to move as part of the African plate, opening the Bay of Biscay. Seafloor spreading continued to propagate northwards during the late Cretaceous into the Rockall Trough. The exact timing and duration of spreading within the Rockall Trough is unclear. However, anomaly 34 passes across the mouth of the Trough, is translated to the west by the Charlie-Gibbs fracture zone, and lies south of the Rockall Plateau. This implies that seafloor spreading had ceased in the Rockall Trough by anomaly 34 time. Comparison of weak magnetic anomaly lineations in the south of Rockall Trough with modelled profiles indicates that a continuation of the mid-Atlantic ridge into the mouth of the Trough existed in pre-anomaly 34 time, with the accretion of up to 120 km of oceanic crust (Roberts *et al.*, 1981). This conclusion is in agreement with the earlier reconstructions of the north Atlantic to anomaly 34 time by Kristofferson (1978) and Srivastava (1978) which showed on geometric grounds the existence of a narrow continuation of pre-anomaly 34 oceanic crust into the Rockall Trough.

Spreading ceased in the Rockall Trough just prior to anomaly 34 time when the spreading axis jumped westward to open the southern Labrador sea, forming the first split between the Rockall Plateau and north America. This shift of axis initiated the Charlie-Gibbs fracture zone and formed the east-west trending transform margin, and north-south trending rifted margin of the rectilinear south-west Rockall Plateau (Kristofferson, 1978). The new axis propagated northwards, with seafloor spreading established in the north Labrador sea by anomaly 31 time. Spreading in the north Atlantic continued in this mode until immediately prior to anomaly 24 time, with Greenland effectively moving as part of the Eurasian plate. Although there may

have been slight movement of up to 60 km between Greenland and Rockall during this time, movement of this magnitude would not have resulted in seafloor spreading magnetic anomalies, and may easily have been taken up by crustal attenuation (Roberts *et al.*, 1979).

Immediately prior to anomaly 24, spreading was initiated between the Greenland and Eurasian plates about the Reykjanes ridge in the north-east Atlantic, the Aegir axis in the Norwegian sea, and the Mohns ridge in the Greenland sea. Spreading continued in the Labrador sea, and a ridge-ridge-ridge triple junction came into existence to the south of Greenland. The direction of motion of Eurasia with respect to north America did not change appreciably at this time as evidenced by the relatively straight trend of the Charlie-Gibbs fracture zone. As a result of the new northerly component of motion of Greenland with respect to north America, spreading in the Labrador sea became highly oblique to the ridge axis, resulting in the formation of closely spaced SSW-NNE trending fracture zones, and an associated magnetic quiet zone in the central Labrador sea (Roots & Srivastava, 1984). Spreading continued uninterrupted in this configuration until just after anomaly 21 time, when spreading in the Labrador sea slowed down considerably, to finally cease by anomaly 13 time. Again, the direction of relative motion between the Eurasian and north American plates did not alter appreciably as a result of the deceleration in the Labrador sea, and spreading about the Reykjanes ridge therefore reoriented from a southeast-northwest direction to a more east-west direction, with the appearance of numerous closely spaced fracture zones striking in the new direction of spreading (Vogt & Avery, 1974 ; Voppel & Rudloff, 1980). These were interpreted as an attempt by the Reykjanes ridge to attain a minimum work configuration, most quickly achieved by splitting into numerous normally-spreading ridge segments sep-

arated by fracture zones. These disappeared by anomaly 7 time, when spreading about the Reykjanes ridge became oblique. Nunns (1980) attributed the disappearance of the fracture zones in the Reykjanes basin with the reorientation of the Jan Mayen microcontinent in the Norwegian-Greenland sea. This dissipated stresses set up across a dextral offset in the ridge axis south of the Norwegian-Greenland sea by the change in spreading direction. Since anomaly 5 time, spreading in the north Atlantic between the Azores and Iceland has continued uninterrupted about the present axis.

On the basis of the synthesis of the plate tectonic evolution of the north Atlantic presented above, it can be concluded that the present structural isolation of the Rockall Plateau has been achieved by three independent phases of continental rifting and seafloor spreading. Possible spreading in the Rockall Trough during the late-Cretaceous split Rockall Plateau from the UK continental shelf (Roberts *et al.*, 1981). Following a westward jump of the ridge axis to the Labrador sea immediately prior to anomaly 34 time, spreading between the Eurasian plate (including Greenland and Rockall Plateau) and north America formed the east-west transform and adjacent north-south rifted margins which give the south-west Rockall Plateau its rectilinear appearance. Seafloor spreading continued in this mode until anomaly 24 time when the initiation of spreading between Rockall and Greenland resulted in the formation of the Reykjanes basin, and a ridge-ridge-ridge triple junction to the south of Greenland. This final phase completed the isolation of Rockall Plateau. Since anomaly 24, spreading in the Reykjanes Basin has continued uninterrupted about the present axis.

### 1.3 Dipping Reflectors.

#### 1.3.1 General Structure.

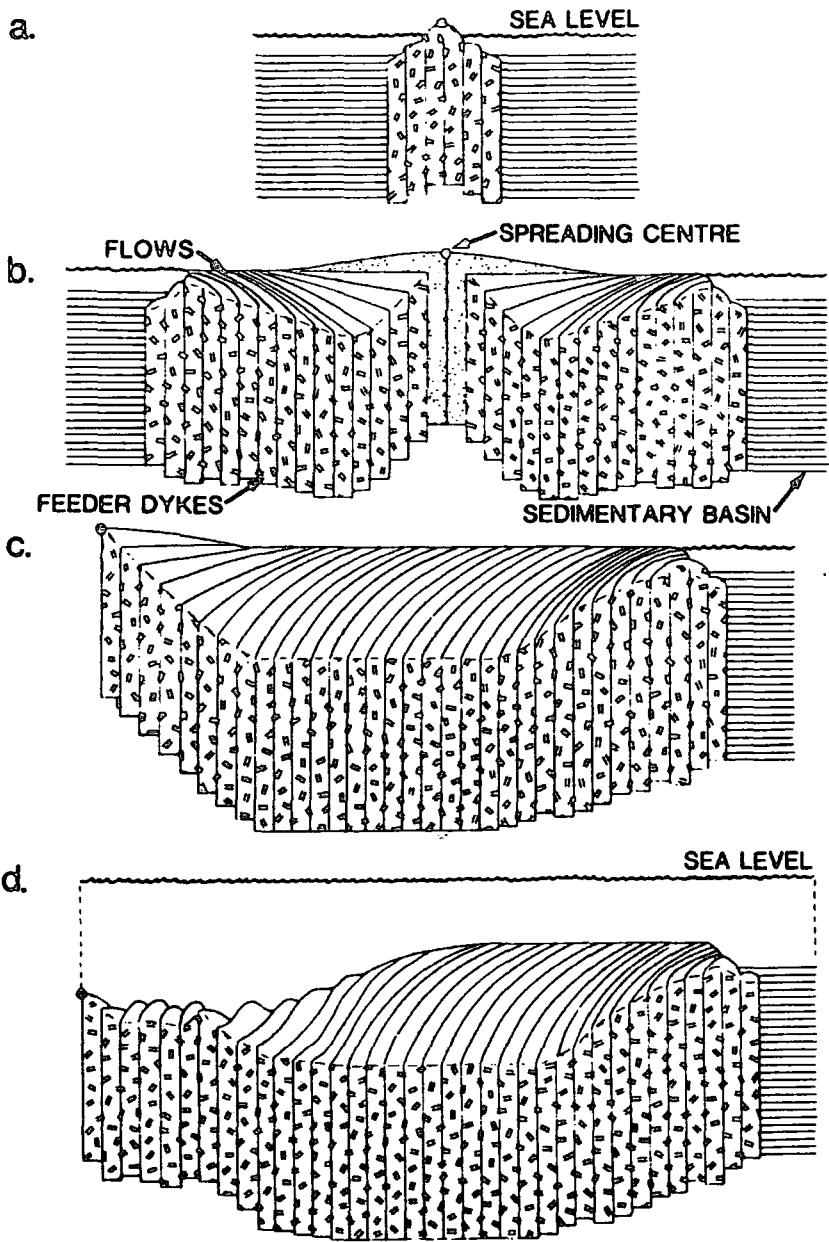
A common problem in understanding the evolution of passive continental margins is the observation that some of these exhibit sequences of seaward-dipping reflectors. The sequences exhibit certain common structural features (Hinz, 1981), although these may vary in detail from location to location. Characteristics commonly associated with the dipping layers include a consistently seaward dip, with individual reflectors diverging down-dip, displaying a gentle upward convexity and down-dip increase in dip. A distinct unconformity is associated with the upper boundary of the dipping sequences, whereas the base is unclear and difficult to define. The seaward limit of the sequences is often indistinct, with individual reflectors becoming weaker and discontinuous. These effects combine to form structures which vary from wedge-shaped seaward dipping sequences such as described by Mutter (1984) on the Norwegian margin, to structures composed of individual offlapping reflectors forming an extended seaward prograding sequence (Roberts *et al.*, 1984). The basement associated with dipping reflector sequences is often unusually smooth, a feature noted by Eldholm & Sundvor (1980) in multichannel seismic data from the Norwegian margin. The mode of formation of the dipping reflector sequences observed on passive continental margins remains in dispute, but they are thought to lie at or near the continent-ocean boundary, and therefore may provide a useful tool in determining its position if a model for their production can be verified. Two principal hypotheses have been put forward to explain the seaward-dipping reflector sequences, and these are described in detail in the next two sections.

### 1.3.2. Mutter's Model - "Subaerial Seafloor Spreading".

By analogy with crustal accretion processes occurring in Iceland (Bodvarson & Walker, 1964), in which individual lava flows combine to produce igneous units exhibiting the arcuate dipping structure characteristic of the dipping reflector sequences observed on the Norwegian and other margins, Mutter *et al.* (1982) proposed a model in which the dipping reflector sequences are formed during the earliest phase of oceanic crustal accretion by a process of "subaerial seafloor spreading". They argued (Mutter *et al.*, 1982 ; Mutter, 1985) that during the early stages of seafloor spreading, exceptionally voluminous production of volcanic material at the active centre may cause the ridge to build up to sea level, where subsequent eruptions of lava are able to flow to a greater lateral extent under the prevalent subaerial conditions. Crustal accretion occurs along a zone of dyke injection centred on the axis of extension, with the distribution of feeder dykes, and therefore the build-up of flows being greatest at the centre of the zone of intrusion. As the crust moves apart, successive flows overlay and depress earlier flows, causing individual flow units to rotate and dip towards the spreading centre. This process continues as long as the rate of lava production remains sufficient to maintain the spreading centre above sea level. Once the spreading centre falls below sea level, flow lengths are reduced, and less extensive lava bodies are produced. Eventually the outflow rate falls to a level consistent with normal mid-ocean spreading centres, with the accretion of normal oceanic crust. This process is illustrated schematically in figure 1.5 reproduced from Mutter (1985).

This hypothesis has several testable implications for the structure of volcanic passive margins. The process of subaerial seafloor spreading takes place entirely within oceanic crust, and consequently dipping reflector sequences produced in this

DIPPING REFLECTORS: SEAFLOOR SPREADING MODEL  
AFTER MUTTER et al (1982).





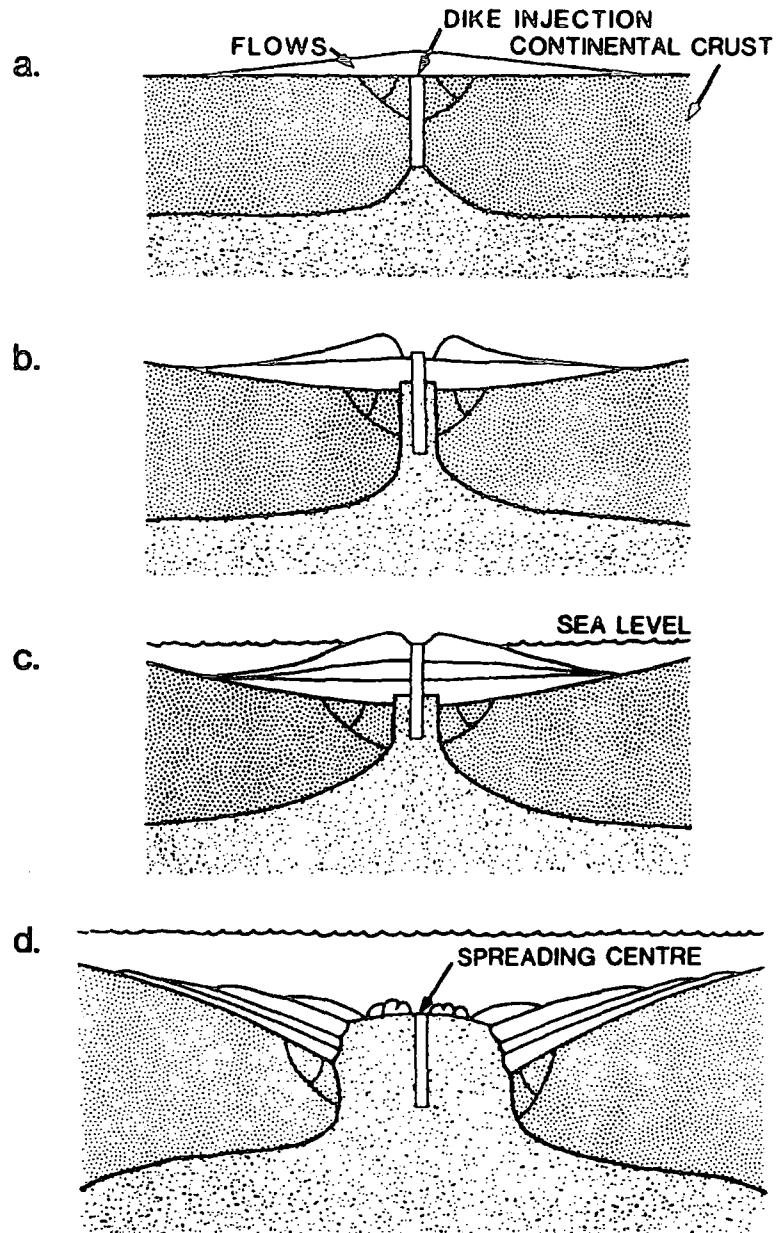
manner will form part of the oceanic crust. The ocean-continent boundary is thus located landward of the dipping reflector sequences. Additionally, since the dipping reflectors thus produced form part of the oceanic crust, it is expected that they would be associated with recognisable seafloor spreading magnetic anomalies. These may not be developed in their typical form due to the difference in basement structure thus formed. The initially high lava production rates postulated would result in the formation of unusually thick oceanic crust, which would thin as production rates fell. The oldest oceanic crust would therefore be expected to be thickest (Mutter *et al.*, 1984). Finally, the model predicts the existence of mirror-image sets of dipping reflector sequences on conjugate passive margins.

### **1.3.3 Hinz's Model.**

Hinz (1981) proposed an alternative model based on the recognition of dipping reflector sequences on passive continental margins throughout the world, and the observation that they appear to be restricted to the landward side of the oldest recognisable seafloor spreading anomaly.

A four stage evolution was proposed which is schematically illustrated in figure 1.6 reproduced from Hinz (1981). During the first stage, stretching and rifting of the continental crust is accompanied by dyke injection and subaerial or shallow water extrusion of lavas along linear zones. Crustal stretching continues, with contemporaneous extrusion of volcanic rocks which build up around the axis of extrusion. Subsidence of the resulting lava pile caused by the loading of existing lavas by flows from subsequent eruptions results in the reversal of dip of the flow units towards the active centre in a manner akin to that described in the subaerial seafloor spreading model of Mutter *et al.* (1982). Continued subsidence due to deep crustal processes

DIPPING REFLECTORS: RIFT STAGE VOLCANIC MODEL  
AFTER HINZ (1981).



and loading by further igneous activity increases reflector dips, and the reduced elevation of the active centre relative to sea level causes decreased flow lengths. The lava pile is subject to continued erosion during all stages, with the redeposition of volcanic debris and sediments between eruptions. Subsequent cooling of the crust causes further subsidence, with reduced outflow of lava until seafloor spreading and the accretion of normal oceanic crust commences.

The model described above is similar to that of Mutter *et al.* (1982) in that it predicts mirror image sets of dipping reflector sequences on conjugate margins, and attributes their seaward dips to the loading of existing flows by lavas from later eruptions. However, it makes radically different predictions concerning the position of the ocean-continent boundary and the nature of the crust underlying dipping reflector sequences. In Hinz's (1981) model the lavas are erupted onto stretched continental crust prior to the onset of seafloor spreading. Consequently the ocean-continent boundary is implied to exist at the oceanward limit of the dipping reflector sequences. The unconformity forming the top of the extrusive sequences therefore marks the onset of seafloor spreading. Clear magnetic anomaly lineations associated with seafloor spreading should be restricted to the seaward side of the dipping reflector sequences, although their constituent magnetic properties might be expected to result in some form of magnetic signature.

A variant of the models presented above was proposed by Smythe (1983). This accepts that the dipping reflector sequences were formed by subaerial seafloor spreading, but with lavas from the earliest eruptions flowing onto continental crust at the onset of seafloor spreading. This model therefore implies an ocean-continent boundary position intermediate to those of Mutter and Hinz, at the oceanward limit of the earliest dipping reflector where it passes into the first feeder dyke. Dipping

reflector sequences therefore form part of the oceanic crust, but lie in part over continental crust.

The Voring Plateau region of the Norwegian margin, and the south-west margin of the Rockall Plateau have been the subject of intense geophysical study in an attempt to determine the nature and process of formation and evolution of dipping reflector sequences observed on volcanic passive continental margins. In the next two sections syntheses of the results and conclusions of these studies are presented.

#### 1.3.4 The Voring Plateau.

The Voring Plateau (figure 1.7) is divided into inner and outer zones by the buried Voring Plateau Escarpment (VPE) (Talwani & Eldholm, 1977) which is thought by some to define the ocean-continent boundary (Talwani *et al.*, 1981 ; Mutter *et al.*, 1982 ; 1984 ; Mutter, 1985). Multichannel seismic reflection profiles have revealed extensive dipping reflector sequences forming a wedge seaward of the VPE on the Outer Voring Plateau (Talwani *et al.*, 1981) (figure 1.7b) . An additional wedge of dipping reflectors was identified seaward of the main unit between the Voring and Lofoten fracture zones, separated from the main wedge by a structural high of diffuse seismic character (Skogseid & Eldholm, 1987). Individual reflectors within the main wedge appear to converge landward, and flatten out to near horizontal adjacent to the structural high of the VPE. At several locations a horizon termed 'K' was identified as possibly marking the transition from feeder dykes to extrusives at the base of the main dipping reflector wedge near the summit of the Outer Voring Plateau (Talwani *et al.*, 1983 ; Mutter *et al.*, 1984 ; Mutter, 1985). Anomaly 24 continues from the Lofoten Basin to the north-east onto the Voring Plateau, and appears to be associated with the main dipping reflector wedge



(figure 1.7) (Talwani *et al.*, 1981). Detailed velocity analysis of multichannel seismic reflection, ESP, and sonobuoy data (Mutter *et al.*, 1984) revealed a velocity-depth structure similar to that of Iceland, which is consistent with that of oceanic crust of up to twice normal thickness. The dipping layers themselves are characterised by a velocity structure typical of greatly thickened oceanic layer 2. A low velocity zone was detected above horizon 'K' for which no explanation has been given.

The evidence required to confirm the volcanic origin of the dipping reflector sequences, and to distinguish between the two alternative interpretations of the nature of horizon "K" was obtained during legs 38 and 104 of the DSDP operations on the Norwegian margin. Leg 38 (Talwani, Udentsev *et al.*, 1976) drilled two holes (338 & 342, figure 1.7), which penetrated the unconformity forming the top surface of the wedge of dipping reflectors on the Outer Voring Plateau. These were found to consist of early Tertiary tholeiitic and alkali basalts similar in composition to the plateau basalts of the north Atlantic Tertiary igneous province (Kharin, 1976). Subsequently, Leg 104 (Leg 104 Scientific Party, 1986), (hole 462, figure 1.7), succeeded in drilling an entire dipping reflector sequence, penetrating horizon "K" forming the base of the sequence, and sampling the upper part of a lower volcanic series. This showed the dipping reflector sequences to consist of a number of tholeiitic lava flows interleaved with volcanoclastic horizons. Horizon 'K' was correlated with a thick pyroclastic sequence which was underlain by the lower series comprising <sup>Basalt to</sup> andesite lava, <sup>the andesite</sup> flows interpreted from strontium isotope analysis as being continentally-derived. This observation is in conflict with the interpretation of horizon 'K' as representing the transition from feeder dykes to extrusives in the subaerial seafloor spreading model of Mutter *et al* (1982).

A model for the formation of the Outer Voring Plateau volcanic margin was

proposed by Skogseid & Eldholm (1987) which incorporated the results of Leg 104 with the ideas of Mutter *et al.* (1982) and Hinz (1981). In summary, they suggested that the evolution of the Voring Plateau consisted of the following main phases summarised in figure 1.8. Continental extension was followed by late Paleocene intrusion and extrusion of magma accompanied by further continental stretching to form the "plateau basalt" sequences underlying horizon 'K'. The onset of seafloor spreading in the early Eocene at a subaerially exposed spreading centre akin to that of Iceland resulted in the formation of the main dipping reflector sequence, with the earliest lava units flowing onto the plateau lavas overlying heavily intruded continental crust. Horizon 'K' corresponds to the boundary between these two extrusive sequences. Finally, following a reorganisation of the plate boundary which produced the oceanward dipping reflector wedges observed between the Voring and Lofoten fracture zones, normal oceanic crustal accretion began in the early Eocene.

This model implies that the main dipping reflector unit of the Voring Plateau was formed as part of the oceanic crust by a subaerial seafloor spreading mechanism, with the earliest flows overlying crust of continental origin. The location of the continental boundary was restricted to the region between the VPE and the landward flank of anomaly 24B. Skogseid & Eldholm (1987) considered that the determination of the position of the ocean-continent boundary within this region is a matter of definition since the crust is likely to be highly intruded, and suggest that its description as transitional in nature between oceanic and continental is more appropriate. They conclude that neither model of Mutter *et al.* (1982) and Hinz (1981) completely accounts for the observed structure of the main dipping reflector unit adjacent to the continental margin since, despite its formation by a process of oceanic crustal accretion, part of the wedge overlies crust which, although possibly

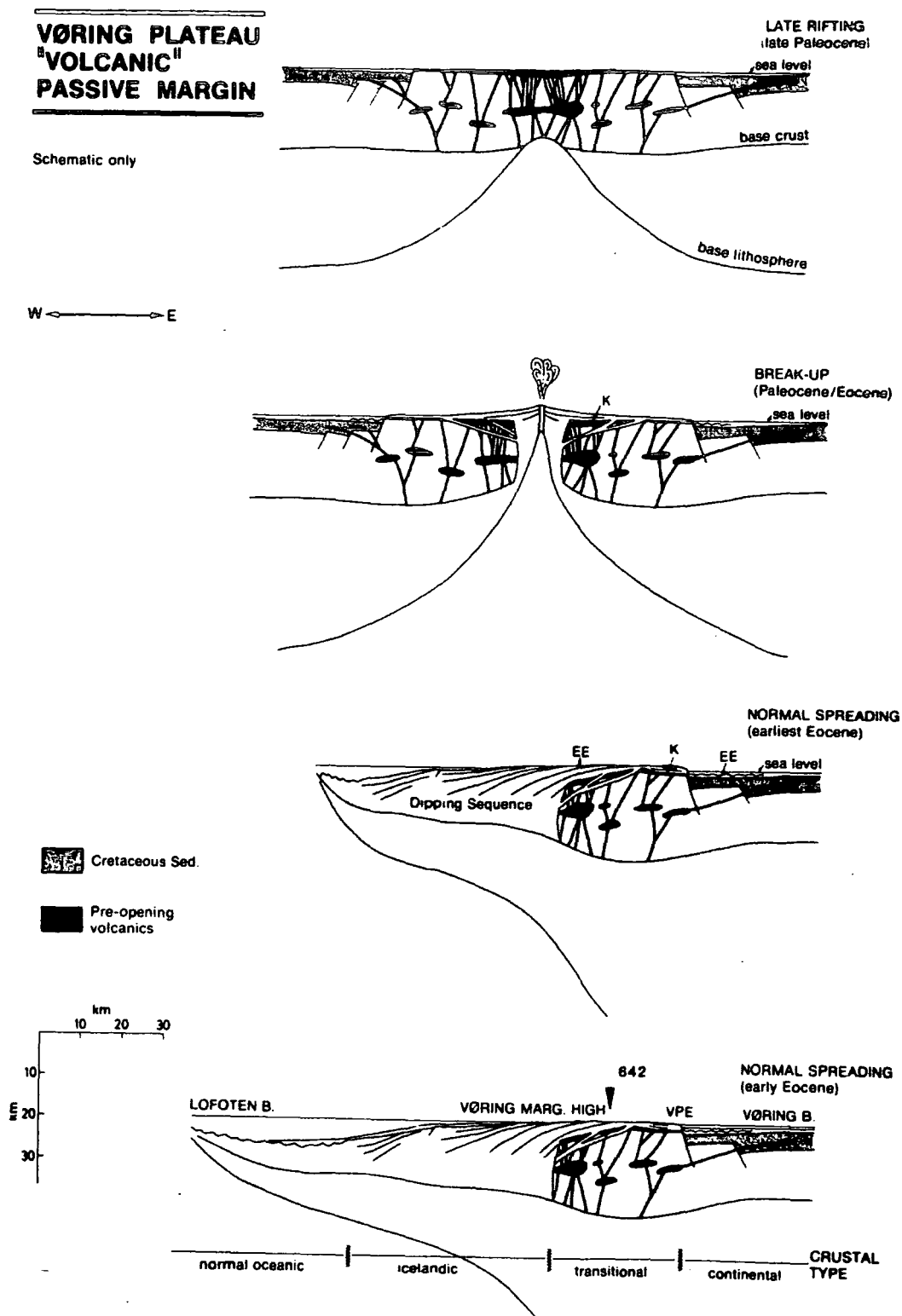


**Figure 1.8** Schematic illustration of early Tertiary formation of Voring Plateau passive continental margin. Structural position of DSDP Leg 104 site 642, and horizon "K" shown. (Reproduced from Skogseid & Eldholm, 1987).



of continental origin, is likely to be so heavily intruded as to make its classification meaningless.

### 1.3.5 The Rockall Plateau.

A suite of dipping reflectors were identified on the south-western margin of the Rockall Plateau underlying a distinct seismic unconformity (Roberts *et al.*, 1979 ; 1984) as illustrated in figure 1.10. On the basis of the high interval velocities associated with the sequence, and the nature of the overlying sediments (sampled during DSDP Leg 48), it was concluded that these were composed of a sequence of interbedded clastics and extrusives possibly up to 7 km in thickness. The structure of the reflectors varies along margin strike. On some profiles they flatten with depth, whereas on others they appear to diverge (Roberts *et al.*, 1984). The sequences ubiquitously terminate against a linear ridge or "outer high". Schuepbach & Vail (1980) suggested that outer highs form as a result of thermo-mechanical uplift of continental basement along a narrow longitudinal zone within a rift graben during a late rifting phase immediately preceding the formation of the first oceanic crust. The basement high thus formed splits longitudinally on initiation of seafloor spreading to form outer highs of continental origin on conjugate continental margins. West of the outer high on the south-west Rockall Plateau margin, oceanward dipping reflectors are observed in undisputed oceanic crust. However these are of more impersistent character than those east of the outer high (Roberts *et al.*, 1984).

The DSDP drilled several holes on the south-western Rockall Plateau in order to attempt to determine the origin and structure of the dipping reflector sequences and the outer high. DSDP Leg 48 (Montadert & Roberts, 1979) attempted unsuccessfully to penetrate the dipping reflector wedge in two locations (holes 403

# Rockall Plateau, Bathymetry.

61°N  
13°W

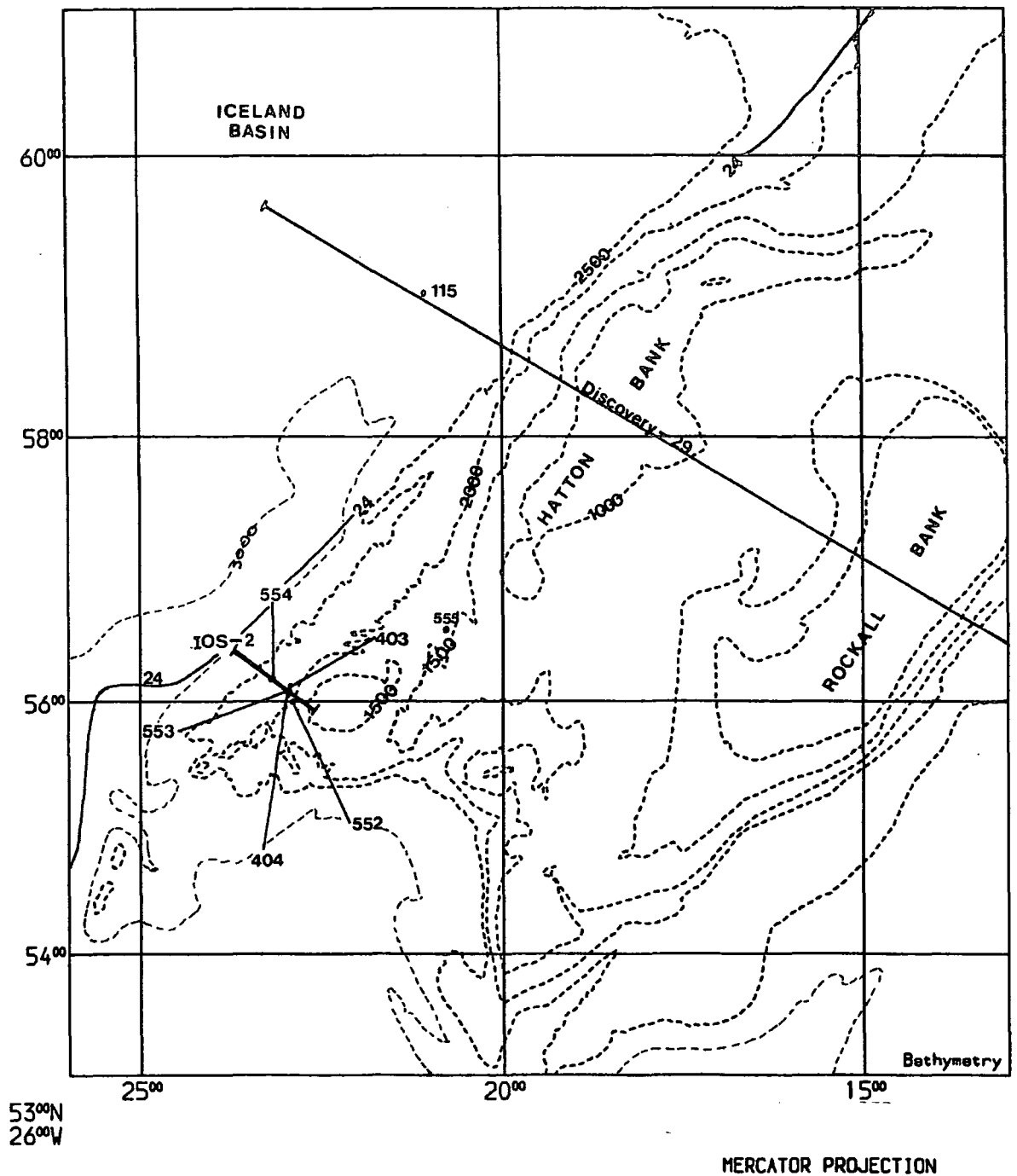


**Figure 1.9** Map of Rockall Plateau region, north Atlantic showing anomaly 24, DSDP Legs 12, 48, & 81 drill sites, and position of MCS lines Discovery-29, and IOS-2. (Redrawn from Scrutton, 1972 ; Roberts *et al.*, 1984 ; Magnetic anomaly lineations from Vogt & Avery, 1974 ; Voppel *et al.*, 1978).

& 404, figure 1.9). They concluded, from observations described earlier, that the sequence consisted of interbedded clastics and extrusives. Leg 81 penetrated the dipping reflectors in two positions (holes 552 & 553, figure 1.9) on the south-west Rockall Plateau (Leg 81 Scientific Party, 1982). At site 552 a single volcanic flow was sampled at total depth which was found to consist of tholeiitic basalt. Site 553 penetrated the upper 183 m of a sequence of volcanic flows which were similarly found to consist of tholeiitic basalt. The tops of the basalt sequences encountered during drilling were correlated with a high amplitude seismic event defining the top of the dipping reflectors. Paleomagnetic and radiometric measurements imply that the basalts comprising the dipping reflectors were erupted during the reverse polarity interval between anomalies 25 and 24B (Roberts *et al.*, 1984). Lead isotope analysis of the basalts from site 553 showed that they contain a component of lead derived from a continental source (Morton & Taylor, 1987), from which it was concluded that the dipping reflectors were extruded through continental crust. The structure of the dipping reflector sequences underlying site 553 imply eruption from a position seaward of their present location, suggesting that they overly crust of continental affinity. Landward of the dipping reflectors, a sequence of strong, flat-lying reflectors was penetrated at site 555 during DSDP Leg 81, and found to correspond to late Paleocene subaerial or shallow marine flood basalts of varying thickness (Roberts *et al.*, 1984).

DSDP Leg 81 site 554 (figure 1.9) was located on the crest of the outer high in order to determine its nature and origin. This encountered a sequence of basalts interbedded with sandstones and conglomerates formed by the weathering and break-up of the top surfaces of the basalt flows in a shallow marine environment. Anomaly 24B is observed to partly overlap the outer high. These observations suggest that

the outer high adjacent to the south-western margin of the Rockall Plateau was formed as result of igneous activity associated with the onset of seafloor spreading rather than during a late rift phase of uplift of continental basement prior to the onset of seafloor spreading (Roberts *et al.*, 1984).

Gravity models across the Hatton-Bank margin (Wigginton, 1984) and south-west Rockall margin (Roberts & Ginsburg, 1984) support the conclusion that stretched continental crust underlies the dipping reflector sequences of the south-west Rockall Plateau, although the models were crude in the sense that no immediate deep refraction results were available to constrain lower crustal structures. These and other models are reviewed in greater detail in chapter 4, section 4.2.

Based on Leg 81 results and a synthesis of the geology of East Greenland, Roberts *et al.* (1984) proposed a model for the development of the south-west Rockall margin which is summarised below.

Thin late-Cretaceous and early-Paleocene sediments deposited on Precambrian basement were overlain by lava flows extruded in the early anomaly 25/24B period. This was followed by increased dyke injection and rapid, voluminous eruption of lavas centred at the incipient spreading axis, accompanied by crustal stretching. Subsidence initiated by crustal extension was enhanced by the load of the rapidly accumulating lava pile during this phase. The igneous activity subsequently migrated westward to become partly submarine, resulting in a widespread period of pyroclastic volcanism. This phase preceded uplift of the central part of the rift valley above sea-level which resulted in the creation of the outer high representing the formation of the first oceanic crust in anomaly 24B time. Spreading subsequently continued under shallow marine conditions. This sequence is illustrated in figure 1.10 reproduced

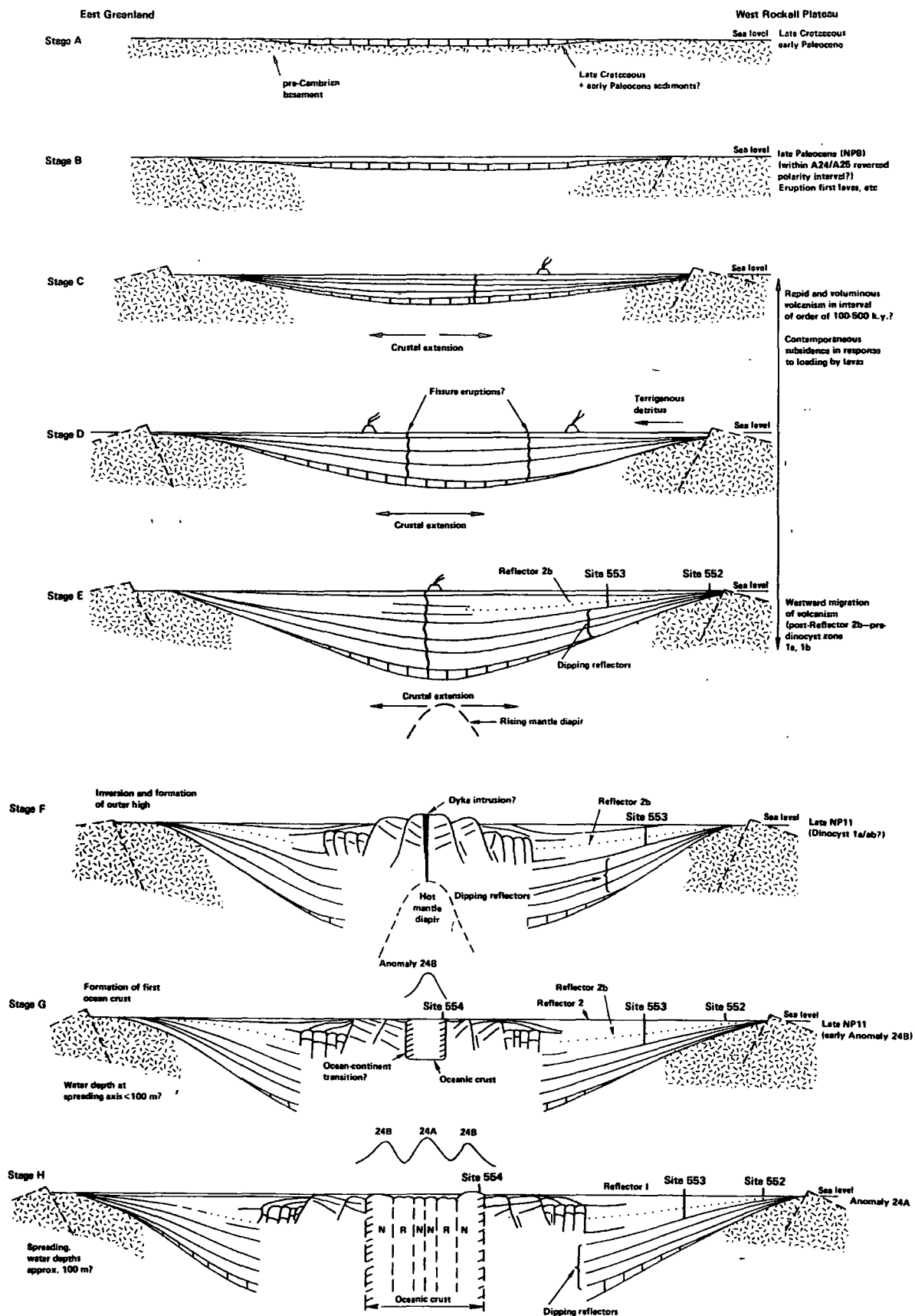


Figure 1.10 Schematic illustration of the sequence of evolution of the south-west Rockall Plateau passive continental margin. (Reproduced from Roberts *et al.*, 1984).

from Roberts *et al.* (1984).

This model implies that the dipping reflector sequences of the south-west Rockall Plateau overlies crust of continental affinity, entirely landward of anomaly 24B and the ocean-continent boundary. However, Roberts *et al.* (1984) suggest that the increasingly intense intrusion of the crust accompanying crustal extension and extrusion of the dipping reflectors would result in a gradual transition within the zone of dyke injection from fully continental to fully oceanic crust. This concept is similar to the proposed transitional nature of the crust between anomaly 24B and the VPE on the Outer Voring Plateau. (Skogseid & Eldholm, 1987) (section 1.3.4). In both cases, neither the model of Mutter *et al.* (1982) nor that of Hinz (1981) provides a satisfactory explanation of the structure of the observed dipping reflector sequences, although the Hinz model comes very close.

#### 1.4 The 1985 Survey, and its Objectives.

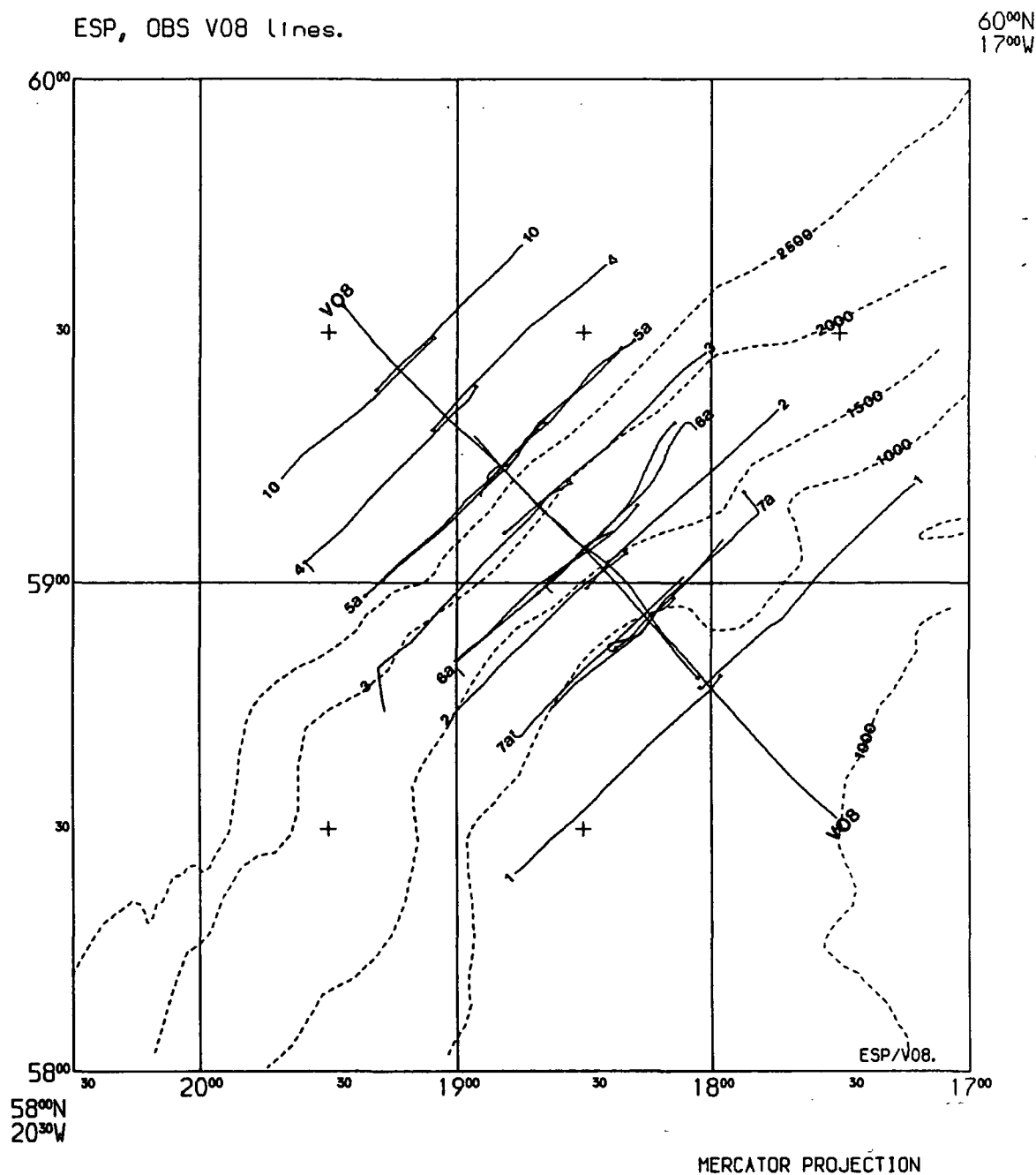
The principal objective of the 1985 Durham/Cambridge two-ship cruise was the detailed investigation of the structure of the continent-ocean transition of the Hatton Bank volcanic passive continental margin. This is a "starved margin" in that the sedimentary cover is very thin or absent, thus allowing maximum resolution of the underlying crustal structure.

In order to map the velocity structure within the crust together with its lateral variations across the continent-ocean transition, a total of eight two-ship expanding-spread profiles (ESP) were shot along margin strike within a 200 km by 150 km box completely straddling the continent-ocean transition. Four of these used explosive sources, and were intended to reveal the deep crustal velocity structure down to the Moho. The remaining four used an airgun source, and were intended to reveal the

details of the shallower velocity-depth structure. A long dip-line was shot through the mid-points of the ESPs using ocean bottom seismometers (OBS) to provide additional constraints on the lateral velocity structure across the margin. The ESP and OBS coverage of the continent-ocean transition is illustrated in figure 1.11. A grid of single-ship multichannel seismic profiles were shot along the ESP and OBS lines to map the thickness and configuration of sediments and upper crustal reflectors within the survey area, and therefore facilitate correction of the ESP and OBS data for variations in the shallow structure (figure 1.12).

Four two-ship synthetic aperture profiles (SAP) were shot across the continent-ocean transition (figure 1.13). The SAP technique aims to provide greater resolution of stacking velocities of deep, weakly reflecting horizons, and thereby improve the quality of the final seismic sections by increasing the effectiveness of the stacking process. The SAP profiles were therefore ideally suited to reveal lateral variations in velocity, and to image the deep crustal structure of the continent-ocean transition. In particular it was hoped to reveal the detailed structure of sequences of seaward-dipping reflectors observed elsewhere on the Hatton Bank margin (eg. Roberts *et al.*, 1984), and determine their position relative to the continent-ocean boundary.

Ancillary objectives included the study of the crustal structure of Hatton Bank, the Hatton-Rockall basin, and Rockall Bank by shooting a single long SAP across Rockall Plateau, and the determination of the velocity-depth structure within the Rockall Trough in order to clarify the nature of the crust underlying Rockall Trough using a single explosive ESP. Underway measurements of bathymetry, and gravity and magnetic fields were made throughout the cruise in order to provide extra constraints on models of crustal structure based on the results of the seismic experiments.



and 10,  
**Figure 1.11** Map showing the explosive ESPs 1-4, airgun ESPs 5a-7a and variable-offset line V08 shot across the continent-ocean transition west of Hatton Bank during the 1985 cruise.



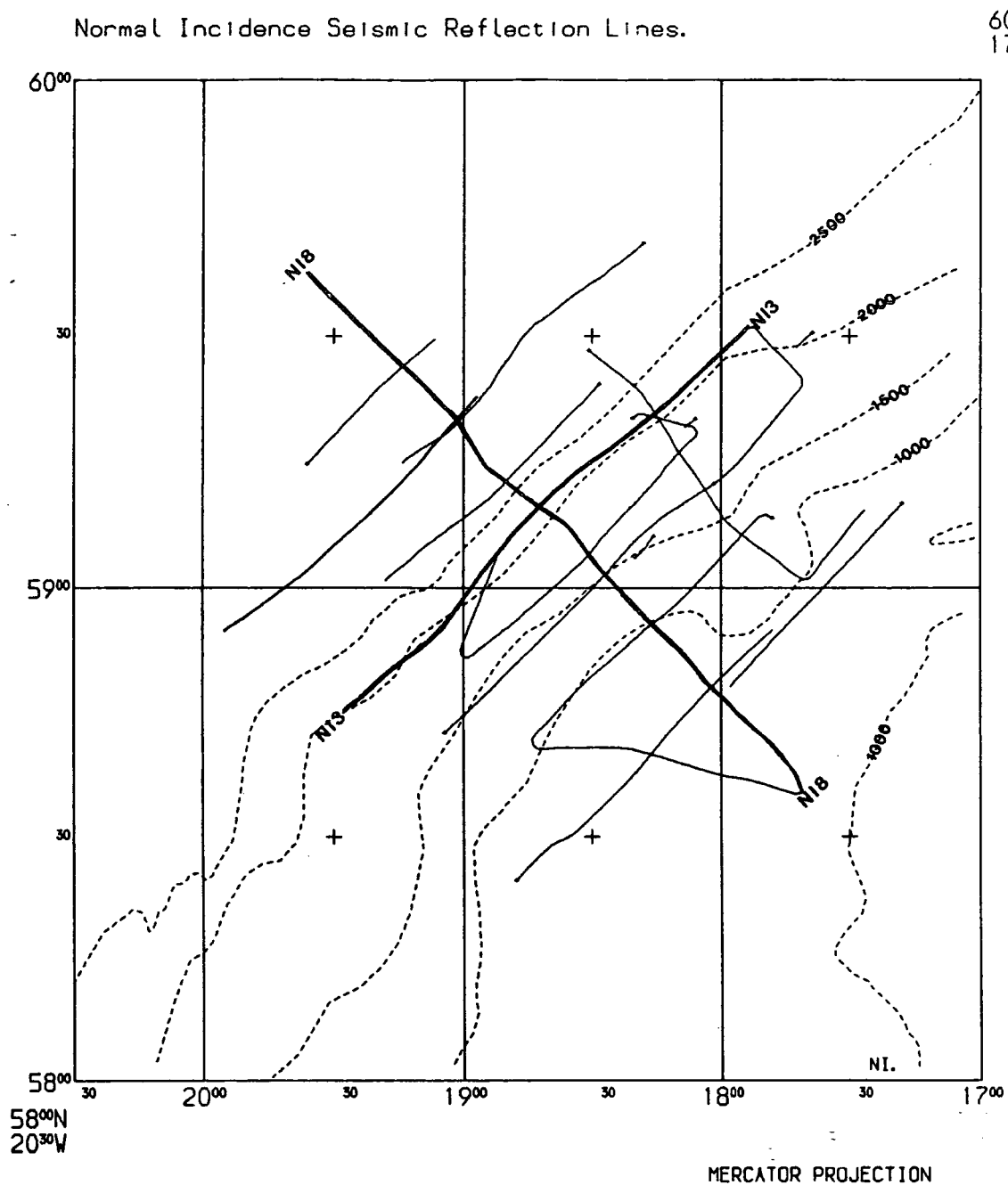


**Figure 1.12** Map showing the grid of normal incidence seismic reflection profiles shot in the vicinity of the continent-ocean transition west of Hatton Bank during the 1985 survey. Lines NI8, and NI3 referred to later in this thesis are indicated.

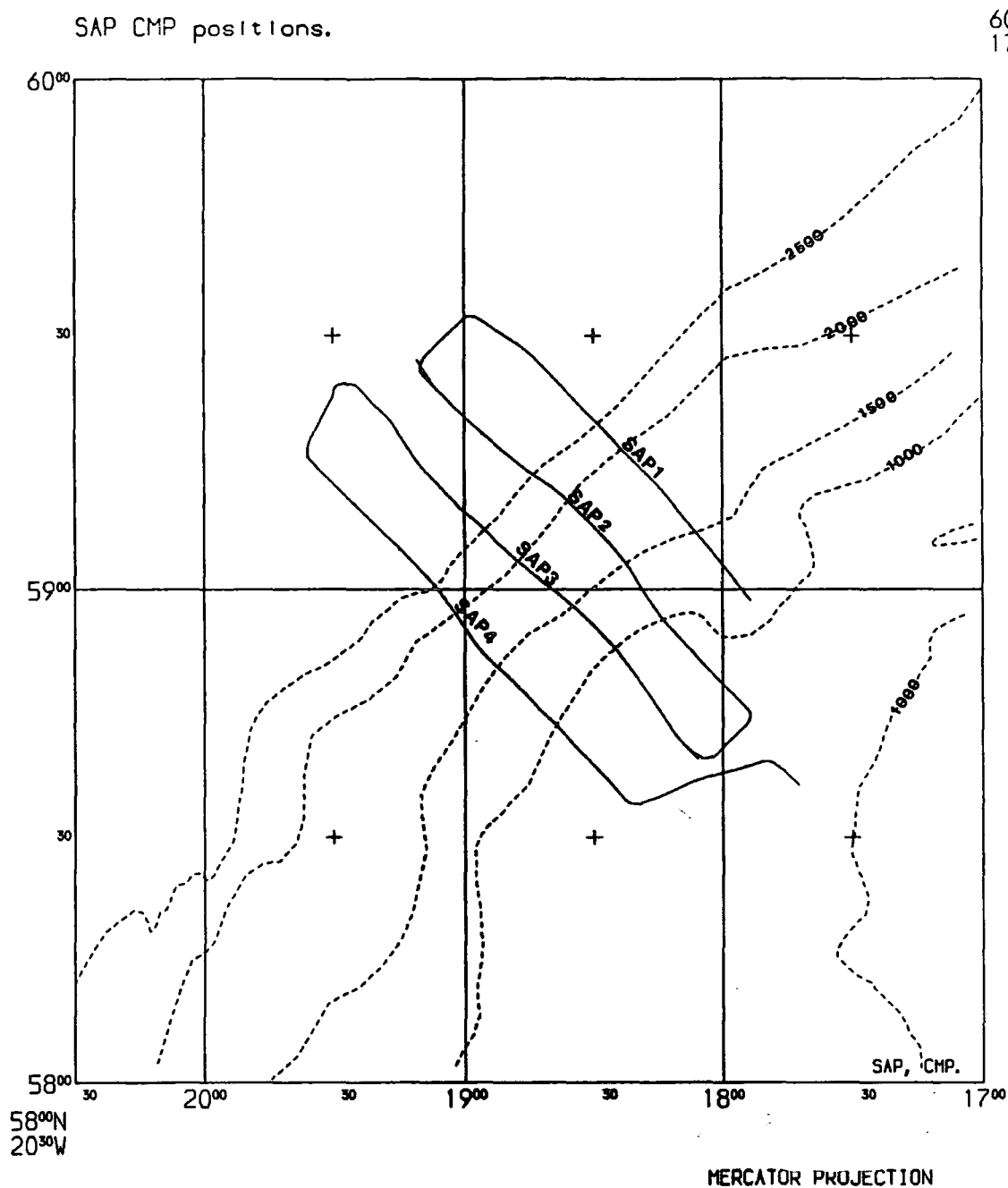


**Figure 1.13** Map showing the four two-ship synthetic aperture profile seismic reflection lines (SAPs 1-4) shot across the continent-ocean transition west of Hatton Bank during the 1985 survey. CMP positions are given on the CMP position chart in the back pocket.

The cruise resulted in the acquisition of large volumes of seismic, potential field, and bathymetric data as illustrated in figure 1.14, which shows the tracks of both ships within the 1985 survey area. These have subsequently been worked on by groups of researchers at Durham, Birmingham and Cambridge Universities. The ESP data, the variable-offset OBS data, and the normal incidence seismic reflection data, have been analysed at the University of Cambridge. Where used, the results of these studies are described within the text, and the relevant source is quoted. The SAP, bathymetry, and potential field data have been processed and analysed at Durham, and form the basis of this thesis.

### **1.5 Outline of present study.**

Chapter 2 describes the techniques of the acquisition of the potential field and SAP data, together with the preliminary reduction of these data prior to further processing and modelling.

In chapter 3 the sequences involved in the processing of the SAP seismic data from the initial demultiplex, through brute stack and velocity analysis, to the final stack stage, are described and illustrated. The digital signal processing techniques used to improve signal:noise ratio and event resolution at relevant stages in the sequence are briefly discussed.

Chapter 4 presents the results of gravity modelling based on the ESP-defined crustal velocity model of White *et al.* (1986). It is shown that a density model based on these results alone cannot reproduce the observed gravity profile across the continent-ocean transition. Additional contributions in the form of density gradients within the underlying upper mantle, based on the results of numerical thermal modelling of the lithosphere, are required to reconcile observed and modelled gravity

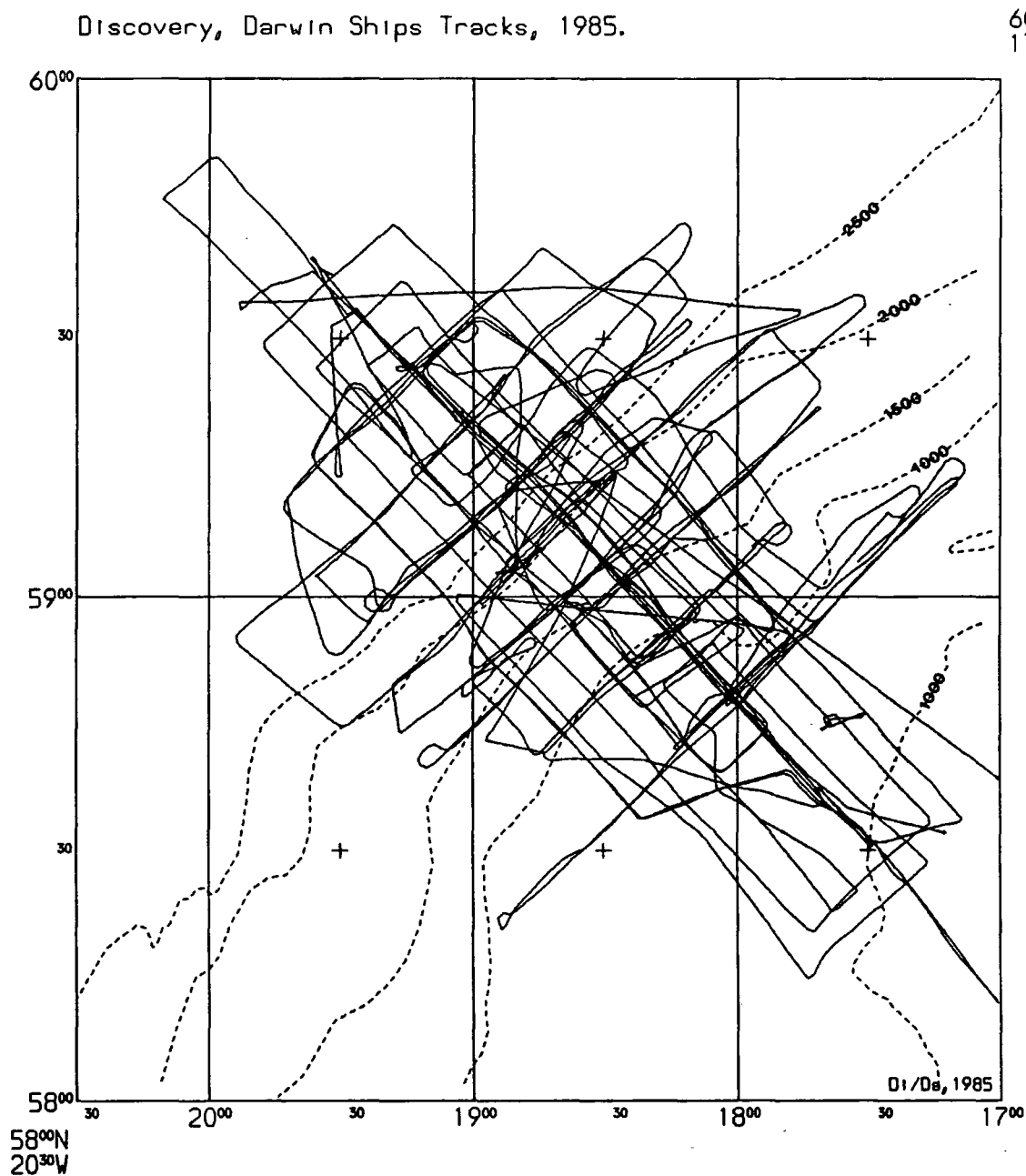


**Figure 1.14** Map showing the RRS Discovery and RRS Charles Darwin ships tracks within the survey area during the 1985 Durham, Cambridge, and Birmingham Universities two-ship cruise to the Hatton Bank continental margin.

anomaly profiles.

Chapter 5 describes the analysis of the magnetic anomaly data. Oceanic magnetic anomalies 21 and 22 are clearly developed in the survey area, whereas anomalies 24 and 23 cannot be clearly identified. Their positions are reconstructed from other known anomaly lineations, and used to infer the location of the continent-ocean boundary west of Hatton Bank. A zone of arcuate, high amplitude anomalies is interpreted as due to extrusive and intrusive igneous activity, and the character of the magnetic anomalies recorded on the continental slope is used to infer the presence of a volcanic basement in this area.

Chapter 6 describes the interpretation of the SAP profiles in terms of three distinct sequences; the continental sequence which consists of lavas extruded onto stretched continental crust, the oceanic sequence which consists of post anomaly 24B oceanic crust, and the late sequence formed as the result of igneous activity on the margin some time after the onset of seafloor spreading. Dipping reflectors formed within each sequence are described. The overlying sedimentary structure is used to infer a lower limit for the timing of the late sequence igneous activity.

Chapter 7 presents a summary of the results presented in chapters 4,5, and 6, together with the discussion of points of interest arising therefrom. A scheme is proposed in which detailed examination of the structure of the seaward-dipping reflector sequences can be used in conjunction with the definition of other geophysical parameters to more accurately locate the position of continent-ocean boundary at volcanic passive continental margins.

## CHAPTER (2)

### Data acquisition and preliminary processing.

In this chapter, a brief description is given of the techniques and equipment used in acquisition of the navigation, bathymetry, magnetic, gravity, and SAP seismic data during the 1985 survey of the continent-ocean transition west of Hatton Bank. Gravity, magnetic, and navigation data were sampled and digitally recorded every second onto magnetic tape by the ships data logger. These data were subsequently reduced and processed according to the descriptions given below by the members of the shipboard computer group whilst at sea.

#### 2.1 Navigation.

Two principal navigation systems were used during the 1985 survey. The first consisted of the TRANSIT satellite navigation system (Stansell, 1978). This system is based on the determination of position by combining a knowledge of the position of a navigation satellite as a function of time with the Doppler shift of a transmitted signal and the motion of the observer. Continuous dead-reckoning between accurate position fixes is accomplished using the ship's heading and velocities measured by the gyrocompass and electromagnetic logs respectively. After receipt of the subsequent fix latitude and longitude corrections are applied to account for the accumulated dead-reckoning error. This system is acceptable provided sufficiently frequent satellite fixes can be made. Six navigation satellites have been placed in polar orbits around the earth. Each of these takes approximately 100 minutes to circle the earth, and is in sight of a particular point on the surface for about 18 minutes. Each satellite is visible on four passes per day, so that about <sup>5-10 usable</sup> 4 fixes can be made per day. This is usually sufficient provided the fixes are suitably spaced in

time.

Loran-C provided the secondary navigation system. This depends on the determination of the difference in time of receipt of a signal broadcast simultaneously from two shore-based transmitters. From this the difference in distance of the two transmitters from the receiver can be determined. The locus of points which have a constant difference in distance from the two transmitters is a hyperbola which is defined by a single measurement. If a similar measurement is made using signals broadcast from a second transmitter pair, a second hyperbola is defined. The intersection of the two hyperbolae corresponds to the position of the receiver. This concept forms the basis of the Loran-C navigation system.

Both systems were logged on both ships throughout the cruise. Subsequently, <sup>for the RRS Discovery,</sup> two magnetic tapes, both of which contained the geophysical data, with either one or the other of the two separate navigation data sets recorded,

were provided in merge-merge format. Data from the RRS Darwin were provided as individual magnetic tapes containing time and a single geophysical or navigational data set. This was due to difficulties in implementing the new international oceanographic data exchange format at RVS Barry. The data thus provided required merging with the navigation data on the basis of recorded time. A program MERGE (appendix A) was written which matched the recorded times of navigation and geophysical data to produce a single data file of time with associated position and geophysical information. These files were stored on a single tape ready for subsequent use.

## 2.2 Bathymetry.

Bathymetry was recorded continuously along ships tracks using a precision echo

sounder. This consists of a “fish” containing an acoustic transducer which was towed alongside the ship at a known depth. The two-way-traveltime of the seafloor reflection was used to determine seafloor depths assuming an acoustic velocity in seawater of  $1.463 \text{ km s}^{-1}$ . This was output on an analogue recorder, and depths were read from this by the scientific watchkeeper at 6 and 10 minute intervals on the Darwin and Discovery respectively. Measured depths were subsequently entered manually into the ship’s data logger. The data were reduced using the Matthews correction to account for the departure of the acoustic velocity of seawater from the assumed value. The Matthews correction takes the form of adjustments for variations in seawater velocity due to factors such as salinity and temperature, which are dependent upon location (Matthews, 1939).

### **2.3 Magnetics.**

Underway total magnetic field intensity was measured and recorded by both ships using proton precession magnetometers. The sensor is contained in a “fish” which is towed behind the ship in order to reduce the disturbing magnetic effect of the ship’s metallic superstructure. A rule of thumb often applied is that a magnetometer towed two ship-lengths behind the ship will experience a magnetic disturbance of about 3 nT, which can be neglected. During magnetic surveying, readings of the total field were taken automatically and recorded at 1 s intervals. Subsequent on-board processing continued with the application of a spike detection filter, and the readings were averaged over one minute. The total field magnetic anomaly was then calculated by subtracting the theoretical total magnetic field intensity as given by the International Geomagnetic Reference Field formula, IGRF ’85, from the observed value, and logged along with relevant position and time. No further reduction or processing, such as correction for diurnal variation, was carried out



apart from the required merging of Darwin navigation and magnetic anomaly data on the basis of recorded time. Separate files of the magnetic anomaly and position data from both ships were stored on 6250 bpi magnetic tape prior to use. The total coverage of recorded magnetic anomaly data on the continental margin west of Hatton Bank is shown in figure 2.1(a),(b). The interpretation of this data is described in chapter 5.

## 2.4 Gravity.

Underway measurements of the earth's gravity field during the 1985 survey were made using heavily damped Lacoste and Romberg gravity meters mounted on a gyroscopically stabilised platform on each ship. The principle of operation of these instruments has been described in detail by Lacoste (1967).

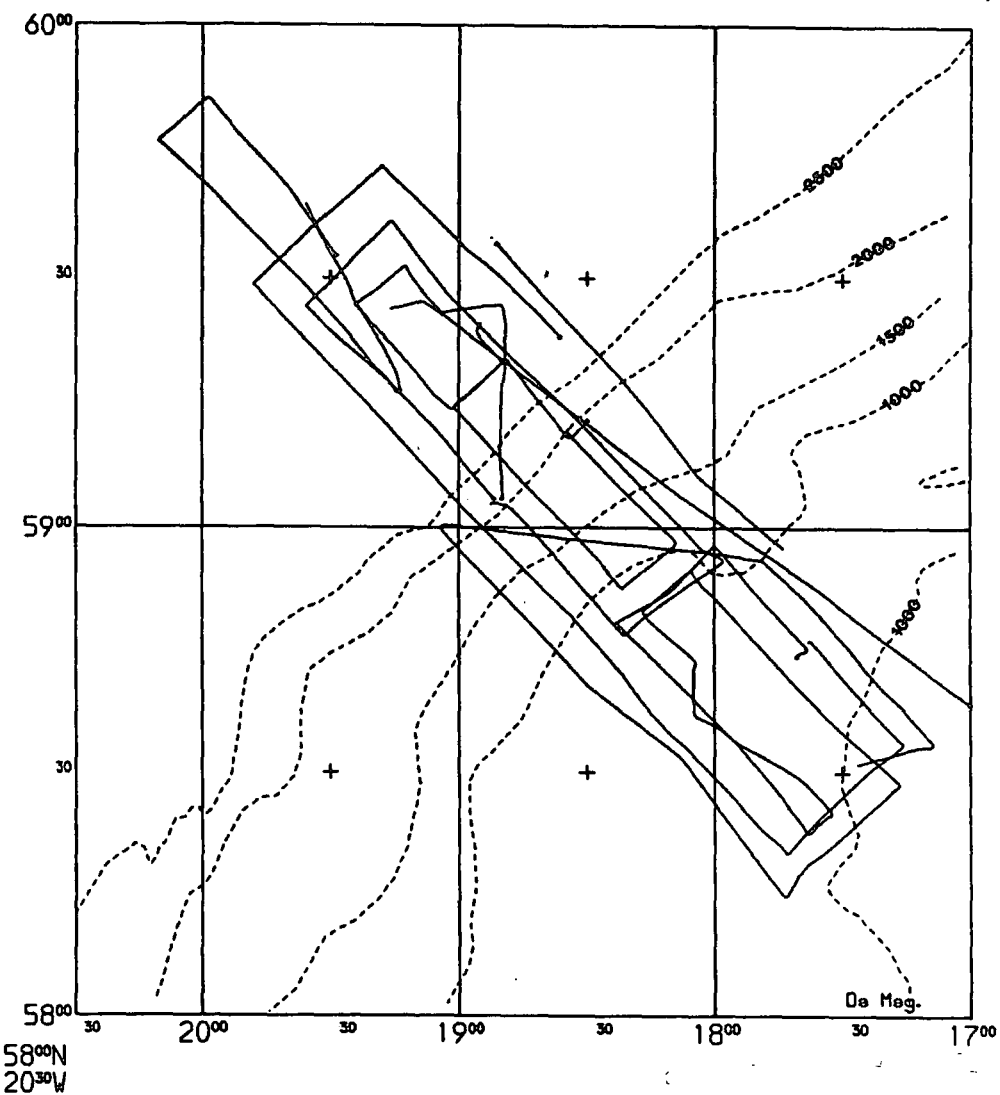
On board ship, the continuously measured effective gravity (the earth's gravity <sup>damped</sup> plus vertical accelerations) corrected for cross-coupling effects, was automatically sampled every second, and averaged over one minute in order to suppress residual vertical accelerations. The average gravity reading was then corrected for the Eotvos effect. The Eotvos correction is applied to counteract for the effect of the variation in the gravity measured by the gravity meter on board a ship which has an eastward or westward component of velocity. These will add to or subtract from the rotational velocity resulting from the earth's rotation, thus changing the centripetal force exerted on the ship, and altering the gravity reading. The Eotvos correction  $dg_e$  is given by

$$dg_e = 7.503 V \cos\phi \sin\alpha + 0.004154 V^2,$$

where  $dg_e$  is in mGals,  $V$  is the ship's speed in knots,  $\phi$  is the latitude, and  $\alpha$  is the ship's heading from true north. The accuracy with which the Eotvos correction can

(a). Rockall Plateau, Darwin Magnetics.

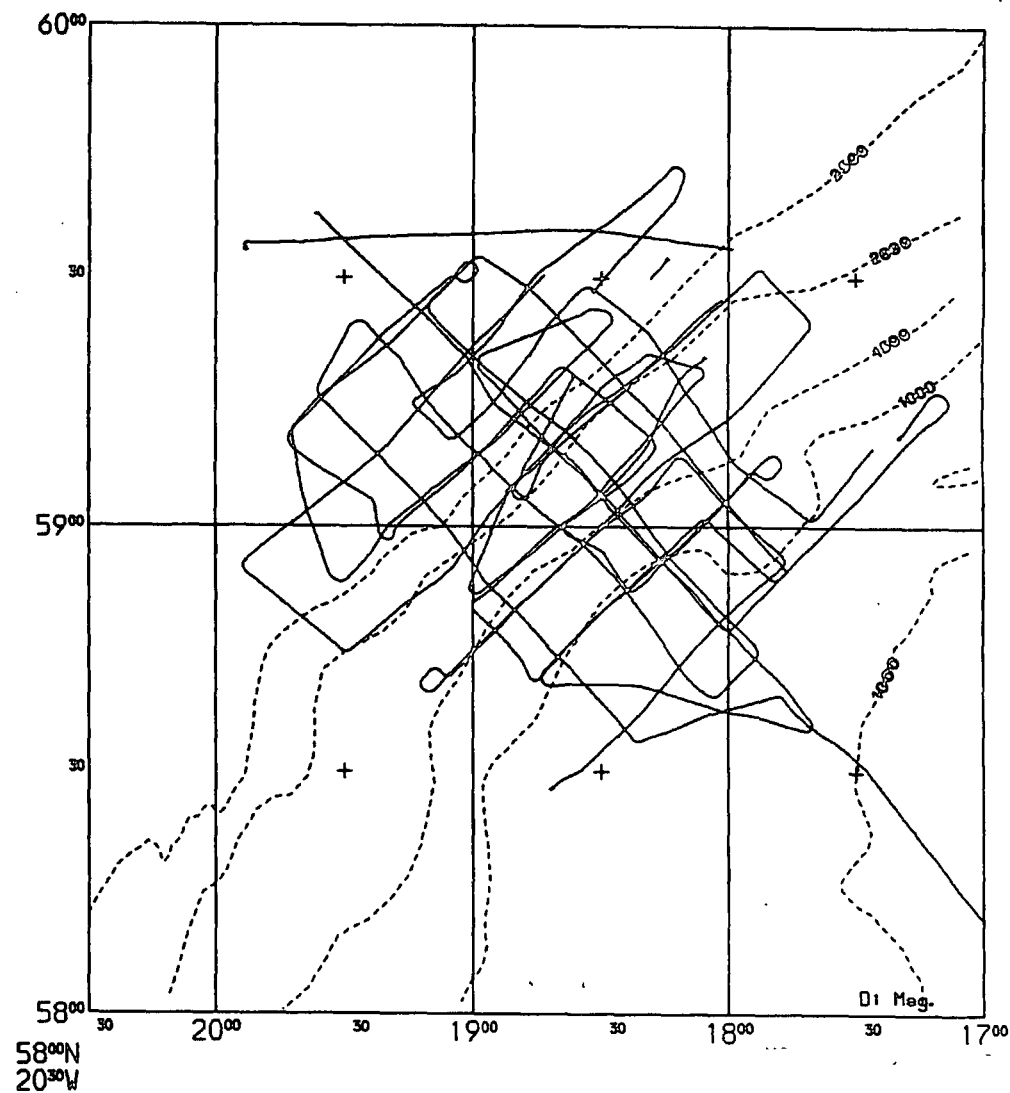
60°N  
17°W



MERCATOR PROJECTION

(b). Rockall Plateau, Discovery Magnetics.

60°N  
17°W



MERCATOR PROJECTION

be made depends upon the accuracy of navigation, heading, and velocity data, and is often the limiting factor in determining the accuracy of marine gravity measurements. The free-air gravity anomaly was subsequently calculated by subtraction of the theoretical gravity field at the position of measurement from the averaged measurement corrected for the Eotvos effect. Theoretical gravity is calculated using the International Gravity Formula of 1967, which gives the variation of normal gravity with latitude on the International Ellipsoid, and is given by  $g(\phi)$  where

$$g(\phi) = 978.049 (1 + 0.0052884 \sin^2 \phi - 0.0000059 \sin^2 2\phi),$$

where  $g$  is in Gals, and  $\phi$  is latitude. The processing and reduction to the gravity data thus described was carried out on board ship using the ship-board computer system.

Since the Lacoste and Romberg gravity meter measures only relative changes in gravity from one location to another, absolute gravity determinations have to be achieved by tying the gravity meter in to a known value of absolute gravity at a given base station prior to embarkation and on return to port. The assumed linear drift of the instrument over the duration of the cruise can then be determined. The details of the various meter constants and tie-ins used during the 1985 survey are given in table 2.1 (a),(b) below. All subsequent processing and reduction of the gravity data was performed at Durham University using the mainframe computing facilities. The Discovery gravity data was provided in merge-merge 3 format on magnetic tape immediately following the cruise. The Darwin data was provided after a delay, and required merging with navigation data prior to further processing. Following the merging of the Darwin navigation and gravity anomaly data, the data from both ships were corrected for drift using the values indicated in table 2.1. Files of drift-corrected gravity anomaly and associated navigation data from both ships

were stored in separate files on 6250 bpi magnetic tape prior to use (appendix B).

**Table 2.1(a).** RRS Charles Darwin.

Meter S84, calibration constant 0.9967. Installed in gravity room, RRS Darwin.

Base Tie Station	Date	Meter Reading	Gravity Transferred to Ship
Ardrossan	14 May 85	12816.0	981575.16
Falmouth	11 June 85	12327.3	981088.50

These figures imply a drift rate of 0.01 mGal/day for meter S84 during the 1985 survey.

**Table 2.1(b).** RRS Discovery.

Meter S40, calibration constant 0.9917. Installed in gravity room, RRS Discovery.

Base Tie Station	Date	Meter Reading	Gravity Transferred to Ship
Glasgow	13 May 85	9868.8	981587.84
Falmouth	10 June 85	9361.0	981089.34

These figures imply a drift rate of 0.17 mGal/day for meter S40 during the 1985 survey.

The free-air gravity anomaly thus calculated contained a component of high frequency noise due to imperfect correction of the ship's motion, and short gaps in data coverage were also present. The readings therefore required interpolating and smoothing prior to further use. A 3-stage program (PROCESS, appendix A) was

written which first searched a given ship's data file for a specified time window of data. The data could be output at the end of this stage, or interpolated linearly during the second stage. Gaps of less than one-hour duration were interpolated and flagged accordingly. Gaps greater than one hour were not interpolated, and flagged as a gap. The data could be output at this stage, or smoothed in the final stage using a moving average operator. The program was written to accept magnetic and bathymetric files as well as gravity files, although the final smoothing stage was not used for these since these data were unaffected by the ship's motion. An example of the use of the program in smoothing a gravity profile along SAP 2 is shown in figure 2.2. The total coverage of ships track along which gravity anomaly data was recorded is shown in figure 2.3(a),(b). The use of the gravity data in modelling the crustal and upper mantle density structure of the continent-ocean transition west of Hatton Bank is described in chapter 4.

## **2.5 Seismic data.**

### **2.5.1 Synthetic aperture profiles.**

The synthetic aperture profile experiment makes use of a multiple source and receiver acquisition geometry to synthesise wide aperture common-mid-point (CMP) data with no gaps in offset coverage (Buhl *et al.*, 1982). In its simplest form, as used during the 1985 survey, the technique employs two ships which sail along the same course at a fixed separation equal to two array lengths, both of which shoot alternately into a single multichannel receiving array towed by the leading ship. This enables the synthesis of an effective array length of twice that actually used. Doubling the source-receiver offset range enables more accurate velocity analysis to be performed on weak reflections from deep, high velocity horizons within the crust

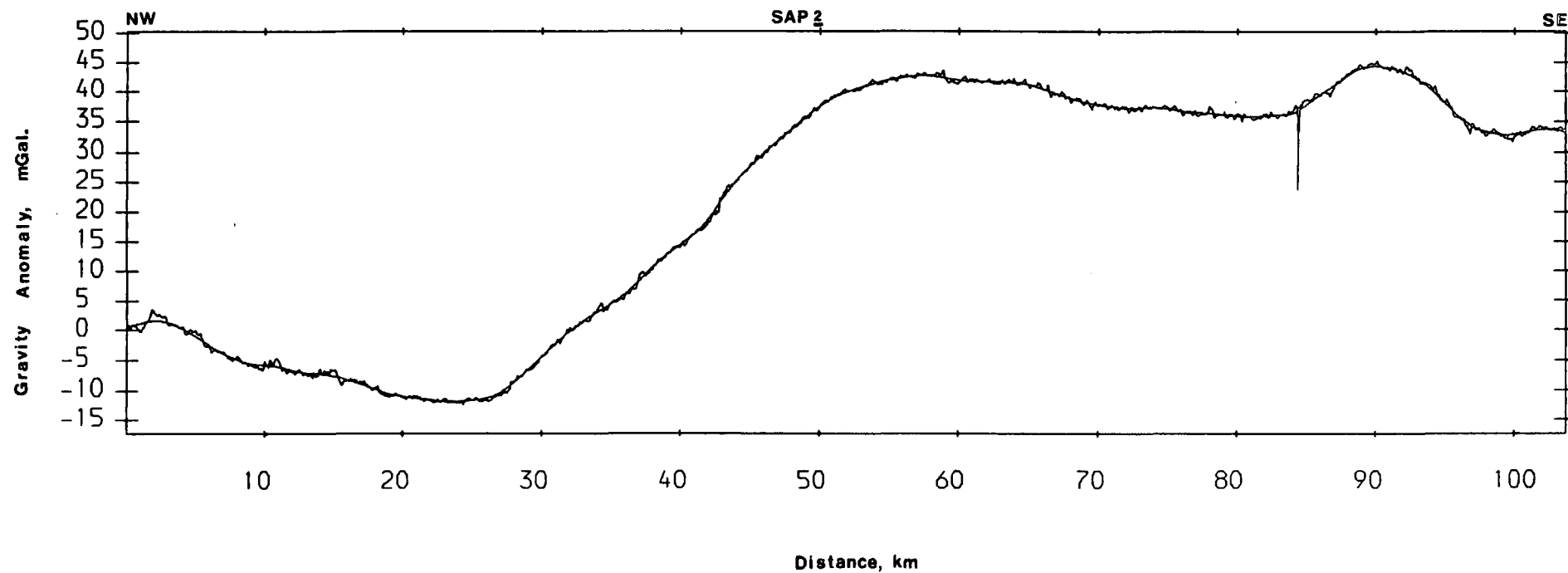
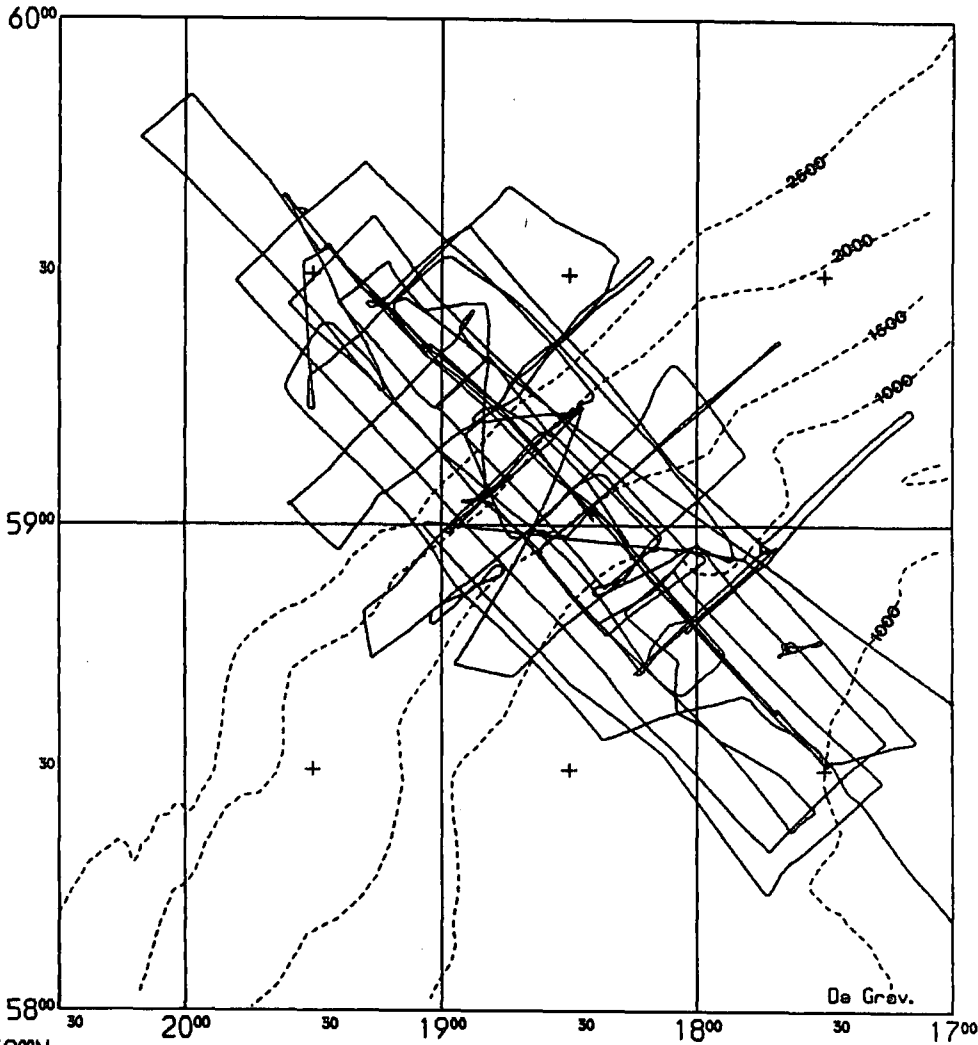


**Figure 2.2** Gravity anomaly data recorded by RRS Charles Darwin along SAP 2 (figure 1.13), smoothed using a 61 sample moving-average operator.

(a). Rockall Plateau, Darwin Gravity.

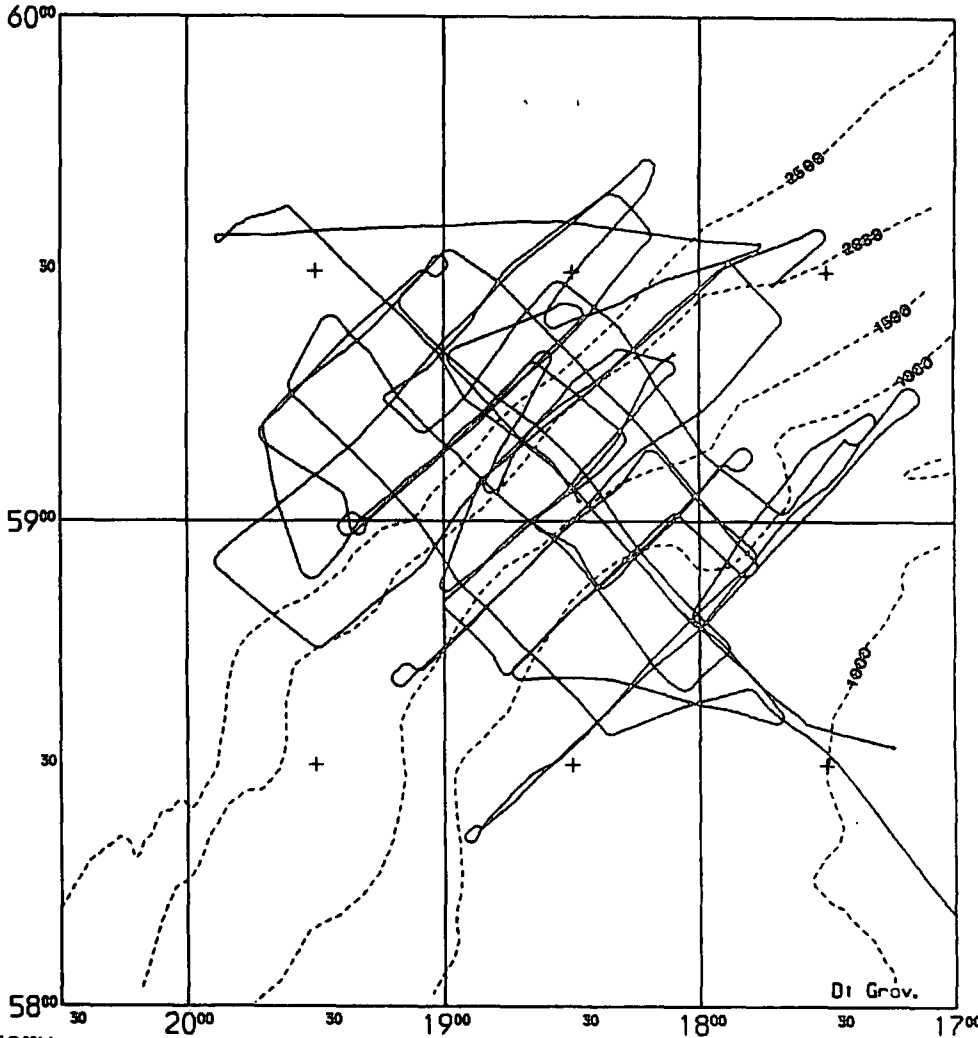
60°N  
17°W



MERCATOR PROJECTION

(b). Rockall Plateau, Discovery Gravity

60°N  
17°W



MERCATOR PROJECTION

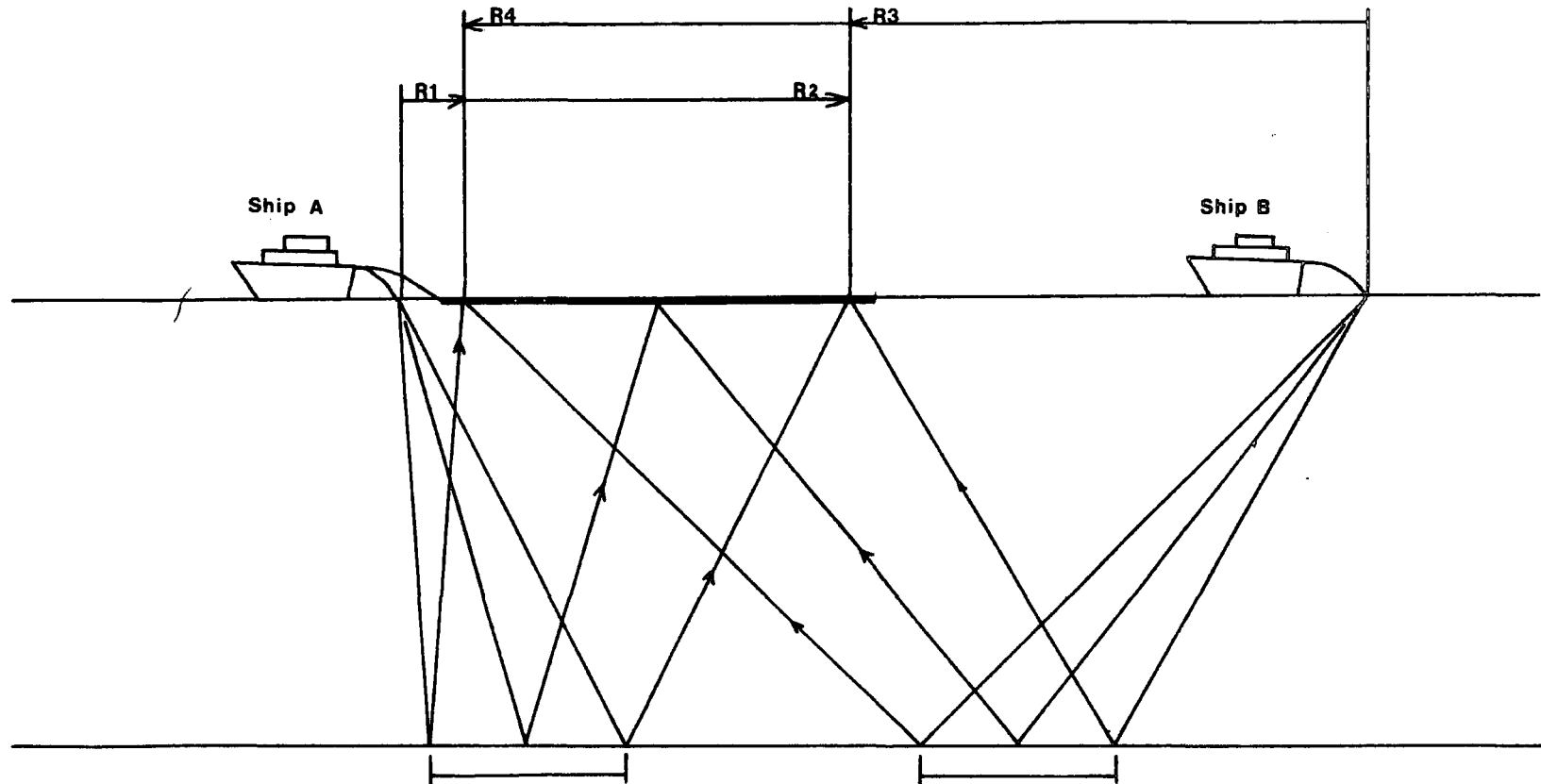
which have a small differential "move-out" of travel time with increased source-receiver offset. Thus the effectiveness of the final stack is increased (chapter 3). The principle of the SAP technique is illustrated in figure 2.4 which shows the acquisition geometry used during the 1985 survey to shoot four SAPs across the continent-ocean transition west of Hatton Bank (figure 1.13).

During the 1985 survey, both ships used identical airgun arrays which comprised individual 1000, 466, 300, and a 160 cu in capacity airguns pressurised to approximately 1950 psi towed behind the ship. Each ship fired alternately every 40 s, so that a shot was fired every 20 s. The receiving array was towed by RRS Discovery as the leading ship, and comprised a Teledyne Exploration Hydrostreamer with 96 hydrophone groups arranged in sets of four within each 100 m section of streamer, which had a total length of 2.4 km. Six depth sensors and levelers spaced along the streamer were used to maintain the array at its optimum operating depth when in use. An auxiliary channel was connected to a single hydrophone at the beginning of the streamer which acted as a water break channel to measure the separation of the source and receiver. During profiling, bearings of the tail-buoy of the streamer were taken to provide an estimate of the streamer "feathering". This effect is due to cross-currents which cause the streamer to follow a path which is offset from that of the towing ship. The array was configured to give forty-eight 50 m active sections. With the ship steaming at 4.7 knots and a shot interval of 20 s, a shot spacing of 50 m, equal to a single receiver group spacing, was achieved. The CMP data thus acquired has a fold of cover of 24. The ship-to-ship range was measured using a trisponder ranging system. This comprised a master transmitter aboard the RRS Darwin which broadcast an interrogating signal to a slave transmitter on board the RRS Discovery. On receipt of the interrogation signal, the slave immediately em-



Offset coverage from ship 'B' shot =  $R3 - R4$ .

Offset coverage from ship 'A' shot =  $R1 - R2$ .



Sub-surface coverage of ship 'A' shot.

Sub-surface coverage of ship 'B' shot.

Figure 2.4 Synthetic aperture profile acquisition geometry.

mitted a reply signal which was detected by the master. The time between initial transmission and subsequent receipt of the return signal provided a measure of the ship separation. Trisponder ranges were continuously monitored and used to effect the Darwin course and speed changes necessary to maintain a fixed ship separation. Trisponder ranges were recorded on the Darwin shipboard data logger.

Seismic energy reflected from underlying horizons was detected by the multi-channel array and logged using a SERCEL SN385 portable seismic data acquisition system. This is a dedicated data logging system which digitised and recorded the input signals at a 4 ms sampling rate on to 8 inch, 1600 bpi magnetic tapes in SEG-B format (Northwood *et al.*, 1967). Filters were provided for each of the 48 channels. These consisted of an 8 Hz low-cut filter, a high-cut 77.2 Hz antialias filter, and a 50 Hz notch filter, each of which could be selected as required. The SERCEL acquisition system synchronised the firing of both airgun arrays. It generated a fire pulse at the required time interval to fire the Discovery airguns. Darwin guns were fired remotely by using a tone break system controlled by the SERCEL. This consisted of a VHF radio link between the two ships. The transmitter aboard the Discovery broadcasted a continuous frequency tone which was broken by the SERCEL fire pulse at the required Darwin shot instants. A receiver on Darwin detected the breaks in tone and generated a fire pulse to trigger the airgun array.

Following the cruise, the SEG-B multiplexed SAP seismic data were transported to the department of Geological Sciences at Durham University, where subsequent processing of the data was performed using the dedicated seismic reflection processing system of the Department. The processing of the data and its subsequent interpretation is described in detail in chapters 3 and 6 respectively.

### 2.5.2 Expanding spread profiles.

The Expanding Spread Profile (ESP) data have been processed and analysed at the University of Cambridge by Sue Fowler, George Spence, and Bob White. Since the results obtained from these studies have been used in various parts of this thesis, a brief description of the ESP technique will be given here.

In contrast to the two-ship SAP experiment where both ships maintain a constant separation and steam along the same course, the ESP technique uses two ships which steam away from each other at the same speed, one ship (RRS Darwin) shooting at regular intervals, the other (RRS Discovery) receiving the wide-angle reflections and refractions from the underlying crustal structure. The acquisition geometry is such that all received arrivals bottom at the same common-mid-point between the two ships (figure 2.5). Thus the experiment yields wide aperture common-mid-point data which can be inverted and modelled to derive detailed velocity-depth information at a single geographical location (Stoffa & Buhl, 1979). Depending upon the power of the sources used, source-receiver offsets of up to 100 km can be successfully used.

During the 1985 survey, four explosive ESPs designed to image the deep velocity structure of the continent-ocean transition were shot along the strike of the margin west of Hatton Bank. These were positioned successively down the margin from the continental shelf to the adjacent ocean basin, and interweaved with six airgun ESPs designed to determine the detailed upper crustal velocity structure of the margin (figure 1.11). During shooting of the explosive ESPs, charge sizes ranged from 2.1 kg at the closest offsets, to 100 kg at the farthest offsets of up to 100 km. Both ships steamed at 5 knots, with a shot interval of 7 minutes, resulting in the ships separating by approximately one

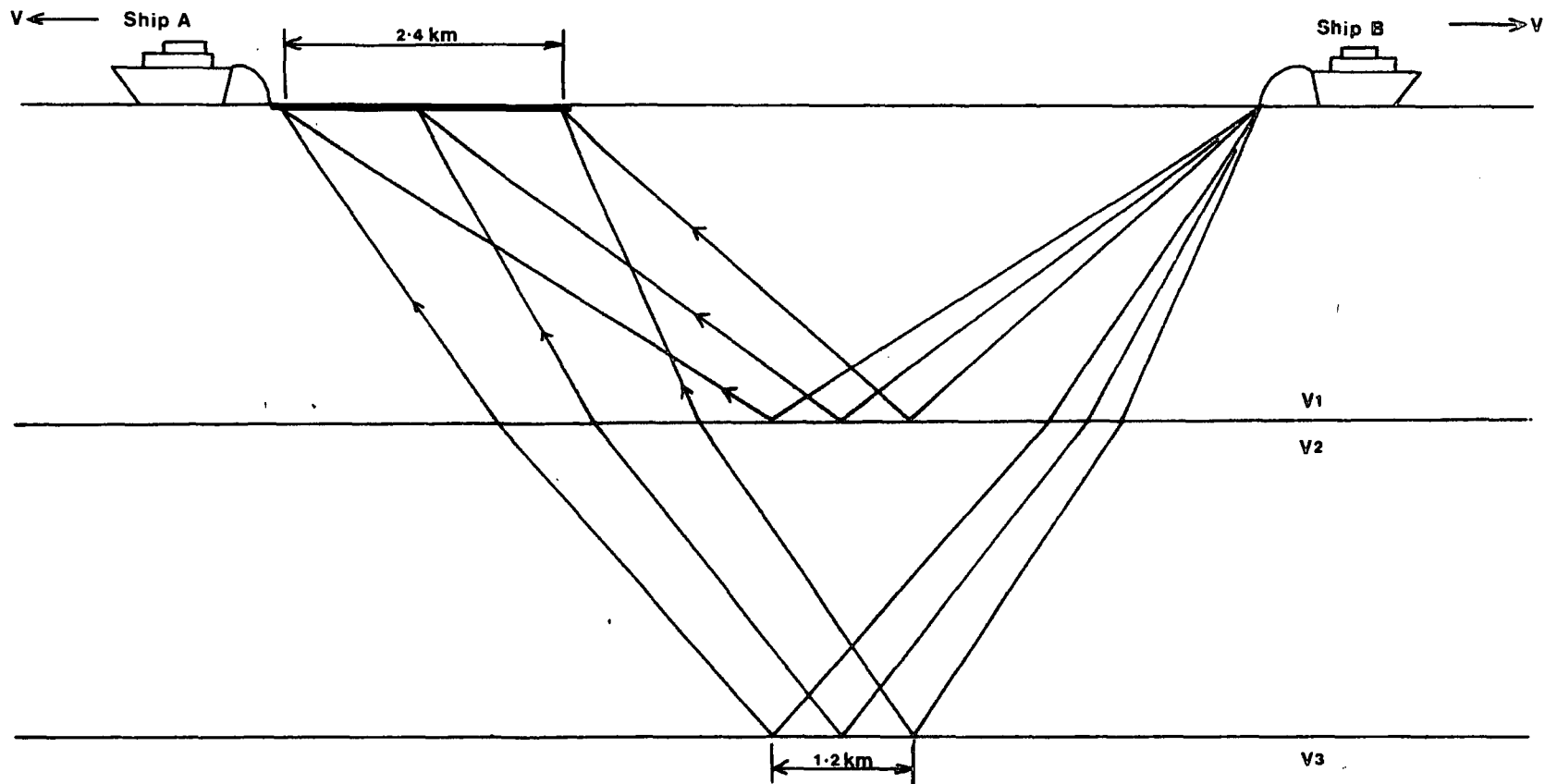


**Figure 2.5** Expanding spread profile acquisition geometry. Ship 'B' shoots into receiving array towed by ship 'A'. The reflection zone does not move as the ships separate. Horizontally travelling refractions are also recorded but are not shown.

array length<sup>every shot.</sup> During shooting of the airgun ESPs, the source comprised a 5-gun array of three 1000 cu in, and two 300 cu in airguns pressured to approximately 1950 p.s.i. These were fired every 60 s, so that at a ship speed of 5 knots, eight shots could be fired within a single array spacing. The airgun ESPs were shot out to a source-receiver separation of 35 - 40 km. The 48 channel output from the receiving array was recorded at a 4 ms sampling rate using the SERCEL acquisition system.

The processing, modelling and interpretation of the airgun and explosive ESP data was carried out at the University of Cambridge, a detailed account of which is given by Spence *et al.* (1988) and Fowler *et al.* (1988) respectively.

## CHAPTER (3)

### Processing of synthetic aperture (SAP) data.

#### 3.1 Introduction.

The purpose of the seismic reflection technique is to produce an accurate cross-sectional image, or seismic section, of the sub-surface seismic structure of the survey area, which can subsequently be interpreted in terms of the geological structure it represents.

The acquisition of multichannel seismic reflection data enables sophisticated digital signal-enhancement techniques to be employed during data processing in an effort to improve the quality of the final section, and so facilitate its final interpretation. The process of transforming the raw field data into a final stacked seismic section involves several stages. Demultiplexing of field tapes into common-shot gathers is followed by sorting, where shot gathers are translated into common-mid-point (CMP) gathers. By utilising various velocity analysis techniques on the CMP gathers, stacking velocities can be determined which are used to correct traces within each CMP gather for the effect of increasing travel-time with source/receiver offset, or “move-out”. These “moved-out” traces are algebraically summed or “stacked” to produce a single stacked trace. The ordered arrangement of stack traces forms the final seismic section. Digital signal processing techniques can be used at the velocity analysis, and pre- and post-stack stages in an attempt to improve resolution.

The processing of four synthetic aperture (SAP) seismic reflection profiles acquired across the Hatton-Bank continental margin, through all stages from demultiplex to final stack, was carried out at Durham University using the Department

of Geological Sciences reflection processing system. The velocity analysis of SAPs 1, 2, and 3 were performed by the author, whereas SAP 4 velocity analysis was performed by Dr. A. Bowen. The subsequent job of stacking of the SAPs was shared equally by the author and Dr. A. Bowen.

### **3.2 The processing system.**

#### **3.2.1 Hardware.**

The seismic reflection processing system hardware used to process all SAP data comprised the following. A DEC PDP 11/34 processor running the RT-11 V3.0 SJ operating system with 256 kbytes of memory. This is host to peripheral devices consisting of a Floating Point Systems FPS 120B array processor acting as a high-speed arithmetic device, a 20 Mbyte Pertec disc drive containing the RT-11 system software and acting as storage volume for small parameter and data files, a larger 300 Mbyte Winchester disc drive used to store applications programs and large data files, three dual density 800/1600 bpi tape drives, a Versatec plotter, and a Systime terminal. The system hardware configuration is reproduced from Hobbs (1985) in figure 3.1.

#### **3.2.2 Software.**

The Durham University seismic reflection processing system software has been continuously developed since the original package was written by Poulter (1982). This has been necessitated by hardware modifications, and the changing nature of the data sets to be processed. The current processing system was written by Dr. A. N. Bowen between 1984 and 1987 to deal with the special requirements of two-ship SAP data. The programs fall into the broad categories of demultiplex, sort, velocity

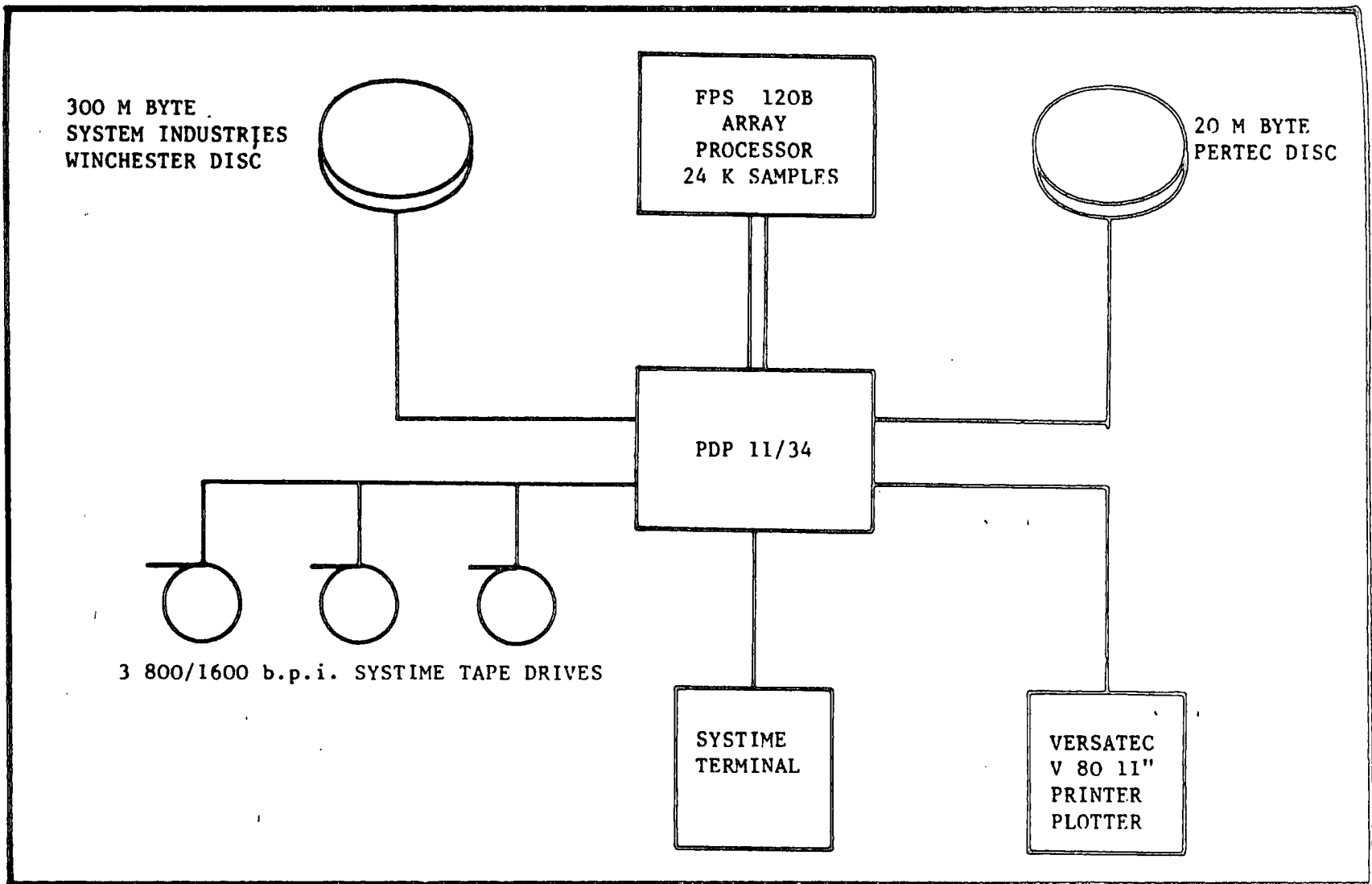


Figure 3.1 Present configuration of the seismic reflection processing system  
(Reproduced from Hobbs, 1985).



analysis, processing, and plotting, with auxiliary disc file and tape drive utilities. Many individual programs are chained so that the user need only invoke a single routine to execute an entire program suite. For a more detailed description of the current processing hardware/software the reader is referred to Hobbs (1985) and Bowen (1987a).

### **3.3 Seismic data processing.**

#### **3.3.1 Demultiplex.**

The demultiplex program (Bowen, 1987b) reads 1600 bpi multiplexed field tapes recorded in SEG-B format (Northwood *et al.*, 1967), and writes 1600 bpi SEG-Y format (Meiners *et al.*, 1972) demultiplexed common-shot gathered tapes. The demultiplexed data is ready for the next stage in the processing sequence, that of sorting into common-mid-point (CMP) gathers.

#### **3.3.2 CMP sort.**

In conventional single-ship seismic reflection profiling, the sorting procedure is a simple matter of re-organising the shot records into CMP bins according to a pattern determined by ship speed, shot interval, and receiver group spacing, all of which are assumed, in the simplest case, to remain constant throughout the profile. The technique is thus termed a "pattern sort".

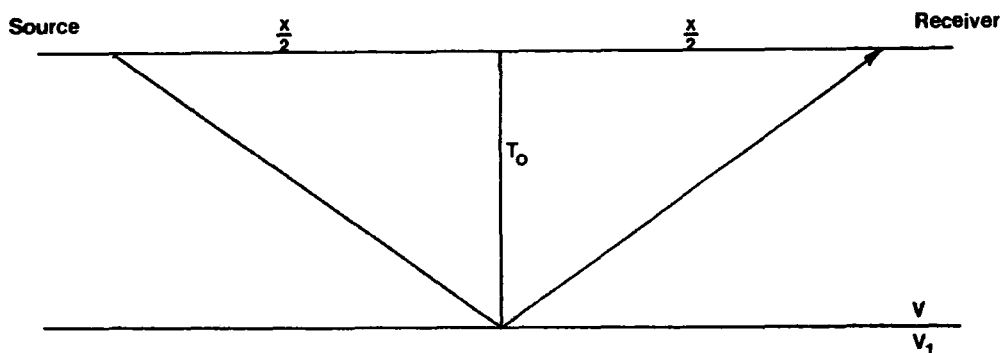
In two-ship CMP profiling these simple assumptions are no longer valid since ranges and bearings between the ships continuously vary. Therefore it is necessary to determine the absolute shot-receiver mid-point position of each trace from navigation data, and subsequently allocate sort traces to CMP bins on the basis of their absolute mid-point positions. This approach ensures that traces are correctly

binned regardless of ship course and speed alterations.

This technique was used at Durham to sort the demultiplexed SAP data into CMP sorted gathers prior to velocity analysis and stacking, using the absolute mid-point location suite of programs developed by Dr. A Bowen (1987c). An example of a typical CMP sorted gather is shown in figure 3.2 .

### 3.3.3 Velocity analysis and CMP stack.

The CMP stack method relies on the application of a correction to non-zero offset traces to account for the effect of increased travel-time with offset within a CMP gather, prior to algebraically summing or stacking the traces into a single zero offset trace. Although the principles and techniques of velocity analysis and CMP stack are well known, a brief description of these will be included here.



For the simple case of a single constant velocity horizontal layer, the travel time between shot and receiver is given by

$$T(x)^2 = T_0^2 + \frac{x^2}{v^2}$$

where  $x$ =source/receiver offset, and  $T_0$  =zero offset travel time.

Reflections from this layer within a CMP gather will therefore lie on a hyperbolic trajectory determined by the layer velocity. This simple concept can be extended to a multiple plane-layer case. In this situation the travel time of rays reflected from

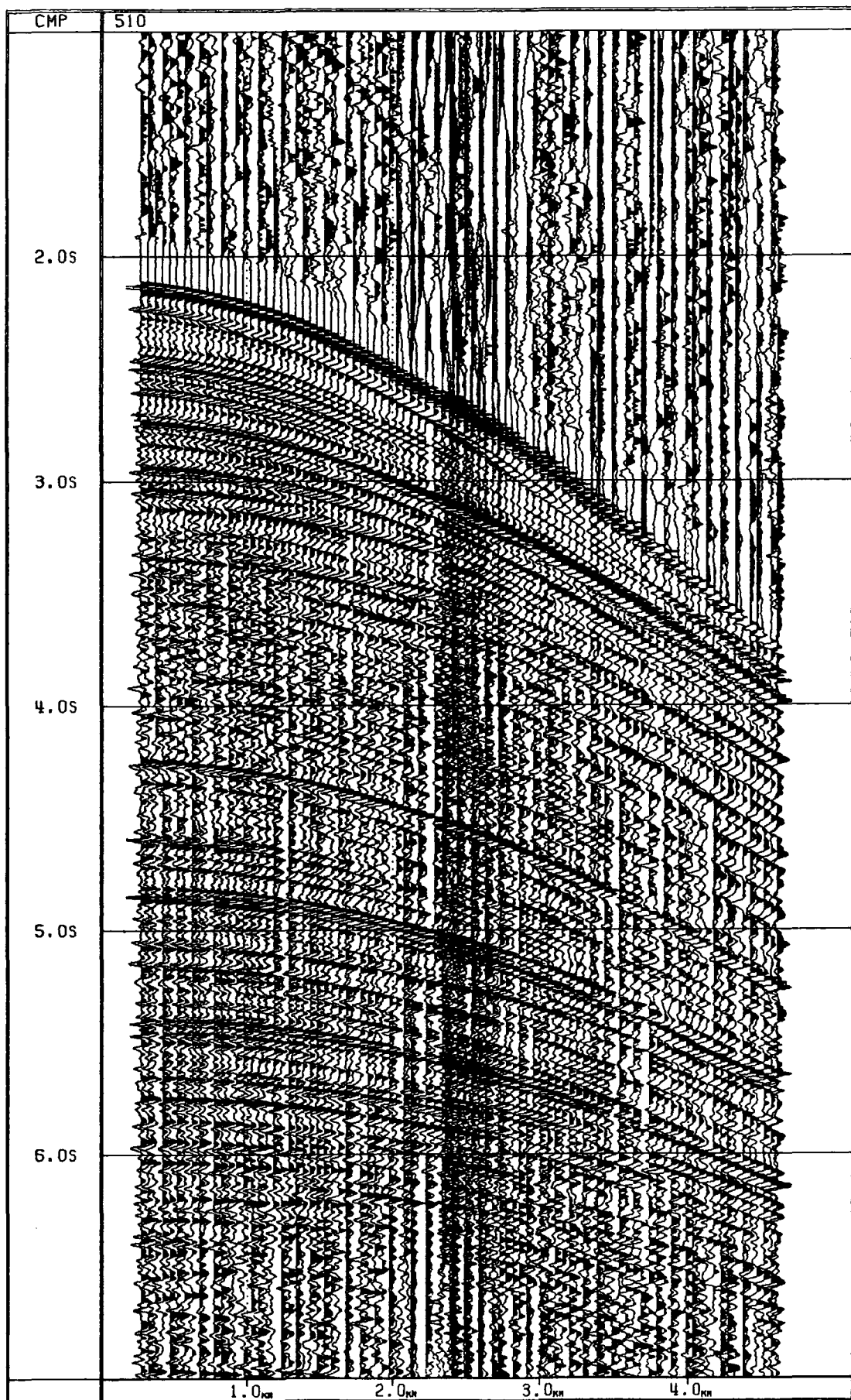


Figure 3.2 SAP1, CMP Gather 510.  
Raw CMP-sorted gather.

the  $n^{\text{th}}$  layer is given by the equation

$$T^2(x) = c_1 + c_2x^2 + c_3x^4 + c_4x^6 + \dots \quad 3.1$$

(Taner & Koehler, 1969), where the coefficients  $c_1, c_2, \dots$  are functions of layer thickness and interval velocity. In practice, terms containing powers of  $x$  greater than  $x^2$  are neglected, giving an accuracy of about 2%. This approximation reduces equation 3.1 to

$$T^2(x) = c_1 + c_2x^2,$$

where

$$c_1 = \left( \sum_{i=1}^n \Delta T_i \right)^2 = T_0^2,$$

and

$$c_2 = \frac{\sum_{i=1}^n \Delta T_i}{\sum_{i=1}^n V_i^2 \Delta T_i} = \frac{1}{V_{\text{rms}}^2}.$$

Therefore

$$T^2(x) = T_0^2 + \frac{x^2}{V_{\text{rms}}^2}, \quad 3.2$$

where

$$V_{\text{rms}}^2 = \frac{\sum_{i=1}^n \Delta T_i V_i^2}{\sum_{i=1}^n \Delta T_i},$$

represents the rms velocity to the  $n^{\text{th}}$  layer defined by Dix (1955), and  $V_i, \Delta T_i$  are the interval velocity and travel time within the  $i^{\text{th}}$  layer respectively.

This is the hyperbolic travel-time equation. The equation can be used to determine the time shift, or “normal move-out” (NMO) required to correctly align primary reflections on traces within a CMP gather to ensure that they are correctly stacked, whilst attenuating multiples and improving signal : noise. The application

of the NMO correction is a dynamic process which varies with time down the trace according to velocity, and is given by

$$\Delta T(x) = T(x) - T_0 .$$

Substituting equation 3.2 for  $T(x)$  gives

$$\Delta T(x) = [T_0^2 - \frac{x^2}{V_{rms}^2}]^{\frac{1}{2}} - T_0 ,$$

which is the required NMO correction. Application of the NMO correction prior to stacking thus requires a knowledge of the rms velocity function relevant to a particular CMP gather. Velocity analysis is a process which enables the rms velocity function to be estimated. Accurate determination of the velocity function is crucial in that incorrectly moved-out primary reflection signal strength will add incoherently when stacked. Information lost in this way cannot be recovered by subsequent processing.

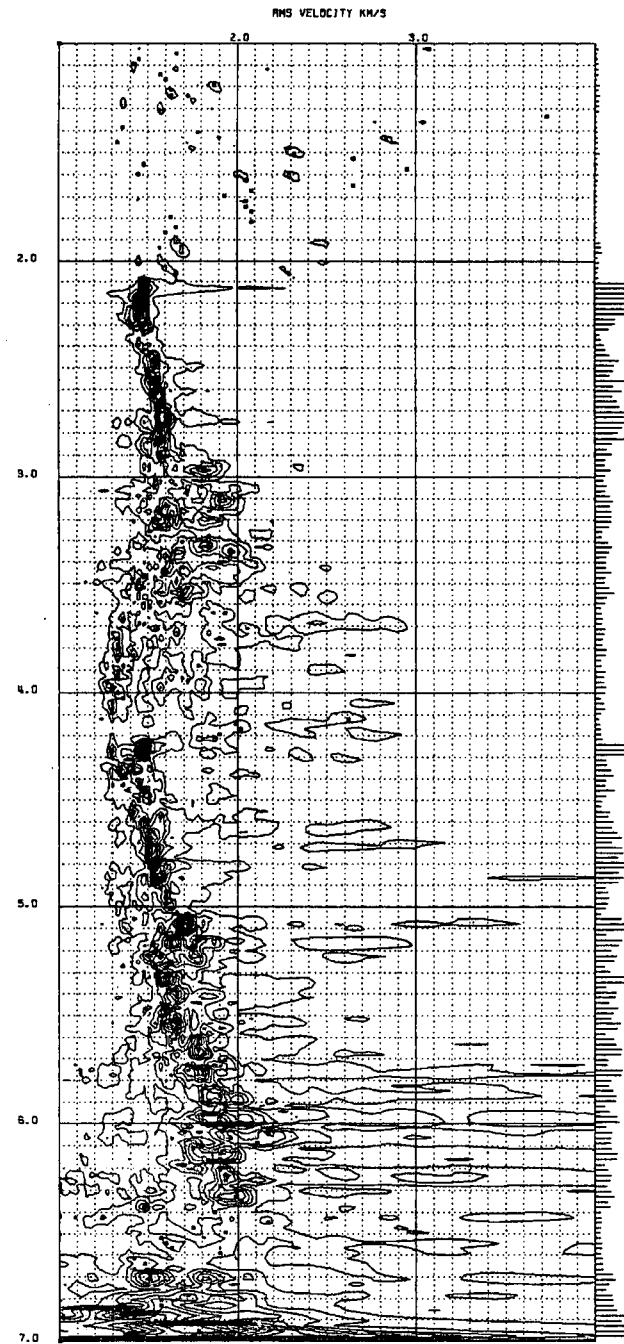
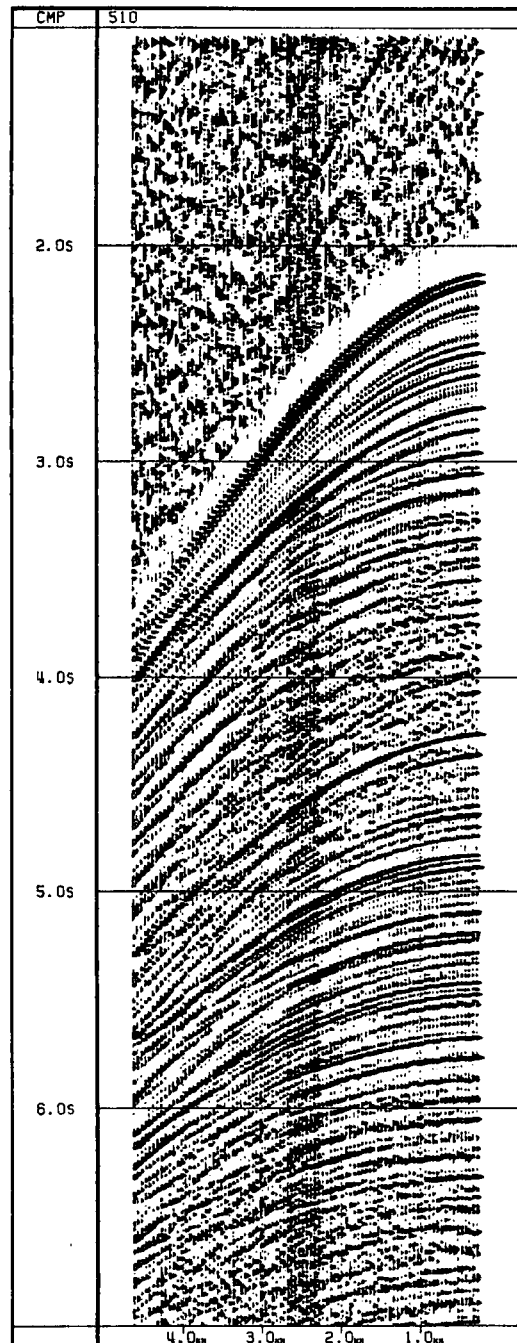
The technique of velocity analysis most commonly used, and which was used to analyse the SAP data at Durham, involves an automatic search for optimum stacking velocities as a function of zero-offset travel time. A stacking velocity within a specified range is used to apply the NMO corrections appropriate for the trace offsets within a CMP gather. A multichannel coherence measure is then applied to the moved-out traces which indicates the degree of match between the traces at a series of zero-offset times. The stacking velocity is then incremented, and the process repeated. The coherence measure used is the semblance coefficient (Taner & Koehler, 1969 ; Næidell & Taner, 1971), defined as the normalised output : input energy ratio given by  $S_c$  where

$$S_c = \frac{\sum_{t=T}^{T+\Delta T} \left( \sum_{i=1}^n A_{t,i} \right)^2}{n \sum_{t=T}^{T+\Delta T} \sum_{i=1}^n (A_{t,i})^2} ,$$

and  $A_{t,i}$  = amplitude of trace  $i$  at time  $t$ . The summation over a gatewidth  $\Delta T$  acts as a semblance smoothing function.

The application of this procedure results in the calculation of semblance coefficients as a function of zero-offset travel time and stacking velocity  $V_s$  within the limits specified for search. Peaks in the semblance spectrum correspond to the coherent alignment of seismic wavelets along a reflection trajectory across the CMP gather, and indicate the optimum stacking velocity function which will result in the best alignment of primary events during NMO correction prior to stack. Care must be taken to ensure that the semblance maxima picked correspond to primary reflection events, and not coherent noise such as multiples. Velocity analyses are displayed in the form of a contour plot of semblance coefficients as a function of zero-offset travel time and stacking velocity for ease of interpretation. A velocity analysis of CMP gather 510, SAP 1 is shown in figure 3.3 .

The velocity resolution of velocity analysis is greatest at large offsets where small changes in rms velocity result in relatively large changes in differential move-out. The maximum source-receiver offset which can be achieved in conventional single-ship reflection profiling corresponds to the physical length of the receiving array used. The SAP technique as used in the 1985 survey enables the synthesis of a maximum source-receiver offset of double the physical streamer length (chapter 2), thus increasing the resolution of the stacking velocities of deep, high velocity layers which have little differential move-out.



FIRST CMP GATHER NUMBER: 510

NO. OF CHANNELS = 104  
 SAMPLES PER CHANNEL = 3072  
 TRACE DELAY MS = 1000.0  
 LEVEL OF INTERPOLATION = 4  
 SAMPLING INTERVAL MS = 4.0  
 START OF ANALYSIS MS = 1000  
 END OF ANALYSIS MS = 7000  
 TIME STEP MS = 24.0  
 HANNING GATEWIDTH MS = 32  
 SEMBLANCE GATE MS = 32  
 START VELOCITY KM/S = 1.00  
 END VELOCITY KM/S = 4.00  
 VELOCITY STEP KM/S = 0.03  
 MIN. CONTOUR VALUE = 0.03  
 CONTOUR INTERVAL = 0.05

Figure 3.3 SAP1, CMP Gather 510.  
 Velocity analysis of source-receiver depth corrected,  
 Band-pass filtered, and Range-corrected gather.

If the ground is homogeneous, then the stacking velocity closely approximates the rms velocity (Al-Chalabi, 1974) for a given reflector. By assuming  $V_s = V_{rms}$ , the interval velocity of the appropriate layer can be estimated by using the Dix equation (1955) given by

$$V_n^2 = \frac{V_{r,n}^2 \sum_{i=1}^n \Delta T_i - V_{r,n-1}^2 \sum_{i=1}^{n-1} \Delta T_i}{\Delta T_n},$$

where  $V_n$  = interval velocity of  $n_{th}$  layer,  $V_{r,n}$  = rms velocity to  $n_{th}$  layer, and  $\Delta T_i$  = traveltimes within  $i_{th}$  layer.

The accuracy of interval velocities determined from stacking velocities is limited by various factors (Tiley, 1984). The hyperbolic traveltimes assumption fails increasingly for greater source-receiver offsets. Conversely the stacking velocity resolution increases with increased offsets, since more of the reflection trajectory is sampled during velocity analysis (chapter 2). The offset at which the hyperbolic approximation fails significantly relative to the increase in resolution is model dependent. For a multiple plane layer case the sense of the hyperbolic approximation error is such as to increase interval velocities derived from stacking velocities (Tiley, 1984).

#### horizontal

In contrast to the assumption of plane parallel layers, boundaries will generally have dips. Experiments using various dips and interval velocities have shown that traveltimes trajectories remain nearly hyperbolic in such cases. Increased dips result in increased apparent velocities, flattening out reflection traveltimes curves. Thus interval velocities derived from stacking velocities in areas of consistently dipping beds will be too high (Taner & Koehler, 1969).

Traveltimes errors may be introduced by lateral and vertical velocity gradients within the earth. However modelling (Tiley, 1984) suggests that the errors intro-



duced in this manner are unlikely to exceed a few tenths of a percent.

The velocity analysis and CMP stack techniques prove to be extremely robust even in areas of complex geological structure, and errors introduced in the ways described above tend to be of the order of a few percent (Tiley, 1984). However, it is important that these effects are understood, and taken into account if necessary.

In practice, semblance velocity analysis is performed on CMP gathers containing noise, both coherent and random. Coherent noise may include seafloor and interlayer multiples, layer reverberations, source wavelet ringing, refractions, and out of plane reflections. Incoherent noise includes that generated by wave action, the streamer, the ship propellers, and scattered energy from seafloor or sub-surface irregularities.

Figure 3.2 shows a typical gather from SAP1. The area in the centre of the gather where the trace density increases is a region of overlap of trace offsets originating from shots by both ships. The far offset traces originate from Darwin shots, the near from Discovery. It can be seen from the overlap region that the seafloor arrival appears slightly earlier on Darwin traces than on Discovery traces for comparable offsets. This effect was assumed to be due to streamer feathering producing a range error in the source-receiver offsets determined during CMP sort. The effect is corrected by a process involving cross-correlating between traces from different ships to determine the Darwin trace lag. This is used to calculate and correct for the range error in the Darwin traces.

Additionally, low and high frequency random noise is apparent on all traces in the gather. This is easily removed by the application of a band-pass filter which rejects frequencies outside the band of interest. The effect of applying a band-pass

filter with a 5-70 Hz pass band, and range correction on CMP gather 510 is shown in figure 3.4. The high and low frequency noise has been suppressed, and the range error in the Darwin traces eliminated. In addition the gather has been corrected for source and receiver depth. This correction involves time-shifting the traces within a gather to account for the fact that source and receiver are submerged, so that both appear to be at the surface. These three processing steps form the basis for further processing and velocity analysis.

A velocity analysis of the source-receiver corrected, band-passed, and range corrected CMP gather 510 from SAP 1 is shown in figure 3.3. The analysis shows clear, well resolved semblance maxima corresponding to identifiable primary events down to approximately 3.1 s two-way-traveltime. Below this the contour plot becomes less clear, with generally low semblance values. Examination of gather 510 indicates the presence of high-amplitude, low velocity arrivals in the far-offset traces giving rise to peaks in the semblance plot at velocities sometimes lower than that of the seafloor reflection. These appear to be vibratory in nature, but their origin remains unclear. Their low velocity and offset dependence suggest that they may be trapped S-wave conversions originating at the sediment/basement interface. Whatever their cause, their presence severely degrades velocity analyses. These arrivals are present to a greater or lesser extent on most of the SAP data. At 4.25 s traveltime an arrival corresponding to the first seafloor multiple is evident with a velocity of about  $1.49 \text{ km s}^{-1}$ . Below the seafloor multiple the semblance plot is swamped by multiple arrivals.

It is possible to attempt to remove the identified multiples and reverberations by using the technique of predictive deconvolution (Peacock & Trietel, 1969). This method relies on the periodic nature of multiples in forming a prediction error filter

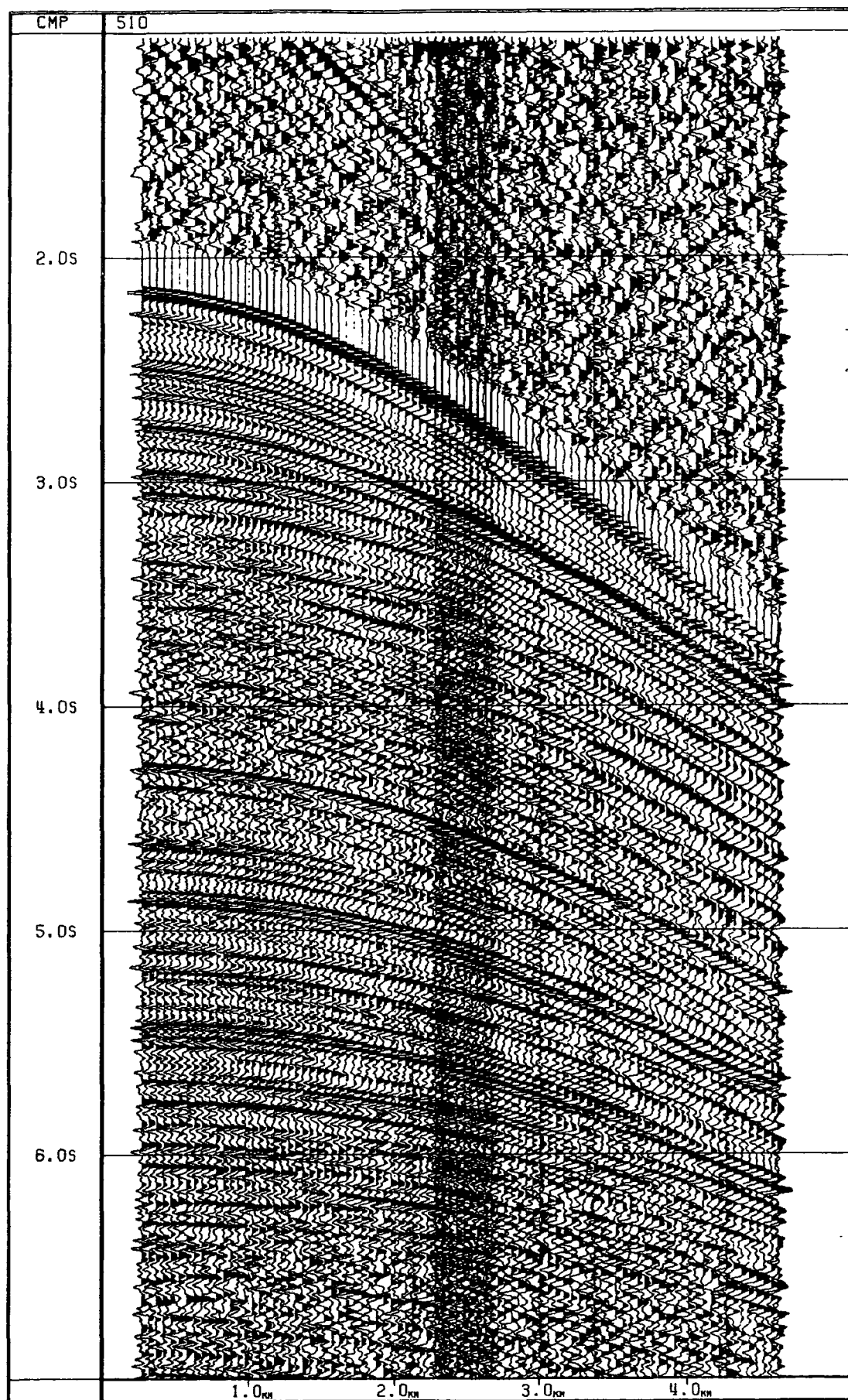


**Figure 3.4** SAP1, CMP Gather 510.

Source-receiver depth corrected, band-pass filtered,  
and range corrected gather.

designed to remove the predictable portion of a trace which will to a good approximation equal the repetitive energy forming the multiples. Design of a suitable predictive deconvolution operator involves choosing an active filter length which should span, a prediction interval which should be less than, and an autocorrelation window length which should include many cycles of, the periodicity to be removed. Examination of the autocorrelation function of traces within a gather may aid in the design of a suitable predictive deconvolution operator by revealing periodicities not apparent from inspection of the gather alone.

The autocorrelation function of CMP 510 is shown in figure 3.5. Clear reverberations are visible in the far offset trace autocorrelations, with a period of 135 ms. These correspond to the reverberations visible in the gather. A peak in the trace autocorrelation at a lag of 2.1 s corresponds to the first seafloor multiple. Below this the autocorrelation display shows that the gather is severely contaminated by multiple energy. In addition, reverberations are evident at lags of 1 and 3 s labelled A & B in figure 3.5, which are not immediately recognisable as such on the gather plot. These have similar periods to the far offset reverberation. The application of two predictive deconvolution filters was used to suppress the identified multiple energy. The first, designed to remove the short period reverberation, used a prediction gap of 95 ms, an active filter length of 120 ms, with a design autocorrelation window of 4000 ms. The second, designed to remove the seafloor multiple train, employed an active length of 1000 ms, an autocorrelation window of 7000 ms, with the prediction gap calculated automatically to follow the expected seafloor multiple position ( an option included in the processing program (Bowen, 1987d)). True amplitude plots of the original and deconvolved gathers are shown in figure 3.6.

Examination of figure 3.6 reveals that the strength of the seafloor multiple train

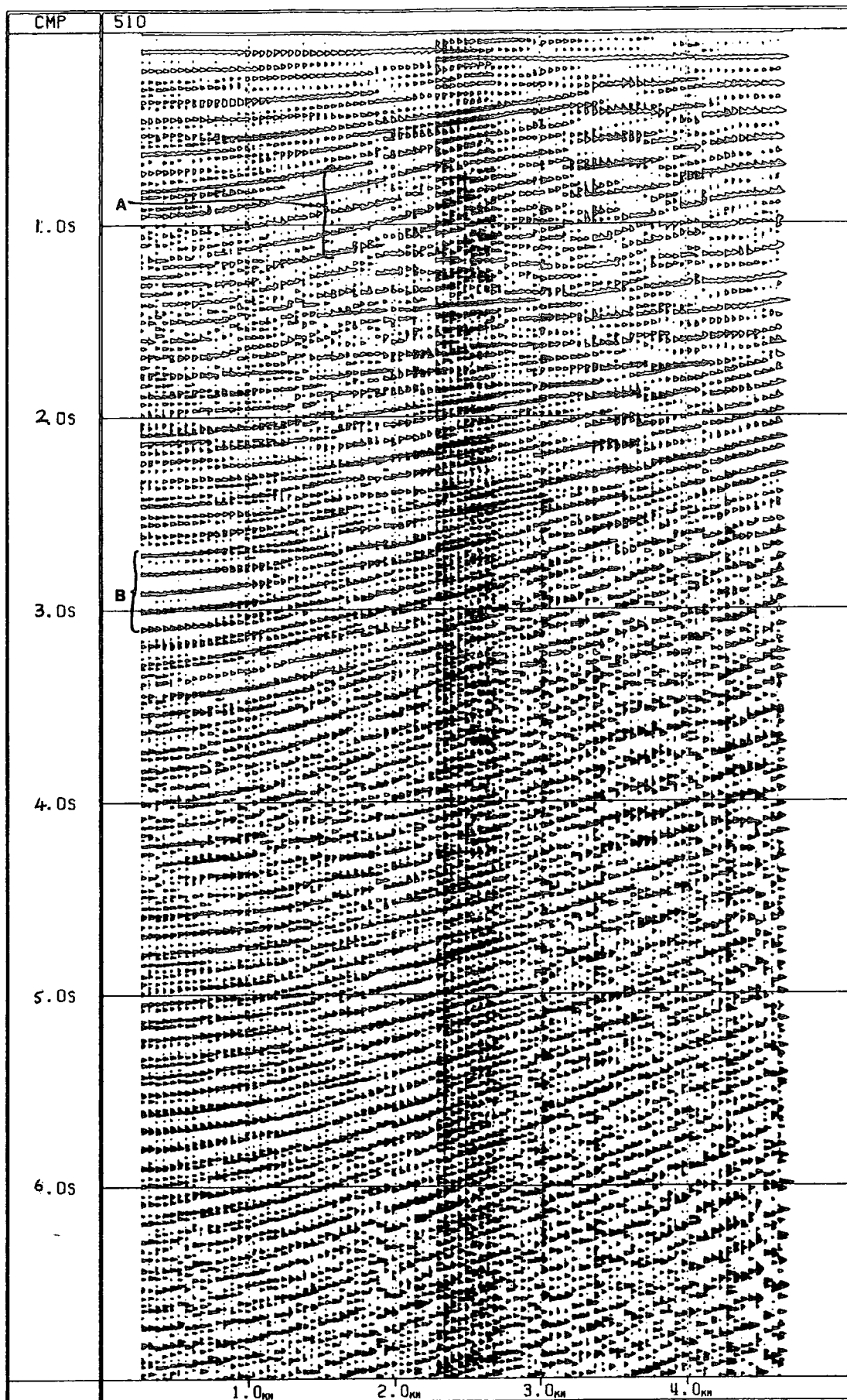
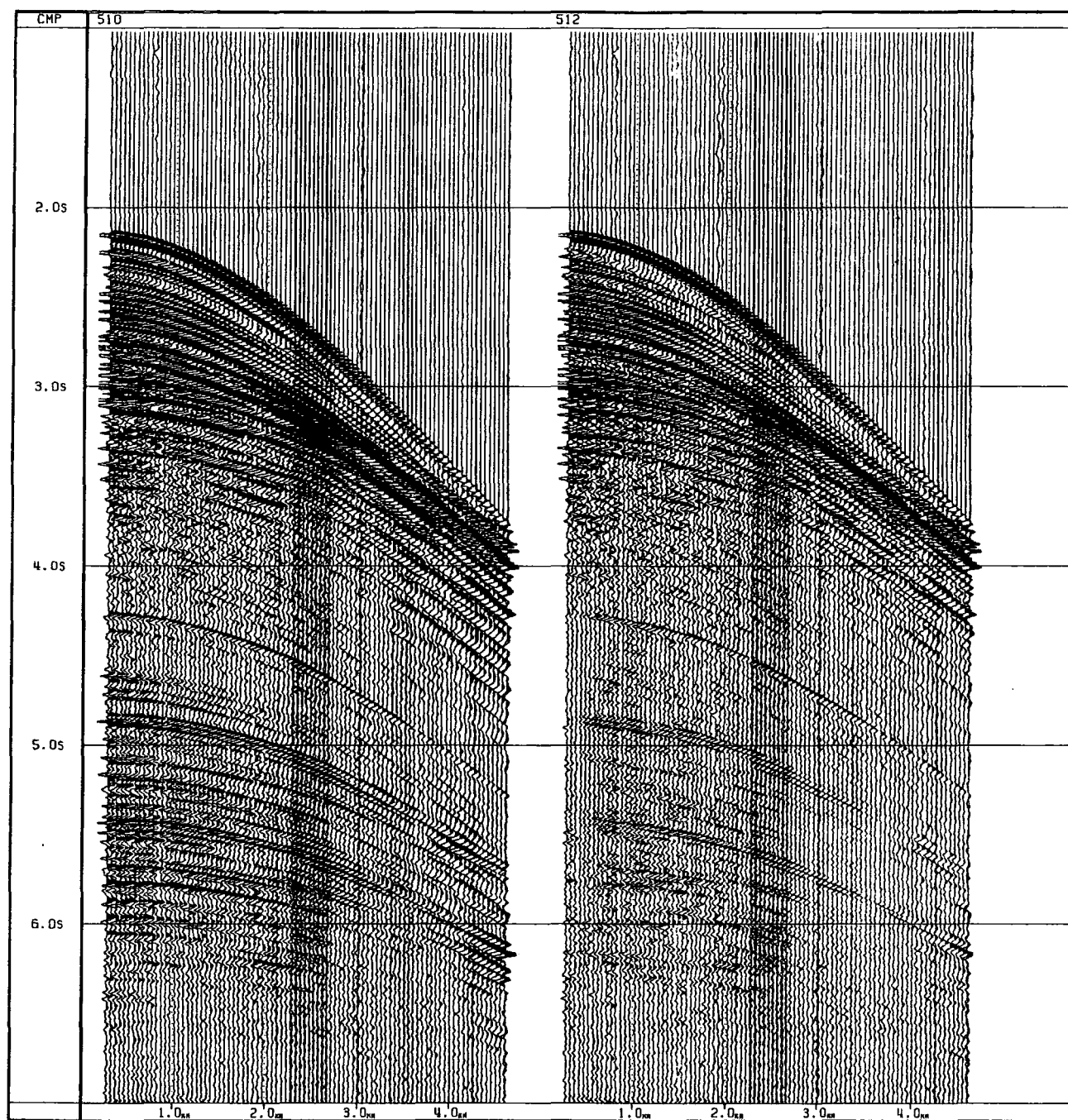


Figure 3.5 SAP1, CMP Gather 510.

Trace autocorrelation function, raw gather.

See text for description of A,B.



**Figure 3.6** SAP1, CMP Gather 510.

True relative amplitude gather plots.

(a) No deconvolution.

(b) Predictive deconvolution, designed to remove seafloor multiple and reverberation.

and far offset reverberation has been significantly reduced. In addition, the autocorrelation of the deconvolved gather (figure 3.7) shows that the reverberations A & B have also been attenuated. Subsequent velocity analysis on the deconvolved gather confirms the conclusions reached. The semblance plot (figure 3.8) has been “tidied up” by the deconvolution process. In particular a semblance peak has appeared at a travel time of 3.26 s and rms velocity of  $1.95 \text{ km s}^{-1}$ , which was previously obscured by a lower velocity multiple arrival.

However, although indicating the possible presence of energy in the higher velocity region, there are still no clear semblance peaks visible below 3.3 s, and the effects of the low velocity reverberation and sea floor multiple have not been completely removed.

A technique which can be employed to discriminate against low velocity arrivals is known as velocity filtering. This relies on the fact that multiples have a lower apparent velocity than primaries. Velocity filtering a gather involves moving-out the traces according to a false velocity function designed to over-correct primary reflections, and under-correct multiples. A filter is then applied to the moved-out gather which passes over-corrected primary, and attenuates under-corrected multiple arrivals. The false NMO is subsequently removed, leaving the original gather with its multiple content strongly attenuated. This process was implemented by Hobbs (1985) using the technique described by Ryu (1982) as an option in the seismic processing program.

In using the velocity filter option, care must be taken to ensure that an appropriate velocity function is applied. If the velocities are too high, then primary events will be removed along with multiples. The technique works well on gathers

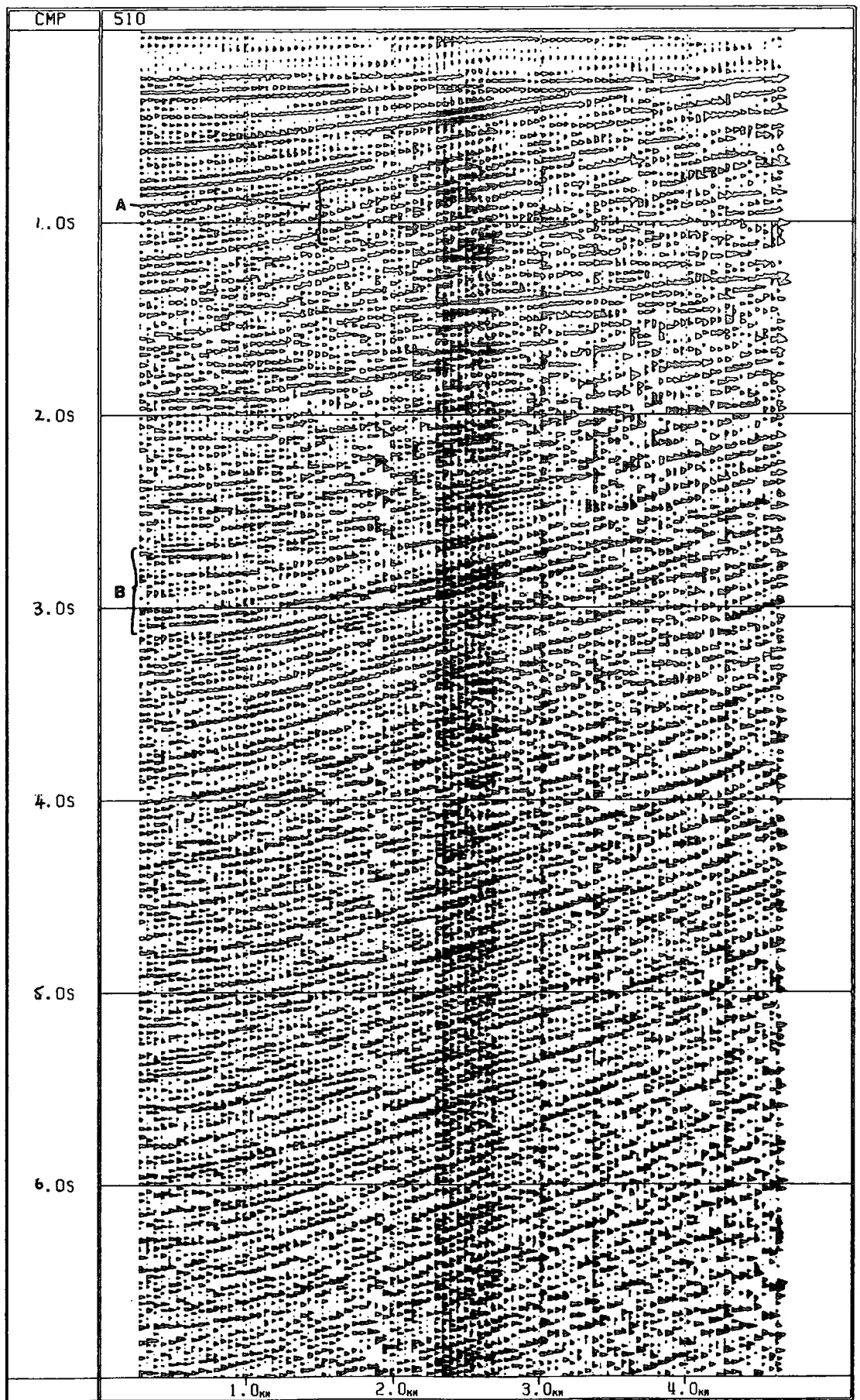
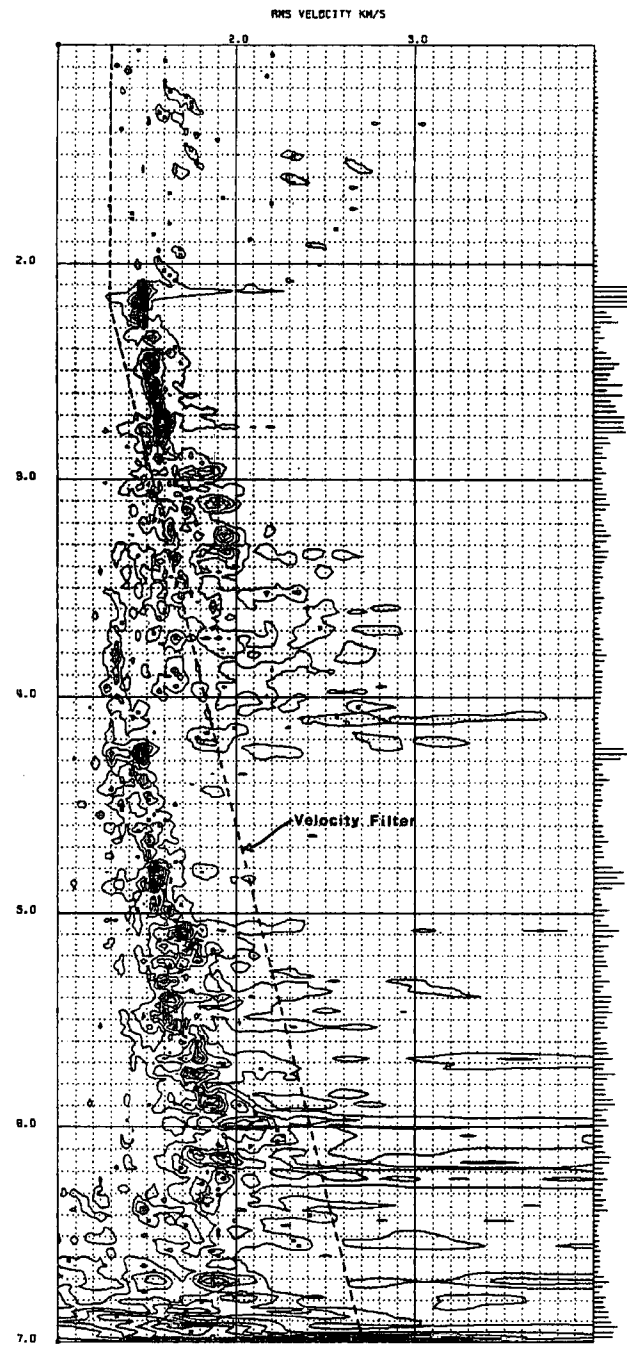
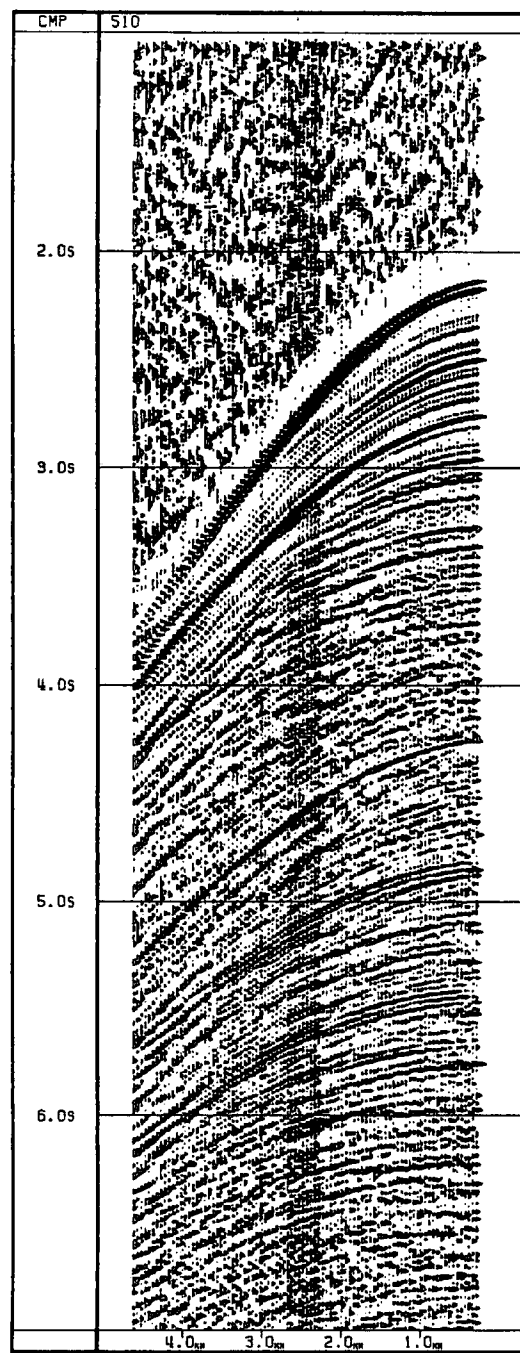


Figure 3.7 SAP1, CMP Gather 510.

Trace autocorrelation function following predictive deconvolution to remove seafloor multiple and reverberation.

See text for description of A,B.





FIRST CMP GATHER NUMBER: 510

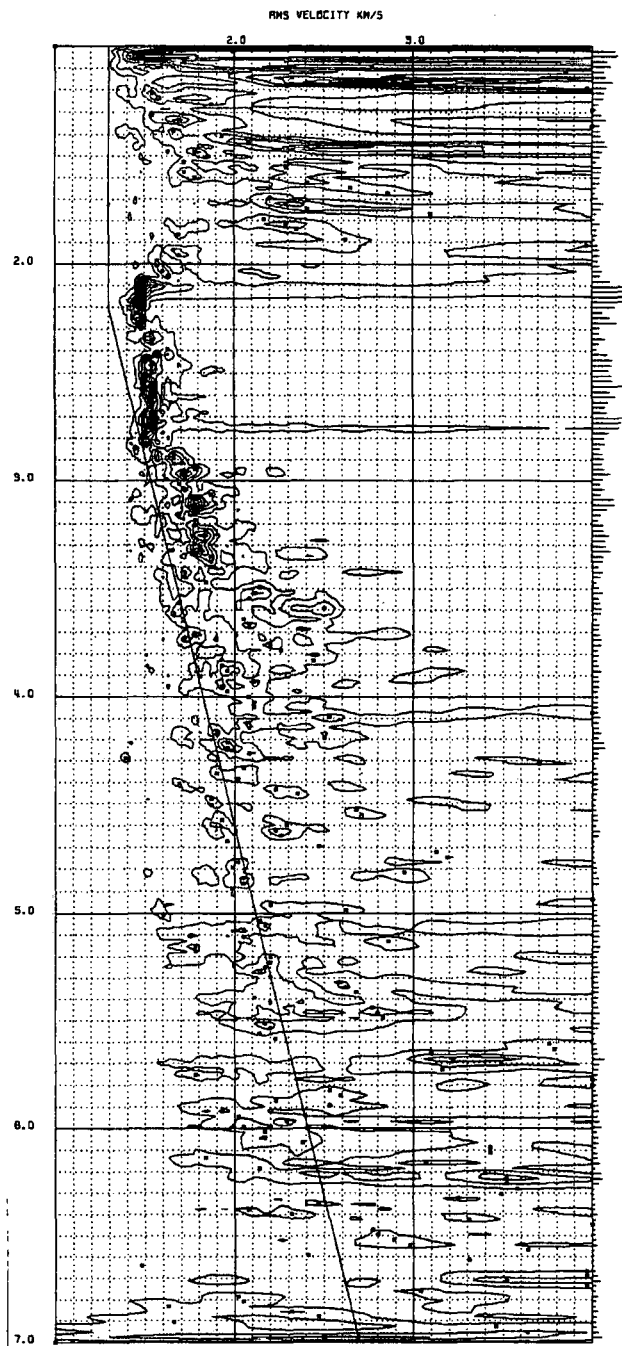
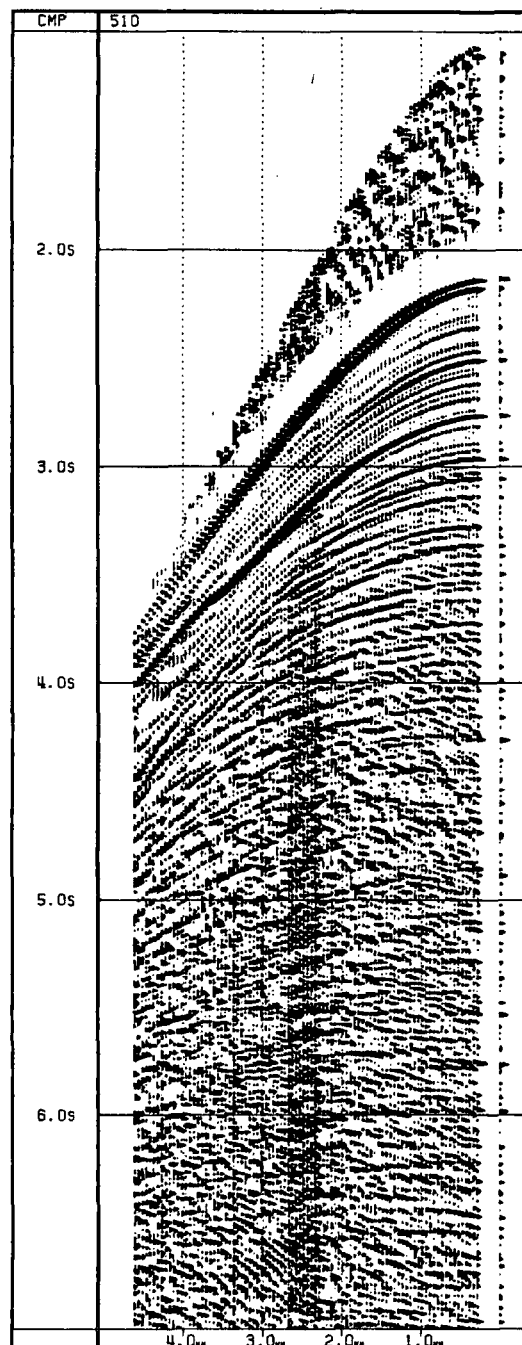
NO. OF CHANNELS = 104  
 SAMPLES PER CHANNEL = 3072  
 TRACE DELAY MS = 1000.0  
 LEVEL OF INTERPOLATION = 4  
 SAMPLING INTERVAL MS = 4.0  
 START OF ANALYSIS MS = 1000  
 END OF ANALYSIS MS = 7000  
 TIME STEP MS = 24.0  
 HANNING GATEWIDTH MS = 32  
 SEMBLANCE GATE MS = 32  
 START VELOCITY KM/S = 1.00  
 END VELOCITY KM/S = 4.00  
 VELOCITY STEP KM/S = 0.03  
 MIN. CONTOUR VALUE = 0.03  
 CONTOUR INTERVAL = 0.05

Figure 3.8 SAPI, CMP Gather 510.  
 Velocity analysis of deconvolved gather.

in which there is significant differential move-out between multiple and primary reflection trajectories.

A velocity filter was designed on gather 510 as shown in figure 3.8, to leave identified primary events unaffected, whilst attenuating any residual low velocity reverberation and seafloor multiple, in an attempt to reveal any obscured primary events. The result of velocity analysis is shown in figure 3.9 which reveals further semblance peaks at a travel time of about 3.6 s, and rms velocity  $2.5 \text{ km s}^{-1}$ .

The first second of traveltimes in the far offset traces appear discontinuous, and still contain residual low velocity arrivals. The discontinuous nature is caused by interference between overlapping residual low velocity arrivals and higher velocity trajectories, and to the presence of a basement refraction visible on the raw gather. Wide-angle reflections caused by reflection of incident energy close to the critical angle may also be present at these offsets. All these effects will degrade the velocity analysis, and consequently should be removed by muting. This process selectively sets portions of trace to zero according to a defined mute function. The muting process should be used with care since thoughtless application will truncate reflectors and reduce velocity resolution. This is more important for higher velocity arrivals whose reduced move-out requires that more of the reflection hyperbola be sampled in order to achieve sufficient resolution. A mute function was designed to remove the identified section of gather 510 as shown in figure 3.10, and velocity analysis carried out on the deconvolved, muted and velocity filtered gather with the result shown in figure 3.11. Peaks in the semblance spectrum are evident at traveltimes over 4 s. These may represent true primary energy, but should be treated with suspicion since they occur at approximately the traveltime of the seafloor multiple, and may be artefacts produced by its removal. Checks employed to verify semblance



FIRST CMP GATHER NUMBER: 510

NO. OF CHANNELS = 104  
 SAMPLES PER CHANNEL = 1536  
 TRACE DELAY MS = 1000.0  
 LEVEL OF INTERPOLATION = 1  
 SAMPLING INTERVAL MS = 4.0  
 START OF ANALYSIS MS = 1000  
 END OF ANALYSIS MS = 7000  
 TIME STEP MS = 24.0  
 HANNING GATEWIDTH MS = 32  
 SEMBLANCE GATE MS = 32  
 START VELOCITY KM/S = 1.00  
 END VELOCITY KM/S = 4.00  
 VELOCITY STEP KM/S = 0.03  
 MIN. CONTOUR VALUE = 0.03  
 CONTOUR INTERVAL = 0.05  
 VELOCITY FILTERING APPLIED  
 OPERATOR DIMENSION = 13

Figure 3.9 SAP1, CMP Gather 510.  
 Velocity analysis of deconvolved  
 and velocity filtered gather.

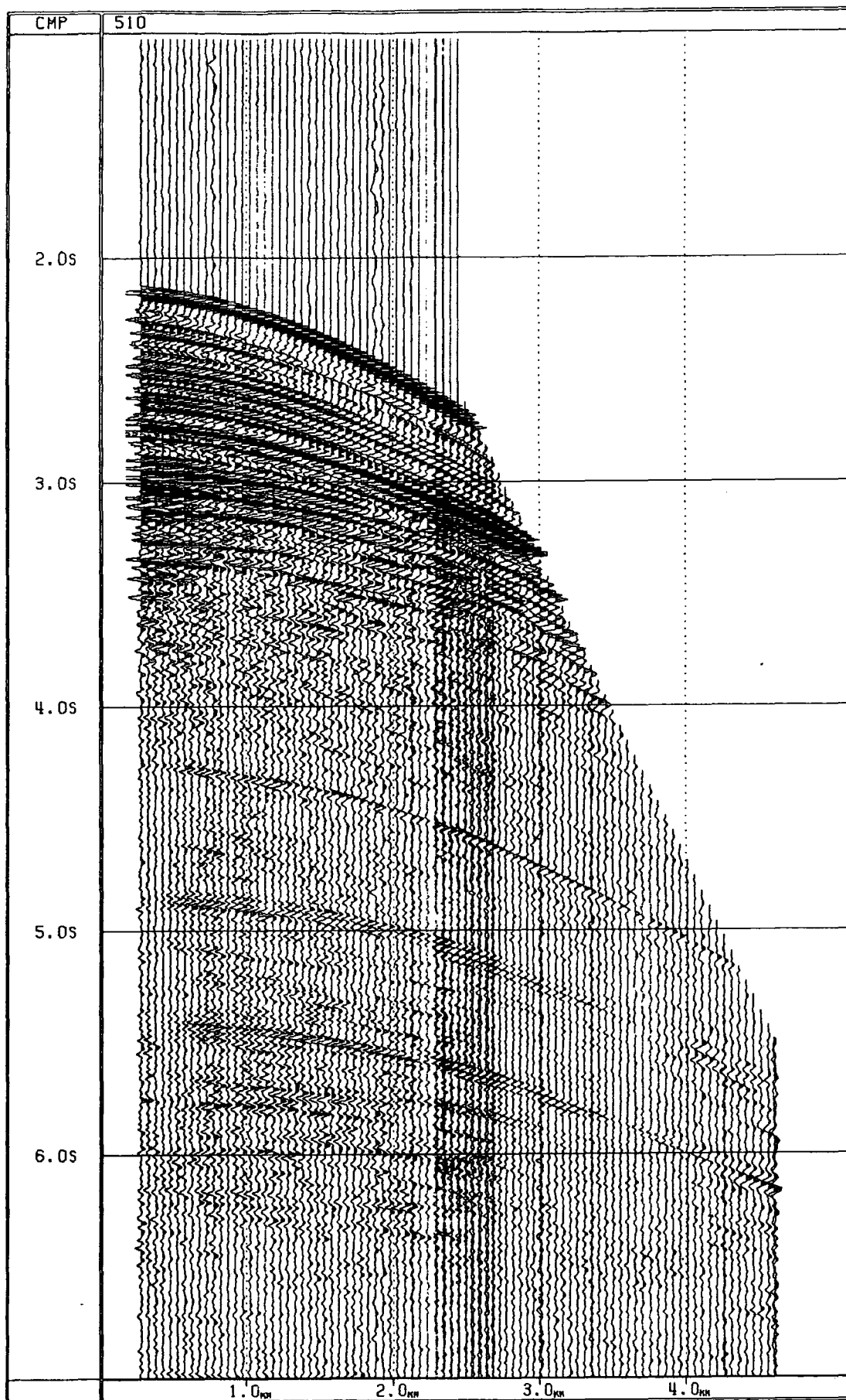
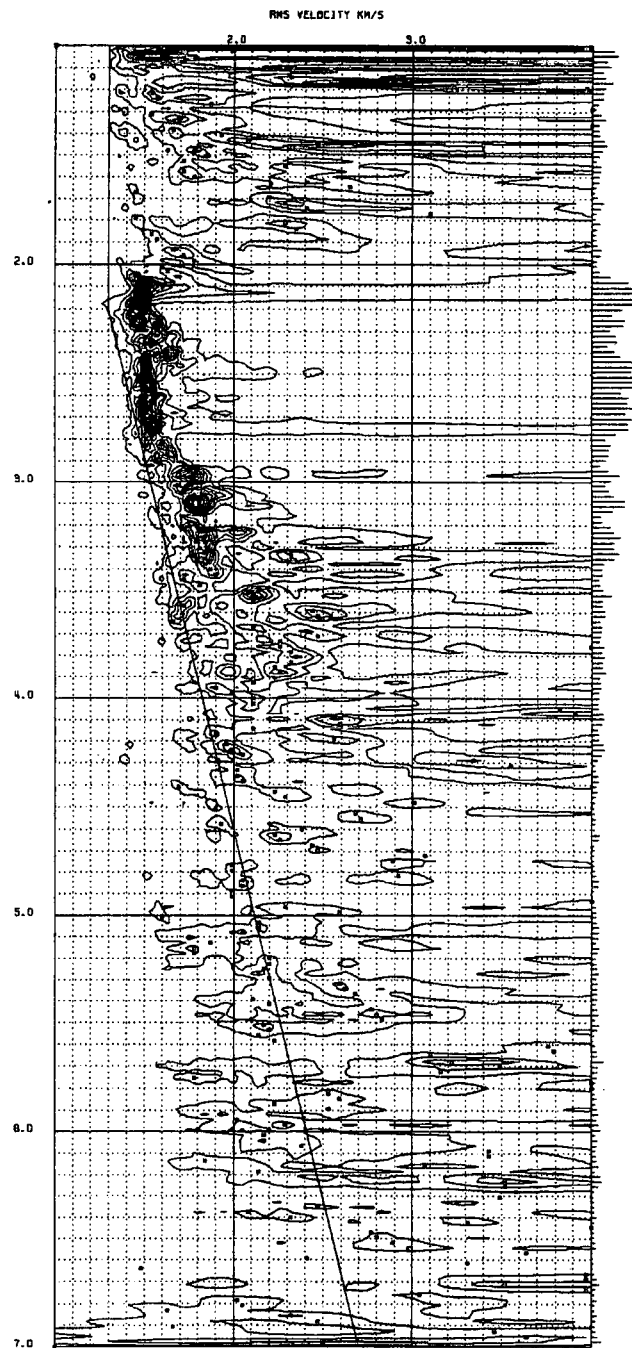
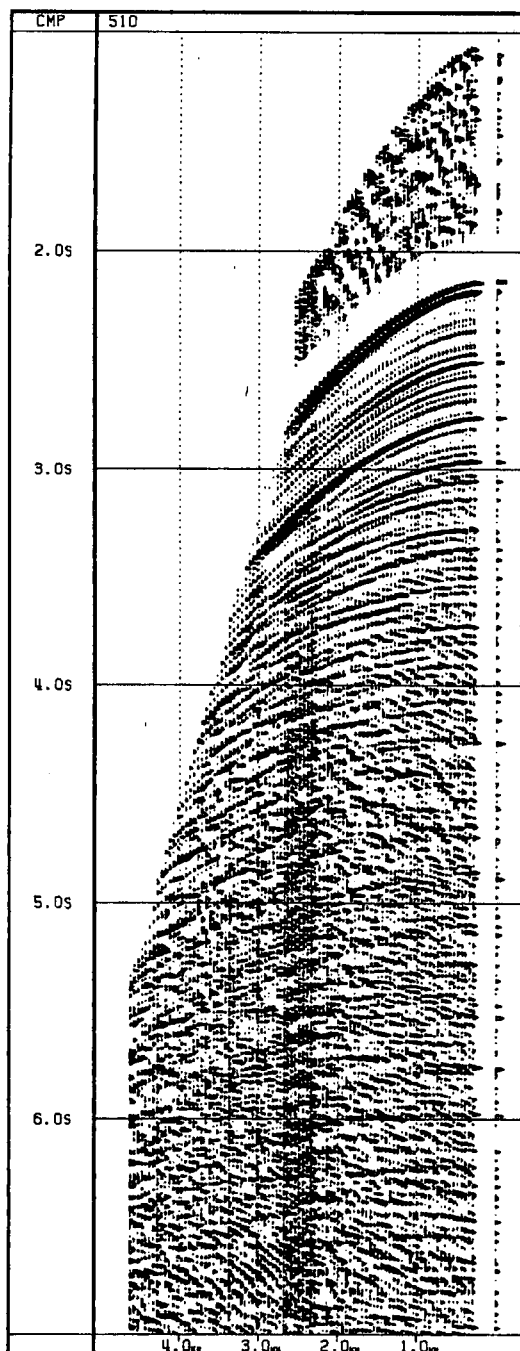


Figure 3.10 SAP1, CMP Gather 510.

Mute applied to deconvolved gather.



FIRST CMP GATHER NUMBER: 510

NO. OF CHANNELS = 104  
 SAMPLES PER CHANNEL = 1536  
 TRACE DELAY MS = 1000.0  
 LEVEL OF INTERPOLATION = 1  
 SAMPLING INTERVAL MS = 4.0  
 START OF ANALYSIS MS = 1000  
 END OF ANALYSIS MS = 7000  
 TIME STEP MS = 24.0  
 HANNING GATEWIDTH MS = 32  
 SEMBLANCE GATE MS = 32  
 START VELOCITY KM/S = 1.00  
 END VELOCITY KM/S = 4.00  
 VELOCITY STEP KM/S = 0.03  
 MIN. CONTOUR VALUE = 0.03  
 CONTOUR INTERVAL = 0.05  
 VELOCITY FILTERING APPLIED  
 OPERATOR DIMENSION = 13

Figure 3.11 SAP1, CMP Gather 510.  
 Velocity analysis of deconvolved, muted,  
 and velocity filtered gather.

picks are discussed later in this section.

Once a set of velocity analyses have been performed on the chosen CMP, a velocity function can be picked. Several checks are available to ensure the correct choice of stacking velocity. In general stacking velocities increase with depth. Semblance peaks at the same velocity as earlier ones are likely to be multiples. Picks should correspond to arrivals identified on brute stack and gather plots where possible. Interval velocities resulting from a set of stacking velocities should be appropriate for the rock types expected, and usually increase with depth. General consistency with the velocity structure obtained by ESP modelling should be maintained. Once a velocity function has been constructed, its effectiveness in correctly aligning reflections can be assessed by moving the gather out and inspecting for over- and undercorrected arrivals. Velocities derived from basement refractions, where these are clearly visible, provide additional checks on interval velocities derived from stacking velocities. Inconsistencies should be resolved by referring back to velocity analyses, or by additional processing and velocity analysis to clarify particular areas.

In areas of poor signal:noise, additional velocity analysis techniques can be employed to give velocity information where semblance analysis failed. Constant velocity gathers (CVG) and stacks (CVS) may be used, in which the gather or group of gathers is moved out (and stacked in the case of CVS) using a range of stacking velocities. That which best aligns a given reflector provides a stacking velocity pick. Semblance averaging, in which semblance functions from adjacent velocity analyses are averaged, can suppress isolated random peaks, and reduce background semblance levels. In practice these techniques were time consuming, and provided little extra information, but were sometimes useful in confirming or eliminating existing semblance picks.

The velocity function picked for CMP 510 is shown in table 3.1, and the moved-out gather is shown in figure 3.12. This indicates the the velocity function is correct, with well aligned arrivals. The far offset distortion is a consequence of the NMO correction, and is discussed later in this section.

**Table 3.1.** SAP 1, CMP 510 Velocity Function.

Layer	Two-way-Traveltime (ms)	RMS Velocity km s <sup>-1</sup>	Interval velocity km s <sup>-1</sup>
1	2110.0	1.48	1.48
2	2279.0	1.49	1.61
3	2610.0	1.54	1.85
4	2760.0	1.61	2.54
5	2970.0	1.76	3.12
6	3260.0	1.96	3.39
7	3600.0	2.50	5.42
8	4285.0	3.30	5.94
9	9490.0	5.91	7.40*

\* - Velocity determined from ESP velocity structure.

Once a satisfactory velocity function has been constructed for a given CMP, the process is repeated at appropriate positions along the profile. These should be such as to provide a suitably well defined velocity model prior to stacking, especially in areas of rapidly changing structure. The sequence outlined above illustrates the approach adopted in the velocity analysis of the SAP data. Processing details and combinations varied according to the position and quality of the gather. Reflections from the Moho were not observed on velocity analyses, due to the contamination of gathers by seafloor multiple arrivals at traveltimes equal to those predicted by ESP results for Moho arrivals. Therefore expected traveltimes and velocities from ESP results were incorporated into all velocity models in defining the Moho layer.

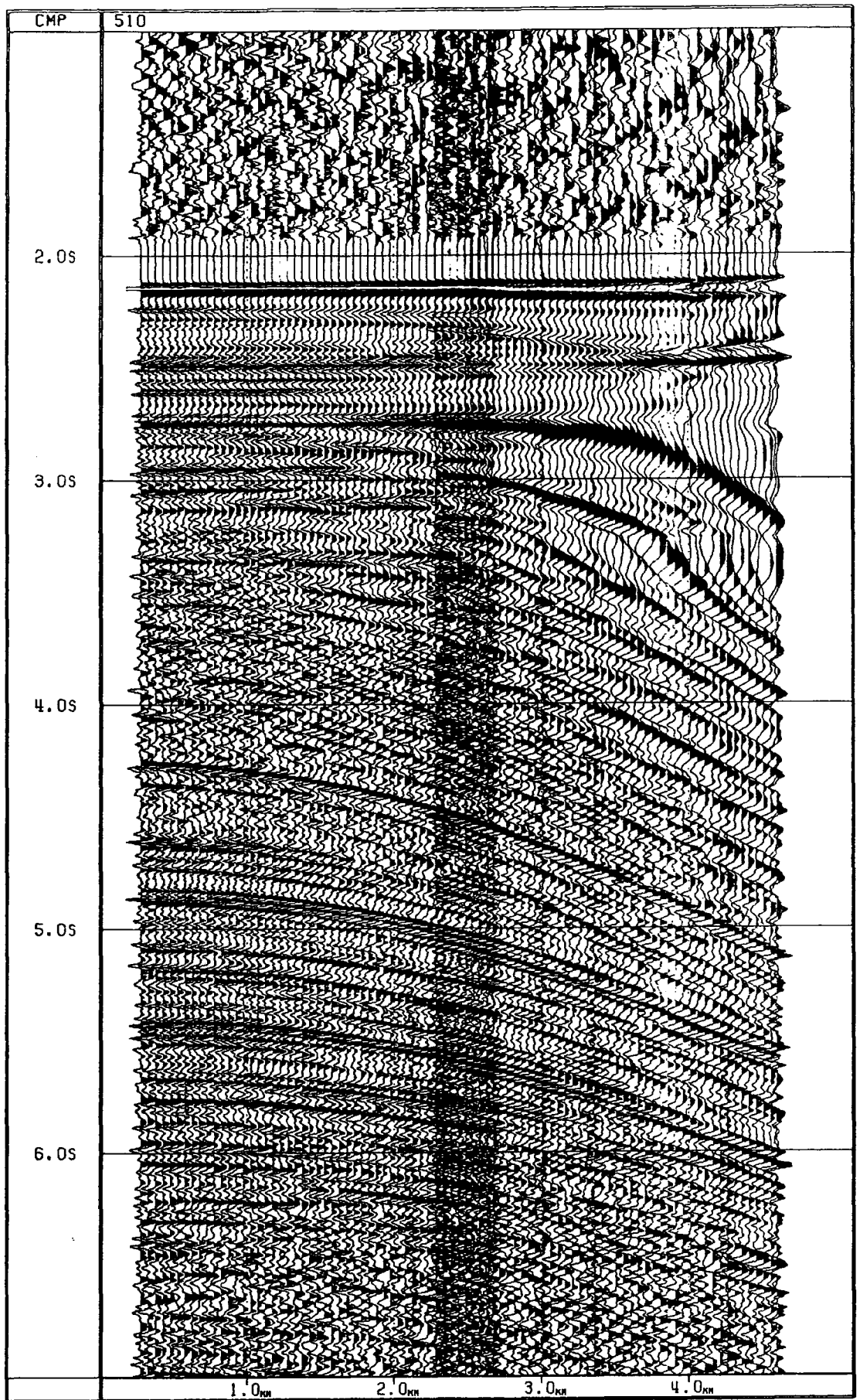


Figure 3.12 SAP1, CMP Gather 510.

Gather moved-out according to displayed velocity function.



It was particularly difficult to obtain velocity information deeper than 0.5 s beneath the seafloor arrival on gathers from the shallow water area on the upper part of the continental margin. This was due to the presence of energy trapped in the water layer giving rise to gathers swamped by seafloor multiples (figure 3.13). Their attenuation during velocity analysis by velocity filtering and predictive deconvolution revealed no further semblance peaks. The removal of wide angle reflections and extensive basement and sub-basement refractions by muting resulted in the excessive truncation of existing reflectors, reducing the velocity resolution of subsequent velocity analysis. However, the refractions were useful in indicating basement interval velocities to be expected from velocity analyses. In these cases, the velocity models were continued by interpolation from adjacent successful velocity analyses using ESP-determined velocity information.

The velocity models resulting from velocity analysis of the CMP gathers were then used in the NMO and stack stages of the processing sequence.

Signal enhancement techniques such as those used to improve velocity analyses can be used at the pre- and post-stack stages to improve the quality of the final seismic section. The processing steps and parameters appropriate to different parts of the profile are determined by trial stacks prior to the final stack. Prior to velocity analysis, an initial stack of each profile was carried out using a very crude velocity model derived from the general velocity structure of the margin by Scrutton (1972). This procedure is aptly termed "brute stacking", and is designed to provide an initial stacked section from which areas of interest can be identified, and subsequent detailed velocity analyses sited accordingly. No processing other than muting between NMO and stack was performed during the brute stack.

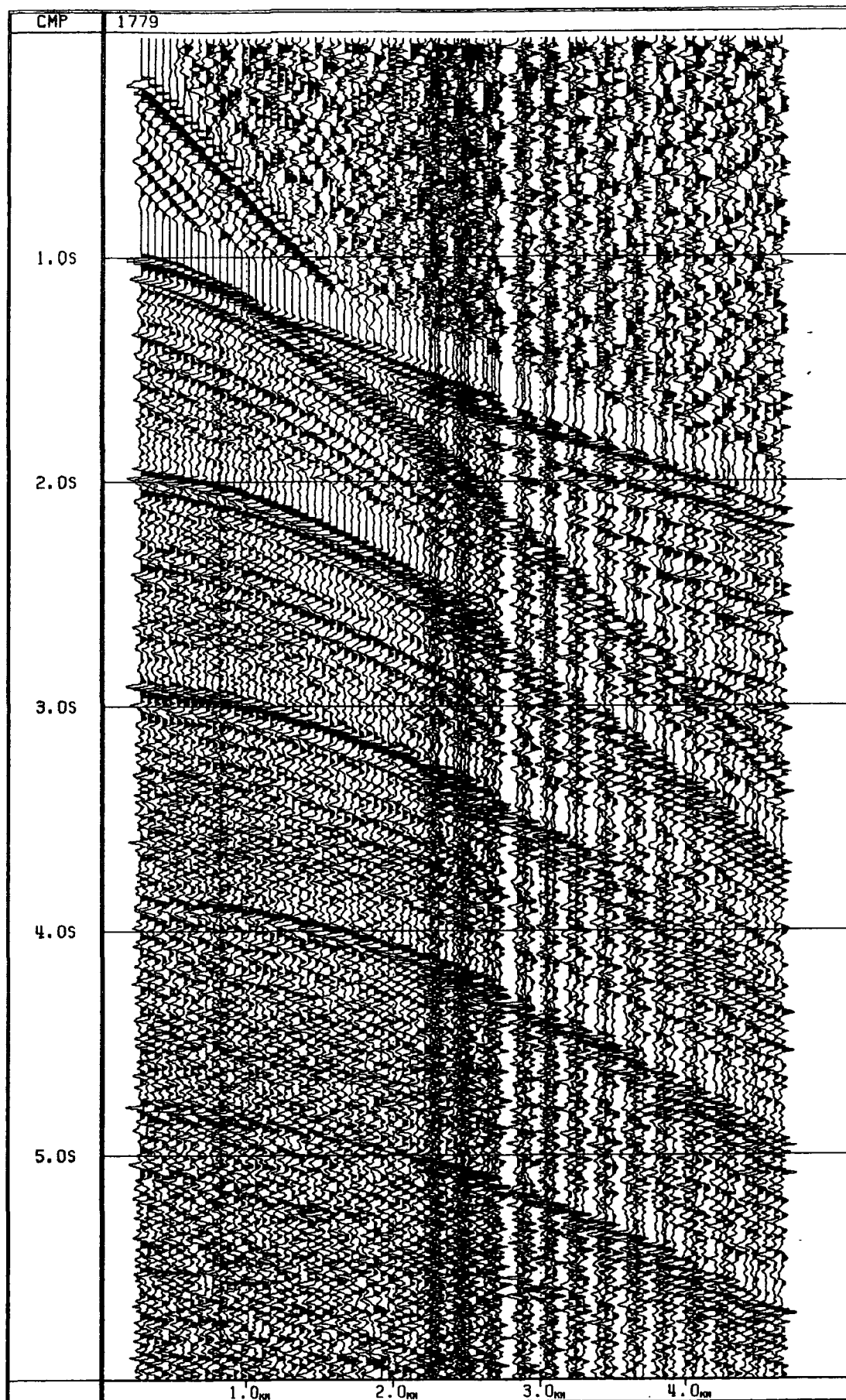


**Figure 3.13** SAP2, CMP Gather 1779.  
Gather plot exhibiting excessive  
seafloor multiple contamination.

The NMO process can introduce distortion into the far-offset traces, a phenomenon known as trace "stretch"<sup>(figure 3.12)</sup>. This is a consequence of the dynamic nature of the NMO correction, and the finite duration of the seismic pulse. During NMO correction, different portions of the seismic pulse representing a single reflector will be moved-out to different degrees according to the velocity function. The effect is removed between NMO and stack by the application of a suitably designed mute function, determined during pre-stack trials. Checks on the effectiveness of the current mute function should be carried out during stack by moving out a gather and establishing that the mute is removing the required portion of gather.

Pre-stack trials and stacking of the SAP data were carried out at Durham by Dr. A. Bowen. Pre-stack processing consisted of the following, generally applied steps. Source-receiver depth correction, bandpass filtering, and range-correction were followed by spherical divergence correction, and the application of short gap predictive deconvolution to remove short period multiples and source signature. The application of a time-varying bandpass filter to account for the depth dependent frequency absorption characteristics of the earth, was followed by long gap predictive or adaptive deconvolution designed to remove the seafloor multiple. The data were then moved-out, muted, and stacked.

The processing of the SAP data resulted in velocity models and final stacked seismic sections of SAPs 1-4 (figures 6.3 to 6.6, in back pocket). Their detailed description and interpretation is described in chapter 6.

## CHAPTER (4)

### Gravity Models of the Hatton-Bank Continental Margin.

#### 4.1 Introduction.

The gravity field across a typical passive continental margin reflects the change in water depth and accompanying variations in crustal thickness. Superimposed upon this are the effects of structural features such as faulting and sedimentary basins, igneous activity, and the transition from oceanic to continental lithosphere. (Wigginton, 1984; Livermore, 1980)  
Recent models have incorporated density gradients in the lithosphere caused by temperature gradients set up by the emplacement of hot oceanic lithosphere against cold continental lithosphere during rifting. This gradation will have a significant effect on the gravity anomaly measured on continental margins, such as the Hatton Bank margin, which are young enough for lateral temperature gradients not to have equilibrated.

The theory of sea-floor spreading predicts a simple relationship between the depth and age of oceanic crust. Hot lithosphere created at mid-ocean ridges migrates away from the ridge crest, cooling and, becoming denser, subsiding to maintain isostatic equilibrium (Parsons & Sclater, 1977).

The North Atlantic between the Azores and Iceland departs from this classical model. Although following a similar subsidence curve, the sea floor is anomalously shallow over most of the region, producing a broad topographic swell centred on Iceland. This swell has been attributed to an unusually hot underlying asthenosphere (Haigh, 1973a,b ; Cochran & Talwani, 1978), combined with the smaller pressure effect of the rising Iceland plume (Bott 1987b). These anomalous features might be

expected to perturb the gravity field measured across North Atlantic continental margins.

The gravity signal measured across the Hatton Bank continental margin is therefore a potentially powerful tool for testing the various hypotheses concerning the formation and evolution of volcanic rifted margins, and in investigating the deep structure of the North Atlantic.

#### **4.2 Past work.**

Scrutton (1972) modelled a gravity profile across the Rockall Trough and Plateau into the Iceland Basin using the results of seismic refraction data as structural control. Refraction velocities were correlated along the profile and layer densities were assigned using the extended velocity-density relationship of Ludwig, Nafe & Drake (1970). In order to achieve a satisfactory fit west of Hatton Bank it was necessary to invoke an oceanic crustal thickness of 12 km combined with an anomalously low density upper mantle, based on isostatic considerations and the low velocity obtained at refraction station E5 by Ewing & Ewing (1959). The gravity results confirmed the continental affinity of the Rockall-Hatton Bank, and showed that the area is in approximate isostatic equilibrium.

More recently Roberts & Ginzburg (1984) used gravity models to determine the position of the ocean-continent boundary with respect to the suites of oceanward dipping reflectors observed on multichannel seismic reflection profiles on the southwest Rockall Plateau. The crustal and upper mantle ocean-continent transition was modelled as an abrupt boundary at the landward limit of anomaly 24B. They concluded that the dipping reflectors are underlain by stretched continental crust, a result supported by recent lead isotope analysis of the DSDP basalts composing

the dipping reflectors (Morton & Taylor, 1987).

Livermore (1980), and subsequently Wigginton (1984) included thermal effects in the upper mantle in modelling gravity profiles across the Hatton Bank continental margin. Assuming the North Atlantic is in isostatic equilibrium (Haigh, 1973a,b) they found the lithospheric density under anomalously shallow oceanic crust of successive ages required to maintain isostatic equilibrium with thermally equilibrated lithosphere of assumed density  $3.33 \text{ g cm}^{-3}$ . The sub-continental to sub-oceanic lithospheric density gradient was assumed to be a linear transition from a normal sub-continental density of  $3.33 \text{ g cm}^{-3}$  to the calculated sub-oceanic lithosphere density for the oldest sea floor adjacent to the Hatton Bank. The ocean-continent boundary was assumed to lie at the landward limit of anomaly 24, and the crustal thickness was varied to achieve a satisfactory fit. They concluded that despite the rather arbitrary upper mantle density distributions employed, the inclusion of thermal effects resulted in more realistic gravity models. Both imply a substantial thinning of the continental crust towards the ocean-continent boundary. In addition Wigginton suggested that the dipping reflectors observed on complementary seismic reflection profiles along the gravity line overlie stretched continental crust in agreement with Roberts & Ginzburg (1984).

Gravity models of the conjugate East Greenland margin include those of Featherstone (1976), Armstrong (1981), and Uruski & Parson (1985). Featherstone and Armstrong acknowledged the likely presence of upper mantle density variations but made no serious attempt to model them. Uruski & Parson included upper mantle density variations in all their models. However, having no refraction data to constrain the deep crustal structure, the models obtained are speculative.

The gravity models so far mentioned illustrate the ambiguity inherent in all gravity modelling. With the exception of Scrutton (1972), all other models had no deep nearby refraction data to constrain lower crustal structure and, where included, upper mantle density gradients were necessarily rather arbitrarily constructed. The detailed definition of crustal structure using deep refraction techniques is a necessary step in reducing the ambiguity in assumed crustal gravity models before meaningful investigations of possible upper mantle density distributions can be made.

### **4.3 Initial models.**

#### **4.3.1 The data.**

As well as four two-ship synthetic-aperture profiles (SAP) across the Hatton-Bank continental margin, ten two-ship expanding-spread profiles (ESP) were shot along strike, completely straddling the margin (chapter 1). Six of these were airgun ESPs intended to image the shallow velocity structure of the crust, the remaining four being explosive ESPs designed to resolve the deeper crustal structure. These data were analysed by using synthetic seismogram full wave reflectivity modelling, and provide constraints on the lateral changes in velocity structure across the margin (White *et al.*, 1986). In addition normal incidence (NI) multichannel seismic reflection profiles were shot both across and along strike on selected lines to give additional information on upper crustal structures. These data provide comprehensive constraints on the crustal structure across the entire continental margin upon which gravity models can be based.

#### **4.3.2 The Crustal Model.**

The mid-points of the ESPs lay approximately along SAP2 and NI8 which were

consequently chosen to provide the bathymetry and sediment layer definitions and the gravity data to make up the profile (chapter 1). The relevant bathymetry and gravity data positions were projected perpendicularly on to a line of section defined by the oceanward and continentward limits of NI8 and SAP2 respectively, and converted to distance along the line of section using the oceanward limit of the line of section as the origin (program XDIST, appendix A). The ESP/SAP2 intersection points were similarly converted into distance along the line of section to provide structural constraints at appropriate positions along the profile. Sediment thicknesses were taken from SAP2 and NI8, converted from two-way-time to depth using an average sediment velocity of  $2.0 \text{ km s}^{-1}$  consistent with SAP2 hyperbolic velocity analysis results (chapter 6).

The crustal structure was defined from the interpretation of the ESP modelling results (White *et al.*, 1986). Two important, well constrained horizons were identified. The first is the Moho at the base of the crust, with sub-Moho velocities in the range  $8.0 \text{ km s}^{-1}$  to  $8.1 \text{ km s}^{-1}$ . The second is a mid-crustal horizon separating an overlying high velocity gradient region with velocities between  $5.0 \text{ km s}^{-1}$  and  $7.0 \text{ km s}^{-1}$ , from an underlying low velocity gradient region with velocities between  $7.1 \text{ km s}^{-1}$  and  $7.4 \text{ km s}^{-1}$ , outlined by the  $7.0 \text{ km s}^{-1}$  isovelocity contour (figure 4.1). White *et al.* interpreted this body as residual igneous material left after extrusion of the dipping reflectors, which underplated beneath the then Moho defined by the top of the high velocity lens, implying that the present Moho is a new boundary.

SAP2 hyperbolic velocity analysis (chapter 6), combined with the ESP modelling (figure 4.1), show that the velocities in the dipping-reflector sequences range from  $3.0 \text{ km s}^{-1}$  at the top to  $6.0 \text{ km s}^{-1}$  at the base of the unit. The  $6.0 \text{ km s}^{-1}$  isovelocity contour approximately coincides with the base of the visible dipping



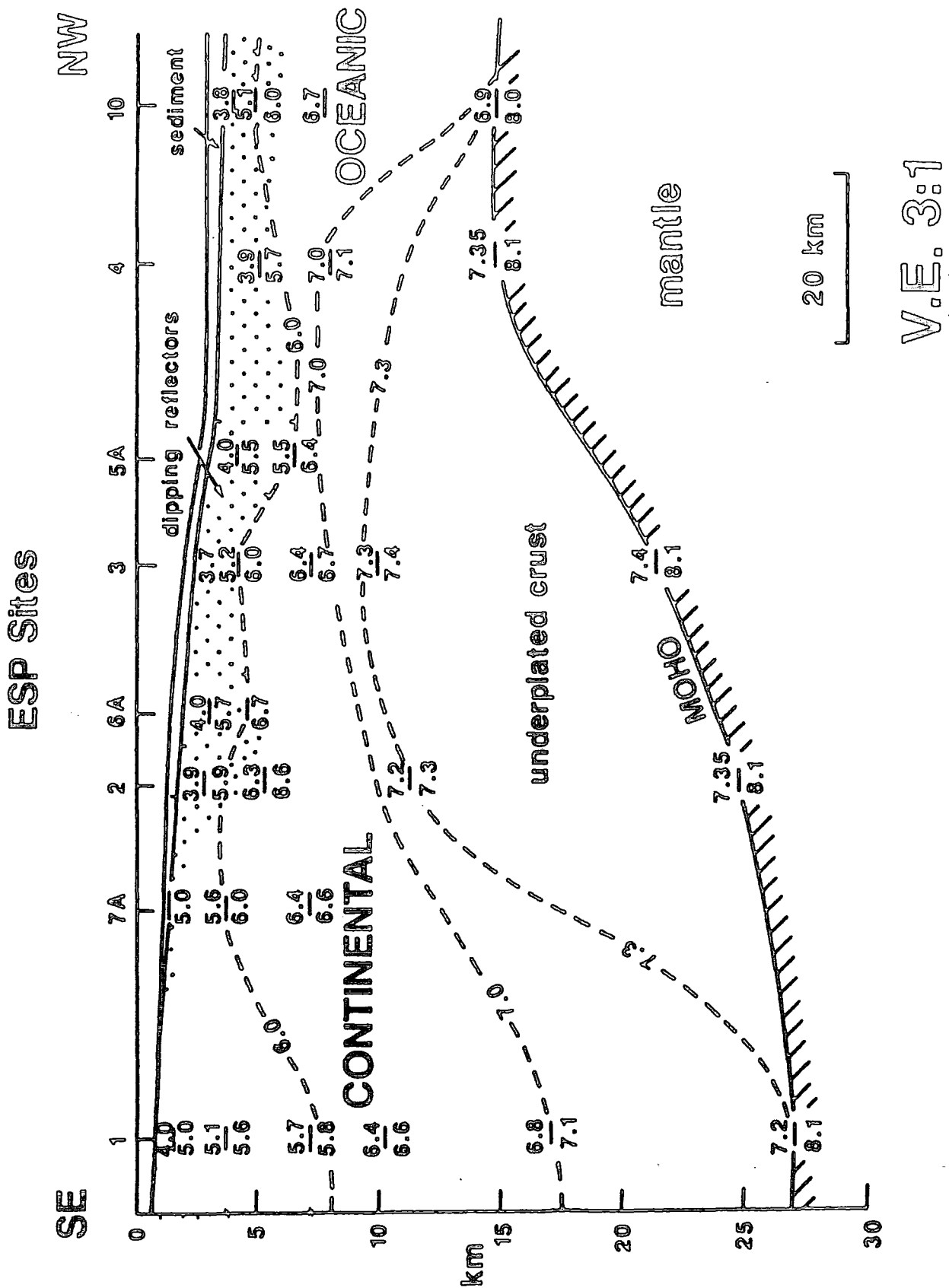


Figure 4.1 Isovelocity contour section across the Hatton Bank continental margin. Velocities are in  $\text{km s}^{-1}$ , isovelocity contour levels 6.0, 7.0, 7.3  $\text{km s}^{-1}$  shown. (Reproduced from White *et al.*, 1986).

reflectors, although in some instances these are seen to extend to greater depths.

The velocity structure of the most landward ESP1 was interpreted by White *et al.* as continental, whereas that of the most oceanward ESPs 4 and 10 are consistent with thick oceanic crust (figure 4.1). The  $7.0 - 7.1 \text{ km s}^{-1}$  horizon on ESP4 and the  $6.7 - 6.9 \text{ km s}^{-1}$  horizon on ESP10 were interpreted as defining the oceanic layer2-layer3 boundary. In between these extremes the thin layer of crust between the dipping-reflector sequences and the underlying underplated lens was ambiguously interpreted as having a velocity structure consistent with stretched and thinned continental crust similar to that observed on the Biscay continental margin (Whitmarsh *et al.*, 1986), or alternatively with that of thick oceanic crust similar to that described in Iceland and on the Voring Plateau (Mutter *et al.*, 1982). They concluded that no distinction between these alternatives could be made on the basis of seismic structure alone.

#### **4.3.3 Assumed crustal structure and densities.**

In producing a gravity model assumptions have to be made concerning the densities to be used to represent various crustal rock types. Density estimates can be made from a knowledge of the crustal velocity structure by using velocity-density relationships (Ludwig, Nafe & Drake, 1970). However, using velocity as the only indication of rock density may result in errors in the calculated gravity comparable in magnitude to the measured gravity (Barton, 1986). This is due to the scatter in the data used to construct velocity-density curves. The effects may be reduced by careful consideration of other constraining factors but cannot be eliminated.

A more acceptable approach is to combine available velocity information with a knowledge of expected rock types to constrain the densities by comparison with di-

rect measurements on appropriate rock samples. This method was used to estimate the densities incorporated in all subsequent gravity models.

#### 4.3.4 The Sediments.

The sediment density used was estimated from the results of the Deep Sea Drilling Project (DSDP) operations on the south-west Rockall Plateau during Legs 48 (Montadert & Roberts, 1979) and 81 (Roberts, Schnitker, *et al.*, 1984), and in the Iceland Basin during Leg 12 (Laughton, Berggren, *et al.*, 1972). An average sediment density of  $1.9 \text{ g cm}^{-3}$  was adopted as consistent with the general results. This is in good agreement with the density obtained from the velocity-density relationship for a sediment velocity of  $2.0 \text{ km s}^{-1}$ , obtained by SAP2 velocity analysis.

#### 4.3.5 Dipping reflectors and lavas.

Dipping reflector sequences have been drilled by the DSDP in two locations in the North Atlantic, one on the south-west Rockall Plateau, the second on the Voring Plateau of the Norwegian margin. On the Rockall Plateau the dipping reflectors were penetrated at sites 552 and 553 during DSDP Leg 81 (Roberts, Schnitker, *et al.*, 1984), and were found to consist of tholeiitic basalt flows intercalated with volcanic debris. On the Norwegian margin a deep drill hole, site 642, succeeded in recovering a complete section through an upper volcanic series, and penetrated a separate underlying volcanic series (Leg 104 Scientific Party, 1986). The upper series composing the entire dipping reflector sequence was found to consist of a number of tholeiitic lava flows separated by layers of volcanoclastic sediments. The lower series basalts were markedly different in composition from those of the upper series, the boundary between the two representing horizon "K" identified from seismic reflection profiles on the Voring Plateau (Mutter *et al.*, 1982). The physical

properties of the upper series Leg 104 (Parson, pers. com.), and Leg 81 (Roberts, Schnitker, *et al.*, 1984) basalts were used to provide an estimate of the average density appropriate for the dipping reflector sequences of  $2.65 \text{ g cm}^{-3}$ . This implies a velocity of  $5.5 \text{ km s}^{-1}$  from the velocity-density relationship, in general agreement with SAP2 velocity analysis (chapter 6).

#### 4.3.6 Oceanic crustal structure.

The broad subdivision of oceanic crustal structure into three main layers (Rait, 1963) has recently been superseded by the recognition that the velocity structure of oceanic crust is more realistically characterised by continuous velocity-depth variations (Lewis, 1978 ; Spudich & Orcutt, 1980). However the subdivision is still relevant in the sense that oceanic layer 2 is a transitional zone with velocity increasing rapidly with depth in contrast to more uniform layer 3 velocity variations. The idea of layer 1 as the oceanic sediment layer remains unchanged.

A consistent picture of oceanic crustal structure has been developed by petrological modelling (Cann, 1970,74 ; Kidd, 1977) and the direct study of onshore ophiolite complexes (Salisbury & Christensen, 1978 ; Christensen & Smewing, 1981), now widely accepted to represent exposed sections through oceanic crust and upper mantle, constrained by observed oceanic velocity structure and direct sampling by drilling and dredging. Oceanic crustal density estimates were based on laboratory measurements made on DSDP core and ophiolite complex samples at appropriate confining pressures and from rock density compilations.

**Oceanic layer 2** forms the acoustic basement and extends to a depth where the velocity reaches about  $6.4 \text{ km s}^{-1}$ . It outcrops at the surface and has been widely sampled by drilling and dredging. It is basaltic in composition, consisting

of an upper sequence of rapidly quenched pillow lavas and lava debris underlain by massive lava flows passing into a sub-vertical sheeted dyke complex, the base of which coincides with the oceanic layer 2-layer 3 boundary. The rapid increase of velocity with depth is due to a corresponding decrease in porosity caused by the closing of pores and microcracks by increasing confining pressures.

ESP10 modelling implies velocities in the range  $3.8 \text{ km s}^{-1}$  to  $6.7 \text{ km s}^{-1}$  for Layer 2. The layer was divided into two sub-layers to maintain continuity of the dipping reflector and lava layer across the model. A density of  $2.65 \text{ g cm}^{-3}$  was considered to be a realistic estimate for the pillow lavas and volcanic debris of upper layer 2. Measurements on highly vesicular DSDP basalts (Hyndman & Drury, 1976), together with pillow basalt and metabasalt samples from ophiolites (Salisbury & Christensen, 1978 ; Christensen & Smewing, 1981) imply that this value is appropriate. For the lower layer 2 region a density of  $2.85 \text{ g cm}^{-3}$  was adopted. This is slightly higher than Hyndman & Drury's average DSDP basalt density of  $2.795 \text{ g cm}^{-3}$ . However this figure includes the upper, highly vesicular and consequently less dense samples implied to be representative of the upper layer 2 region already taken into account. An examination of the distribution of bulk densities of DSDP basalts given by Hyndman & Drury show that the figure is a reasonable estimate. Averaging the densities of lower layer 2 metadolerite samples from ophiolite complexes give a figure of  $2.83 \text{ g cm}^{-3}$  in good agreement. The densities assumed correspond to velocities of  $5.25 \text{ km s}^{-1}$  and  $6.1 \text{ km s}^{-1}$  for DSDP basalts at 0.5 kbar (Hyndman & Drury, 1976), consistent with the velocity structure known from ESP10 and SAP2 velocity analysis.

**Oceanic layer 3** forms the main oceanic crustal unit. Petrological models (Cann, 1970, 74 ; Christensen & Salisbury, 1975), and computer simulations (Kidd,

1977) of oceanic crustal structure and formation processes indicate that layer 3 is formed at the magma chamber of the mid-ocean ridge by the crystallisation of magma in the chamber, with layer 2 dykes forming above the chamber. It is thought to be gabbroic in nature, with an upper layer formed by crystallisation of gabbro from the roof down, and a lower cumulate layer formed by crystal settling from the magma.

The structure determined for ESP10 implies velocities  $6.7 \text{ km s}^{-1}$  to  $6.9 \text{ km s}^{-1}$  in oceanic layer 3. The density was determined in a similar manner to those for layer 2. The average bulk density for ten DSDP gabbro samples was  $2.967 \text{ g cm}^{-3}$ , with a range of velocities between  $6.8 \text{ km s}^{-1}$  and  $7.3 \text{ km s}^{-1}$  (Hyndman & Drury, 1976). These velocities are high compared to those determined from ESP10 and in general for layer 3. However Hyndman & Drury reason that only 2% water-filled voids are required to reproduce the observed average velocities and conclude that fracturing and faulting in the crust is sufficient to cause the required velocity reduction. Measurements on gabbros from ophiolite complexes give an average density of  $2.93 \text{ g cm}^{-3}$ , and a density of  $2.976 \text{ g cm}^{-3}$  was averaged from other published data (Clark, 1966). Consequently a density of  $2.95 \text{ g cm}^{-3}$  was adopted for layer 3. This corresponds to a velocity of  $6.7 \text{ km s}^{-1}$  for oceanic rocks at 1.0 kbar (Christensen & Salisbury, 1975) consistent with ESP10 model results.

#### **4.3.7 Continental crustal structure.**

A general definition of continental crustal structure has proved more elusive than for oceanic crust. However, petrological and seismic observations have resulted in a picture of the continental crust as consisting of upper and lower crustal layers underlying a variable sediment thickness. The boundary between the up-

per and lower crustal regions is thought to represent the seismologically identified Conrad discontinuity where observed. Crustal velocities range from  $5.7 \text{ km s}^{-1}$  to  $6.3 \text{ km s}^{-1}$  in the upper layer, to between  $6.5 \text{ km s}^{-1}$  and  $7.6 \text{ km s}^{-1}$  in the lower crust. Generally a gneissic or granodioritic upper crust passing into granulitic facies (Christensen & Fountain, 1975) possibly overlain by amphibolite facies rocks gives rise to an acceptable fit to the observed data (Meissner, 1986). Further insight into continental crustal structure may be gained by study of obducted continental crust along a great fault. The process of obduction gives rise to a cross-sectional view of the crust. Results of examination of several obducted crustal regions (Fountain & Salisbury, 1981) support the crustal structure indicated of a basal granulite zone below intermediate amphibolite and upper greenschist zones. Seismic investigations however, reveal large variations in detailed crustal structure depending on age and metamorphic history, and the model gives only a broad indication of the crustal rock-types expected within regions of the crust. In assigning densities to the crust, a self-consistent approach combining available geophysical data with the ideas on crustal structure indicated above was adopted.

#### **4.3.8 Continental densities.**

Hall & Simmons (1979) concluded that a three-layer crustal model consisting of an upper region of mixed metamorphic rocks plus granites passing into a mid-crustal region of mixed pyroxene-granulite facies rocks underlain by a third layer of mafic garnet granulites exists in northern Britain. Dredge and DSDP results in the Rockall Plateau region produced pre-Cambrian granulites implying a similar crustal composition (chapter 1).

ESP results indicate velocities between  $7.0 \text{ km s}^{-1}$  and  $7.2 \text{ km s}^{-1}$  for the lower

Hatton-Bank continental crust. These velocities are consistent with a granulitic lower crust for which a density of  $2.95 \text{ g cm}^{-3}$  is considered appropriate (Fountain, 1976 ; Clark, 1966). This compares with a density of  $2.975 \text{ g cm}^{-3}$  for a velocity of  $7.1 \text{ km s}^{-1}$  estimated from the Ludwig *et al.* velocity-density relationship.

For the mid crustal layer, a mean density of  $2.85 \text{ g cm}^{-3}$  was adopted consistent with that given for pyroxene granulites of northern Britain (Hall & Simmons, 1979), having a velocity of  $6.8 \text{ km s}^{-1}$ . A velocity of  $6.6 \text{ km s}^{-1}$  is implied for a density of  $2.85 \text{ g cm}^{-3}$  (Ludwig *et al.*, 1970). These velocities compare well with the range  $6.0 \text{ km s}^{-1}$  to  $7.0 \text{ km s}^{-1}$  determined from ESP modelling.

A density of  $2.65 \text{ g cm}^{-3}$  was assigned to the crust above the  $6.0 \text{ km s}^{-1}$  isoveLOCITY contour. This is a realistic estimate for the average density of lavas underlain by a pyroxene granulite basement, and corresponds to a velocity of  $5.7 \text{ km s}^{-1}$  (Ludwig *et al.*, 1970) in good agreement with the range  $3.8 \text{ km s}^{-1}$  to  $6.0 \text{ km s}^{-1}$  determined by ESP modelling.

#### **4.3.9 Underplated crustal density.**

The ponding of magma at the base of the crust is regarded as an important step in the formation of continental flood basalts (Furlong & Fountain, 1986 ; Cox , 1980). Adiabatic melting of upwelling mantle material is followed by the segregation of melt which accumulates at the base of the crust. The evolved liquids are forced to the surface by the lithostatic pressure when the densities of the differentiating liquids become sufficiently low, leaving the denser cumulates to underplate the base of the crust. This process implies that in areas of flood basalt volcanism such as a volcanic rifted continental margin, a significant addition of gabbroic material to the base of the crust may occur.



Modelling of the underplating process indicates that the velocity structure obtained by ESP modelling is consistent with a quartz-tholeiite or olivine-gabbro composition for the underplated lens for which a density of  $3.05 \text{ g cm}^{-3}$  was estimated (Clark, 1966 ; Christensen & Smewing, 1981 ; Christensen & Salisbury, 1975). This is consistent with calculated densities of the component fractions involved in melt segregation (White, pers. com.).

#### 4.3.10 Upper mantle density.

Models of the density distribution within the earth's mantle must be consistent with the available geophysical and petrological data. These constraints include the seismic compressional and shear-wave velocities, Poisson's ratio, gravity, and petrological evidence from possible mantle-derived rocks (Ringwood, 1975). These data imply a peridotitic composition for the upper mantle.

From gravity and seismic data, and an estimate of the mean density of continental crust, it was concluded that the most probable density of the upper mantle lies between  $3.3 \text{ g cm}^{-3}$  and  $3.4 \text{ g cm}^{-3}$  (Ringwood & Green, 1966 ; Ringwood, 1969 ; Woollard, 1970 ; Ringwood 1975). Petrological models of the upper mantle included the pyrolite model (Clark & Ringwood, 1964) which postulates a synthetic peridotitic or "pyrolite" composition for the upper mantle. Resultant density distributions calculated from the known component densities, thermal expansions and compressibilities, are in general agreement with those calculated from gravity and seismic investigations. Upper mantle density distributions are, however, largely uncertain within the bounds provided by the geophysical and petrological constraints. A value of  $3.33 \text{ g cm}^{-3}$  was consequently chosen on the basis that it lay between the limits stated above and is a commonly assumed value in gravity modelling (e.g.

Scrutton, 1972 ; Livermore, 1980 ; Wigginton, 1984). A density of  $3.32 \text{ gcm}^{-3}$  is implied from the velocity-density relationship of Ludwig *et al.* for the ESP derived sub-moho velocity of  $8.1 \text{ km s}^{-1}$ , in good agreement with the assumed density.

#### 4.4 Gravity models.

##### 4.4.1 ESP control.

The density estimates were incorporated into the crustal model described to give an initial density model (figure 4.2). The model is continuous across its length with the identified layer 2-layer 3 boundary on ESPs 4 and 10 joined smoothly to the  $7.0 \text{ km s}^{-1}$  isovelocity contour, with a uniform density upper mantle. The model thus makes no a priori assumption concerning the position of the ocean-continent boundary except that it lies somewhere between ESPs 1 and 4. The model implies an average continental crustal density of  $2.84 \text{ g cm}^{-3}$ , and an average oceanic crustal density of  $2.87 \text{ gcm}^{-3}$ . These compare with the average continental and oceanic densities of  $2.84 \text{ g cm}^{-3}$  and  $2.86 \text{ g cm}^{-3}$  estimated by Worzel (1974). The oceanic density is slightly higher than that given by Worzel. However considering the anomalously thick oceanic crust in the area and the fact that the figures quoted are estimated means from various locations, a discrepancy of 0.4% is regarded as acceptable. This crustal model was used as the initial model for those which follow.

The modelled gravity profile is shown in figure 4.3, and displays a fairly good correlation with the shorter wavelength features of the observed gravity profile. However, the long wavelength discrepancy of up to 70 mGal across the model reflects the fact that the model with a uniform density upper mantle is not in isostatic equilibrium. The lack of compensation of the model is illustrated in figure 4.4 which shows the general increase in mass/unit area down to 80 km depth oceanwards from

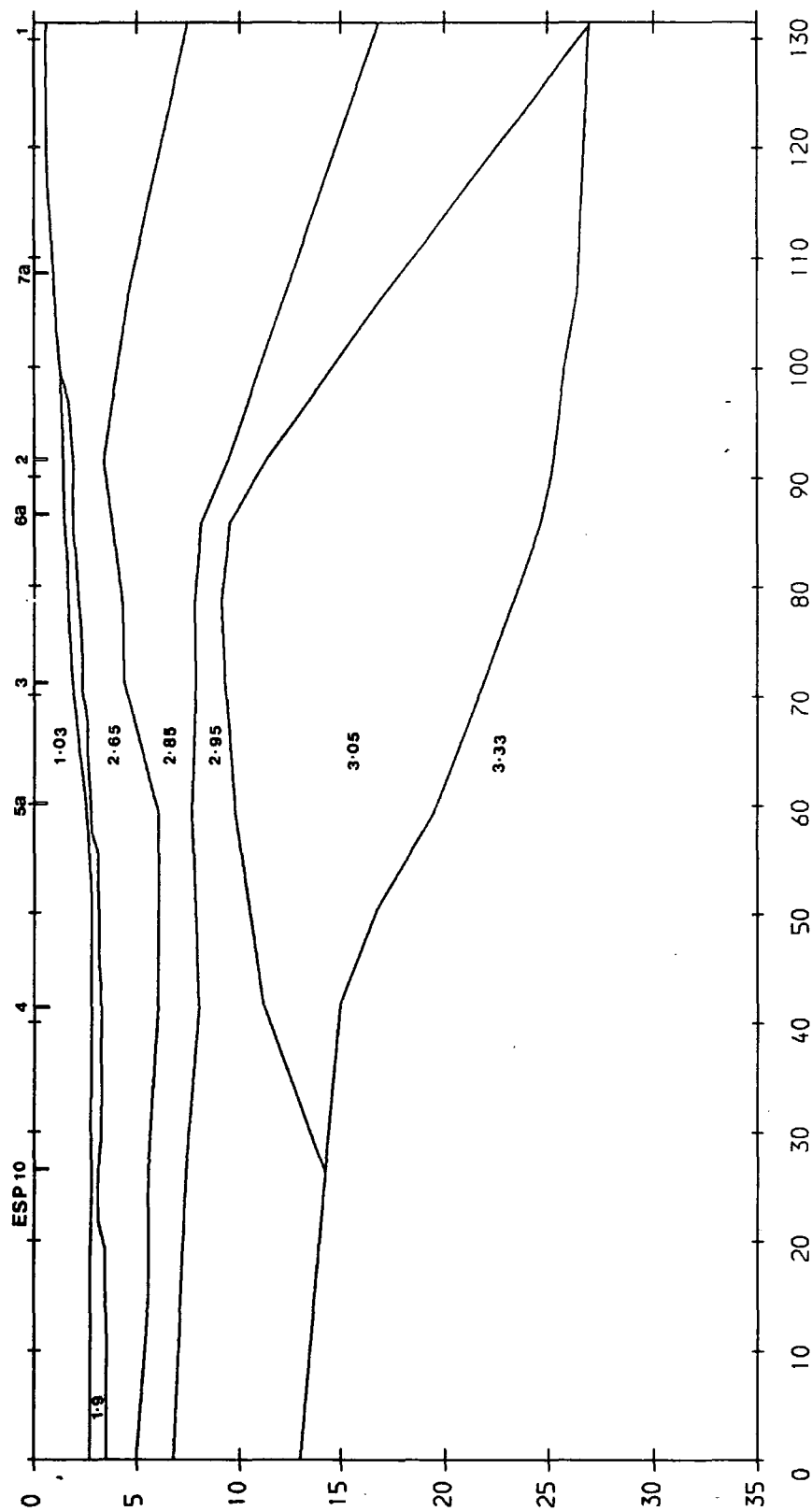


**Figure 4.2** Density model based on the ESP isovelocity contour model of White *et al.*, (1986) (figure 4.1). Densities are in  $\text{g cm}^{-3}$ .

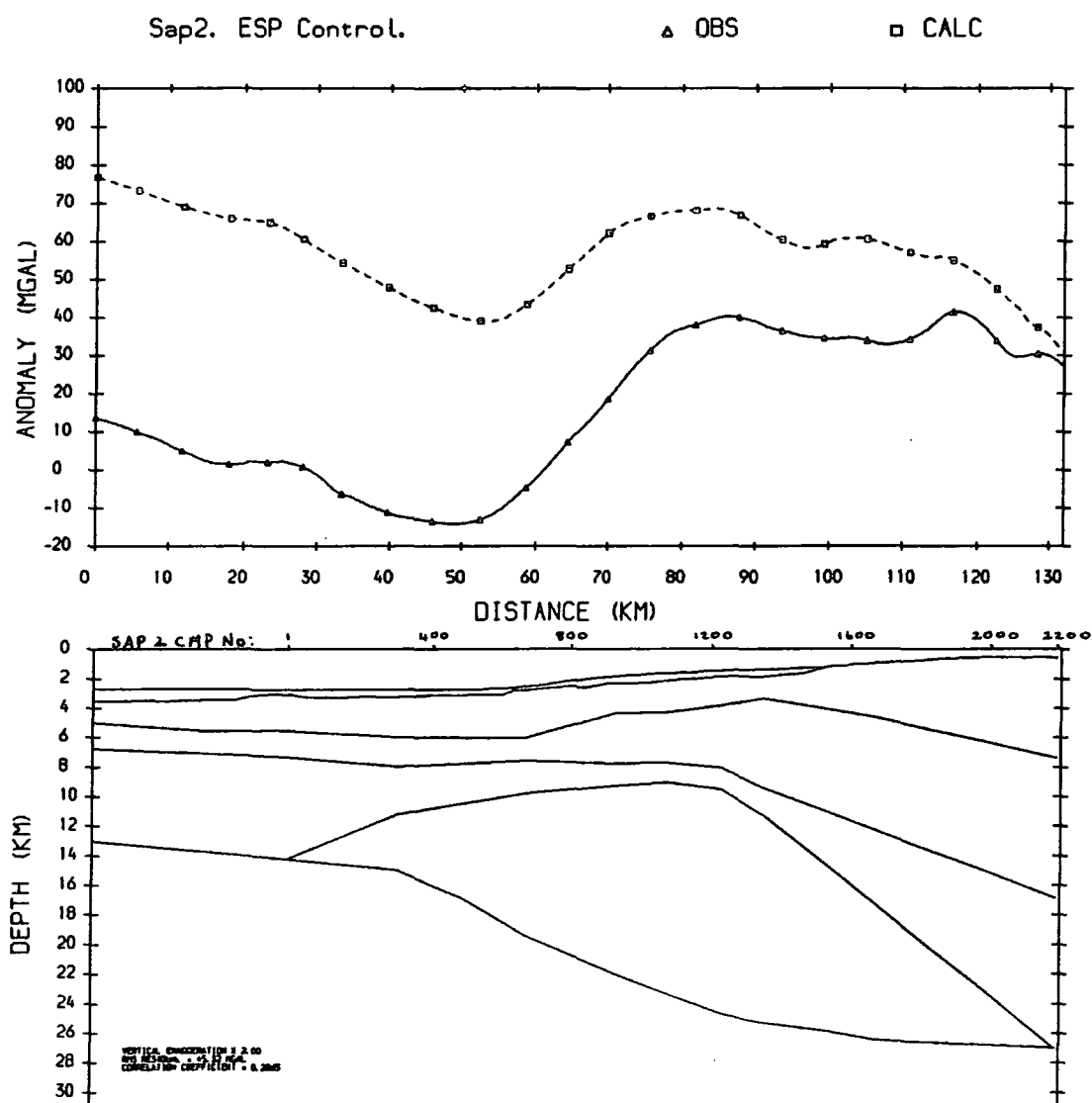


**Figure 4.3** The gravity model resulting from the density model shown in figure 4.2. The solid line is the observed, and the broken line is the calculated gravity profile.

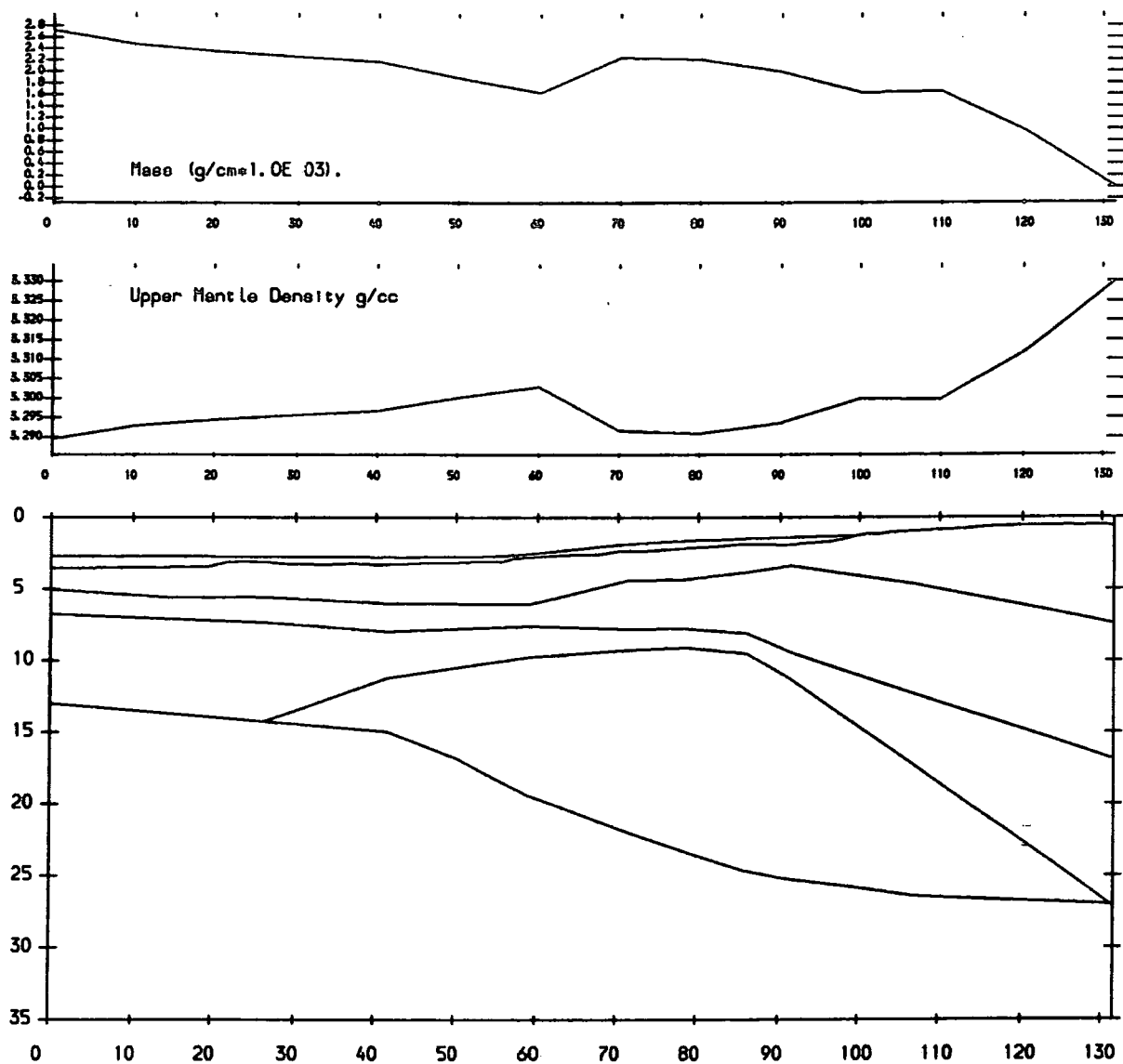
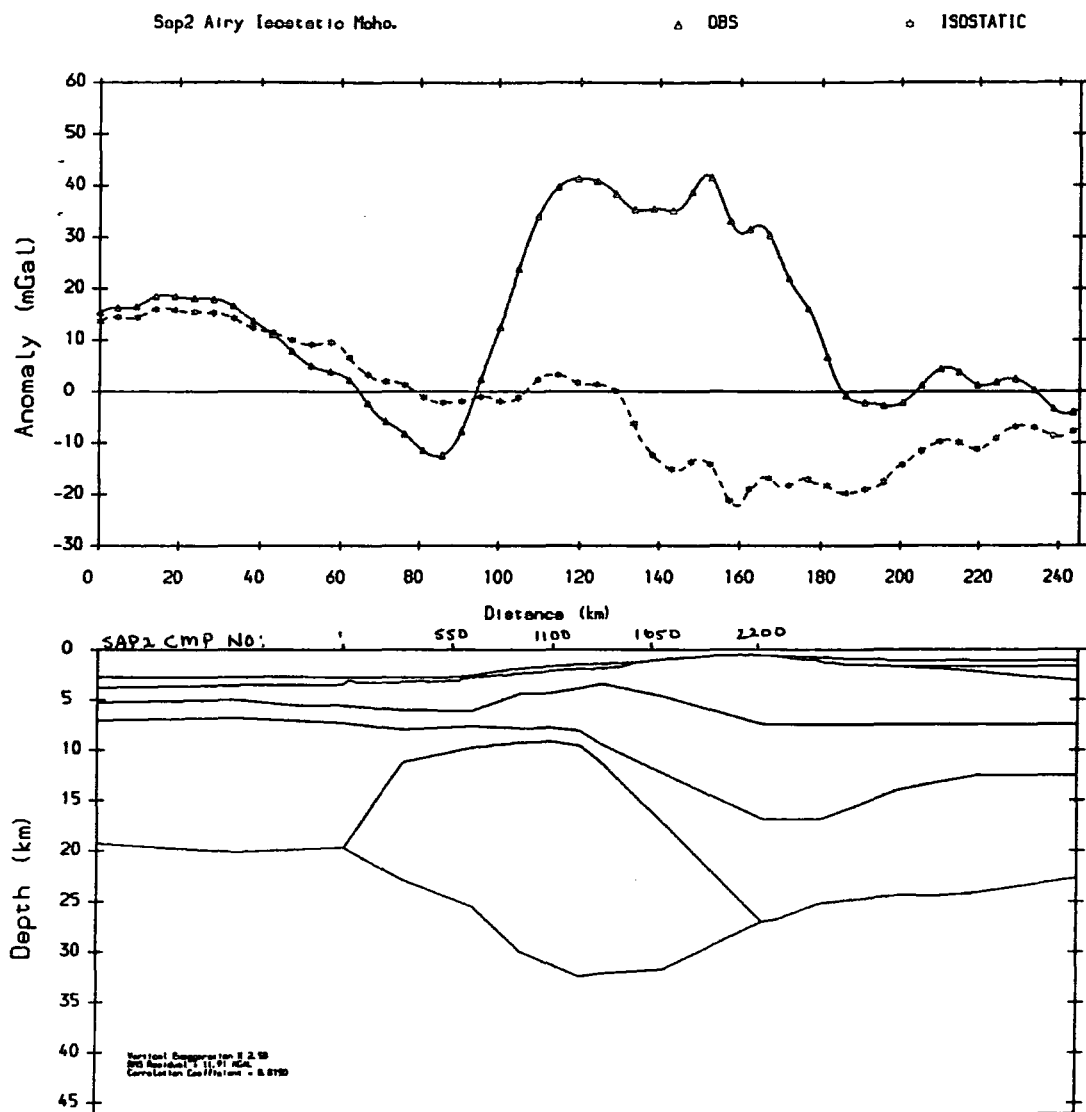


Figure 4.4 Illustration of the increase in mass per unit area down to a depth of 80 km for the model shown in figure 4.3. Also shown is the calculated upper mantle density distribution required to maintain the model in isostatic equilibrium with a depth of compensation of 80 km.

ESP1.

In order to check the assumption that the margin is in isostatic equilibrium, a local Airy isostatic model was constructed in which compensation of the adopted crustal model was achieved by variations in depth to the crust/mantle boundary assuming a constant upper mantle density of  $3.33 \text{ g cm}^{-3}$ , and a depth of compensation of 80 km. The resulting model is shown in figure 4.5. This indicates that the margin is in approximate isostatic equilibrium, with the magnitude of the isostatic anomaly not exceeding 20 mGal.

In addition, the isostatic anomaly shows a distinct oceanward high and continentward low. This phenomenon has been described on other passive continental margins, and two alternative explanations have been proposed (Rabinowitz & LaBrecque, 1977). Firstly the effect may be the result of the cooling and subsidence of oceanic lithosphere which is mechanically coupled to the adjacent buoyant continental lithosphere. The cooling and subsiding oceanic lithosphere will pull the adjacent continental lithosphere down, which in turn will support the oceanic lithosphere flexurally. Alternatively, volcanic material injected at elevations higher than the mid-ocean ridge in the early stages of rifting may result in a basement high in the oceanic crust adjacent to the ocean-continent transition, which is not accompanied by compensating variations in the crust/mantle boundary. The oceanic lithosphere and basement high is initially thermally supported, and subsequently flexurally supported as described earlier. Both mechanisms result in an uncompensated basement high and low ocean- and continentward of the ocean-continent transition respectively. The oceanward and continentward high and low in the isostatic gravity anomaly is the result of these mechanisms. The latter explanation was favoured by LaBrecque & Rabinowitz on the basis of available shallow reflection



**Figure 4.5** Local Airy isostatic model, with compensation of the crustal model achieved by variations in depth to the Moho. The calculated isostatic anomaly is shown as a broken line.

seismic data and local Airy isostatic gravity models.

The observed gravity signal therefore indicates that the margin is effectively in local isostatic equilibrium, a conclusion supported by flexural studies of the margin using SEASAT altimetry (Fowler, 1986) which imply a low flexural rigidity and an effective elastic thickness of only 5 km for the margin.

The discrepancy between calculated and observed gravity may have its origin in the crust in the form of an increase in continental crustal densities, or in the upper mantle in the form a density contrast between sub-oceanic and sub-continental regions. If the former is correct, an estimate of the average increase in continental crustal density may be obtained by using the slab formula

$$\Delta g = 2\pi G \Delta \rho \Delta t,$$

where  $\Delta g$  = gravity discrepancy,  $\Delta t$  = slab thickness,  $\Delta \rho$  = density contrast, and  $G$  = the universal gravitational constant.

Using this formula the required crustal density increase is of the order of  $0.08 \text{ g cm}^{-3}$  for  $\Delta t = 20 \text{ km}$ , and  $\Delta g = 70 \text{ mGal}$ . A corresponding increase in the underplated lens density would be necessary to maintain the density contrast at the lower crust/underplated lens boundary, and preserve the shape of the calculated anomaly. An increase in continental densities of  $0.08 \text{ g cm}^{-3}$  implies an average continental crustal density of  $2.92 \text{ g cm}^{-3}$ , substantially higher than that of  $2.87 \text{ g cm}^{-3}$  calculated for the modelled oceanic crust. This is in contrast to the observation that average oceanic crustal densities are generally higher than those of continental regions.

Crustal densities were chosen on the basis of consistency with available geophys-



ical data. Increasing these densities by as much as  $0.08 \text{ g cm}^{-3}$  would be inconsistent with this approach, and would result in unreasonably high average continental crustal densities relative to average oceanic densities. Therefore the existence of a density contrast in the upper mantle resulting from the non-equilibration of the rift thermal anomaly is inferred to be the source of the modelled gravity discrepancy, and the mechanism by which isostatic compensation of the margin is achieved. An estimate of the density contrast in the upper mantle down to 80 km required to reconcile the discrepancy can be made using the slab formula. Using a gravity discrepancy of 70 mGal, the density contrast was calculated to be of the order of  $0.03 \text{ g cm}^{-3}$ .

#### **4.4.2 ESP control and upper mantle density gradient.**

In order to model the long wavelength component, a density gradient in the mantle part of the lithosphere was constructed such that the margin is everywhere in local isostatic equilibrium. Assuming a depth of compensation of 80 km consistent with lithospheric thicknesses calculated by Haigh (1973a,b) for the North Atlantic, and an equilibrium sub-continental upper mantle density of  $3.33 \text{ g cm}^{-3}$  at ESP1, the upper mantle density variation required to maintain equilibrium across the model was calculated by equating the pressure at appropriate points along the model to that calculated at ESP1. The calculated density gradient of  $0.038 \text{ g cm}^{-3}$  was represented by a series of 10 km wide blocks with an appropriate density contrast estimated from the calculated upper mantle density distribution (figure 4.4), incorporated into the initial gravity model. The resulting gravity profile is shown in figure 4.6 and shows a much improved fit over figure 4.3. There are clear short wavelength misfits, one centred on ESP6a of about 20 mGal, and a second landward of ESP7a. However, examination of the contoured gravity (back pocket)

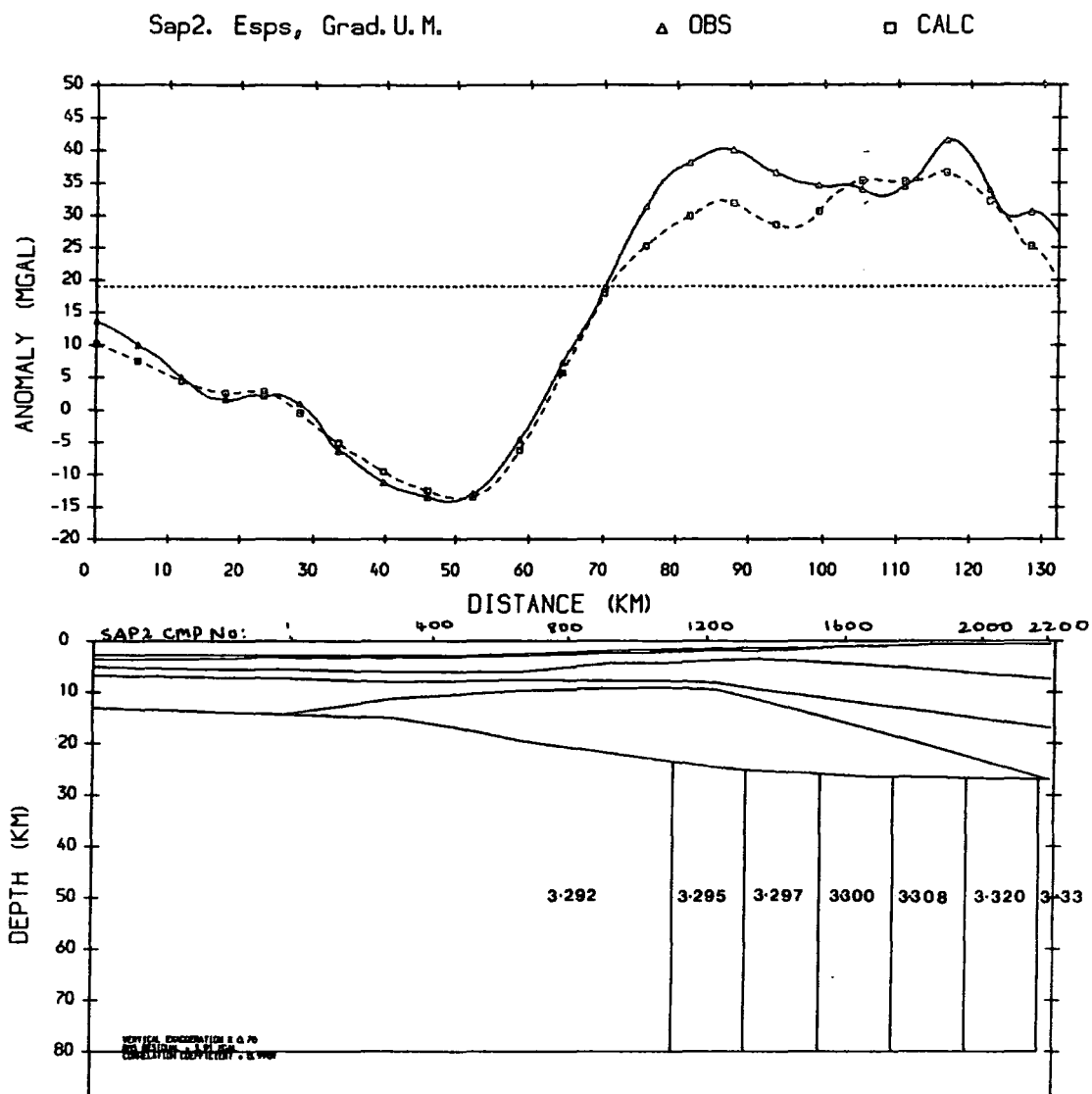


Figure 4.6 The gravity model of figure 4.3 including a lateral density gradation within the upper mantle derived from figure 4.4.

and magnetic (figure 5.5) maps suggests that these features are due to local three-dimensional effects within the crust, a conclusion supported by the seismic evidence from SAP2 which shows a disrupted region within the crust between the termination of the upper set of dipping reflectors at CMP 1200 and the abrupt truncation of an intra-basalt unconformity at CMP 900. This is interpreted as a post-rift volcanic event (chapter 6). The discrepancy at ESP6a was modelled as an intrusive body of density  $2.8 \text{ g cm}^{-3}$  and the resultant gravity model is shown in figure 4.7, indicating a good correspondence between calculated and observed gravity. The representation of the intrusive body is schematic and is intended as an indication of the presence of an anomalous body, not as a definition of its probable structure. Clearly it may equally be represented by a narrow dyke-type structure extending to depth.

In order to better constrain the model it was decided to extend it ocean- and continentwards. The observed gravity profiles used in modelling up to now were obtained by extracting ship track segments along the required line of profile from the main gravity data sets, smoothing for wave noise, and joining the segments to produce a single observed gravity profile. This process was time-consuming and inefficient. The gravity data sets collected were large and spatially dense, often having numerous tracks from both ships running approximately along the same path (chapter 2). Consequently a program (UDDERSTK, appendix A) was written which formed a representative profile along a desired line of section. This program extracted all data from the main data sets within a specified perpendicular distance from the desired profile line, and projected these data points perpendicularly onto the line of profile. The data were subsequently binned and stacked into appropriate bin sizes, and finally low-pass filtered in the wavenumber domain to remove any residual

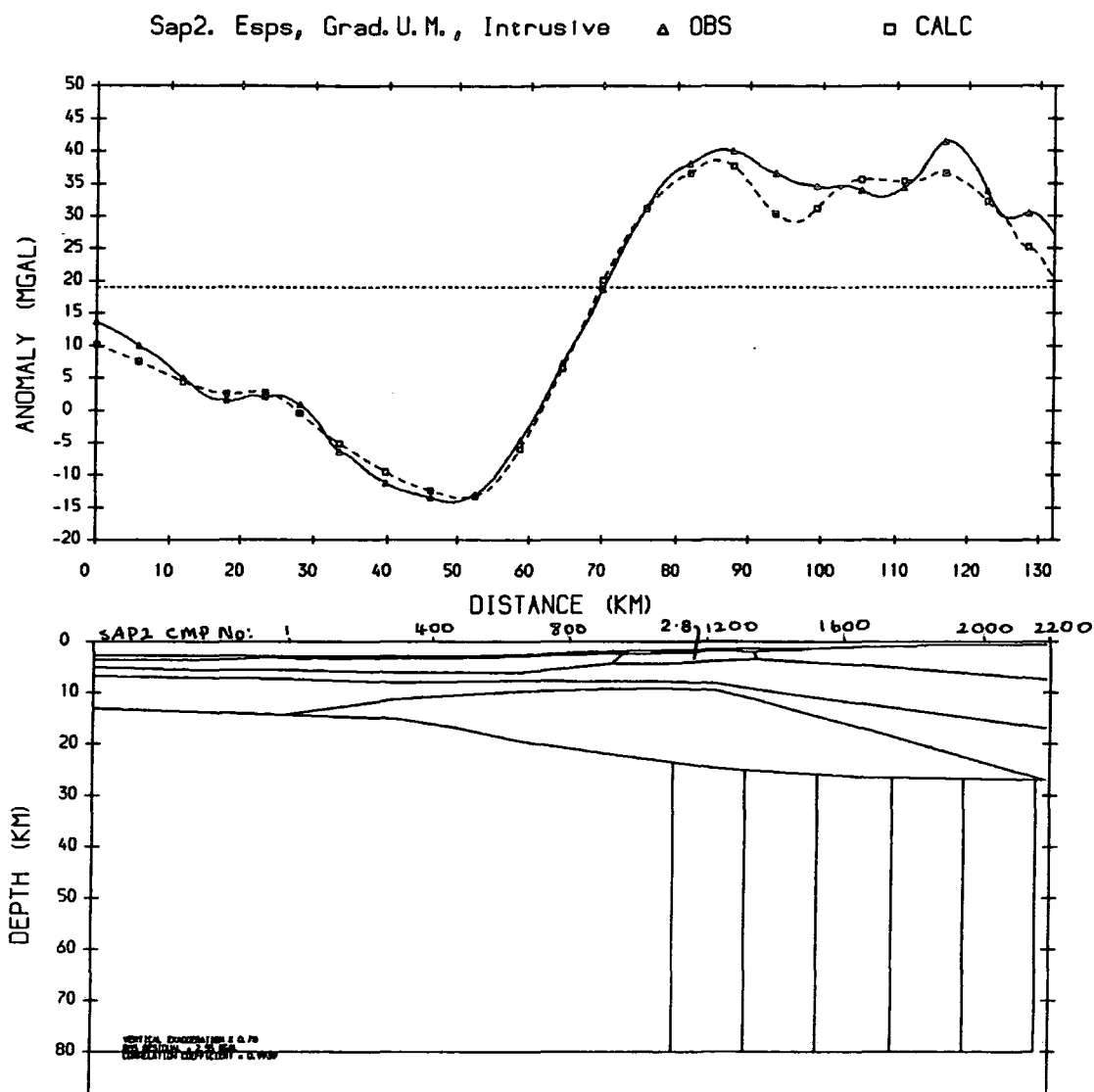


Figure 4.7 The gravity model of figure 4.6 with an intrusive included to model the mismatch at ESP 6a.

high wavenumber noise. This approach was considered most efficient in that the data only required drift-correcting prior to processing. Any anomalous readings due to ship turns, wave motion, equipment faults, data gaps and uncorrected meter-drift were eliminated during processing. The resultant profiles were considered to be better representations of the average gravity along a modelled section, whilst retaining short wavelength variations. Examples of extracted data, binned and stacked, and final profile stages are illustrated in figures 4.8 and 4.9. Bathymetry sections were constructed as described in section 4.3.2. Continentward of ESP1 the crustal layer and moho positions were constructed to be consistent with the results of a deep refraction line shot in the Rockall-Hatton Basin (Scrutton, 1972). New gravity models were constructed and are shown in figures 4.10 - 4.12. These show similar results to the initial models.

#### 4.5 Model implications.

The theory of sea floor spreading predicts a simple relationship between the age and depth of the sea floor (Parsons & Sclater, 1977). Observed depths can be affected by sediment loading, abnormal oceanic crustal thickness, and anomalous upper mantle temperatures. Depths corrected for these effects can be compared to predicted oceanic depths to check for consistency of the modelled oceanic floor with the Parsons & Sclater age/depth relationship. The depth of oceanic floor of age ( $t$ ) in ma B. P. is given by the relation

$$d(t) = 2500 + 350(t)^{\frac{1}{2}}.$$

For crust of age 55 ma B. P. this corresponds to a depth of 5.1 km.

A sediment load of thickness  $h_s$  will depress the crystalline basement by an

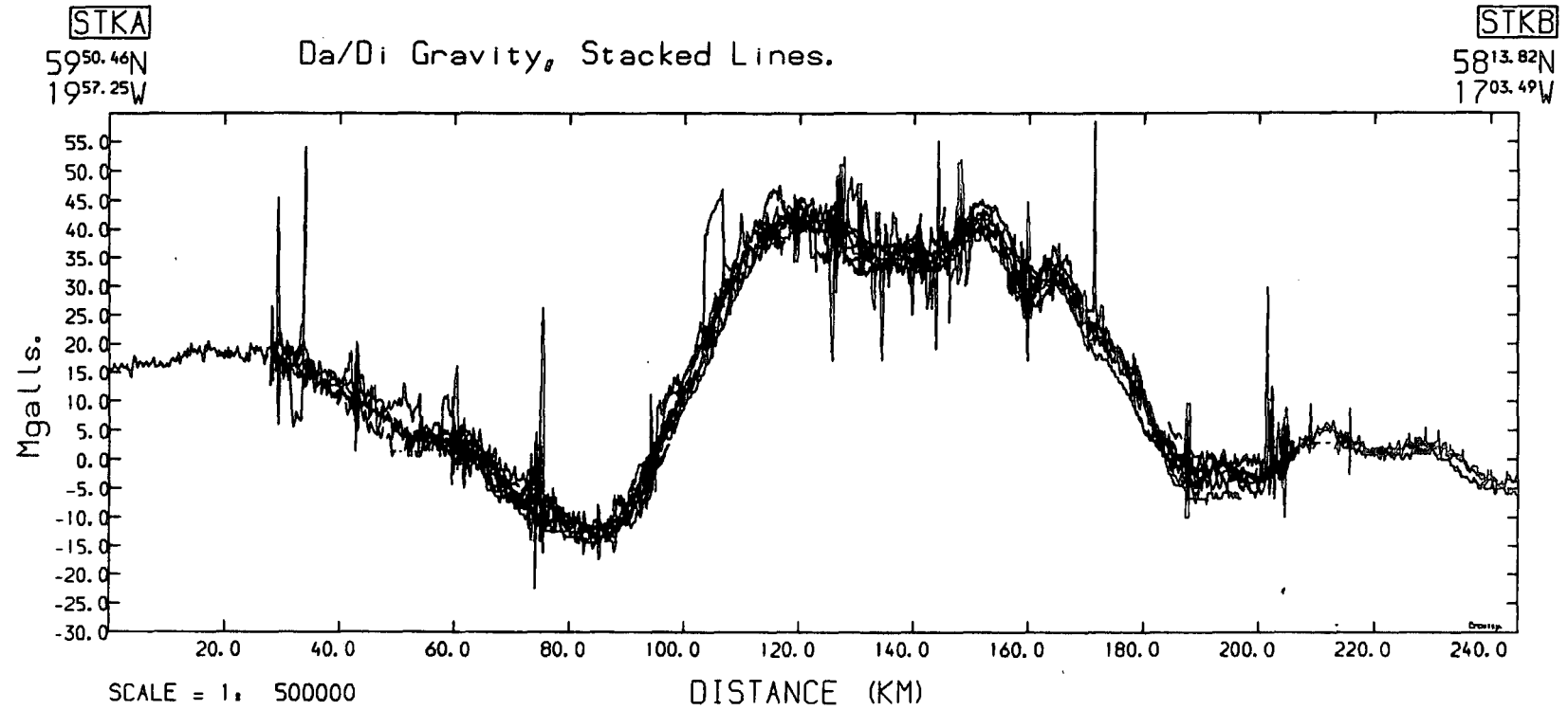
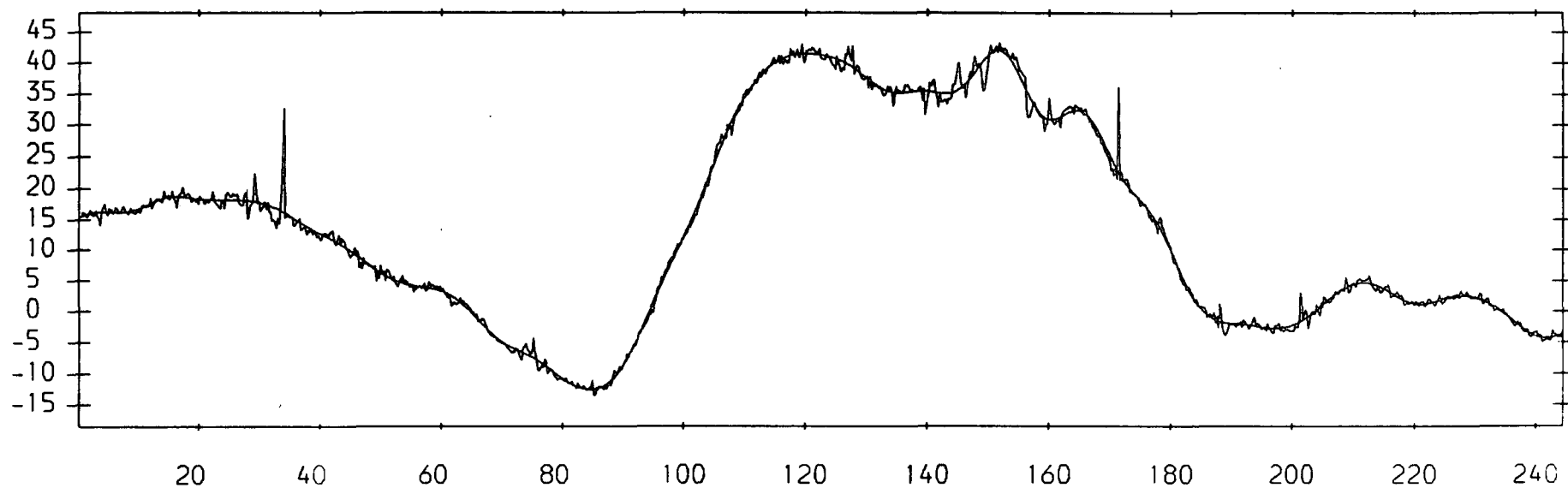
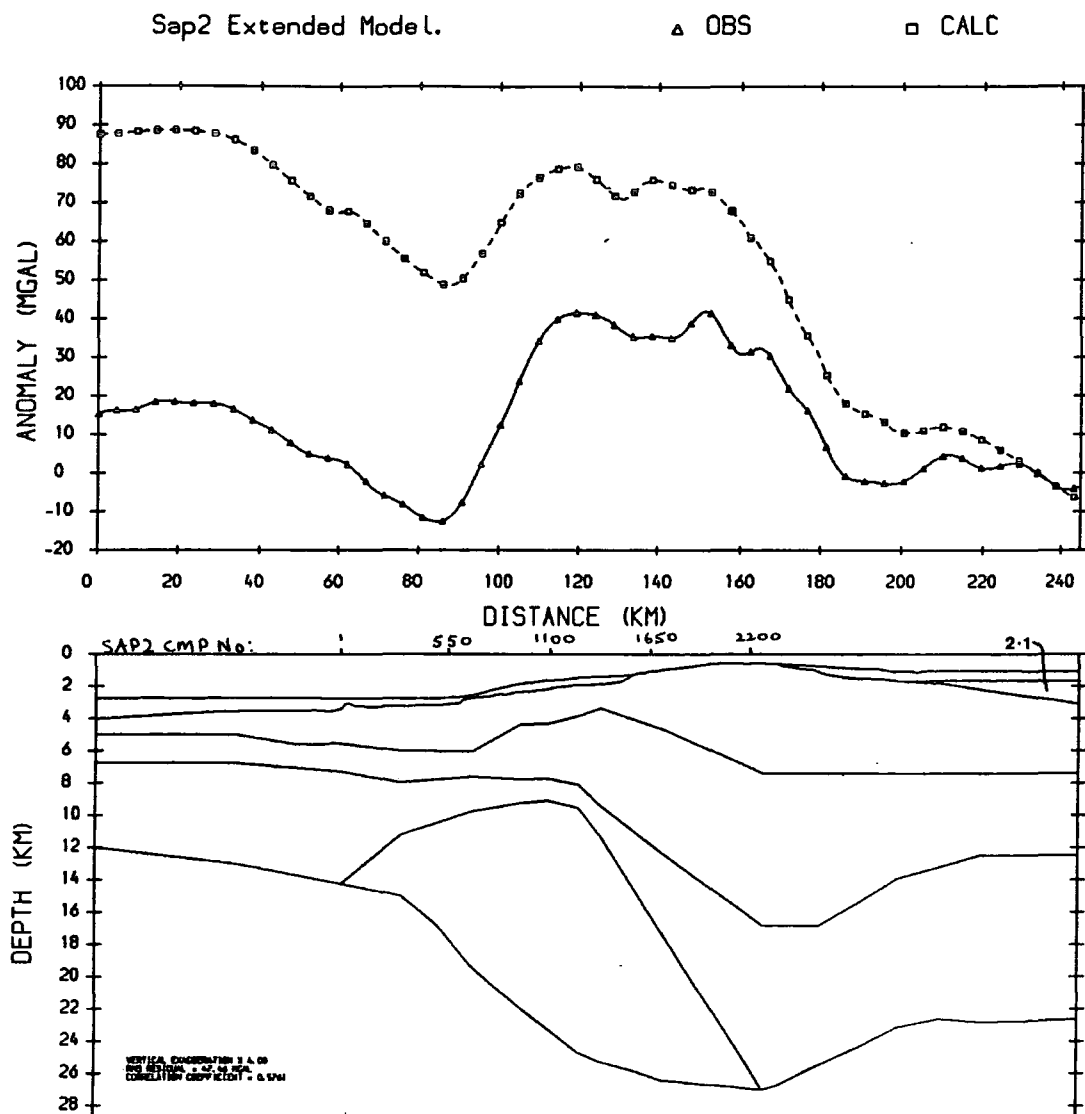


Figure 4.8 Illustration of the data extracted from within a 5 km perpendicular distance of a line of profile along SAP2, and NI8, prior to binning, stacking, and low-pass filtering.



**Figure 4.9** The data illustrated in figure 4.8, binned and stacked into a single, noisy representative profile. Superimposed is the final, low-pass filtered gravity profile used in subsequent gravity models.



**Figure 4.10** A version of the gravity model shown in figure 4.3, extended using the synthesised gravity profile of figure 4.9.



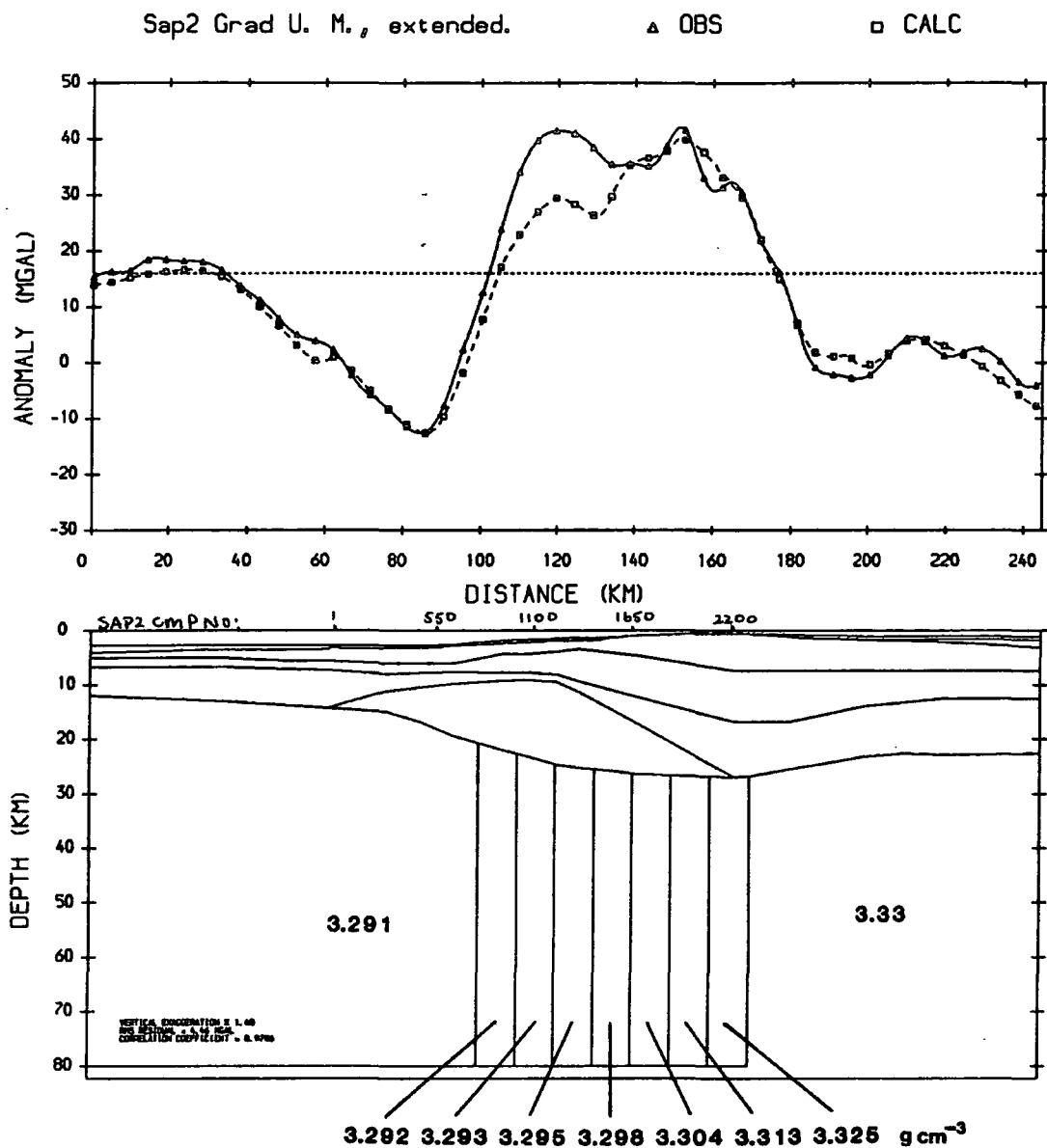


**Figure 4.11** A version of the gravity model shown in figure 4.6, extended using the synthesised gravity profile of figure 4.9.

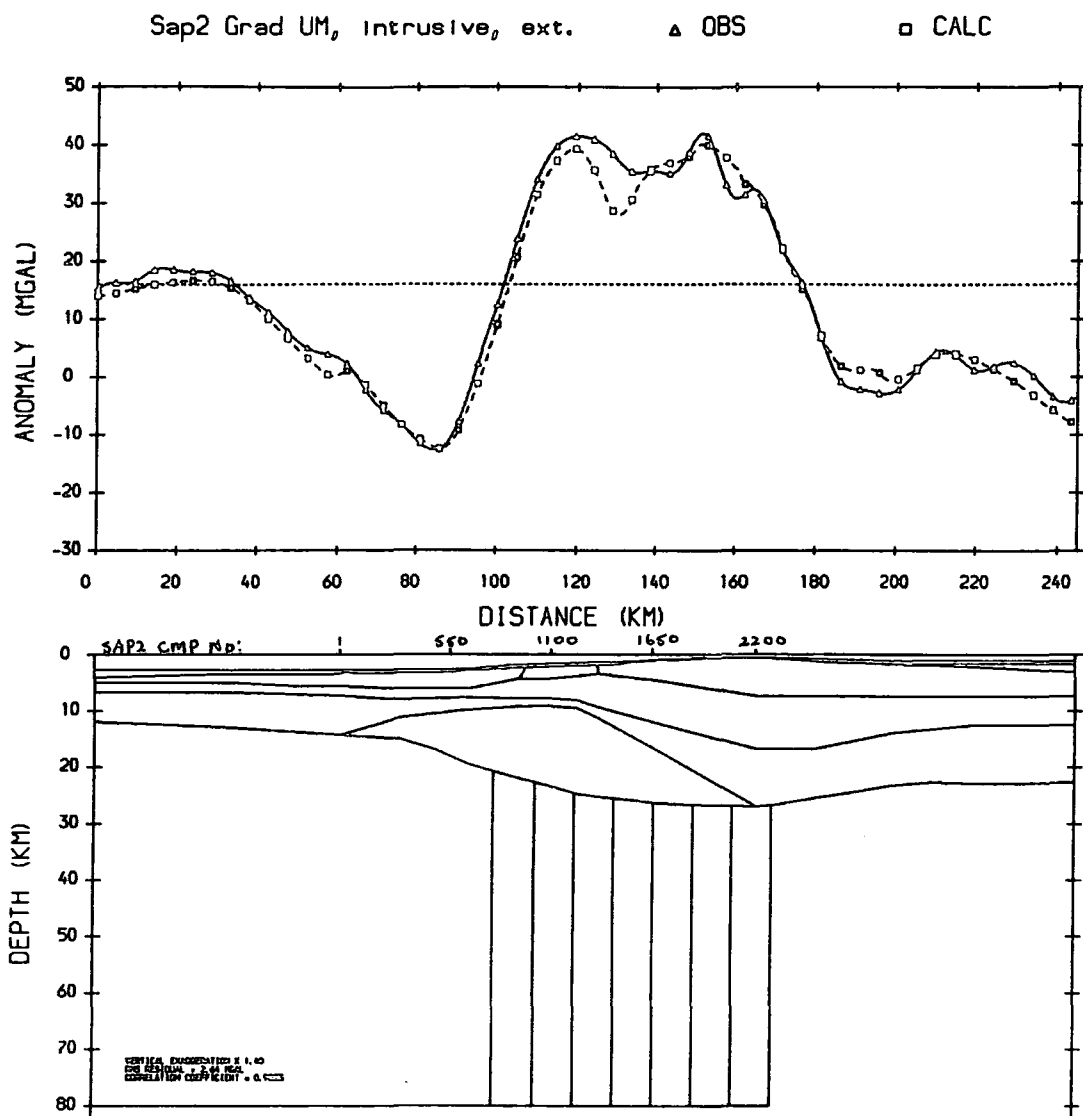


**Figure 4.12** A version of the gravity model shown in figure 4.7, extended using the synthesised gravity profile of figure 4.9.

amount  $\delta s$  where

$$\delta s = \frac{h_s(\rho_m - \rho_s)}{(\rho_m - \rho_w)}$$

and  $\rho_m, \rho_w, \rho_s$  = mantle, water, crustal densities. Similarly the water depth is affected by variations in crustal thickness by an amount  $\delta w$  where

$$\delta w = \frac{\delta c(\rho_c - \rho_m)}{(\rho_m - \rho_w)}$$

and  $\rho_c$  = crustal density,  $\delta c$  = difference between observed and normal oceanic crustal thickness. An estimate of the thickness for crust of age 55 ma B. P. of 6.07 km was obtained from published curves of oceanic layer thicknesses as a function of sea floor age (Christensen & Salisbury, 1975). The effect of a change in upper mantle density is to cause a depth variation given by

$$\delta h = \frac{h_1 \Delta \rho_1}{(\rho_w - [\rho_1 + \Delta \rho_1])}$$

where

$$\rho'_1 = \rho_1 + \Delta \rho_1$$

$$h_1 = D - (h_c + h_w)$$

and

$D$  = depth of compensation,

$h_c + h_w$  = water + crustal thickness,

$\rho_1$  = equilibrium upper mantle density,

$\rho'_1$  = anomalous upper mantle density,

$\Delta \rho_1$  = density contrast.

These corrections were applied to observed depth data (program DEPTH, appendix A). Figure 4.13 shows the corrected sea floor depths and indicates that they are consistent with those predicted by the age/depth relation of Parsons & Sclater (1977).

The density gradient obtained was used to imply a corresponding average temperature contrast between sub-oceanic and sub-continental lithosphere.

The volume of a constant mass of lithosphere at temperature  $\theta$  is given by

$$V_{\theta} = V_0(1 + \alpha\theta)$$

where  $\alpha$  = volume thermal expansion coefficient,  $V_0$ =volume at  $T_0$

For a temperature contrast of  $(\theta_2 - \theta_1)$ ,

$$\frac{V_2}{V_1} = \frac{\rho_1}{\rho_2} = \frac{(1 + \alpha\theta_2)}{(1 + \alpha\theta_1)}$$

Expanding binomially..

$$(1 + \alpha\theta_1)^{-1} = 1 - \alpha\theta_1 + \text{h.o.t.}$$

Therefore

$$\frac{\rho_1}{\rho_2} = 1 + \alpha(\theta_2 - \theta_1)$$

$$\Delta\theta = \frac{1}{\alpha} \left( \frac{\Delta\rho}{\rho_2} \right)$$

For  $\Delta\rho = 0.038 \text{ g cm}^{-3}$ ,  $\alpha = 2.5 \times 10^{-5}$ , and  $\rho_2 = 3.33 \text{ g cm}^{-3}$  then  $\Delta\theta = 460 \text{ K}$ .

This is an average temperature contrast for the mantle part of the lithosphere, and is clearly an unacceptable figure. Geothermal models (Pollack & Chapman, 1977), and thermo-mechanical models of the Nova-Scotia margin (Beaumont *et al.*, 1982), conclude that the temperature contrast should average 150 K over 80 km, with a

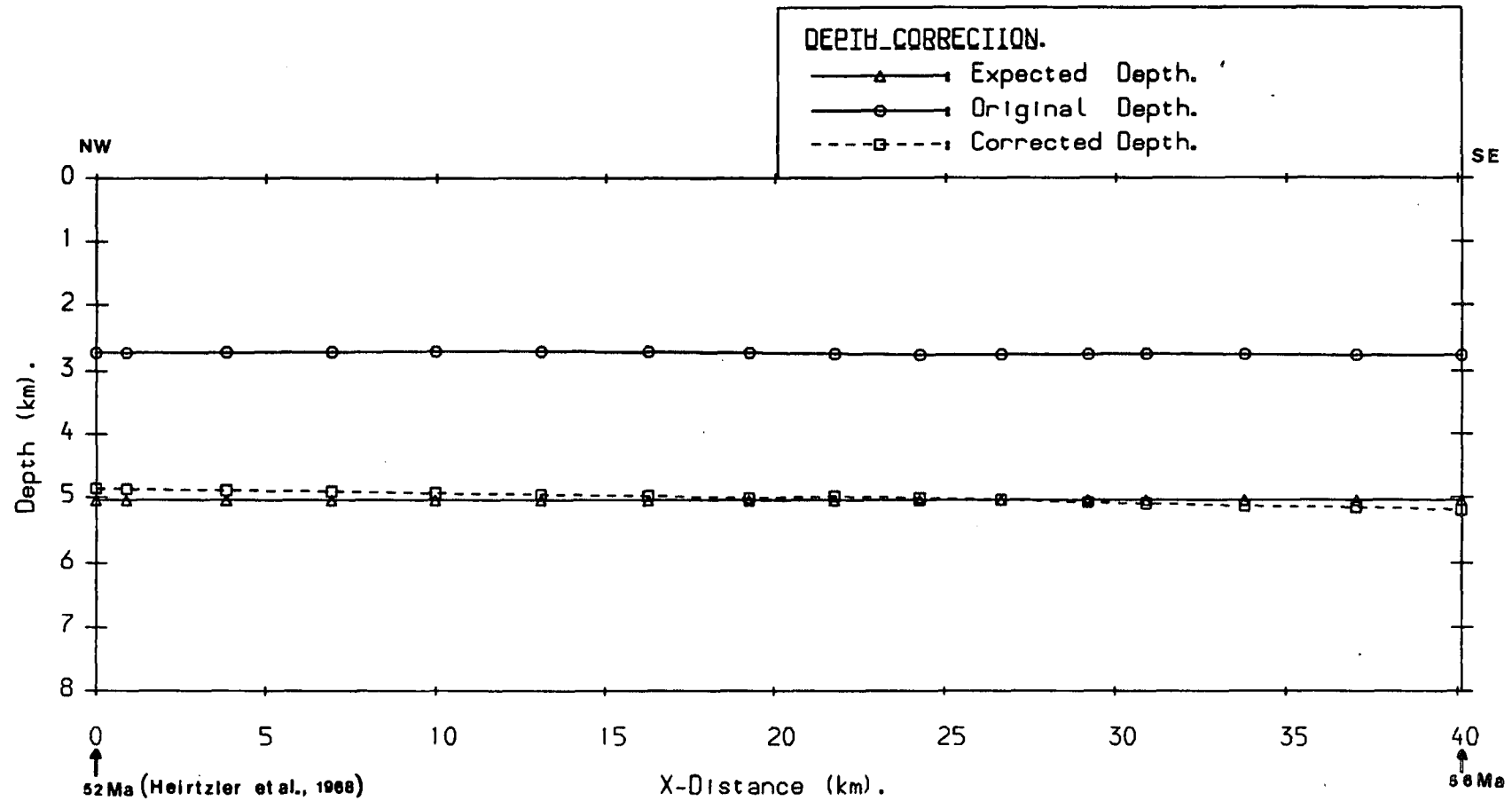


**Figure 4.13** Observed ocean depths corrected for sediment load, abnormal crustal thickness, and anomalously low density upper mantle, compared to the depths predicted by the Parsons & Sclater (1977) empirical age/depth formula.

variation of about 250 K at the base of the lithosphere. The density distribution is therefore more complicated than that assumed by this and previous models, despite the good fit obtained.

In order to gain a more rigorous insight into the thermal structure of a rifted margin, simple thermal models of the rifting process were used. The thermal development of the margin was studied by defining the thermal structure of the lithosphere at rift and numerically solving the 2-dimensional heat-flow equation (1) to obtain the thermal structure of the margin at subsequent times since rift. This was done for various rifting geometries to examine the magnitude and form of the resulting temperature and density distributions in an attempt to explain the anomalously high temperature contrast implied by gravity modelling.

#### 4.6 Thermal models.

The study of the thermal development of the margin requires the solution of the 2-dimensional heat flow equation for thermal conduction

$$\frac{\partial^2 V}{\partial x^2} + \frac{\partial^2 V}{\partial z^2} = \frac{1}{k} \frac{\partial V}{\partial t} \quad (1)$$

where convection is assumed absent, heat generated by radioactivity is ignored, and

$k = \frac{K}{\sigma \rho}$  = thermal diffusivity,

$K$  = thermal conductivity,

$\sigma$  = specific heat,

$\rho$  = density,

$V$  = temperature function  $V(x, z, t)$ .

This is most easily solved numerically by utilising a finite-difference scheme (Carslaw & Jaeger, 1959). The initial thermal model was taken to be a uniform 125 km thick lithosphere, instantaneously stretched and thinned over a rifting zone extending from unstretched,  $\beta = 0$  lithosphere to maximally stretched,  $\beta = \beta_{\max}$  lithosphere, with passive upwelling of asthenosphere into the space created by lithospheric thinning (McKenzie, 1978). Temperature gradients are linear from 0 °C at the surface, to 1300 °C at the lithosphere/asthenosphere contact (figure 4.14). This thermal model was set up on a finite difference grid by dividing the lithosphere into blocks of dimension ( $e_x, e_z$ ), and allocating the relevant temperatures to the centres of each block representing the temperature nodes to be used in the finite difference calculations.

The relevant finite difference representations of the partial derivative terms for the  $(m,n)^{\text{th}}$  block at time  $i$  (figure 4.15) are

$$\frac{\partial^2 V}{\partial x^2} = \frac{V_{m-1,n,i} + V_{m+1,n,i} - 2V_{m,n,i}}{e_x^2}$$

$$\frac{\partial^2 V}{\partial z^2} = \frac{V_{m,n-1,i} + V_{m,n+1,i} - 2V_{m,n,i}}{e_z^2}$$

$$\frac{\partial V}{\partial t} = \frac{V_{m,n,i+1} - V_{m,n,i}}{\tau}$$

where

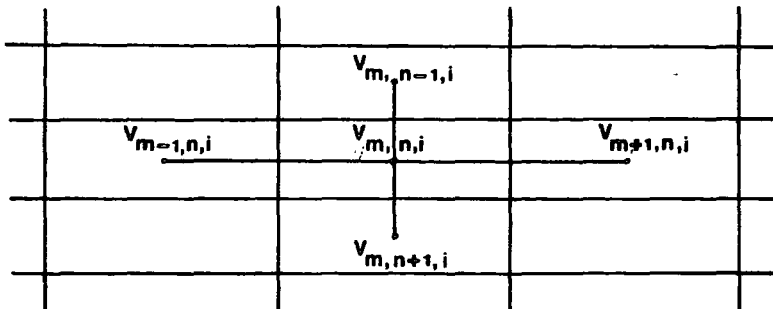


Figure 4.15

$e_x, e_z$  = block dimension,

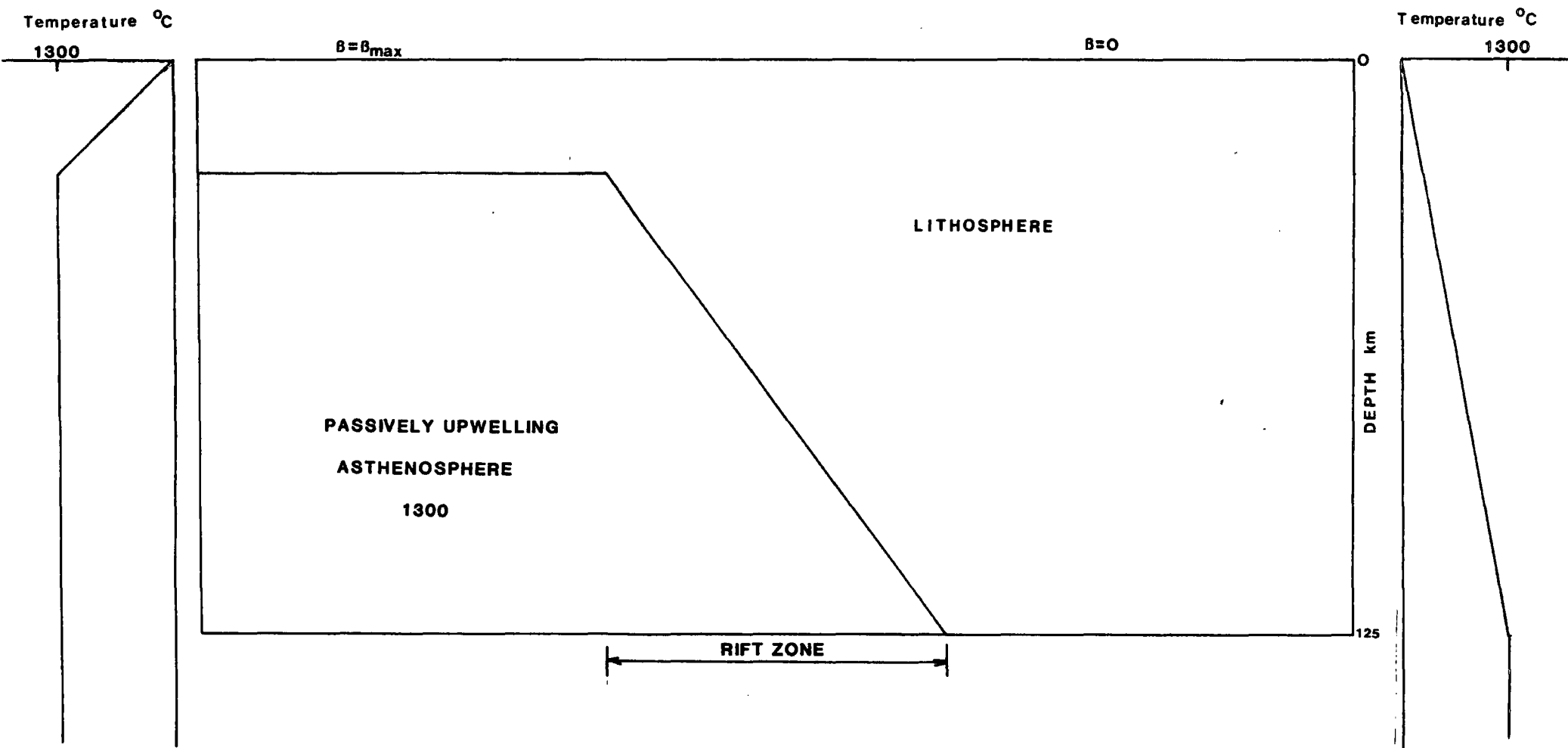


Figure 4.14 Schematic illustration of the thermal model of the lithosphere at rift.



$\tau$  =time step.

Substituting partial derivatives in (1) and re-arranging gives

$$V_{m,n,i+1} = Me_z^2(V_{m-1,n,i} + V_{m+1,n,i}) + Me_x^2(V_{m,n-1,i} + V_{m,n+1,i}) \\ - V_{m,n,i}[2M(e_x^2 + e_z^2) - 1]$$

where

$$M = \frac{\tau k}{e_x^2 e_z^2}$$

The scheme is stable subject to the condition

$$\frac{k\tau}{e^2} \leq \frac{1}{2}$$

(Carslaw & Jaeger, 1959), and provides a method for obtaining the thermal structure of the margin at successive times since rift given an initial model. A program HEAT (appendix A) was written to calculate the solution to the 2-D heat-flow equation at required times since rift, the output of which was contoured to provide a visual display of the temperature field using the SURFACE 2 contouring package (Sampson, 1975).

#### 4.6.1 Program tests.

The program HEAT was checked by comparing modelled and theoretically derived temperature distributions for simple bodies for which analytical solutions of equation (1) are known.

To check the prescribed boundary conditions and main body finite-difference calculations, the temperature distribution of a square of side  $2l$ , initially at  $100^\circ\text{C}$  with zero surface temperature was used. The analytical solution reproduced from Carslaw & Jaeger (1959), p174, figure 22 is shown in figure 4.16, along with that modelled using program HEAT for an appropriate time given by  $kt/l^2 = 0.08$ . The comparison indicates good agreement between theoretical and modelled solutions.

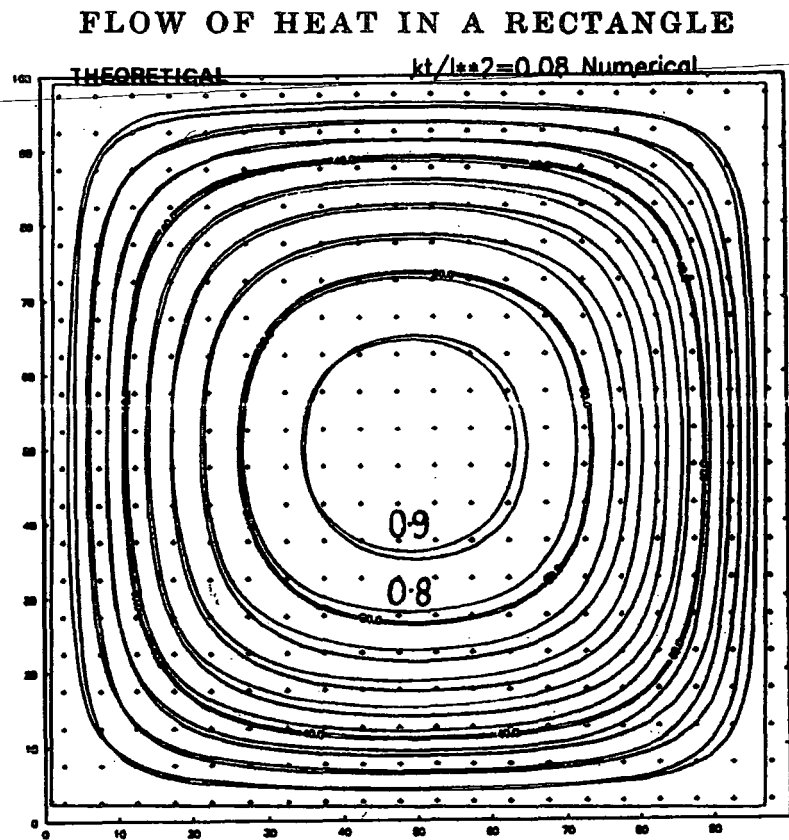


**Figure 4.16** Test of the thermal modelling program, showing the numerical and theoretical solution of equation (1) for a unit square, initially at 100° C, at 7.7 Ma after release.

To test the validity of the approximation made at model limits, comparisons between modelled and theoretical solutions for the rectangular corner  $x > 0, z > 0$  with initial and surface temperatures of 100 and zero  $^{\circ}\text{C}$  respectively were made. The analytical solution of equation (1) for this problem is given by

$$V(x, z, t) = V_0 \operatorname{erf}\left(\frac{x}{2\sqrt{kt}}\right) \operatorname{erf}\left(\frac{z}{2\sqrt{kt}}\right)$$

---

Carslaw & Jaeger p 171, equation (2).

This was modelled by maintaining the surfaces  $x=z=0$  of a 100 km square at zero temperature, and allowing the body temperature to evolve with time, assuming body limit boundary conditions at the surfaces  $x=z=100$  km (figure 4.17(a)). Theoretical and modelled solutions for successive times are shown in figures 4.17 (a-c). These show that for small times, when there exist no appreciable temperature gradients perpendicular to the model limit surfaces, the correspondence is good. However, as the solutions progress, this condition becomes increasingly less well satisfied at the corner  $(x,z)=(100,100)$ , and departures from theory are seen. Away from the corner correspondence remains close. This problem can be postponed by increasing the model dimensions such that the calculated temperature distribution is unaffected by errors introduced in this way over the time interval of interest. This result implies that the model limits of the lithosphere should be placed sufficiently far from the rift zone as to be largely unaffected by the large horizontal temperature gradients therein.

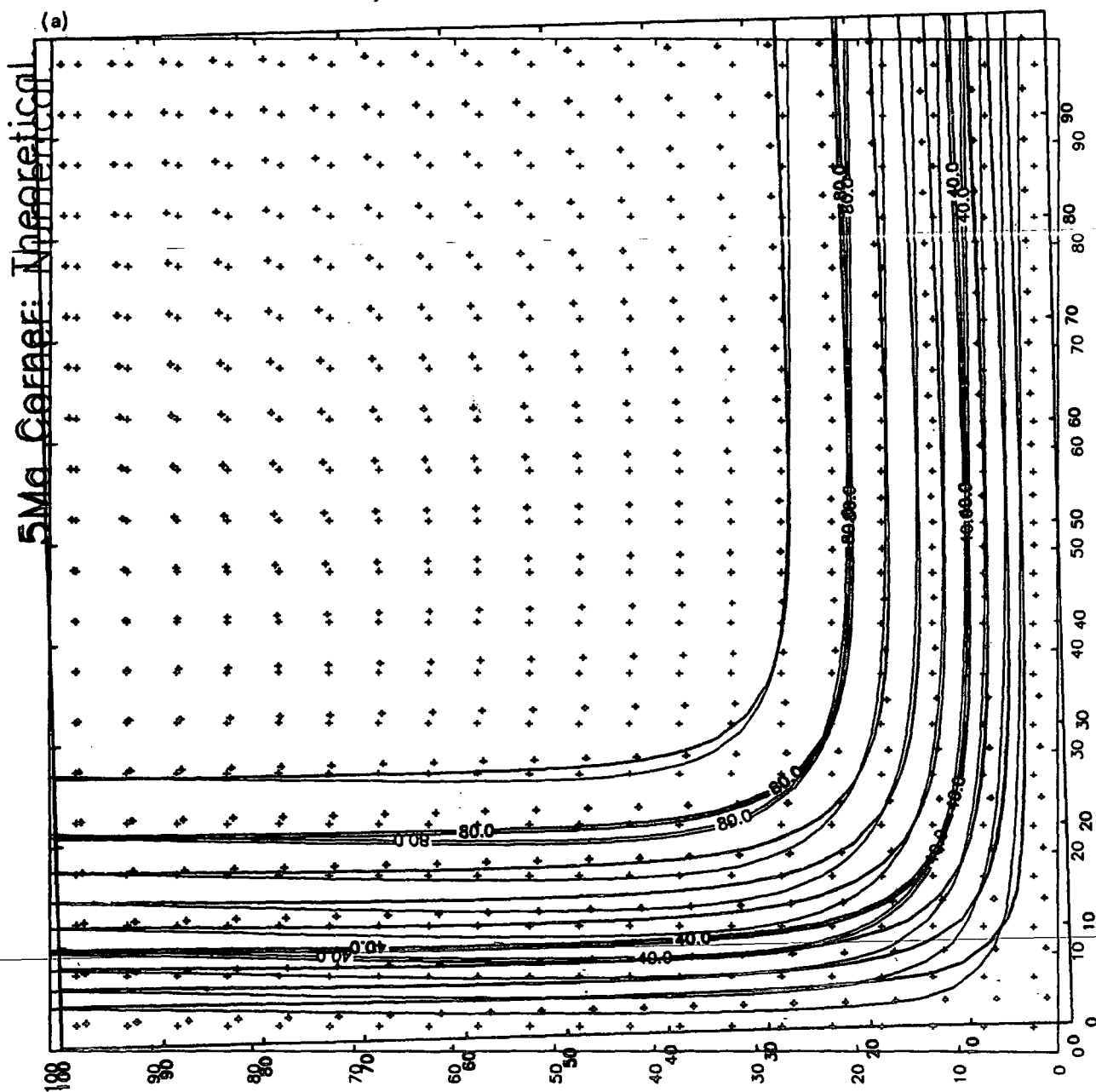
#### 4.6.2 Thermal models.

The following values were assumed for lithospheric thermal parameters during finite-difference calculations:-

$$\text{Thermal conductivity} = 3.14 \text{ W m}^{-1} \text{ K}^{-1}$$

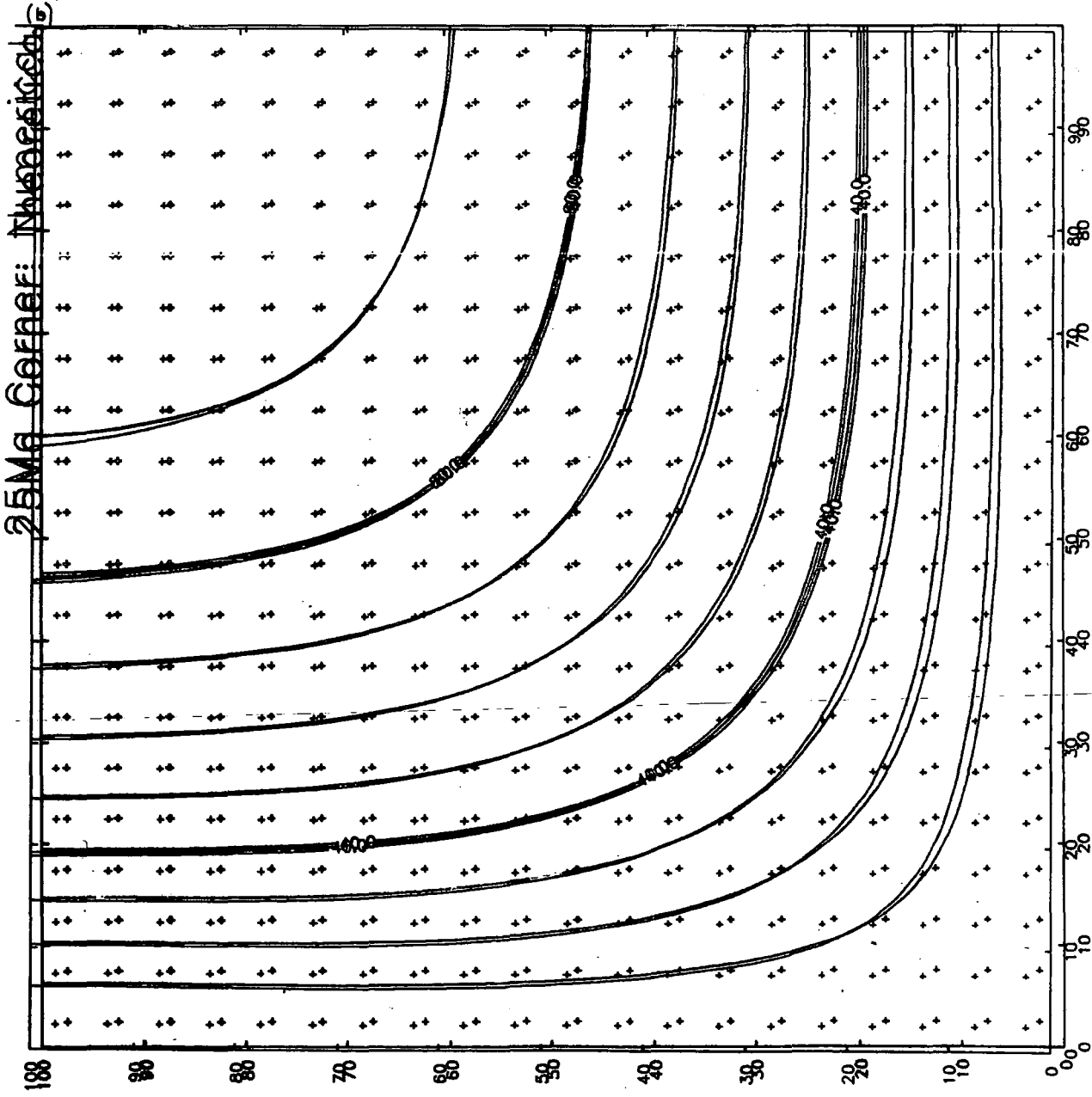
$$\text{Specific heat} = 1275.0 \text{ J kg}^{-1} \text{ K}^{-1}$$

Figure 4.17(a)-(c) Test of the thermal modelling program showing numerical and theoretical solution of equation (1) for a unit corner, initially at 100° C. Solutions are for (a) 5 Ma, (b) 25 Ma, and (c) 50 Ma after release. Theoretical solutions are presented as transparent overlays to facilitate comparison.



Time 15:22:34  
Date 10/2/88

\*\*\*\*\* SURFACE GRAPHICS SYSTEM \*\*\*\*\*  
Plot No. 2  
Date 10/2/88  
Time 15:22:34



Time 19:26:50

Date 10/2/2008

SPACE GRAPHICS SYSTEM

Plot No. 2



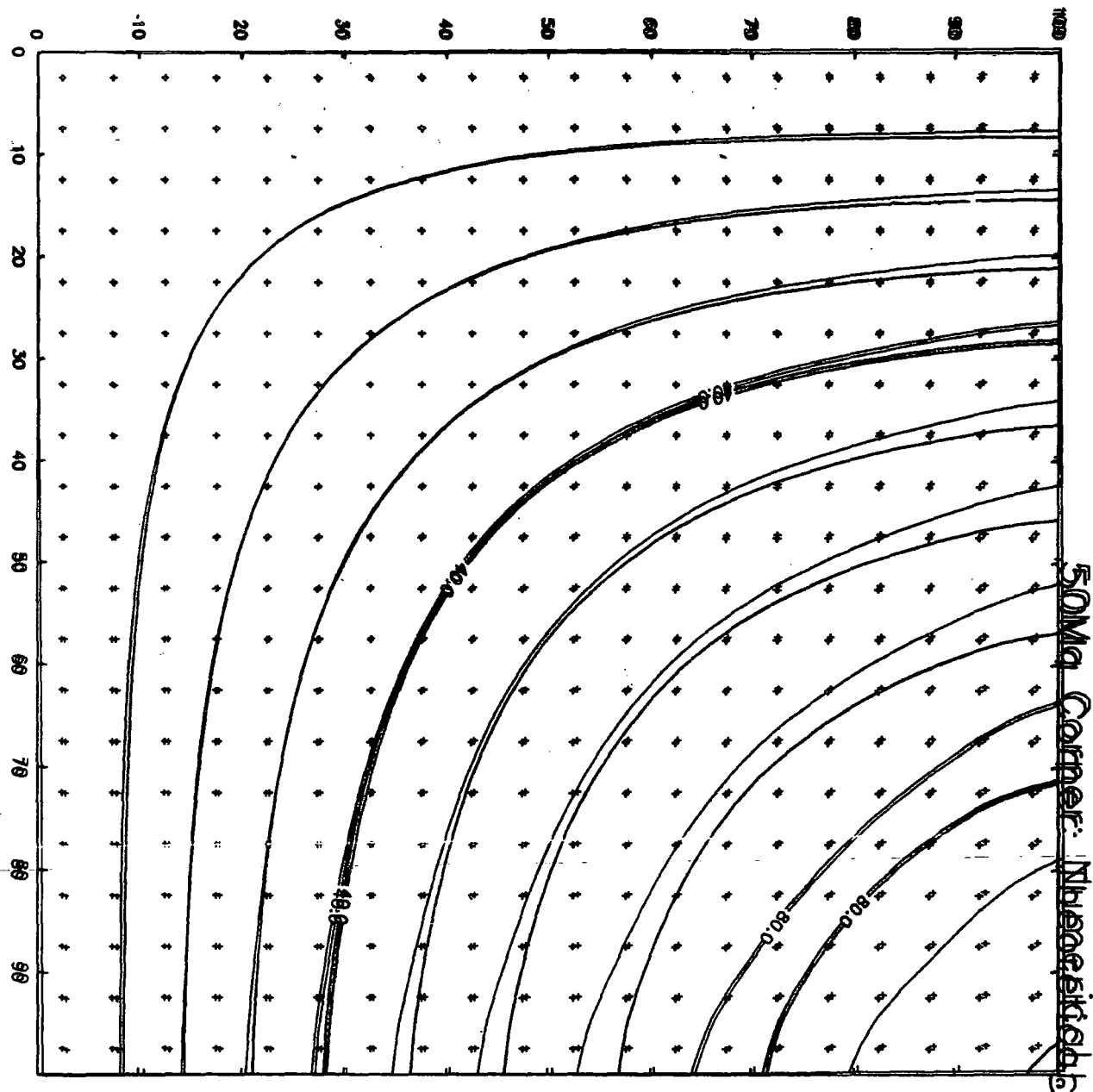


\*\*\*\*\* SURFACE GRAPHICS SYSTEM \*\*\*\*\*

Plot No. 2

Date 10/ 2/88

Time 15:30:12



$$\text{Density} = 3.33 \text{ g cm}^{-3}$$

The degree of lithospheric stretching,  $\beta_{\text{max}}$  was estimated from ESP modelling results by the ratio of unstretched to fully stretched crustal thickness, giving  $\beta_{\text{max}}=5.0$  (figure 4.1).

The lithosphere was represented by a uniform thickness slab, the top and base of which were maintained at 0 °C and 1300 °C respectively. The ends of the model represented model limits rather than actual boundaries. Therefore some approximation had to be made in estimating the temperature distribution across them. The finite-difference calculation of temperatures at model limits involved an imaginary node outside the model at which the temperature was estimated by assuming a linear temperature gradient across the model limit. Sufficiently far from the rift zone and ridge axis, horizontal temperature gradients will be small so their approximation in this manner was considered reasonable, a conclusion supported by comparison between modelled and theoretical results for simple bodies described earlier in this chapter.

Three initial rift models were set up to assess the effect of the initial rifting conditions on the resulting temperature/density distributions. These consisted of models with rift zones of widths 60 km (consistent with ESP modelling results), 120 km, and 20 km, with stretching factor  $\beta=5$ . These models were allowed to develop with time and their thermal structure at 50 Ma post rift was used to deduce average density gradients within the lithosphere. This was done by first determining the average separation of calculated geotherms from the sub-continental geotherm at appropriate positions along the model. Then using the relations

$$\Delta\rho = \alpha\rho_2\Delta\theta : \rho = \rho_0 + \Delta\rho$$

the corresponding average density was found. The program HEAT was written to automatically calculate and plot the resulting density distribution. The results are shown in figures 4.18 - 4.20, , from which it can be deduced that the density

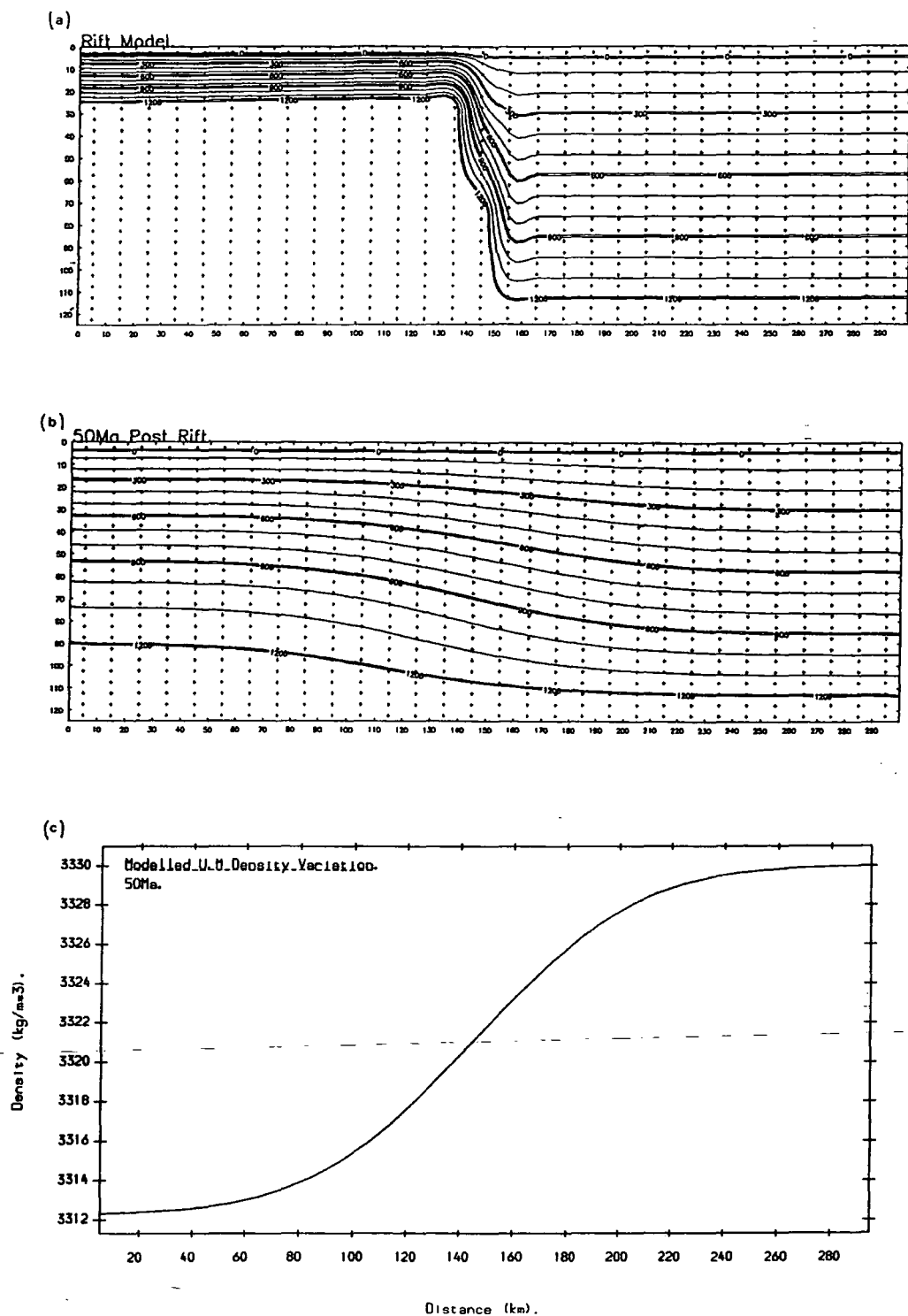


Figure 4.18 Isothermal contour plots of the results of the thermal modelling of a 20 km wide rift.

(a) Rift model.

(b) Temperature distribution within the lithosphere at 50 Ma after rift.

(c) Implied density distribution across the margin.



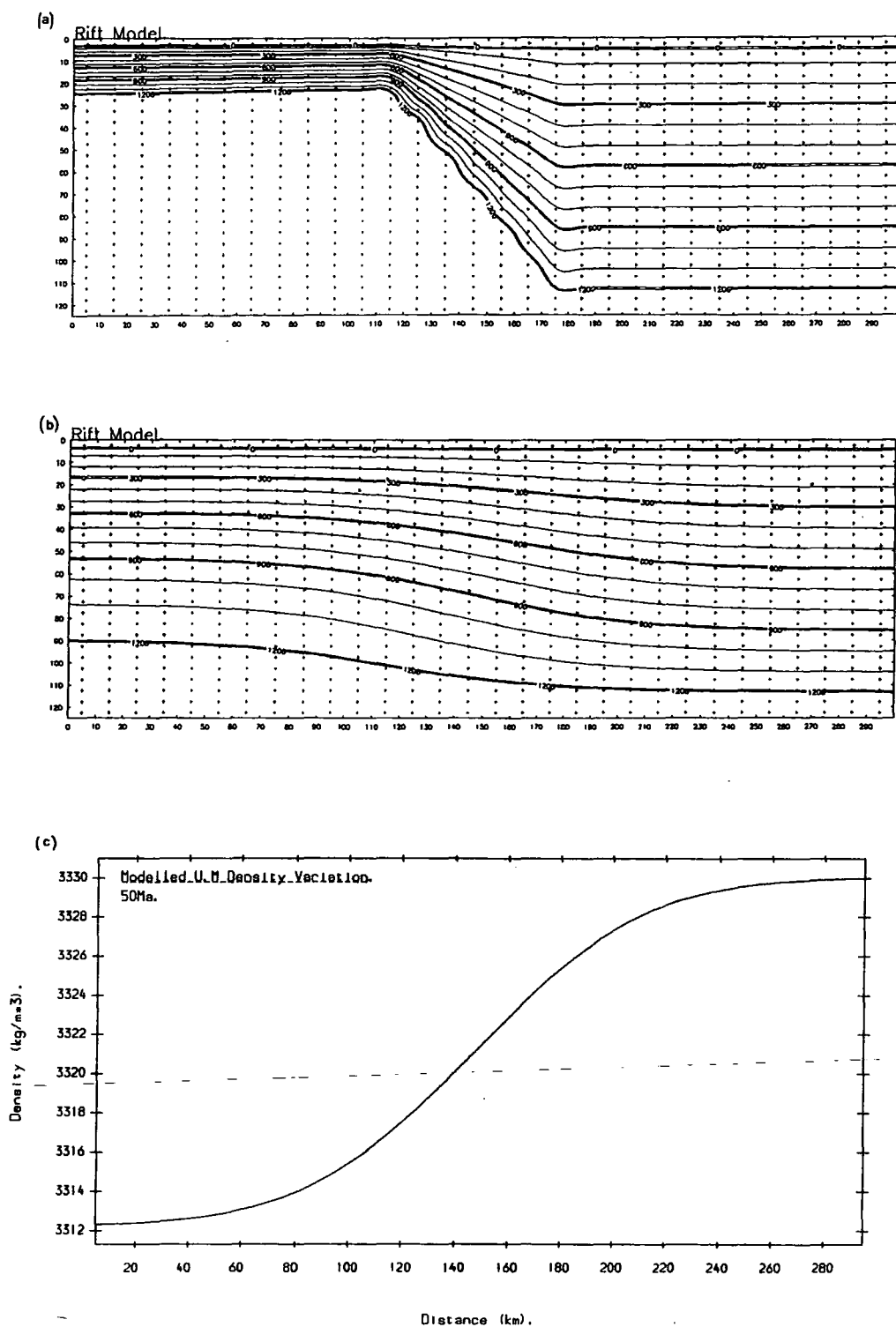


Figure 4.19 Isothermal contour plots of the results of the thermal modelling of a 60 km wide rift.

(a) Rift model.

(b) Temperature distribution within the lithosphere at 50 Ma after rift.

(c) Implied density distribution across the margin.

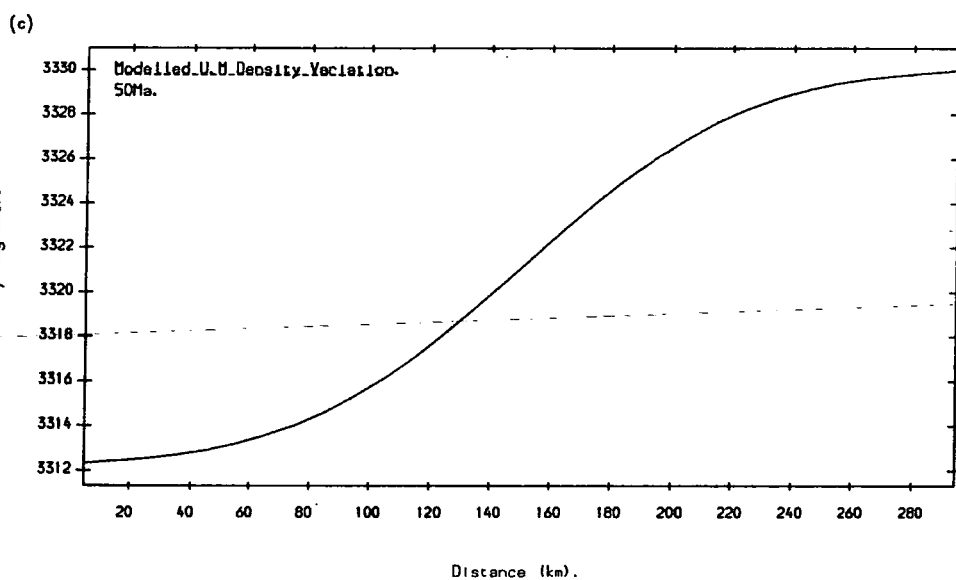
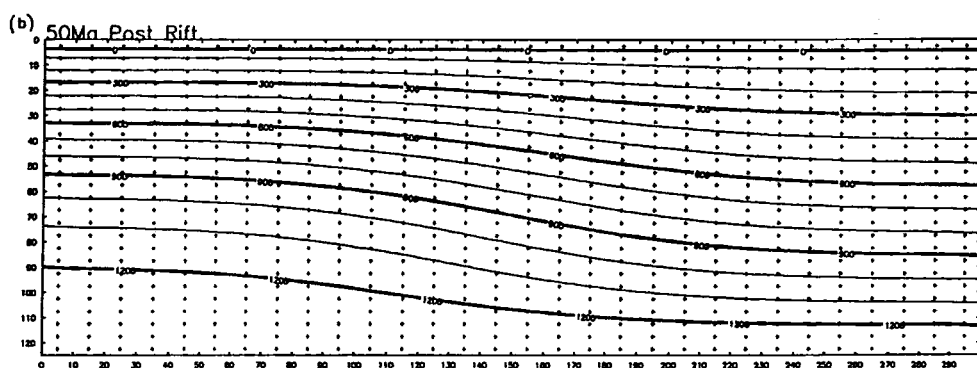
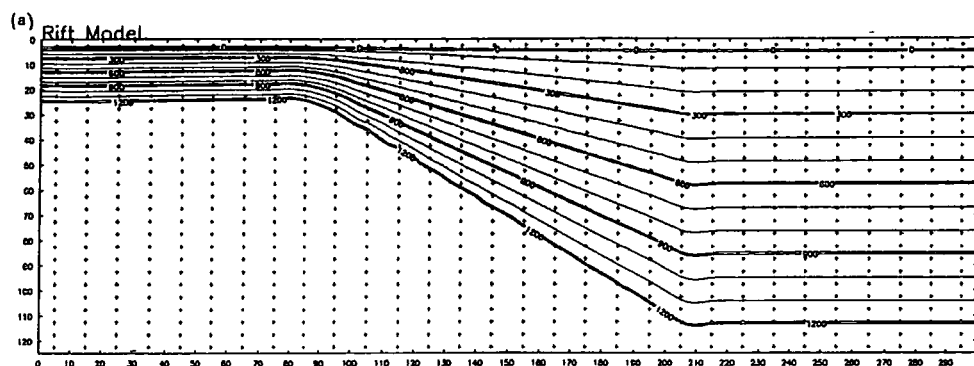


Figure 4.20 Isothermal contour plots of the results of the thermal modelling of a 120 km wide rift.

(a) Rift model.

(b) Temperature distribution within the lithosphere at 50 Ma after rift.

(c) Implied density distribution across the margin.

distributions at 50 Ma for all three initial models are not significantly different. It was therefore decided to use the density gradient calculated from the 60 km rift-zone model to produce a new gravity model.

The calculated density distribution was divided into 20 km wide prisms, and the resulting densities were used to construct a theoretical gradational density upper mantle using the previous crustal model. The resulting gravity model is shown in figure 4.21. Although showing a close general similarity in shape to the observed, the calculated gravity displays a long wavelength discrepancy of 20 mGal across the model. Figure 4.22 reveals that the model is not in isostatic equilibrium, although the mass-balance across the new model is greatly improved by the presence of the gradational upper mantle. Furthermore, the sea floor depths corrected for sediment load, crustal thickness, and anomalous density upper mantle show that the modelled oceanic crustal depths are not consistent with the predictions of the age/depth relation of Parsons & Sclater (1977) (figure 4.23).

#### **4.7 Deep compensation.**

In order to reconcile modelled with observed results it is necessary to look for additional factors which may affect the measured gravity profile. The discrepancy is long wavelength. This implies that it has a deep source, or originates from a gradual oceanwards decrease in average crustal density relative to the upper mantle. It was considered unlikely that the discrepancy would have its origin in the crust for reasons similar to those considered in section 4.4.1. Therefore a deep source was inferred.

Haigh (1973a,b) concluded that the anomalously shallow ocean floor of the North Atlantic between Iceland and the Azores is due to the presence of an unusually hot underlying asthenosphere, with temperatures at the base of the lithosphere of up to 150 K above normal. Cochran & Talwani (1978) similarly concluded that the topographic swell is maintained at depth by mass deficiency in the astheno-

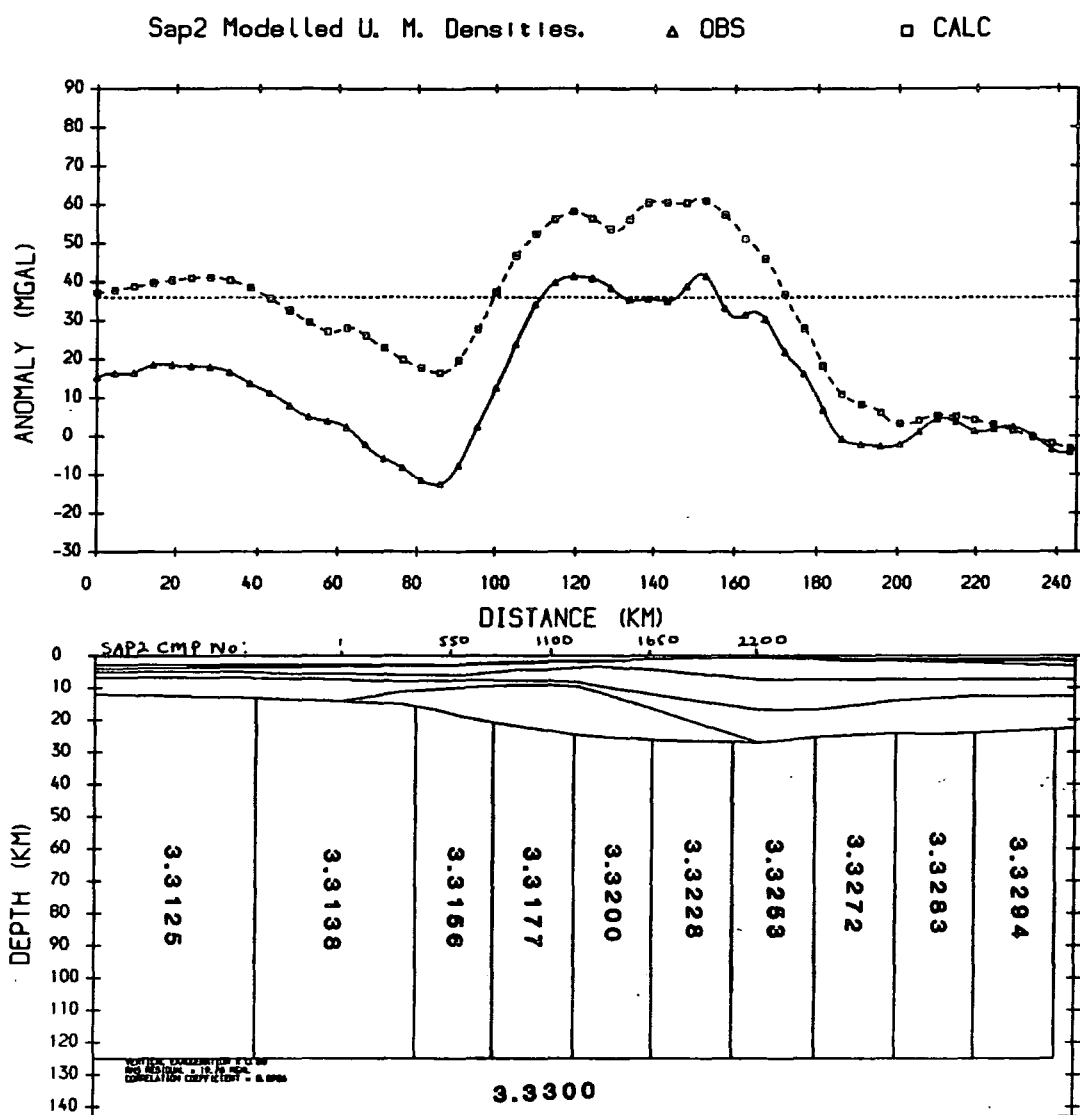


Figure 4.21 Gravity model incorporating the calculated upper mantle density gradient for a 60 km wide rift zone (figure 4.19).

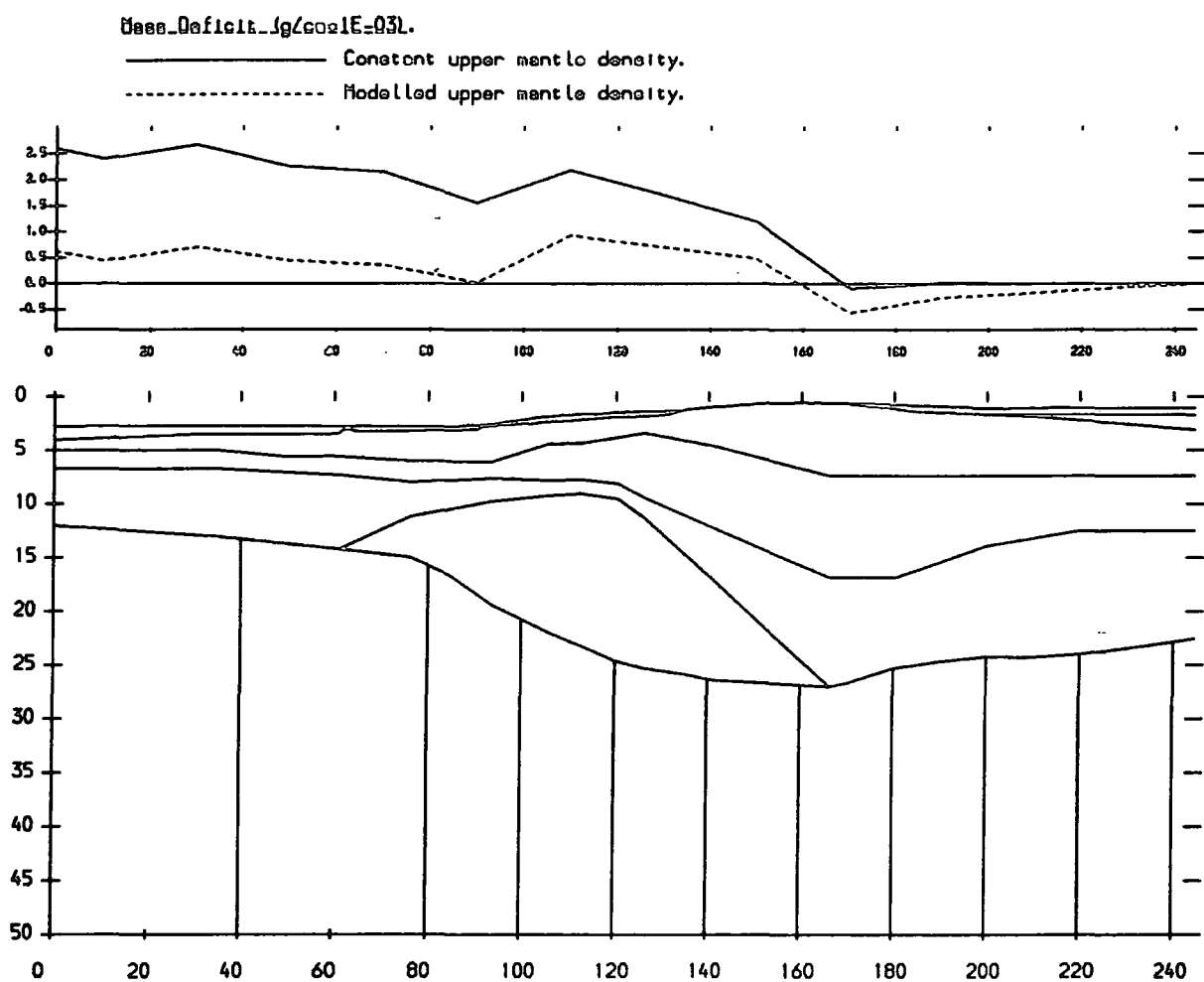
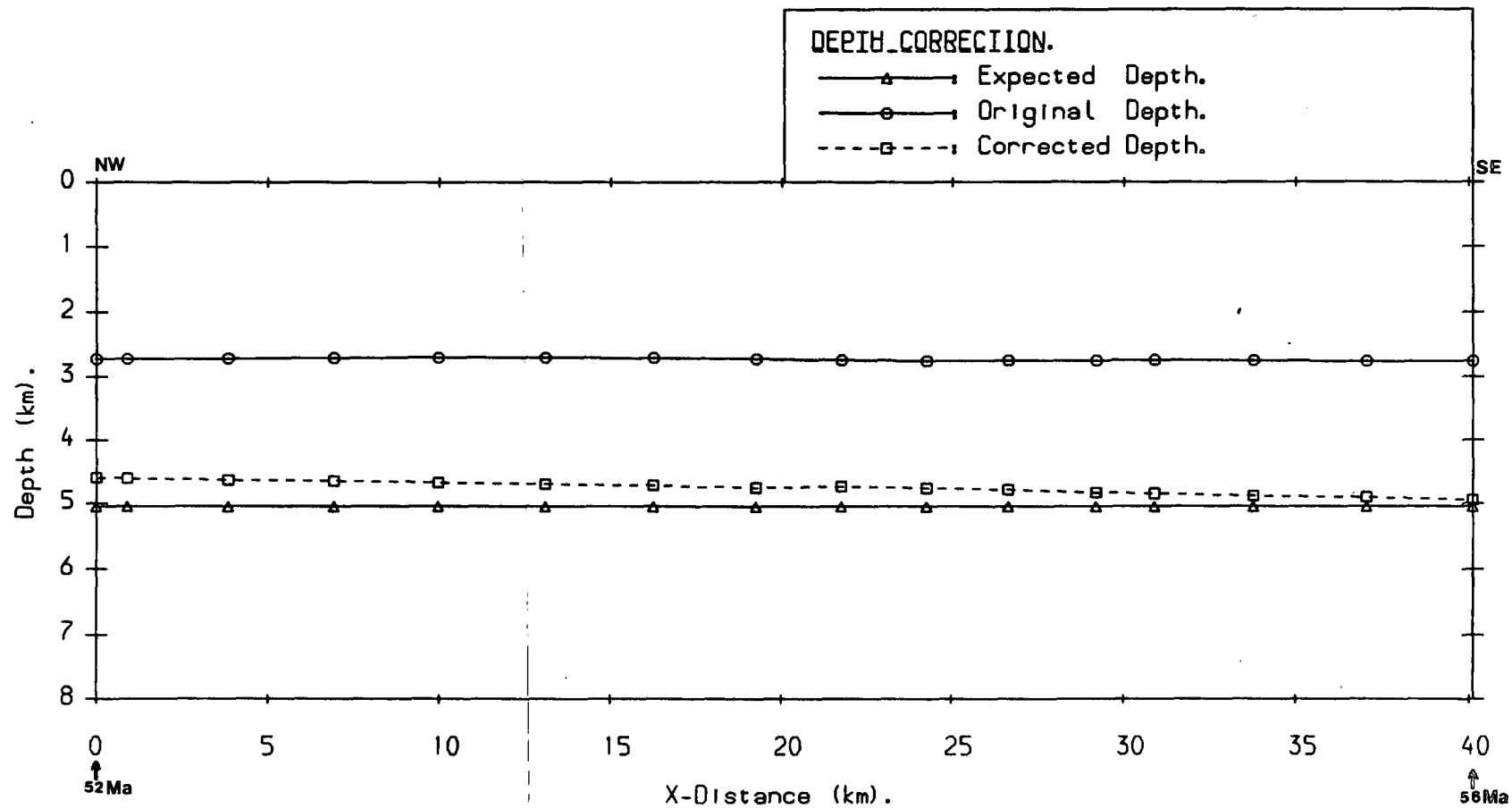


Figure 4.22 Illustration of the degree of isostatic compensation of the gravity model shown in figure 4.21.



**Figure 4.23** Observed ocean depths corrected for sediment load, abnormal crustal thickness, and anomalously low density modelled upper mantle, compared to the depths predicted by the Parsons & Sclater (1977) empirical age/depth formula.

sphere, which could be caused by a 75 K rise in average temperature over 200 km. Bott (1988) takes these ideas further, suggesting that the North Atlantic topographic swell is a result of the combination of two effects. Firstly, deep isostatic compensation by anomalously high asthenospheric temperatures, and secondly a component produced by the pressure anomaly in the upper mantle associated with the upwelling Icelandic plume. Asthenospheric flow from the high pressure region in the vicinity of Iceland towards the low pressure region adjacent to the subducting lithosphere of the Circum-Pacific belt produces pressure gradients in the upper mantle which result in an uncompensated contribution to the topographic swell.

These results suggest that the long wavelength discrepancy may originate in the upper mantle in the form of an asthenospheric temperature/density gradient across the margin possibly combined with a contribution from a plume-generated pressure gradient. The asthenospheric temperature would be expected to increase oceanwards across the margin, resulting in a corresponding decrease in density, and therefore measured gravity signal. The plume effect should contribute in an opposite sense, its uncompensated topographic expression resulting in an increase in measured gravity oceanward towards the plume.

In order to assess whether these mechanisms could reconcile observed and modelled gravity, the gravity model incorporating modelled upper mantle density gradients (figure 4.21) was modified such that isostatic equilibrium was maintained by density gradients in the underlying asthenosphere. The asthenospheric density required to maintain isostatic equilibrium was found by balancing the crustal, lithospheric and asthenospheric mass along the model, assuming a depth of compensation of 200 km. This depth is consistent with Haigh's conclusion that lateral density variations in the asthenosphere may have died out by 200 km, and with previously assumed values (Cochran & Talwani, 1978; Bott 1988). The calculated density distribution is shown in figure 4.24. For simplicity, a straight line was fitted through the distribution, from which asthenospheric densities were deduced.

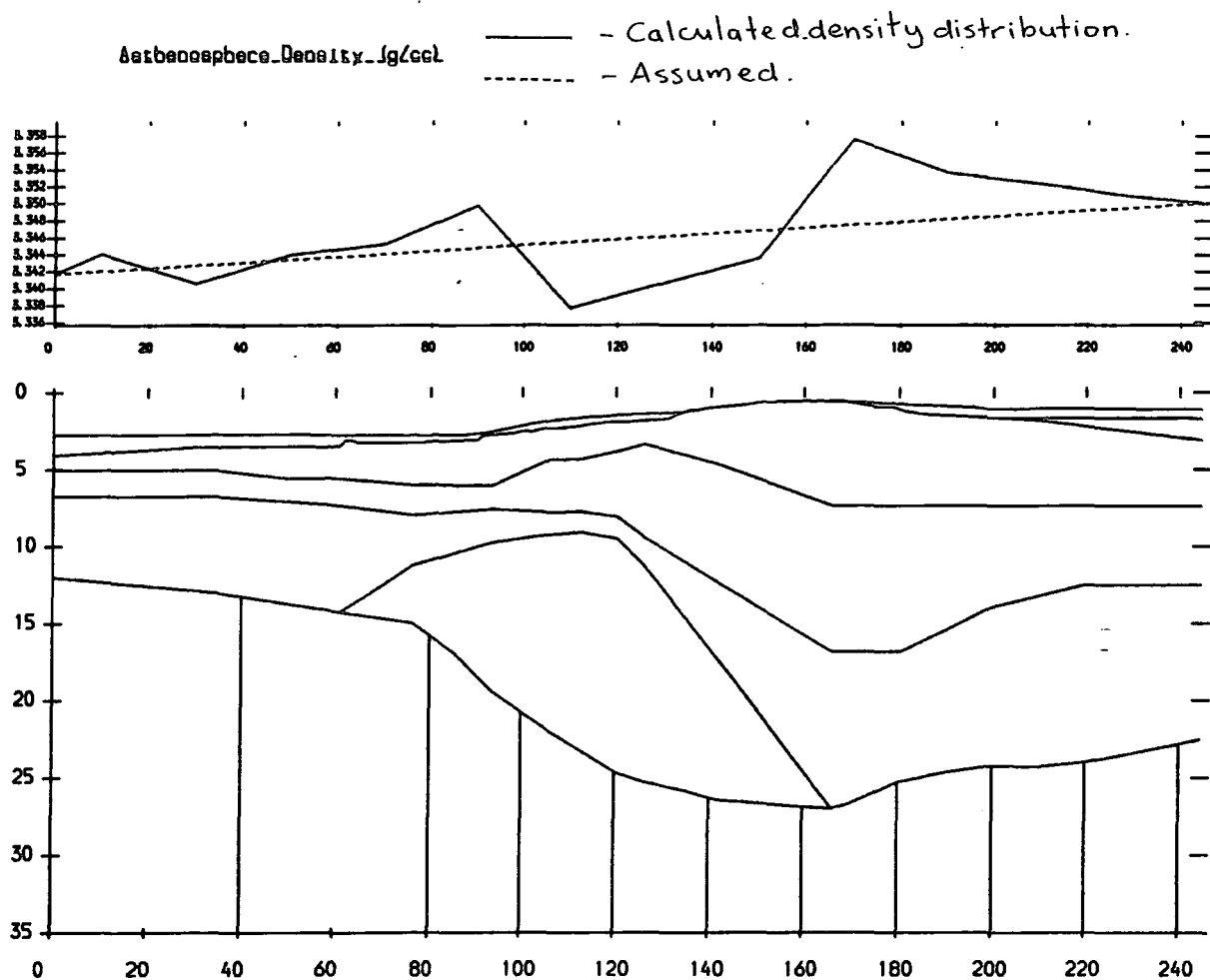


**Figure 4.24** Asthenospheric lateral density variation required to maintain the model of figure 4.23 in isostatic equilibrium. The depth of compensation assumed is 200 km.



Variations about this line are due to local variations in average crustal densities along the model. The resulting gravity model is shown in figure 4.25. In order to improve the fit continentward of ESP1, the Moho position was altered to a final depth of 21.5 km. This compares well with that of 22.0 km obtained by Scrutton (1972) in the Hatton-Rockall Basin.

As in earlier models, short wavelength misfits due to local three-dimensional features within the crust are seen centred on ESP6a and landward of ESP7a. The feature at ESP6a was modelled by an intrusive body of density  $2.8 \text{ g cm}^{-3}$  as described earlier in this chapter. The resultant model, figure 4.26, shows good correspondence between theoretical and observed gravity, indicating that the inclusion of an asthenospheric density gradient alone can adequately explain the long wavelength gravity feature. The model is fully compensated to a depth of 200 km, and the modelled oceanic crustal depths corrected for sediment load, crustal thickness, and anomalous density upper mantle are consistent with the predictions of the age/depth relation of Parsons & Sclater (1977), as indicated by figures 4.27 - 4.28.

#### 4.8 Discussion.

It has been shown that a crustal model defined by ESP modelling alone cannot explain the gravity signal measured across the Hatton-Bank continental margin. This requires additional contributions in the form of density gradients in the underlying lithosphere and asthenosphere due to the non-equilibration of the rift thermal anomaly and the proximity of the Icelandic hot-spot respectively.

The crustal model of White *et al.* (1986) is supported by gravity modelling. That the high-velocity lens is formed by underplating of stretched continental crust is supported by the form and position of the required lithospheric density gradient, which was modelled in a manner consistent with the underplated lens hypothesis. The implications of the final model for the position and nature of the continent-

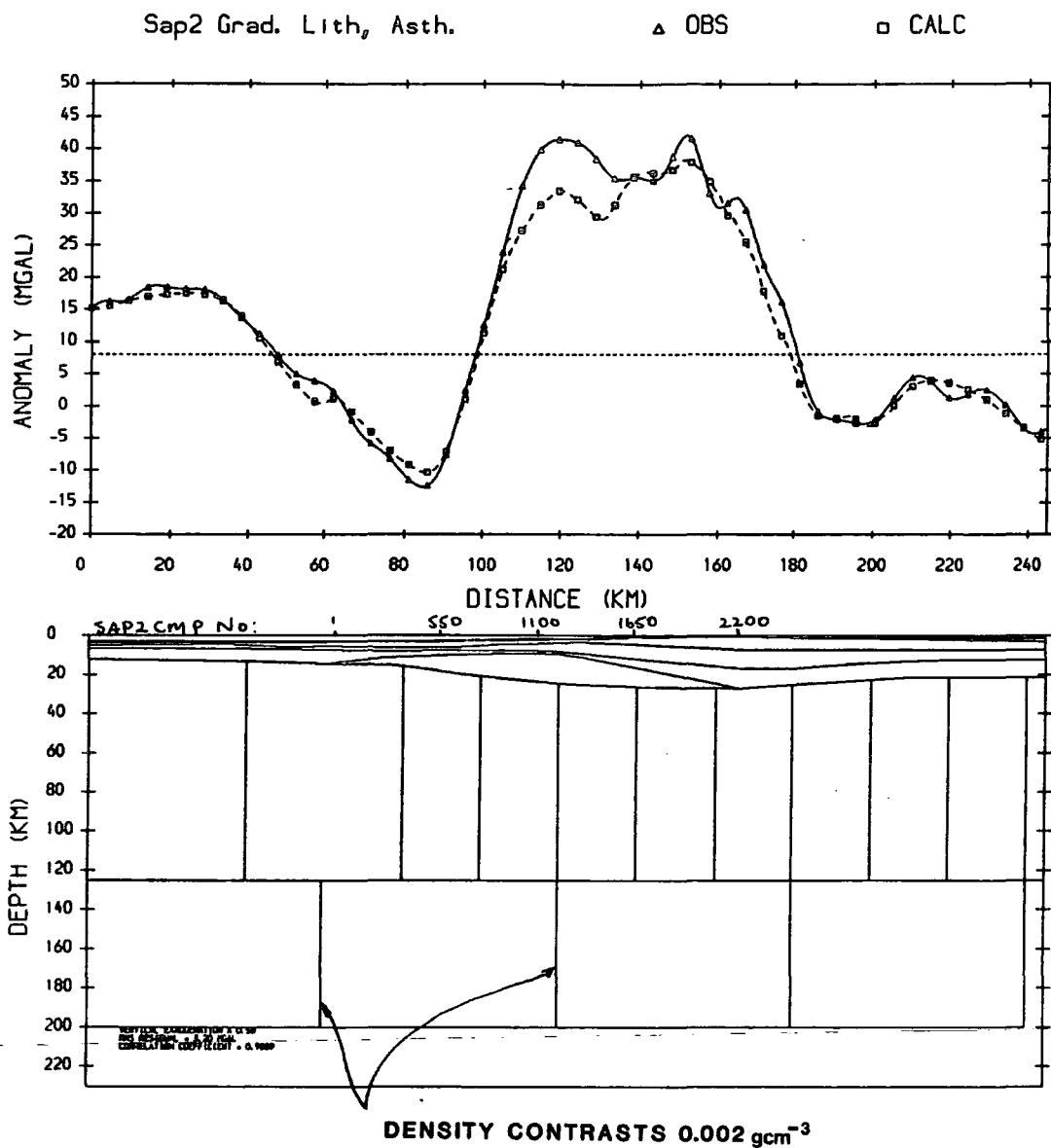


**Figure 4.25** Gravity model of figure 4.21 incorporating the asthenospheric density gradient implied by figure 4.24, with a depth of compensation of 200 km..

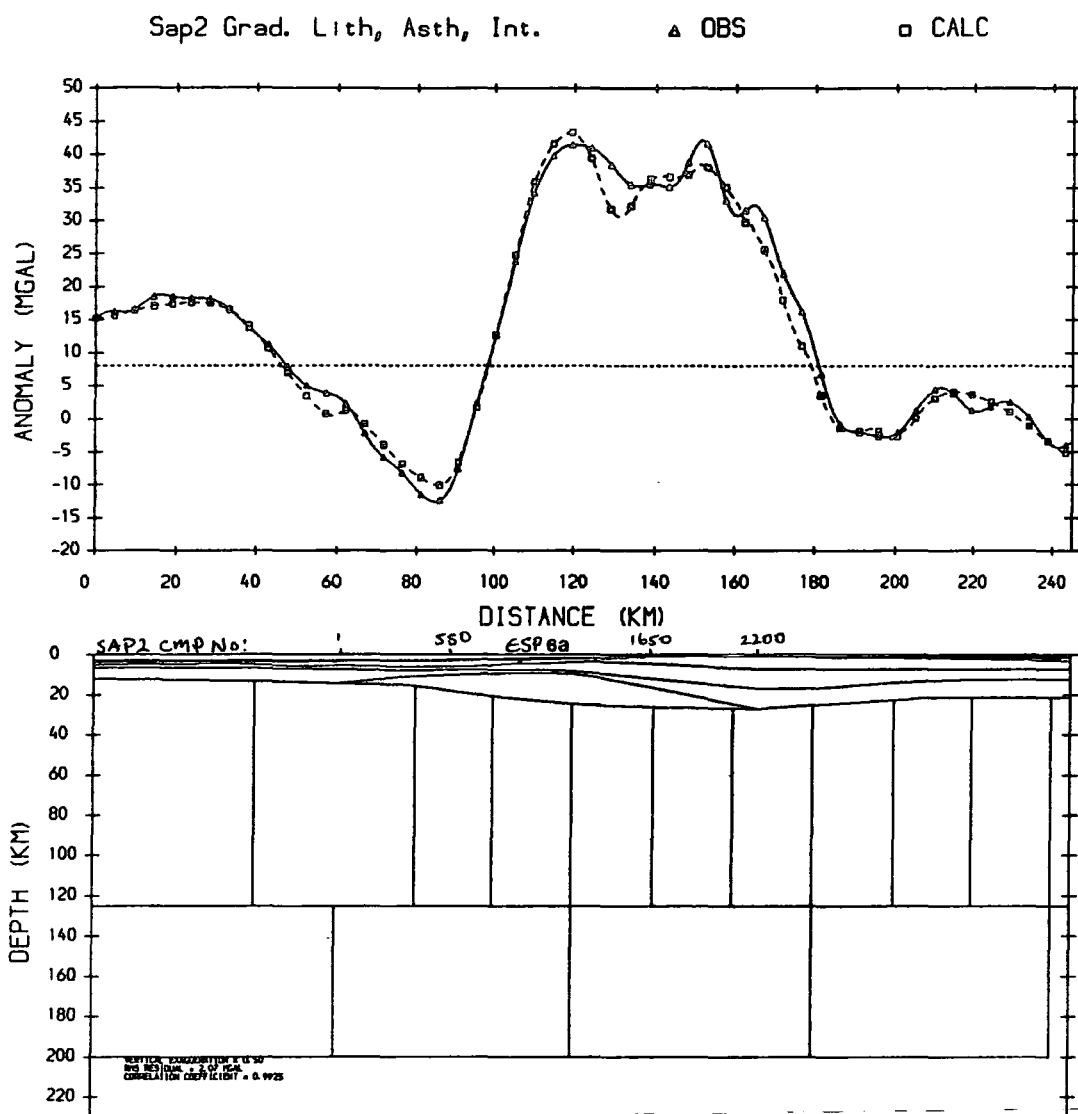


**Figure 4.26** The gravity model of figure 4.25 including an intrusive at ESP 6a to reconcile the observed gravity mismatch.

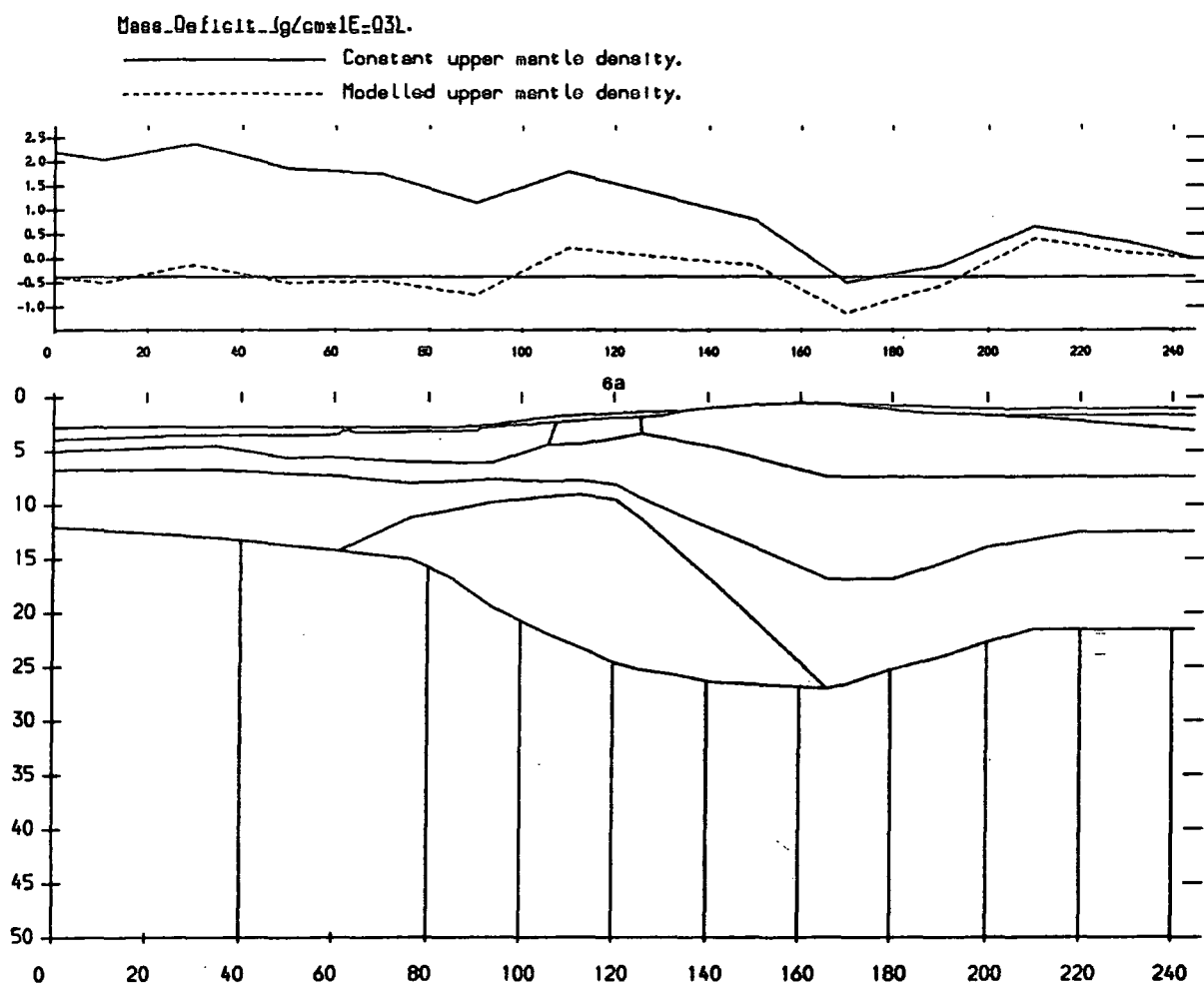
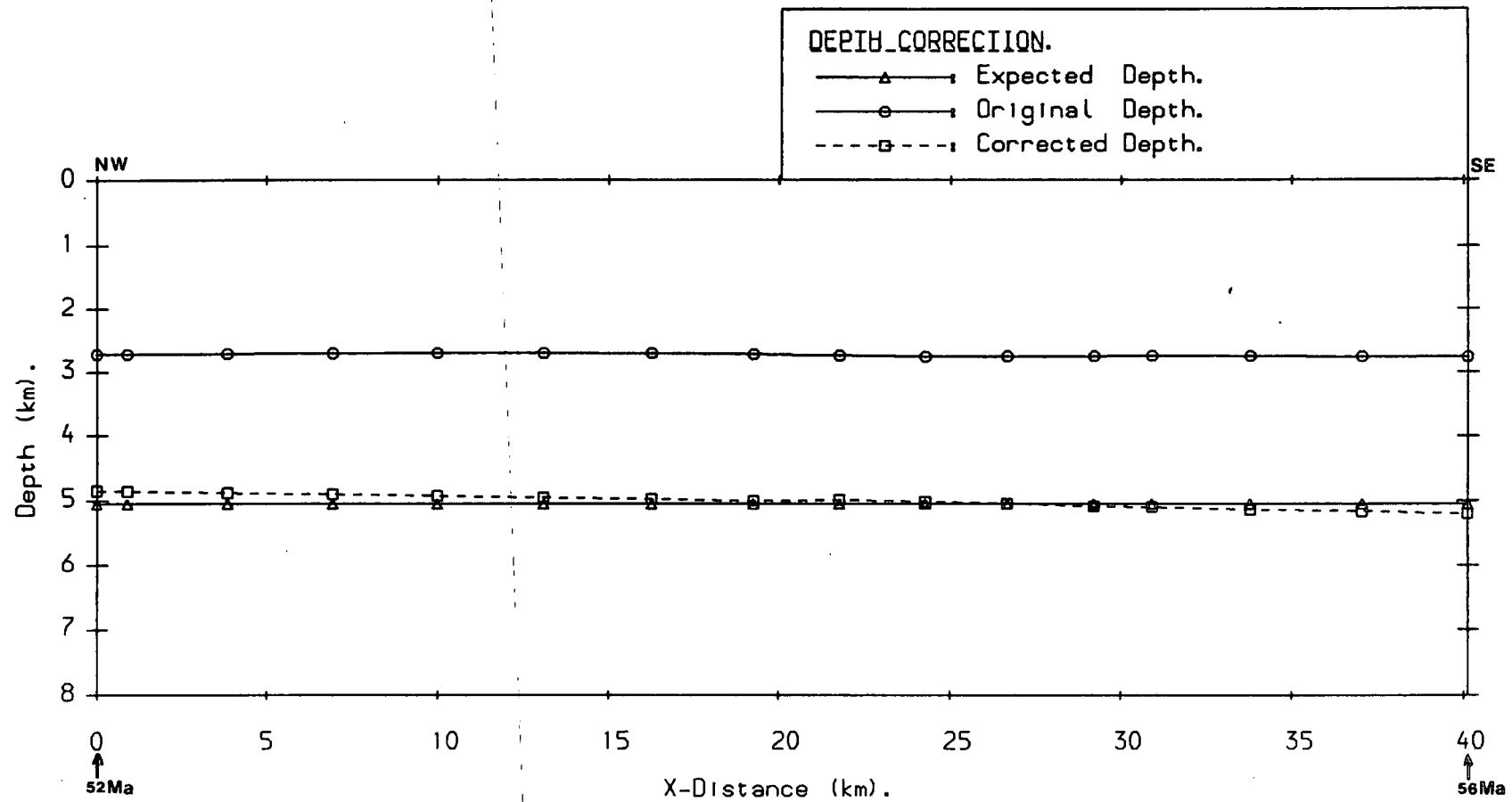


Figure 4.27 Illustration of the degree of compensation of the final gravity model, figure 4.26, indicating that the model is in approximate local isostatic equilibrium.



**Figure 4.28** Observed ocean depths corrected for sediment load, abnormal crustal thickness, and anomalously low density modelled lithosphere and asthenosphere, compared to the depths predicted by the Parsons & Sclater (1977) empirical age/depth formula, with which they show a good agreement.

ocean boundary is discussed in chapter 7 where a consistent hypothesis is developed using additional information from magnetic and seismic data.

The final model is in isostatic equilibrium with compensation occurring by variations in crustal thickness, accompanied by deeper contributions in the form of density gradients in the underlying upper mantle, with a depth of compensation of 200 km.

Although the observed gravity signal is adequately reproduced by the model, several factors remain ambiguous. The lithospheric density gradient calculated by thermal modelling depends critically on the assumed pre-rift lithosphere thickness. Variations in lithospheric thickness result in accompanying changes in modelled lithospheric thermal gradients, which in turn affect the implied asthenospheric density gradient. Furthermore, the asthenosphere density gradient calculated is also inversely dependant upon the assumed depth of compensation, in that a greater compensation depth results in a smaller implied density gradient and vice-versa. The main constraint on the lithospheric model is that the average implied thermal contrast should be consistent with acceptable geothermal estimates in the context of the generally high oceanic upper mantle temperatures of the North Atlantic.

---

The model takes no account of the possible presence of upper mantle pressure gradients across the margin. The effect of such a gradient would be to push the margin slightly out of isostatic equilibrium. Modelling this would require increasing the average crustal density oceanwards to represent uncompensated crustal mass, in turn requiring that the density gradient in the asthenosphere be increased to reconcile calculated and observed gravity signals. Thus the two effects tend to act in opposite senses, the plume-pressure effect resulting in an uncompensated topographic increase, whilst the asthenospheric density gradient produces a decrease, in measured gravity oceanward towards the plume. The resultant measured gravity gives no indication of the proportion contributed by each effect, and without a fix

on one or the other, modelling both was not considered meaningful. Thus the asthenospheric temperature/density gradient calculated is a lower limit for the depth of compensation assumed.

## CHAPTER (5)

### Magnetic Anomaly Interpretations.

#### 5.1 Introduction.

The separation of plates during seafloor spreading gives rise to a systematic pattern of magnetic anomalies. Oceanic crust generated at a mid-ocean ridge cools and acquires a component of remanent magnetisation in the direction of the ambient field. Geomagnetic field reversals result in alternating bands of oppositely polarised rocks which comprise oceanic basement. The length of each polarity segment depends upon the time interval between successive field reversals, and the rate of spreading. Using independently determined geomagnetic field reversal chronologies, marine magnetic anomaly sequences can be calibrated in time to give a corresponding magnetic anomaly time scale (Ness *et al.*, 1980). Subsequent recognition of magnetic anomalies can be used to infer ages of oceanic crust, and to determine the evolution of ocean basins in space and time. Identification of the oldest anomaly adjacent to a passive continental margin enables the timing of the onset of seafloor spreading, and the position of the ocean - continent transition to be determined.

Active seafloor spreading in the north-east Atlantic between Greenland and Rockall began in anomaly 24B time (chapter 1), and has continued uninterrupted to the present about the Reykjanes Ridge. This has resulted in a complete sequence of marine magnetic anomalies 1 to 24 being developed nearly symmetrically about the Reykjanes Ridge which have been extensively studied. This chapter deals with the interpretation of the magnetic anomaly data collected during the 1985 Durham/Cambridge Universities geophysical survey of the Hatton Bank continental margin in terms of the early spreading history of the north-east Atlantic.



## 5.2 Magnetic Anomalies in the North-East Atlantic.

This section summarises the features exhibited by the anomaly pattern observed in the north-east Atlantic based on a general description given by Nunns (1980). Figure 5.1 shows a synthetic profile of anomalies 1 to 24 reproduced from Nunns (1980) which illustrates the important features exhibited by marine magnetic anomalies in the north-east Atlantic. Nunns (1980) identified the following important characteristics.

Anomalies 1 to 5 have high amplitudes and are easily identified by "counting out" from the present axis. Anomalies 5A to 6C do not have a consistently observed structure, and are consequently difficult to identify out of sequence. Similarly anomalies 7 to 12 are difficult to resolve, often coalescing to form a single, low amplitude positive anomaly. Anomaly 13 is distinct as a sharp peak isolated by deep negative troughs. As suggested by La Brecque *et al.* (1977) anomaly 14 has been omitted on the grounds that it is seldom observed on marine magnetic anomaly profiles, and the resulting synthetic anomaly 13 shape more closely resembles observed examples. Anomalies 15 to 18 are again difficult to resolve, forming an irregular, positive anomaly. When developed, anomaly 19 is distinctive as a discrete positive peak flanked by relatively deep troughs. Anomalies 20 to 24 are characteristically well-developed and easily identified. Nunns (1980) pointed out that the negative trough between anomalies 20 and 21 is significantly broader than the other negative anomalies within the 20-24 anomaly sequence. This is a useful feature in preventing misidentification of anomalies within the sequence.

Nunns (1980) synthetic profile assumed a spreading rate of  $2.85 \text{ cm a}^{-1}$  according to the timescale of Hailwood *et al.* (1979) during the anomaly 22 to 24 period

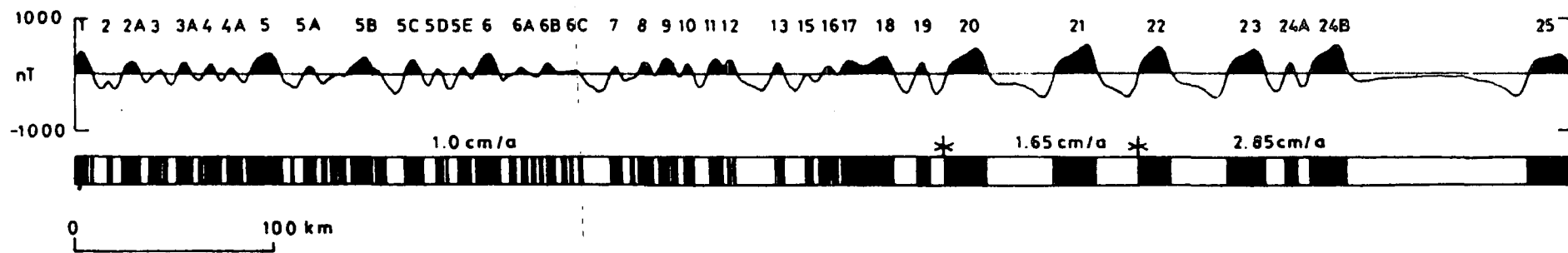


Figure 5.1 Synthetic anomaly profile for the eastern northeast Atlantic reproduced from Nunns (1980). Based on the Hailwood *et al.* (1979) timescale.

which results in a separation of anomaly 24 into separate anomalies 24A and 24B. Similarly Featherstone (1976) showed anomalies 24A and 24B separately resolved in a synthetic profile of anomalies 22 to 24B on the East-Greenland margin which assumed a spreading rate of  $2.4 \text{ cm a}^{-1}$  according to the Heirtzler *et al.* (1968) time scale. Lower assumed spreading rates result in anomalies 24A & B coalescing to form a single, often double-peaked anomaly separated from anomaly 23 by a shallow negative anomaly (eg. Vogt & Avery, 1974 ; Voppel *et al.*, 1979).

In the Reykjanes basin Vogt & Avery (1974) identified numerous closely spaced fracture zones which disturb the anomaly sequence between anomalies 5C and 18 west of the Reykjanes Ridge. Voppel & Rudloff (1980) recognised a similar set of fracture zones east of the Reykjanes Ridge. Their formation was associated by Vogt & Avery (1974) with a change in spreading direction from  $125^\circ$  to  $95^\circ$  about the Reykjanes Ridge following the cessation of spreading on the Ran Ridge in the Labrador sea between anomalies 20 and 13 (Srivastava & Tapscott, 1986). They assumed that the fracture zones were created in an attempt by the Reykjanes Ridge to assume a minimum work configuration, most rapidly achieved by the creation of new transform faults separating small segments of ridge crest. By anomaly 5 time these fracture zones had disappeared, and spreading about the Reykjanes ridge became oblique.

### **5.3 Anomalies 20 to 24 in the Iceland Basin.**

This section presents a synthesis of magnetic anomaly lineations identified in oceanic crust adjacent to Hatton Bank. The magnetic anomalies south-west of the Rockall Plateau continental margin were first studied by Vogt & Avery (1974) who presented an interpretation of a detailed aeromagnetic survey (figure 5.2). The



Figure 5.2 Interpreted aeromagnetic contour map of the north Atlantic between the Reykjanes Ridge and Rockall Plateau. Anomalies 1, 5, 13, 21, 24 are numbered according to the Heirtzler *et al.* (1968) timescale. (Reproduced from Vogt & Avery, 1974).

anomaly sequence 1 to 24 resembles that described in the previous section. In particular the anomaly 20 to 24 sequence is well developed south of  $57.5^{\circ}$  N. North of this latitude anomalies 23 and 24 successively become less distinct. At  $58^{\circ}$  N anomaly 23 appears to be replaced by a wide, low amplitude anomaly (Roberts & Jones, 1975), and it is not clear whether this represents a continuation of anomaly 23 in a modified form, or a feature formed by some mechanism other than seafloor spreading. Similarly the anomaly 24 lineation north of  $57^{\circ}$  N becomes confused.

Vogt & Avery (1974) do not make clear whether their anomaly 24 corresponds to anomaly 24A or 24B or a combination of both. The anomaly assigned by them as 24 corresponds to a narrow, discontinuous feature flanked to its landward side by a broader positive anomaly (figure 5.2). Nunns (1980) considered that Vogt & Avery's anomaly 24 corresponds to anomaly 24A, and that the broad flanking anomaly represents anomaly 24B.

North of Hatton Bank, immediately below the Iceland-Faeroe ridge, Voppel *et al.* (1979) presented the results from a detailed survey across the ocean-continent transition in which they identify anomalies 13 to 24 (figure 5.3). In addition they noted an apparent doubling of anomaly 24 north of  $61^{\circ}$  N. On the conjugate East-Greenland margin, Featherstone *et al.* (1977) observed that anomalies 23 and 24 appear to terminate against the continental scarp at approximately  $64^{\circ}$  N (figure 5.4). He postulated that the missing anomalies were isolated on the Eurasian plate by a westward jump of the ridge axis at anomaly 22 time when an initially sinuous axis attempted to straighten itself. Reconstruction of anomaly 23 and the additional anomaly 24 identified north of Hatton Bank to their corresponding positions on the East-Greenland margin shows a good fit with the position of the missing anomalies apparently confirming the ridge-jump hypothesis (Voppel *et al.*, 1979). In both

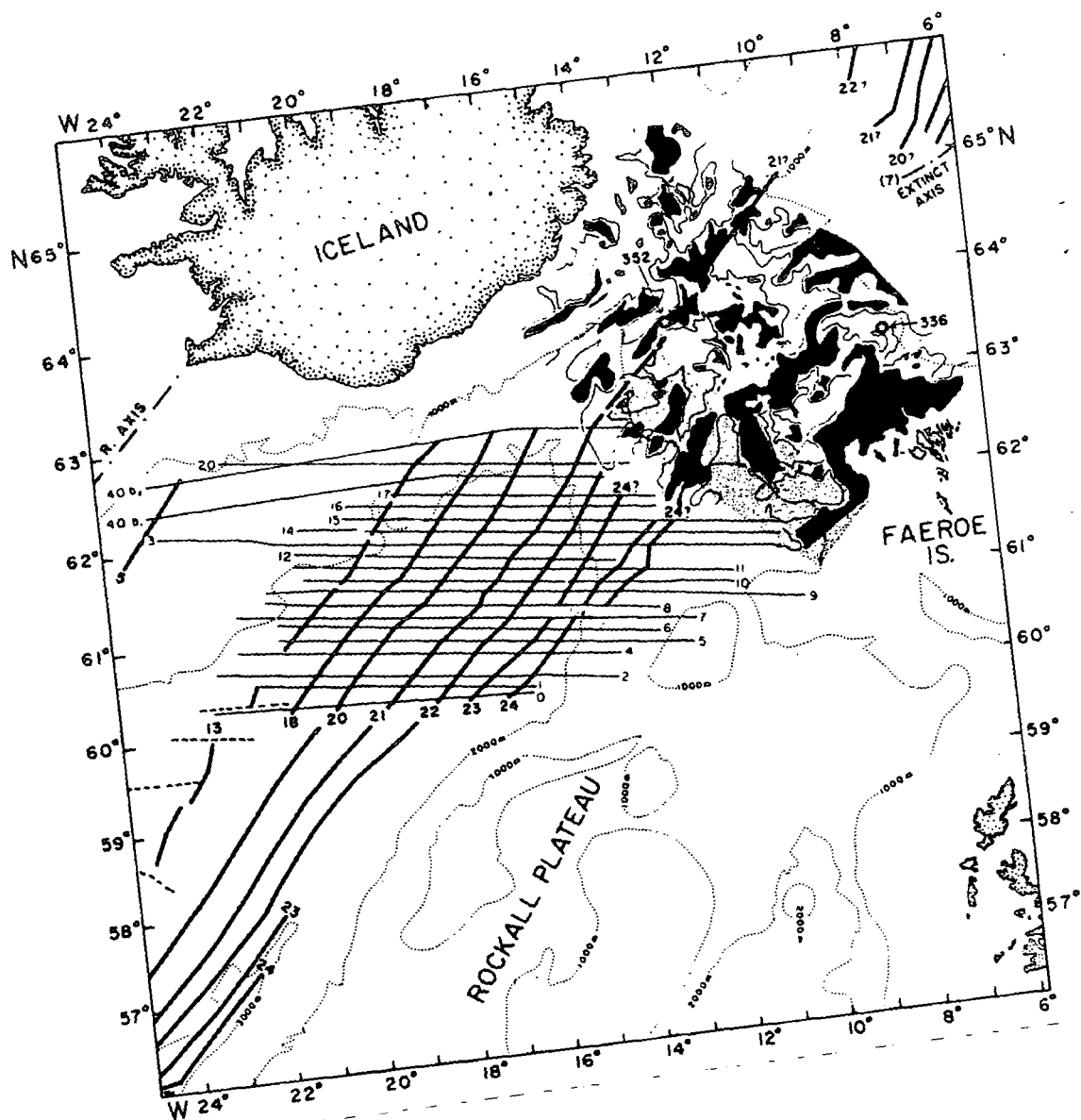


Figure 5.3 Magnetic anomaly lineations identified between Hatton Bank and Iceland-Faeroe ridge. (Reproduced from Voppel et al., 1978)

68°N  
25°W

East Greenland magnetic (Featherstone, 1976).

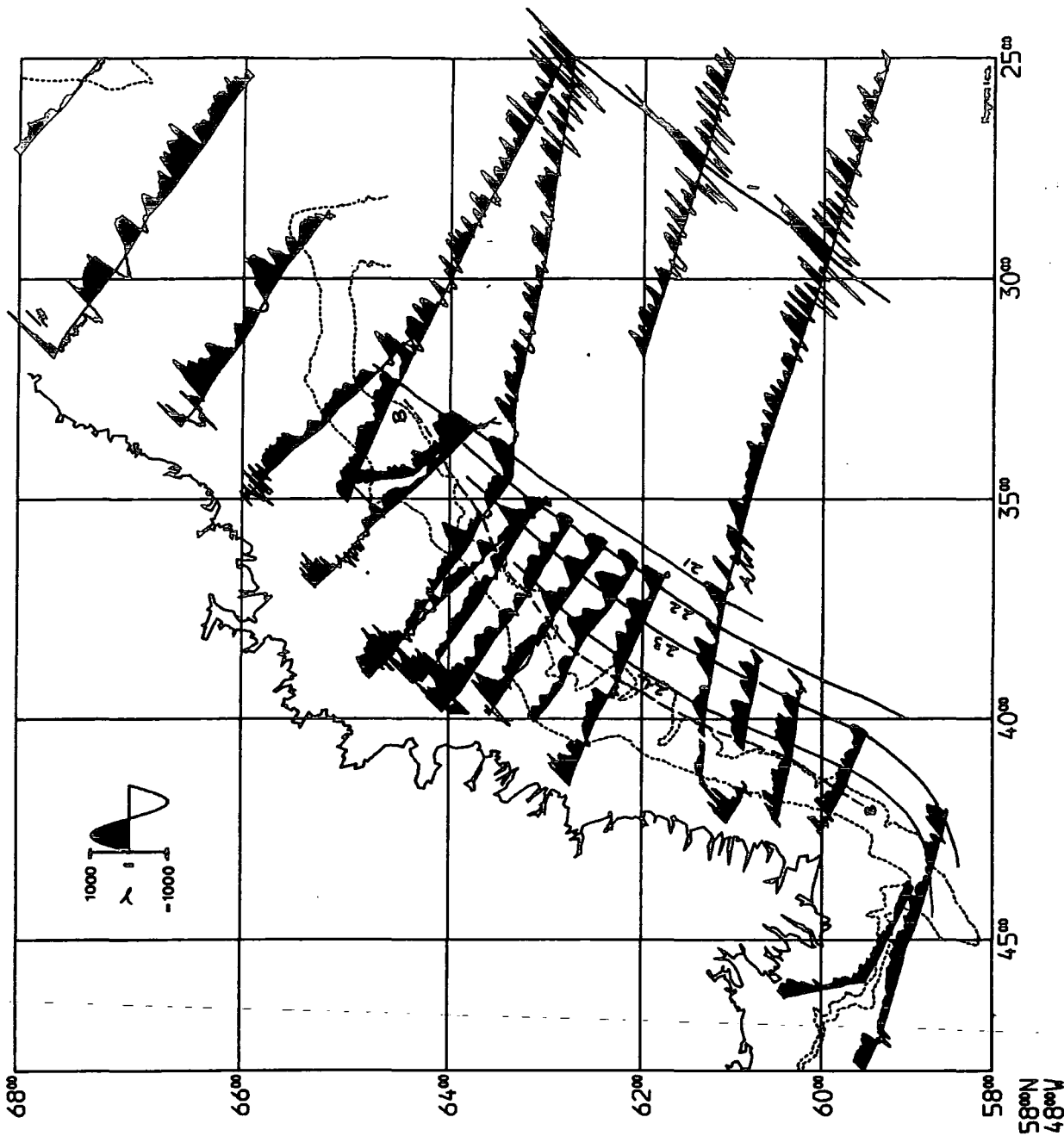


Figure 5.4 Identification and correlation of magnetic anomalies on the East-Greenland continental margin according to Featherstone (1976).

survey areas anomalies 20 to 22 are well developed, with the diagnostic broad negative anomaly between 20 and 21 easily recognised, providing confirmation of correct identification.

The magnetic contour map of Jones & Roberts (1975) extends from the Reykjanes Ridge to the British Isles, providing a link between the survey areas to the north and south of the 1985 survey region on Hatton-Bank. This map is based on a synthesis of magnetic anomaly data available at the time of compilation, and incorporates the magnetic data of Vogt & Avery (1974).

Magnetic anomaly lineations in the East Reykjanes basin used in the rest of this thesis are based largely on the data presented by Vogt & Avery (1974) to the south, Voppel *et al.* (1979) to the north of the 1985 survey area, on Jones & Roberts (1975) magnetic contour map in the intermediate region, on individual tracks from previous Durham University cruises which cross Hatton Bank, and on the data collected during the 1985 survey.

#### **5.4 Timing of the Split between Greenland and Eurasia.**

In this thesis it is assumed that the split between Eurasia and Greenland occurred just prior to anomaly 24B, and that the landward flank of this anomaly marks the continent-ocean boundary. However, it has also been suggested that a substantial width of oceanic crust may have accreted in the north-east Atlantic prior to anomaly 24B. Larson (1984) suggested that over 100 km of pre-anomaly 24B oceanic crust exists on the East Greenland continental margin formed contemporaneously with the Blossville Kyst lavas, based on the recognition of seaward-dipping reflector sequences which were regarded as diagnostic of underlying oceanic crust. Talwani *et al.* (1981) considered that the Voring Plateau Escarpment marks the continent-



ocean boundary on the Norwegian margin. This lies well to the east of anomaly 24B which is itself associated with the most oceanward portion of the dipping reflector sequences observed on the Outer Voring Plateau (Mutter *et al.*, 1982).

Bott (1987. ) has given a discussion of the evidence in favour of continental splitting in the north-east Atlantic occurring immediately prior to anomaly 24B. This is based on a consideration of the geology of East Greenland, a major feature of which is the extensive volcanism associated with continental break-up. This resulted in the thick plateau basalts of the Blossville Kyst and the associated coastal dyke swarm and flexure. Biostratigraphic and radiometric age determinations of the Blossville Group lavas indicate that these were extruded entirely within the reverse polarity anomaly 25/24B interval. The dyke swarm cuts through this group, and is regarded as having been emplaced during the latest stage of lava eruption. The coastal flexure is regarded as being contemporaneous with, or post-dating the emplacement of dykes, and post-dates the lavas.

Bott (1987. ; pers. comm.) considered that the zone of flexure marks the westward limit of a zone of thinned and subsided continental crust formed during a short-lived rift phase which took place before continental break-up. The flexure is unlikely to have post-dated the onset of seafloor spreading. The onset of seafloor spreading must therefore have just predated anomaly 24B. Further evidence for this hypothesis is the lack of a substantial reversely magnetised strip of crust corresponding to the 25/24B negative polarity interval landward of anomaly 24B (eg. Featherstone *et al.*, 1977). Whilst admitting that these arguments are not conclusive, Bott (1987. ) concluded that they favour an onset of spreading in the north-eastern North Atlantic shortly before anomaly 24B.

## **5.5 Interpretation of 1985 survey magnetic anomaly data.**

The data collected during the 1985 Durham/Cambridge Universities Cruise to the Hatton Bank continental margin includes magnetic anomaly intensity recorded almost continuously along ships tracks within a box 100 by 80 km straddling the ocean-continent transition. Included in this data set are two long magnetic profiles run out in to the Iceland basin in an attempt to define as much of the anomaly sequence adjacent to the continental margin as possible. This was in order to facilitate identification and correlation of anomalies with respect to the existing lineation identifications east of the Reykjanes Ridge, and therefore to provide an accurate determination of the position of the ocean - continent boundary.

### **5.5.1 Magnetic anomaly contour map.**

The resulting magnetic anomaly data set is spatially dense, and as a first step in its interpretation, a magnetic anomaly contour map was produced. Ships tracks were annotated with the recorded magnetic anomaly data, and the resulting plots hand-contoured at an interval of 100 nT.

The resulting contour map is shown in figure 5.5 and exhibits several interesting features. The first and most obvious are the series of linear, alternately positive and negative polarity anomalies characteristic of seafloor spreading apparent in the north western region of the survey. By comparison with Roberts & Jones contour map these were tentatively identified as anomalies 21 and 22. These are flanked continentward by a wide positive anomaly. This corresponds to the anomaly discussed in section 5.2 which appears to replace anomaly 23 identified by Vogt & Avery north of 58° N.

This region in turn passes landward into an area of high amplitude anomalies which approximately follow margin strike. The anomalies within this region are distinctly arcuate, bowing to south-east within the survey area. This observation is in contrast to the more linear aspect of anomalies produced by simple seafloor spreading, suggesting an alternative origin. In addition within this region there exists a large anomaly centred at  $59^{\circ} 07' \text{ N}$ ,  $18^{\circ} 30' \text{ W}$  of peak-to-peak amplitude 1700 nT, which is clearly a localised effect within the crust. If the anomaly were to originate from a single, normally magnetised body extending to depth, the resulting anomaly shape would consist of a large positive peak north of a shallow negative peak. The opposite would be true for a similar but reversely magnetised body. In fact the anomaly consists of a large 700 nT negative peak north-west of a slightly larger 1000 nT positive peak. This suggests that the observed anomaly may originate from a reversely magnetised intrusion to the north-west of a normally magnetised intrusion. The region occurs roughly in the expected location of anomaly 24 ; Wigginton (1984) interpreted this as such on the basis of comparisons of earlier Durham University magnetic anomaly profiles across the Hatton-Bank margin with a synthetic profile, and on its continuity with corresponding anomalies to the north and south of the region. This interpretation is treated with caution in view of the apparently anomalous nature of the region which suggests a more complicated history of formation.

Landward of this zone is a region of uncorrelated local anomalies which are of such a wavelength as to prohibit all but the crudest of separations into areas of positive and negative polarity, despite the small track separation. The area corresponds to the upper continental slope and shelf of Hatton-Bank. The wavelength and amplitudes of anomalies within this zone are later used to infer the nature of

the basement on Hatton Bank.

In general the contour map is consistent with that of Jones & Roberts (1975), with an increase in the resolution of detail permitted by the spatially dense data set.

### 5.5.2 Identification and Correlation of Anomalies.

In order to identify and correlate seafloor spreading magnetic anomalies with existing identifications (Vogt & Avery, 1974 ; Voppel *et al.*, 1979), a program (MAGTRK, appendix A) was written which plotted magnetic anomaly intensity perpendicular to tracks. Data from previous Durham University geophysical cruises on the RRS Shackleton which cross the Hatton Bank margin were included with the 1985 survey data and plotted on a Mercator projection. Options within the program included the facility to plot superimposed digitised coastlines, bathymetry, and previously identified magnetic anomaly lineations.

Anomalies 20 to 24 were digitised where identified from the sources previously quoted and superimposed on the magnetic anomaly trackline chart (figure 5.6). Anomalies 20, 21, and 22 positions correlate well with peaks observed on the Shackleton and 1985 survey data, confirming the tentative identification of anomalies 21 and 22 made from the contour map. The prominent broad negative anomaly between anomalies 20 and 21 is easily recognised on the two long Shackleton profiles north and south of the 1985 survey area, providing additional confirmation of the identifications made.

Anomalies 23 and 24 as identified north of the survey area by Voppel *et al.* (1979) correlate well with distinct anomalies in the Shackleton cruise data. South

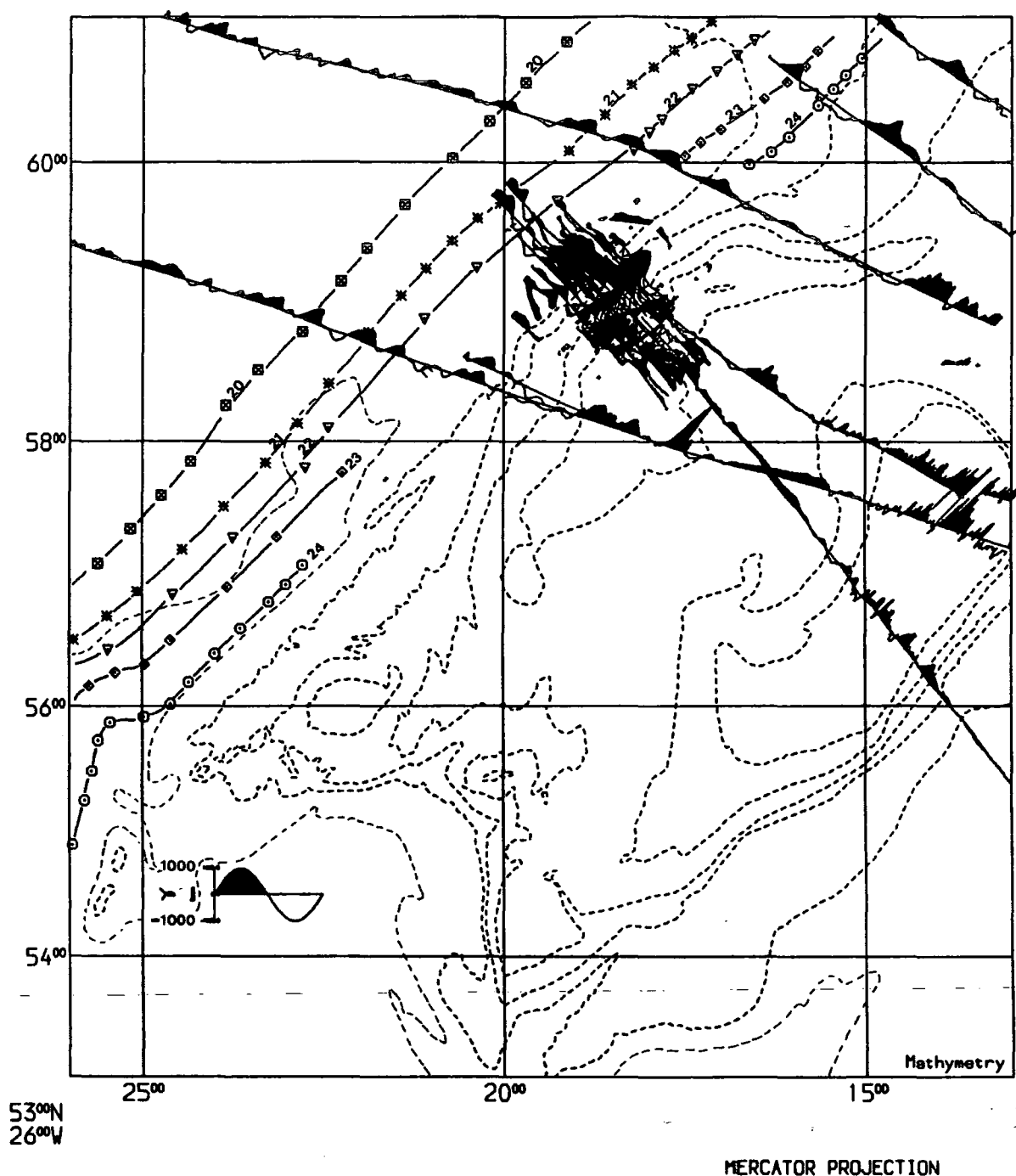


Figure 5.6 Magnetic anomalies on Hatton Bank and adjacent areas plotted perpendicular to ships tracks. Data from 1985 survey, and previous Durham University cruises crossing Hatton Bank. Also shown are digitised anomaly lineations 20 to 24 according to authors cited in the main text.

of the 1985 survey area, well developed seafloor spreading anomalies are observed in the Shackleton data, which show good correlations with digitised anomaly lineations 20, 21, and 22. Further landward, a weak positive anomaly can be seen, separated from a relatively strong, double-peaked anomaly by a distinct negative trough. By a simple "counting out" procedure from the established anomalies, it was tentatively concluded that these correspond to anomalies 23 and 24. This supposition is supported by their continuity with known lineations, and by the double nature of the proposed anomaly 24, which is interpreted as representing anomalies 24A and 24B.

In the 1985 survey data anomalies 21 and 22 are easily recognised. Landward from these, a broad positive anomaly identified from the contour map could possibly be interpreted as a modified anomaly 23. Further east, an arcuate high amplitude positive anomaly might tentatively be interpreted as anomaly 24. This passes further east into the short wavelength, high amplitude anomalies of the upper continental slope and shelf of the Hatton Bank. It is clear that anomalies 23 and 24 cannot be unambiguously identified within the 1985 survey area without a more precise determination of their expected positions.

### **5.5.3 Anomaly 23 and 24 Reconstructions.**

In order to determine the expected positions of anomalies 23 and 24 two techniques of reconstruction were employed. The first involved the rotation of identified anomalies 20 and 21 within the anomaly 20 to 24 sequence adjacent to the Rockall Plateau to the position of anomaly 24B using finite-difference poles and angles of rotation as given by Bott (1985), and Srivastava & Tapscott (1986) respectively. These were plotted along with digitised known anomaly 24 lineations identified north and

south of the 1985 survey region as a check on the degree of match between known and reconstructed anomaly 24 positions.

There is a generally good agreement between reconstructed and actual anomaly positions both north and south of the 1985 survey area (figure 5.7). Reconstruction of anomaly 21 to 24 time using Srivastava & Tapscott's (1986) pole results in a very close correlation to the observed lineation, whereas the corresponding reconstruction of anomaly 20 using Bott's (1985) pole suggests a position slightly oceanward of that observed by Voppel *et al.* (1979) north of the 1985 survey area. This may be due to differences in the detailed shape of anomalies 20, 21, and 24 adjacent to the Hatton Bank margin. Vogt & Avery (1974) observed a progressive straightening of anomalies from 24 to 20, and it may be that this effect is responsible for the observed discrepancy. In the south, both reconstructions place the theoretical anomaly 24B position slightly landward of that given by Vogt & Avery (1974). However, as mentioned earlier, their anomaly 24 was interpreted by Nunns (1980) as corresponding to anomaly 24A, which would be expected to lie oceanward of a reconstruction to anomaly 24B. Both reconstructions place the expected position of anomaly 24B within the survey region along the foot of the continental slope, approximately coincident with the 2500 m isobath. The reconstructions support the tentative identification of anomalies 24A and 24B in the Shackleton data to the south of the survey region which lie slightly oceanward of the reconstructed anomaly 24B position (figure 5.6). Vogt & Avery (1974) pointed out that anomalies 23 and 24 appear to bend out around the basement high of Hatton Bank, with subsequent anomalies straightening out as mentioned earlier. Therefore reconstruction of anomaly 24 using anomalies 21 and 20 would be expected to indicate a position slightly landward of the true position depending on the degree of straightening of

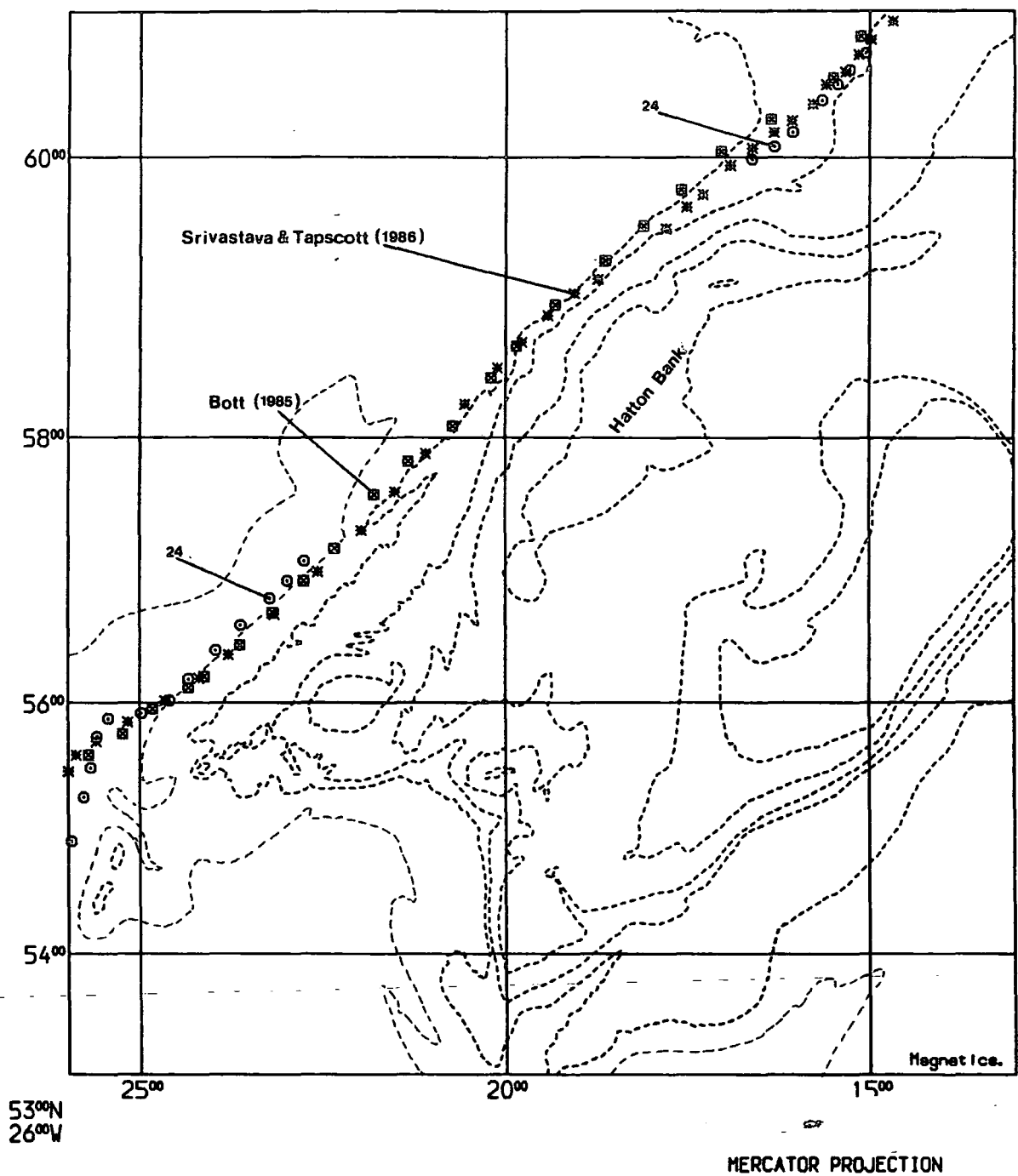


Figure 5.7 Reconstruction of anomaly 24B position adjacent to Hatton Bank using the finite-difference poles and angles of rotation given by Srivastava & Tapscott (1986), and Bott (1985).



later anomalies.

A similar procedure was used to determine the expected anomaly 23 position in the survey area. Anomaly 21 was reconstructed to anomaly 23 time by adapting Srivastava & Tapscott's (1986) finite-difference pole and is shown in figure 5.8. This agrees well with the digitised identified anomaly 23 lineations north of the survey area, but less well to south. Srivastava & Tapscott's pole was determined by fitting anomalies 24 from anomaly 21 time assuming constant spreading rates and directions during this period. The resulting finite-difference pole was adapted by simple interpolation of the angle of rotation given according to the timescale of Ness *et al.* (1980). However, the assumption of constant spreading rate and direction may not have been correct in detail in this region, which may account for the discrepancy observed. The reconstructed position correlates well with the anomaly 23 tentatively identified in the Shackleton data to the south of the survey region.

The second technique of reconstruction involved the closure of the Reykjanes Basin to anomaly 24B time using the total opening poles given by Srivastava & Tapscott (1986), and Bott (1985). Anomaly 24B lineations on the conjugate East-Greenland margin (Featherstone *et al.*, 1977 ; Voppel *et al.*, 1979 ; Uruski & Parson, 1985) were digitised and rotated eastwards to their corresponding position adjacent to the Hatton Bank continental margin as shown in figure 5.9. Reconstructed anomaly 24B positions are consistently well oceanward of digitised identified lineations to the north and south of the survey region. In the vicinity of the survey they lie approximately 30 km oceanward of previous anomaly 24 reconstructions in a location approximately coincident with the expected anomaly 23 lineation.

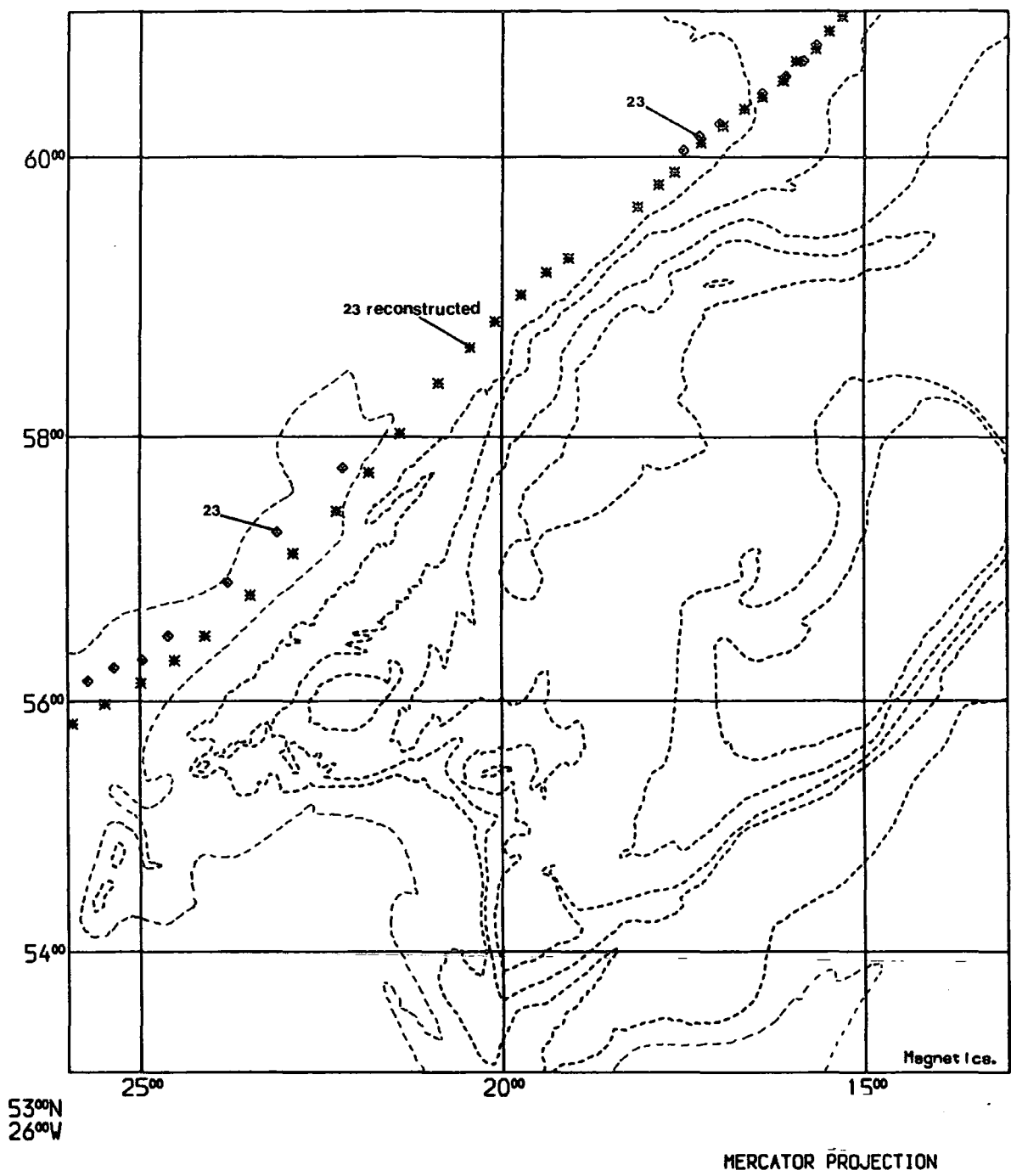
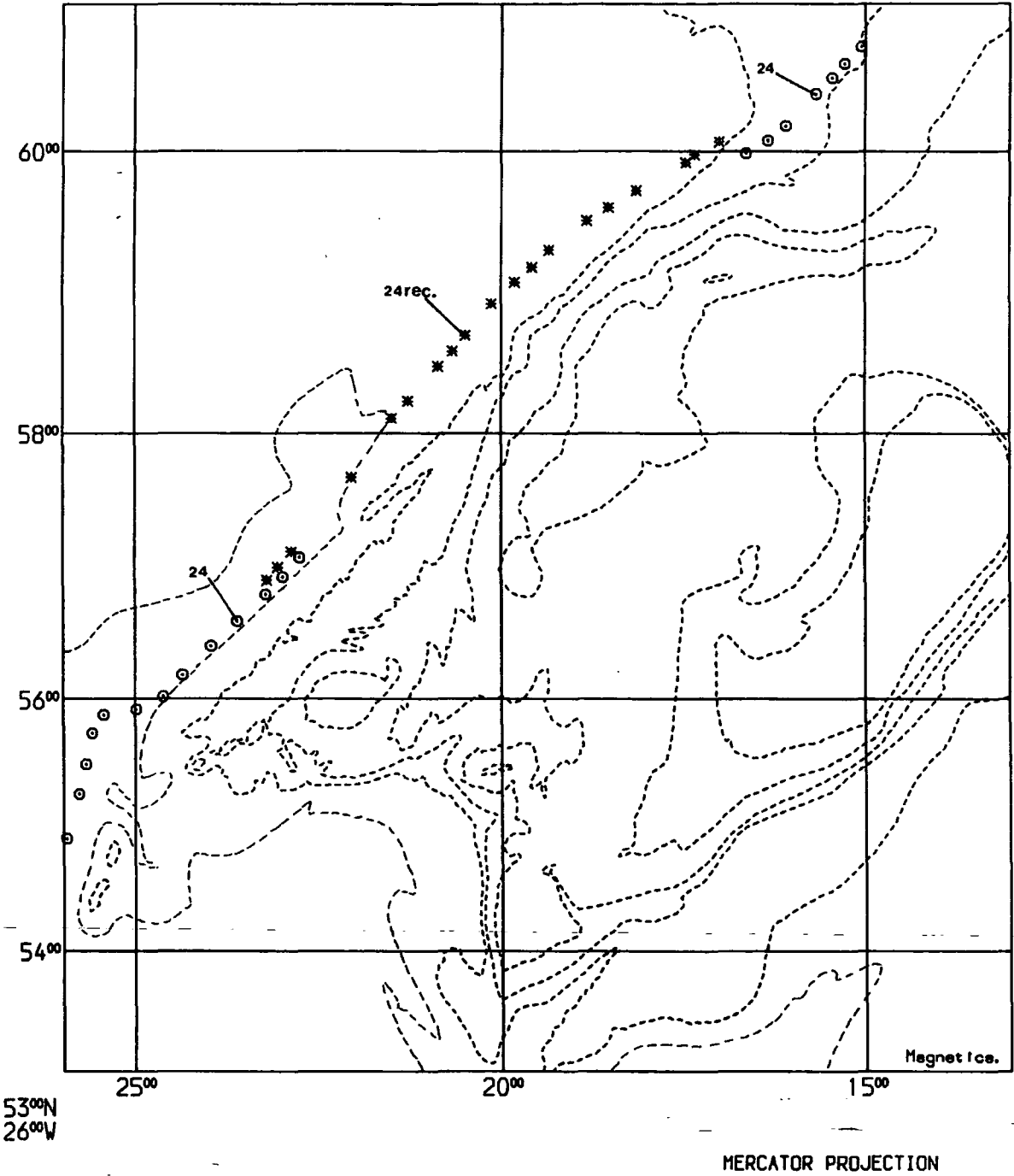


Figure 5.8 Reconstruction of anomaly 23 position adjacent to Hatton Bank using a finite-difference pole and angle of rotation adapted from Srivastava & Tapscott, (1986).



**Figure 5.9** Anomaly 24B identified on the East-Greenland continental margin reconstructed to its position adjacent to Hatton Bank at anomaly 24B time using pole for closure of the north Atlantic as given by Bott (1985).

The angle of rotation required to achieve complete closure of the Reykjanes Basin to anomaly 24B time was determined by rotating the digitised anomaly 24B lineation identified by Featherstone *et al.* (1977) on the conjugate East-Greenland margin eastwards until its position coincided with the anomaly 24B identified in the Shackleton data south of the 1985 survey. The result is shown in figure 5.10, which indicates a good correlation between the observed and reconstructed anomaly 24B lineations in the Shackleton data to the north and south of the 1985 survey, and with that of Voppel *et al.* (1979) to the north. The reconstructed anomaly 24B is placed landward of that identified by Vogt & Avery (1974) to the south, consistent with earlier reconstructions using the finite-difference poles and angles of Bott (1985) and Srivastava & Tapscott (1986). The results of all three anomaly 24B reconstructions are shown in figure 5.11, together with the inferred continent-ocean boundary.

#### **5.5.4 Comparison of observed with reconstructed anomaly 23 and 24 positions.**

**Anomaly 23.** The reconstructed anomaly 23 position corresponds to the oceanward limit of the broad positive anomaly identified on the contour maps of Jones & Roberts (1975) and this thesis (figures 5.12, 5.5) and indicates a good correlation with the weak positive anomaly identified on the Shackleton lines south of the survey region interpreted as anomaly 23 (figure 5.6). A detailed examination of the broad anomaly on the Jones & Roberts contour map reveals that it can be divided into a weak, discontinuous lineation corresponding to the Shackleton anomaly 23 identification, and correlating well with the anomaly 23 reconstruction, and a landward broad positive anomaly (figure 5.13). These two anomalies merge at approximately 58.75° N.

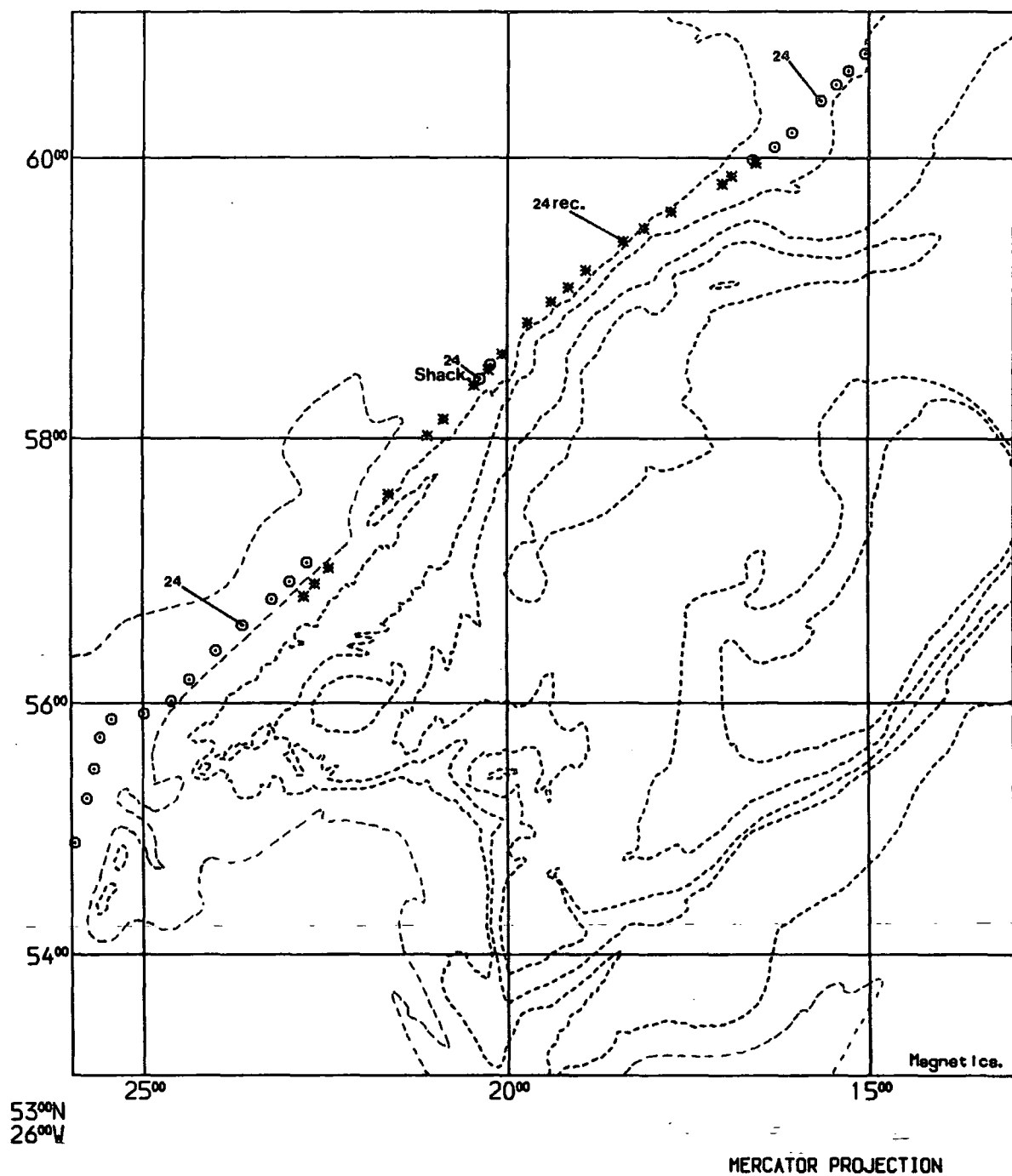


Figure 5.10 Anomaly 24B identified on the East-Greenland continental margin reconstructed to its position adjacent to Hatton Bank at anomaly 24B time using pole for closure of the north Atlantic adapted from Bott (1985).

Rockall Plateau, M24b rec, all three.

61°N  
13°W

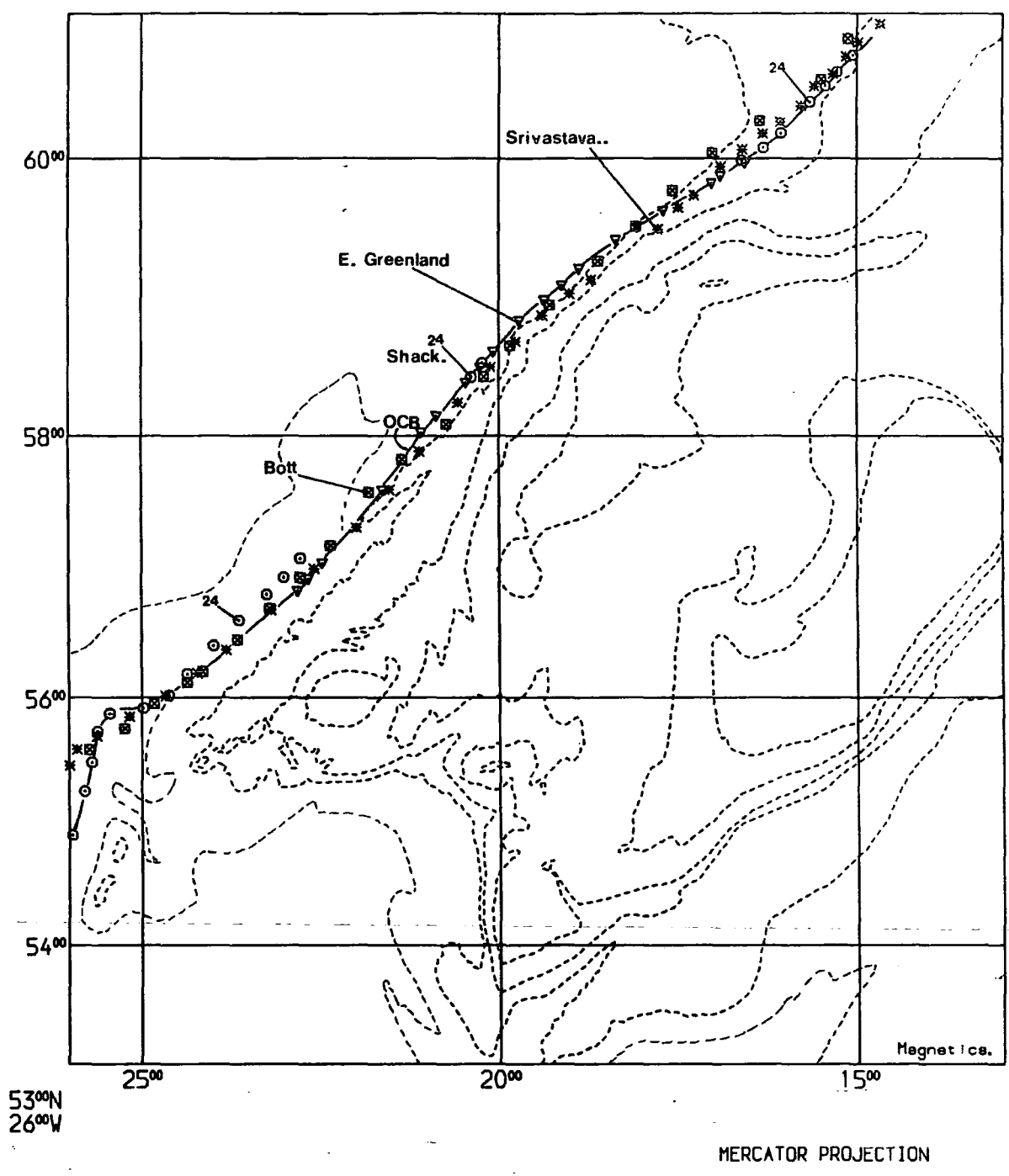


Figure 5.11 Results of all three anomaly 24B reconstructions adjacent to Hatton Bank, together with the inferred ocean-continent boundary.

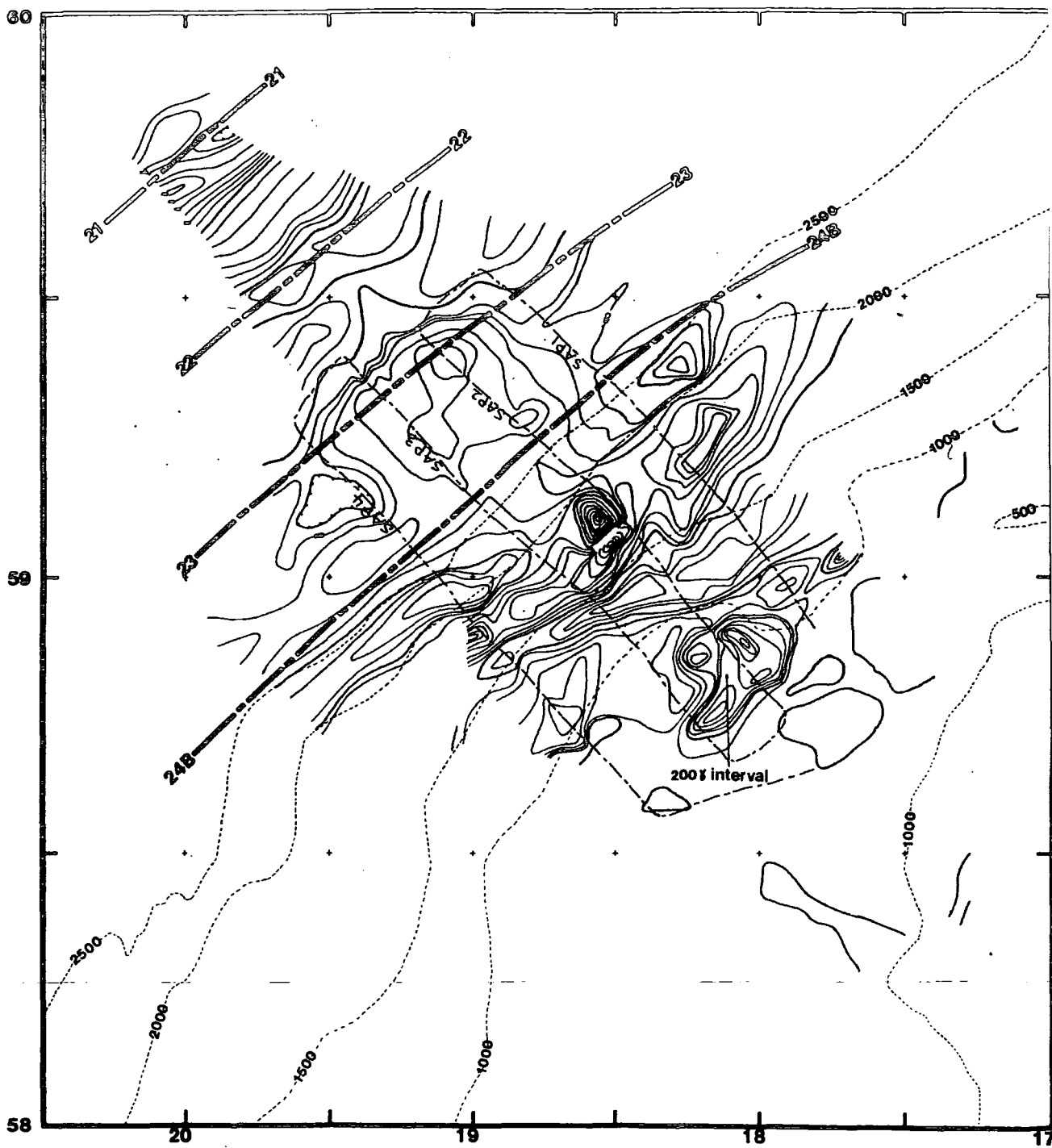


Figure 5.12 Reduction of figure 5.5 with reconstructed anomaly 23 and 24B positions marked. For details of CMP positions, see CMP position chart in back pocket.

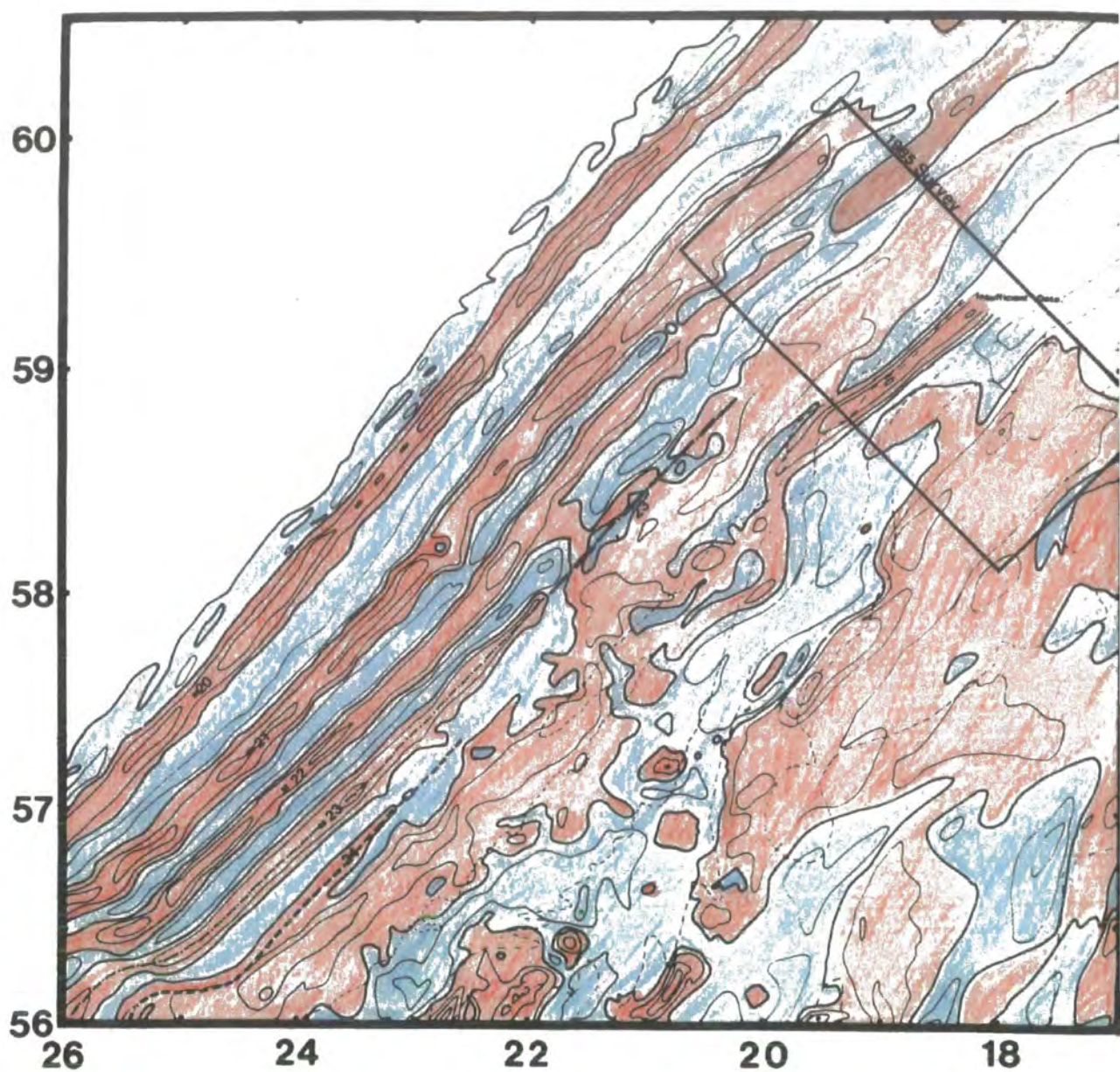


Figure 5.13 Reproduction of part of Jones & Roberts magnetic contour map showing the identifications of Vogt & Avery (1974), and the proposed continuation of anomaly 23 south of the 1985 survey region.



It is suggested on the basis of these correlations that the weak lineation represents a continuation of anomaly 23 identified to the south by Vogt & Avery (1974), and this anomaly may pass through the survey area along the reconstructed position as the seaward portion of the broad anomaly observed on the hand-contoured magnetic map as indicated in figure 5.12. This eventually forms the anomaly 23 identified north of the survey region identified by Voppel *et al.* (1979). If the inferred anomaly 23 position is transferred to seismic reflection profiles, SAPs 1, 2, 3, 4, it can be seen that the reconstructed anomaly 23 lies approximately 20 km from the foot of the continental slope in a region of crust exhibiting clear sub-basement seaward-dipping reflectors (figures 5.14(a),(b)), and having a velocity structure consistent with thickened oceanic crust (White *et al.*, 1986 ; 1987).

**Anomaly 24B.** When transferred to the hand-contoured magnetic map, the reconstructed anomaly 24B lies immediately oceanward of the region of high amplitude anomalies as shown in figure 5.12. No anomaly displaying the characteristic anomaly 24 shape is evident in this position. When transferred to seismic sections SAPs 1, 2, 3, 4, the reconstructed anomaly 24B coincides with the landward end of a lower dipping reflector series which is overlain by what is interpreted to be a late-stage lava sequence extruded some time after seafloor spreading had become established (White *et al.*, 1986). The boundary between the two lava sequences corresponds to a distinct unconformity clearly observed on SAP2 between CMPs 600 and 900, and less obviously on other SAPs (chapter 6). The late-stage lava sequence is identifiable on all four seismic sections, extending well continentward of the reconstructed anomaly 24B position, and coinciding with the region of complicated high-amplitude anomalies. Gravity modelling (chapter 4) suggests the presence of an intrusive body in the region between CMPs 900 and 1200 on SAP2 (figure 5.14)

Figure 5.14 (a) Magnetic anomalies recorded along SAPs 1, & 2, with reconstructed anomaly 23 and 24B positions marked.

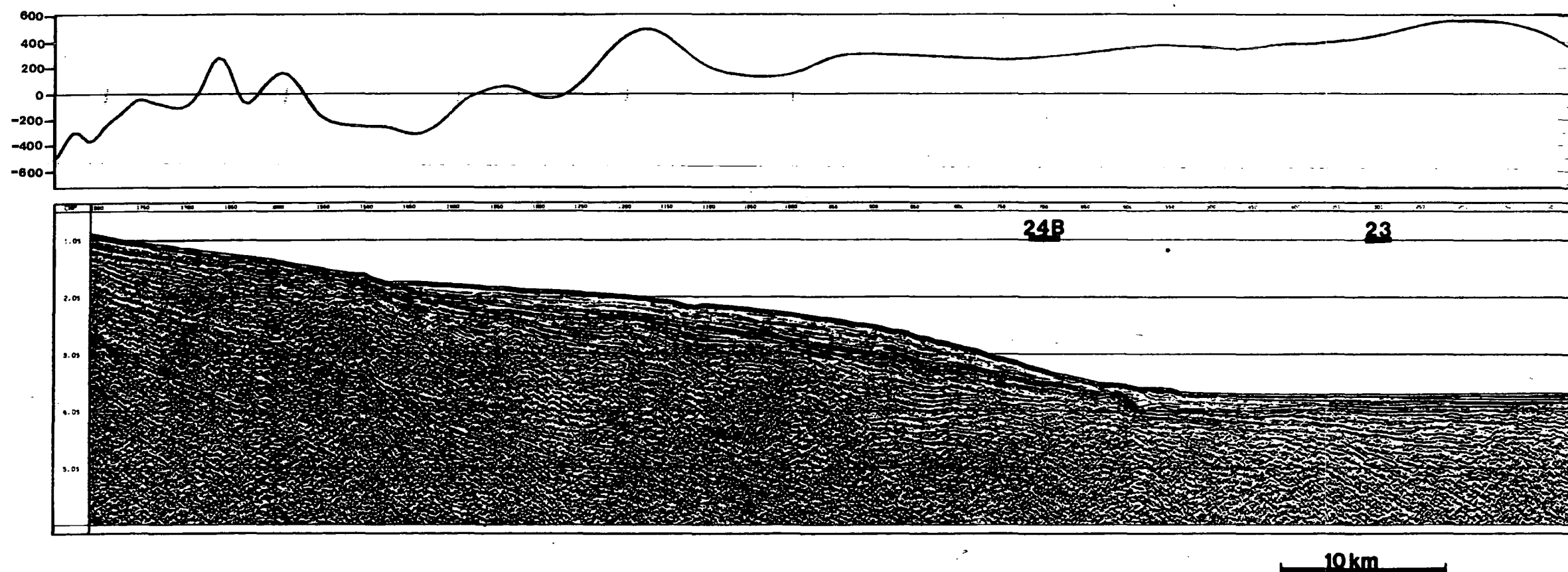
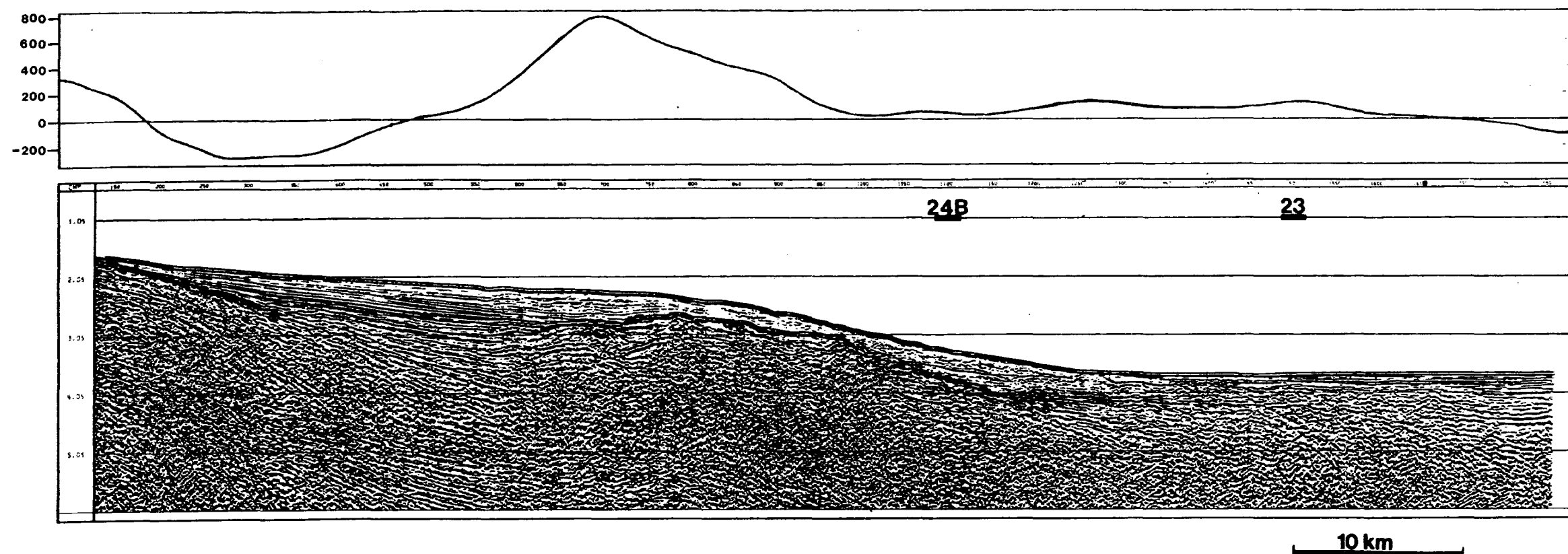
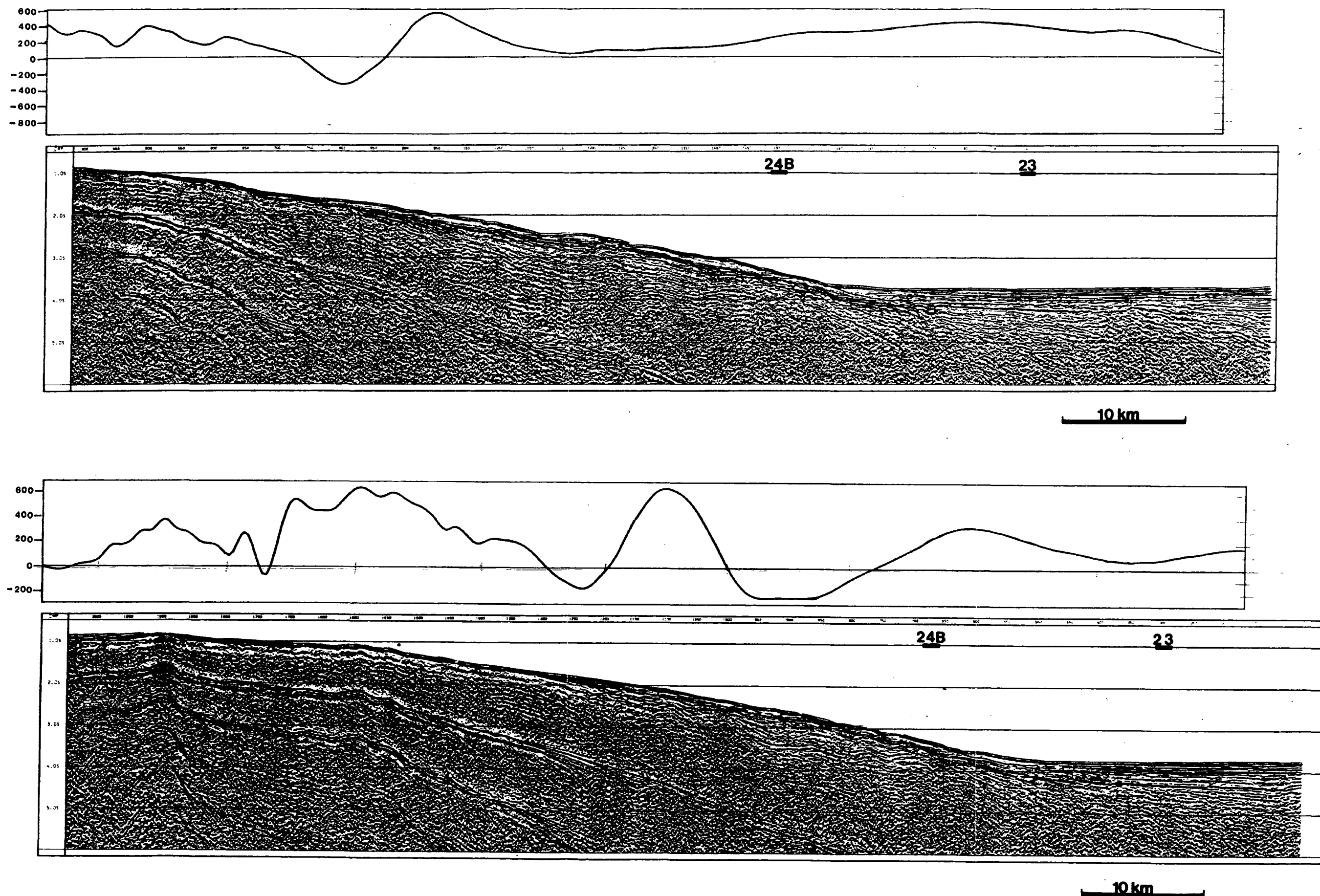


Figure 5.14 (b) Magnetic anomalies recorded along SAPs 3, & 4, with reconstructed anomaly 23 and 24B positions marked.



close to the large local anomaly identified on the hand-contoured magnetic map (figure 5.5)

The evidence suggests that the zone of high amplitude anomalies originates as a result of the late-stage igneous activity, rather than from seafloor spreading. It is suggested that the intra-basalt unconformity observed <sup>on</sup> SAP profiles which coincides with the reconstructed anomaly 24B, represents the top of oceanic crust generated during the earliest stage of seafloor spreading. Anomaly 24 may have originally been present, but the subsequent igneous activity is inferred to have erased or modified this to such an extent that it is no longer recognisable within the survey area.

It is considered unlikely that anomaly 24 was isolated on the Greenland plate by an eastward migration of the ridge axis for the following reason. Since anomaly 23 is inferred to be present adjacent to the Hatton-Bank margin, any ridge jump must have occurred prior to anomaly 23 time. Consequently if the ridge jump has taken place, anomaly 24 on the East-Greenland margin at a position conjugate to the survey area on Hatton-Bank margin should be up to twice the width observed elsewhere on the East-Greenland margin. Figure 5.15 shows the Rockall Plateau rotated to the position it would have occupied at anomaly 24B time. Magnetic anomaly data collected on the East-Greenland margin during earlier Durham University cruises are shown, together with the anomaly 24B identification of Featherstone *et al.* (1977), the inferred line of split west of Hatton Bank, and an outline of the 1985 survey area. Examination of anomaly 24 on the East-Greenland margin adjacent to the 1985 survey shows no evidence of widening with respect to anomaly 24 elsewhere on the margin. Furthermore, the position of the reconstructed ocean-continent boundary shows an excellent agreement with the anomaly 24B lineation identified on the East-Greenland margin by Featherstone *et al.* (1977). These observations provide

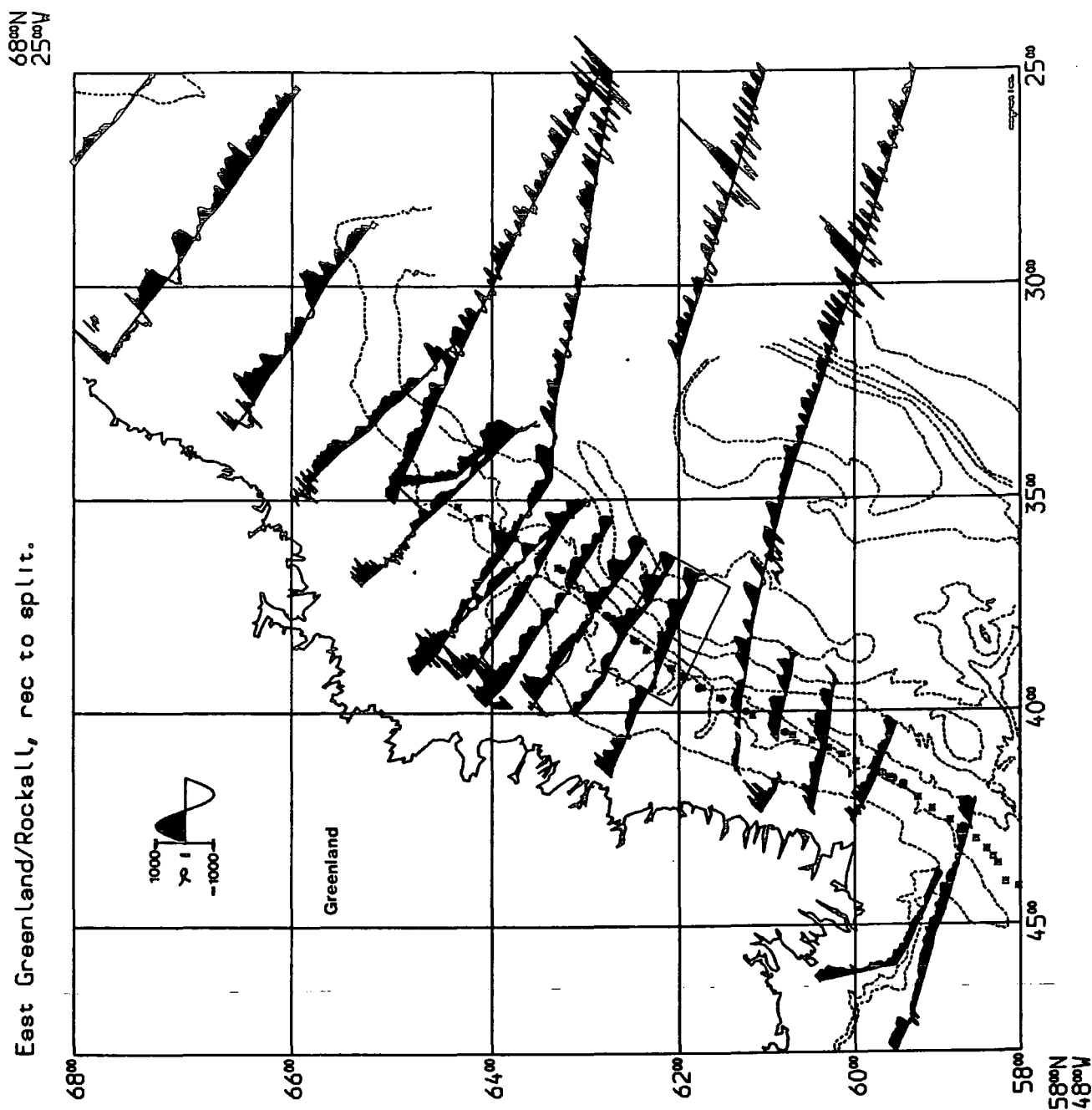


Figure 5.15 Closure of Reykjanes Basin to anomaly 24B time. Magnetic anomalies and anomaly 24B identified adjacent to the East-Greenland margin shown, together with the inferred ocean-continent boundary, and the 1985 survey area.

convincing evidence for the continuity of anomaly 24 within the survey area along the line shown in figure 5.11 prior to its obliteration by subsequent igneous activity.

## 5.6 Nature of the Continental Basement.

Study of the magnetic anomalies found on the upper continental slope and shelf of Hatton Bank can provide evidence concerning the nature of the basement in this region.

The amplitudes of given wavelength anomalies recorded at the sea surface can be downward continued to a position at the seafloor to give an estimate of the anomaly amplitude of that wavelength at oceanic basement level. A comparison of typical magnetic anomaly amplitudes with those of similar wavelength occurring in regions of known basement character provides an indication of the magnetic properties of the basement found on the Hatton Bank.

The magnetic potential in free space satisfies Laplace's equation given by

$$\nabla^2 V = 0$$

where the Laplacian operator  $\nabla^2$  is given by

$$\nabla^2 = \frac{\partial^2}{\partial x^2} + \frac{\partial^2}{\partial y^2} + \frac{\partial^2}{\partial z^2},$$

and

$V$  = magnetic potential field function,  $V(x, y, z)$ . A particular solution of the two-dimensional case of interest is given by

$$V = \sum_i V_i$$

where

$$V_i = D \sin(k_x x) e^{|k_x|z}$$

and  $e^{|k_x|z}$  represents an amplitude which can be used to estimate the attenuation suffered by a particular wavelength in transmission from the seafloor to the sea surface. To a good approximation, the total field magnetic anomaly  $\Delta F$  also satisfies Laplace's equation. Therefore knowing the amplitude and dominant wavelength of a particular anomaly at the sea surface enables its amplitude at the seafloor to be estimated by a process of downward continuation.

Examination and downward continuation of the amplitudes and wavelengths of magnetic anomalies recorded along profiles on the upper continental slope and shelf of the Hatton-Bank (figure 5.14) imply that anomalies typically in the range 700 - 1600 nT are present at the seafloor (table 5.1).

**Table 5.1.** Magnetic anomaly amplitudes.

SAP	CMP	Characteristic wavelength (km)	Depth (km)	Amplitude at Sea surface(nT)	Amplitude at Sea floor(nT)
2	1650	3.6	0.90	350	1670
3	475	4.6	0.75	260	730
4	1760	3.2	0.75	333	1450

Aeromagnetic maps over regions of volcanic basement such as the Tertiary igneous provinces of Skye and Mull indicate anomaly amplitudes of up to 2000 nT for comparable wavelengths. Over the most magnetic metamorphic basement such as the Lewisian found on the Isle of Lewis, substantially lower amplitude anomalies are observed, up to approximately 450 nT. Comparison of these values with those inferred from the Hatton-Bank survey data suggest that the anomalies originate from relatively highly magnetised basement, probably composed of basalt flows of Paleocene to Eocene age (Roberts *et al.*, 1984). The acoustic basement observed on

complementary seismic reflection profiles in the area is generally smooth, consistent with flat-lying lava flows (figure 5.14, and chapter 6).

## 5.7 Conclusions.

Anomalies 21 and 22 have been clearly identified and correlated with the corresponding lineations of previous workers in the area (Vogt & Avery, 1974 ; Voppel *et al.*, 1979). Anomalies 23 and 24A & 24B have been identified in data from earlier Durham University cruises north and south of the present survey region. Anomaly 23 may be developed in the survey area in a region characterised by a velocity/depth structure consistent with that of thick oceanic crust, and exhibiting clear oceanward-dipping reflectors (chapter 6). Anomaly 24 is inferred to have originally been present, but has subsequently been modified by extrusive and intrusive activity after seafloor spreading had become established, to the extent that it can no longer be recognised. Reconstructions place anomaly 24B at a position towards to the landward edge of a lower dipping reflector series formed as part of the oceanic crust, and overlain by a sequence of later volcanic extrusives. Magnetic anomalies associated with the late-stage igneous activity are well developed continentward of the reconstructed anomaly 24B position. These are in turn replaced landward by a more disorganised magnetic anomaly pattern on the upper continental slope and shelf of Hatton-Bank. Comparison of these anomalies downward-continued to the ocean-floor with the magnetic anomaly signatures of volcanic and non-volcanic basement indicate that the basement forming the Hatton-Bank is volcanic in nature.



## CHAPTER (6)

### Interpretation of synthetic aperture profiles (SAP).

#### 6.1 Introduction.

The processing of four SAP profiles, SAPs 1-4, shot across the ocean-continent transition of the Hatton-Bank continental margin was described in chapter 3. This chapter describes the subsequent interpretation of the resulting seismic sections.

Two types of passive continental margin are known to exist from multichannel seismic reflection experiments. The first is characterised by large rotated and subsided fault blocks, with little associated igneous activity, an example of which is the Bay of Biscay margin (Montadert *et al.*, 1979 ; Whitmarsh *et al.*, 1986). The second exhibits the characteristic development of thick sequences of oceanward dipping reflectors with the notable absence of tilted fault blocks, a well documented example of which is the Norwegian Margin (Mutter *et al.*, 1982 ; Hinz, 1981). Drilling has shown these sequences to be volcanic in origin (Leg 104 Scientific Party, 1986). The Hatton-Bank continental margin is an example of the second, volcanic variety.

Although the volcanic origin of the dipping reflector sequences is now widely accepted, there remains considerable debate concerning their formation and evolution. Mutter *et al.*, (1982) proposed a model in which the dipping reflector sequences develop during a period of "subaerial seafloor spreading", with dipping sequences forming entirely within oceanic crust. Alternatively Hinz (1981) postulated that the dipping reflectors are extruded onto stretched continental crust at the incipient spreading axis prior to the onset of seafloor spreading. These models of the formation and evolution of volcanic passive continental margins, and their implications

concerning the position of the ocean-continent boundary are discussed in detail in chapter 1.

Passive continental margins of the dipping reflector type have been widely recognised, and in particular have been shown to exist around much of the north-east Atlantic (Hinz, 1981). The extent to which the volcanic type of margin predominates at the passive margins of the North Atlantic is shown in figure 6.1 reproduced from White *et al.* (1987). Their widespread recognition in seismic data from many other continental margins implies that they may be the predominant type, and an understanding of their formation and evolution is essential in determining the processes involved in the rifting and early seafloor spreading of passive volcanic continental margins.

## **6.2 The Hatton Bank continental margin.**

The Hatton Bank continental margin (figure 6.2) lies far from any sediment source, and consequently has only a thin layer of post-rift sediment. This makes the study of the deep crustal structure of the margin by single and two-ship multichannel seismic techniques particularly effective since the thin sediment layer does little to obscure the deeper sub-basement structure of interest. The purpose of this section is to describe and interpret the four SAP profiles shot across the ocean-continent transition of the Hatton Bank margin. Since the sedimentary layers are thin and play an insignificant role in the margin development, only a brief description of their structure and origin is given here.

Interpreted seismic sections are presented in figures 6.3 - 6.6 which are to be found in the back pocket of this thesis. Projected positions of ESP velocity-depth determinations are marked, together with the zonation scheme described in section



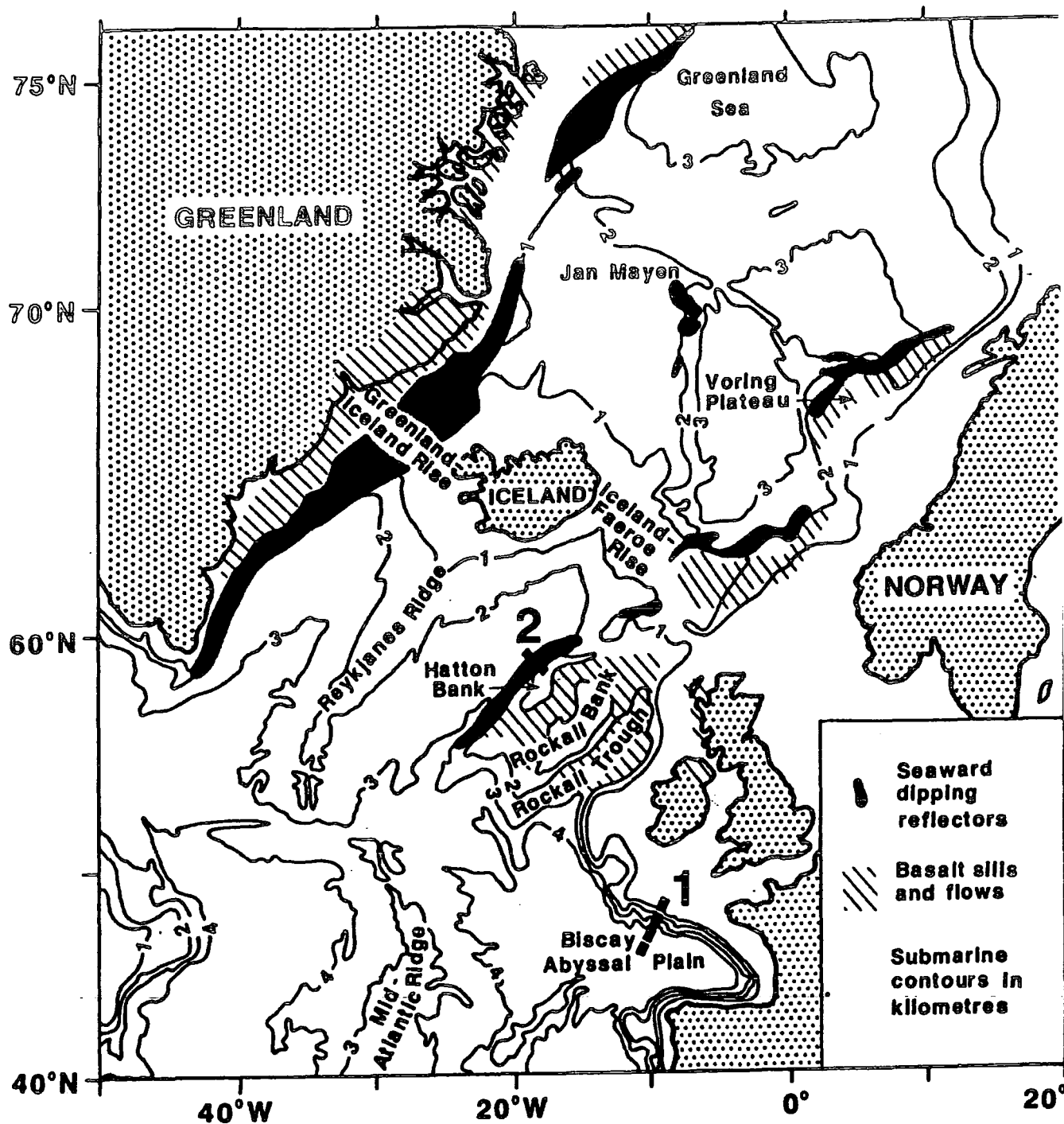


Figure 6.1 Distribution of observed seaward-dipping reflector sequences in the north Atlantic. (Reproduced from White *et al.*, (1987)).

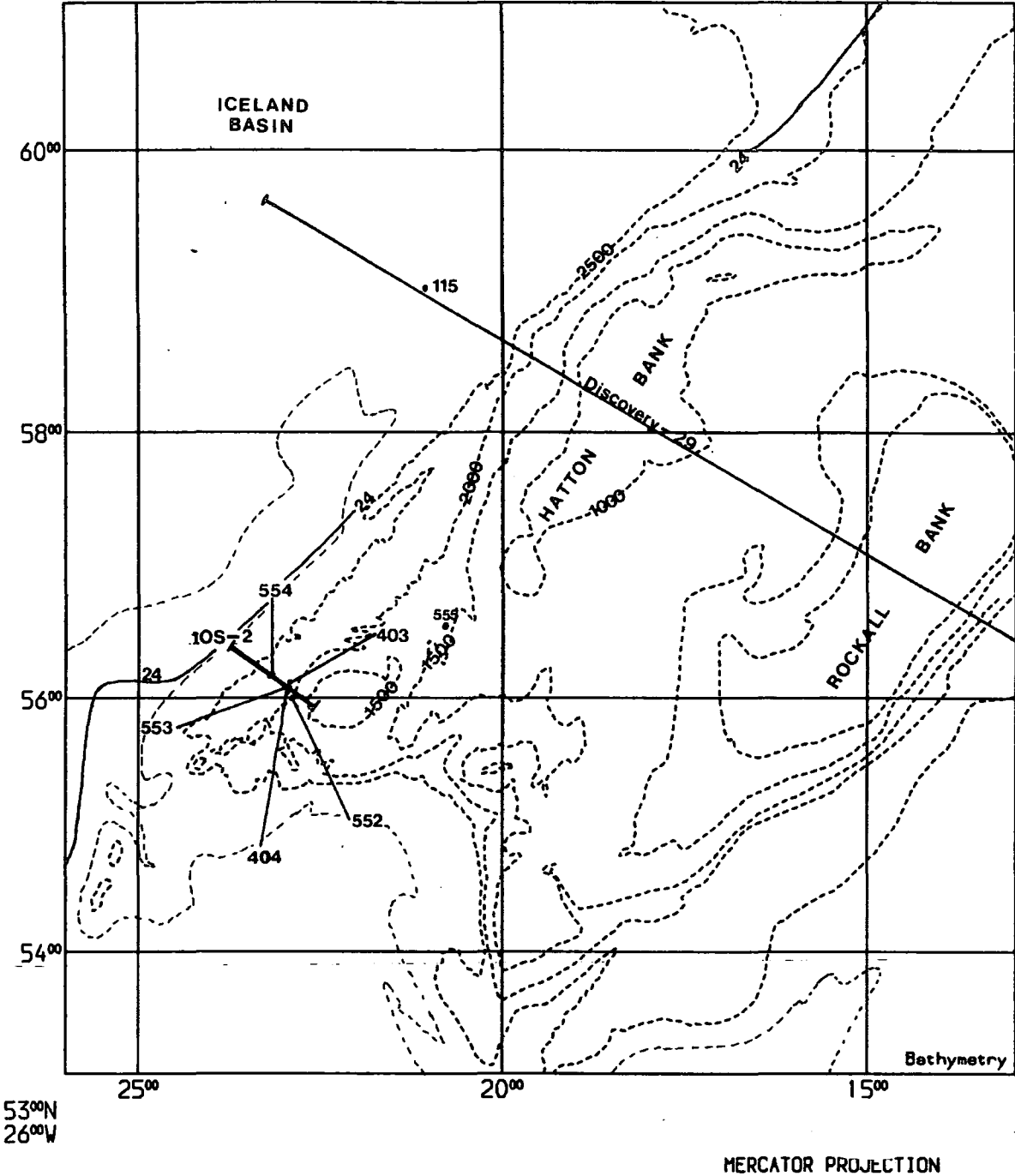
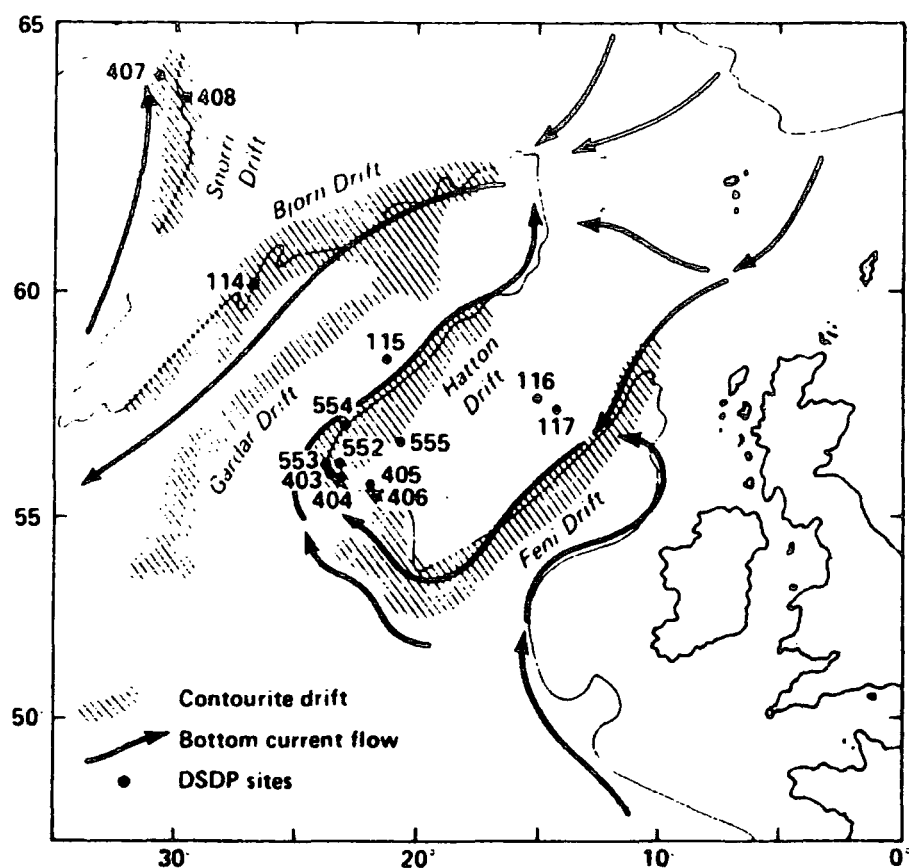


Figure 6.2 Map of Rockall Plateau region, north Atlantic showing anomaly 24, DSDP drill sites, Legs 12, 48, & 81, and position of seismiclines Discovery-29, and IOS-2. (Reproduced from chapter 1.)

6.2.2, and the reconstructed positions of anomalies 23 and 24B. References to SAPs 1, 2, 3, and 4 made in the text refer to figures 6.3, 6.4, 6.5, 6.6 respectively, which should be examined together by lining up the anomaly 24B reconstruction positions on successive SAPs. True dips of reflectors may be found from the time dips by tracing normal rays down to the reflectors.

#### **6.2.1 Sedimentary structure, and acoustic basement morphology.**

Two sedimentary bodies are recognisable on all four SAP sections. The first is the Hatton Drift, a large elongate sediment drift deposited on the margin by a north-east flowing contour current in present day depths of 1600 - 2500 m (Ruddiman, 1972 ; Stow & Holbrook, 1983) (figure 6.7). Drilling during DSDP Legs 48 and 81 on the south-west Rockall Plateau revealed distinct phases of sedimentation within the drift (Stow & Holbrook, 1984). Rapid accumulation of terrigenous sediments and volcanoclastics in late Paleocene to early Eocene was followed by non-deposition until early Miocene. From mid Miocene to the present, nearly continuous sedimentation has taken place. These two sequences are separated by a regional unconformity of Eocene-Oligocene age, identified throughout the north-east Atlantic, and designated R4 by Roberts (1975a) (horizon R of Ruddiman, 1970), which marks a period of downwarping and change in sedimentary regime. The sediments best displayed on SAP 1 between CMPs 250 and 1250(?) are interpreted as representing the same sequences which form the Hatton Drift. Hatton Drift is visible on all SAP profiles as a lens of sediment on the continental slope at travel times between 2.0 and 3.5 s. The assumed mid-Miocene and later drift is largely transparent, but exhibits weak laterally impersistent internal reflectors which show the sediment in-filling and draping basement irregularities. Undulations in the seabed are mirrored in the underlying sediments. This is presumably due to the effect of the current-controlled deposition characteristic of contourites,



**Figure 6.7** Present-day bottom - circulation in the north-east Atlantic. Major sediment drifts, and DSDP Leg 12, 48, & 81 drill sites marked. (Reproduced from Stow & Holbrook, (1984)).

since the undulations do not reflect the acoustic basement topography. On SAP 1 between CMPs 250 and 700 where the drift is thickest, the transparent region is underlain by a zone of relatively strong parallel layers. The uppermost reflector within this group is very gently onlapped to the south-east by the overlying weaker reflectors, and is interpreted as possibly corresponding to reflector R4. In this case, the underlying horizons are suggested to correspond to the Eocene volcanoclastics penetrated by the DSDP operations on the south-west Rockall Plateau. This gentle unconformity, and the underlying reflectors, themselves on-lap acoustic basement to the north-west and south-east within a basement depression between CMPs 200 and 700. Although well developed on SAPs 1 and 2, the Hatton Drift thins progressively towards SAP4, becoming a thin veneer approximately 15 m thick covering the acoustic basement. This effect is probably the result of variations in current velocity along margin strike. On all SAPs, except possibly SAP 3, the characteristic seismic expression of Hatton Drift continues oceanward of the foot of the continental slope where it passes into the oceanic sedimentary unit. The transition between the Hatton Drift and oceanic sequence sediments is unclear. The two sequences appear to interfinger and gradually pass laterally into one another, with no major discernable boundary separating the two.

The oceanic sedimentary sequence lies beyond the foot of the continental slope in the Iceland Basin. SAP profiles show a basement dipping gently westwards, becoming increasingly irregular and indistinct, and overlain by up to 1.0 s two-way-traveltime (TWT) of sediment. These sediments exhibit consistent characteristics on all profiles. Within the oceanic sediments, two sequences can be recognised. The upper sequence consists of a well-layered succession of flat-lying, laterally continuous horizons which extend to approximately 0.4 s TWT below seafloor. Below this, a

sequence of irregular, laterally impersistent reflectors extends to acoustic basement. Near the foot of the continental slope, these two successions appear to be separated by a conspicuous reflector which marks the top of the lower succession, with the upper succession onlapping it to the south-east. The horizon is most clearly seen on SAP 1 extending landwards from CMP 1350 to onlap acoustic basement at CMP 1050. The reflector cannot be recognised on SAP 2. However, possible slumping of sediments at the base of the continental slope of SAP 2, as evidenced by seafloor undulations at CMPs 600 and 550, may have disrupted the underlying sedimentary structure. On SAP 3, the horizon can be identified just above the oceanic acoustic basement at CMP 1700, and correlated landwards to CMP 1575, where it outcrops at the seafloor. Further landwards, at CMP 1500, a weak reflector appears to detach from the seafloor to onlap acoustic basement at CMP 1450. This possibly represents the continuation and termination of the horizon on SAP 3. A similar structure is developed on SAP 4 where a mid-sedimentary horizon at CMP 450 can be followed landwards, possibly outcropping between CMPs 620 and 650, to onlap acoustic basement at CMP 660. The horizon is interpreted as corresponding to reflector R4 (Roberts, 1975a). This implies an Eocene age for the lower oceanic succession, with the post-R4 succession corresponding to early Oligocene and later sediments.

Discovery-29 seismic reflection profile (Scrutton & Roberts, 1971), which passed across the Hatton Bank margin and into the Iceland Basin in the vicinity of DSDP hole 115 (figure 6.2), shows stratified sediments with two prominent reflectors at 0.3 s and 0.8 s TWT below seafloor, above an indistinct basement at 1.0 s TWT. A seismic profile shot across site 115 during DSDP Leg 12 showed a strong horizon at 0.1 s below seafloor (Laughton, Berggren, *et al.*, 1972). The reflector was followed landwards to outcrop at the seafloor in the Maury Channel at the foot of Hatton



Bank as the overlying sedimentary cover thinned to zero. The reflector and underlying sequence were drilled to total depth of 228 m at site 115 (Laughton, Berggren *et al.*, 1972), and were found to correspond to the uppermost part of a series of late Quaternary volcanogenic sandstone beds. It was concluded that these were derived from Iceland, and deposited by a turbidity current mechanism. Similar features are observed within the post-R4 oceanic sediments on SAP profiles, which show a strong horizon at 0.15 s below seafloor with underlying stratification extending to approximately 0.4 s below seafloor. These sediments are interpreted as corresponding to the sequence of volcanogenic sandstones drilled at site 115 and observed on complementary seismic sections.

The acoustic basement exhibits systematic structural variations along the strike of the margin. From the continental shelf of Hatton Bank oceanwards to approximately the beginning of Hatton Drift the acoustic basement is smooth with occasional irregularities. This effect is associated with the presence of flat-lying early Paleocene basaltic flows forming the basement on Hatton Bank as confirmed by the interpretation of the magnetic anomalies recorded in this region given in chapter 5, and by the results of DSDP Leg 81 site 555 which was located in a region of comparable basement on the south-west Rockall Plateau. In the zone approximately coinciding with the Hatton Drift, the acoustic basement is hummocky, and varies in structure along strike. On SAP1 the acoustic basement underlying the Hatton Drift passes from a smooth region overlying a basement wedge of dipping events, into a structural high between CMPs 600 and 1150. This basement high becomes progressively less pronounced down the margin and is recognisable on SAP4 by the character of the acoustic basement between CMPs 650 and 1200. The structure is explained in section 6.4 as being due to post-rift igneous activity on the margin.

Oceanwards from the foot of the continental slope the acoustic basement becomes increasingly irregular and characterised by diffraction hyperbolae. Presumably the differential deposition of Hatton-Drift sediments along margin strike was controlled by the effect of this basement relief on bottom contour currents.

### **6.2.2 Basement reflectors.**

In this section a detailed description of the basement structure observed on SAPs 1 to 4 is presented. To facilitate description, the seismic sections are divided into three zones on the basis of the identification of an upper group of late lavas which define the extent of the central zone 2. From the evidence presented in the text it is concluded that these lavas were clearly extruded after seafloor spreading between Rockall Plateau and East Greenland had become established, and are consequently younger than the pre-rift and post-rift structures which they overlie to the south-east and north-west respectively. The structure of each zone is described separately, and interpreted in terms of three structural sequences. The continental sequence is defined as the crust composed of the pre-rift lavas and generally seaward-dipping reflectors to the south-east, the oceanic sequence as the post-rift oceanic crust to the north-west of the reconstructed position of anomaly 24B, and the late sequence as the post-rift igneous group defining the extent of zone 2 formed as the result of post-rift igneous activity.

**Zone 1.** This is the most landward zone, and occurs on the upper continental slope and shelf of Hatton Bank. The acoustic basement in this zone is generally smooth, with little or no associated sediment cover. The basement of zone 1 forms the continental sequence; within this sequence weak reflectors are sub-parallel and conformable with the acoustic basement. On SAP 2 between CMPs 1750 and 1800

at 0.4 s sub-basement TWT, more steeply north-westerly dipping events are evident. These are relatively weak, and die out at CMP 1750. They are unconformable with the overlying sub-parallel reflectors, but the surface of unconformity separating the two reflector series is not clearly visible. The nature of the implied unconformity remains unclear ; there appear to be no overlying reflectors which would make it possible that the dipping events correspond to reverberations within an upper layer, and similar features are not evident in corresponding positions on adjacent SAPs. It is possible that the structures represent two lava successions, the first extruded on to continental basement which were subsequently tilted to the north-west and eroded prior to extrusion of the second which form the upper sub-parallel reflectors. The sub-parallel reflectors become more diffuse on SAP 3, and are barely visible on SAP 4, reflecting the relatively low signal:noise ratio of these sections relative to SAPs 1 and 2. This effect was presumed due to the increased acoustic impedance of the seafloor in regions of thin or absent sedimentary cover. Irregularities in the basement of SAP 4 at CMPs 1900 and 1600 correspond to distinct anomalies in the magnetic data recorded along the SAP profiles (chapter 5, figure 5.14b), which imply localised dyke intrusion.

Zone 1 displays the short-wavelength, high-amplitude magnetic anomalies inferred in chapter 5 as originating from a volcanic basement. The smooth basement with underlying sub-parallel internal layering associated with irregular, high-amplitude magnetic anomalies is consistent with the presence of nearly flat-lying lavas overlying continental crust. The strong seafloor multiple train within zone 1 on all SAPs obscures any underlying reflecting horizons. Therefore the base of the proposed lavas was not observed, and consequently their thickness cannot be estimated from the SAP profiles.

Synthetic seismogram modelling at ESP1 within zone 1 revealed a velocity-depth structure (figure 6.8) which was interpreted as typical of continental crust (White *et al.*, 1986 ; 1987). Assuming upper continental crustal velocities of approximately  $6.0 \text{ km s}^{-1}$  (eg Smith & Bott, 1975), the velocity structure determined at ESP 1 can be used to obtain a rough estimate of the possible thickness of lavas overlying the continental basement of zone 1. The crustal velocity-depth model of White *et al.* (1986) shows velocities rising to  $6.0 \text{ km s}^{-1}$  at a depth below seafloor of approximately 7.0 km. A shallower interface at 3.5 km below seafloor, separating underlying  $5.6 \text{ km s}^{-1}$  material from overlying  $5.1 \text{ km s}^{-1}$  material, may alternatively represent the base of the lavas. Thus a thickness of between 3.5 and 7.0 km of lavas is implied by the crustal velocity structure. This is consistent with the results of the interpretation of seismic reflection profiles (Roberts *et al.*, 1984) and gravity modelling (Roberts & Ginsburg, 1984), allied with the results of DSDP operations on the south-west Rockall Plateau, which imply lava thicknesses of up to 6 km in a region of comparable basement.

**Zone 2.** The general structure of zone 2 is similar on all four SAPs. To the south-east, a sequence of seaward-dipping reflectors can, on closer inspection, be divided into an upper sub-series corresponding to late sequence reflectors, and an underlying sub-series corresponding to the oceanward continuation of the continental sequence comprising the basement of zone 1. This structure is best displayed on SAP 1 between CMPs 250 and 600. A north-western reflector sequence can similarly be subdivided in to upper and lower subseries corresponding to late sequence reflectors and the landward continuation of the zone 3 oceanic sequence reflectors respectively. This structure is well developed on SAP 2 between CMPs 600 and 900. The two reflecting sequences of zone 2 are separated by a central opaque region con-

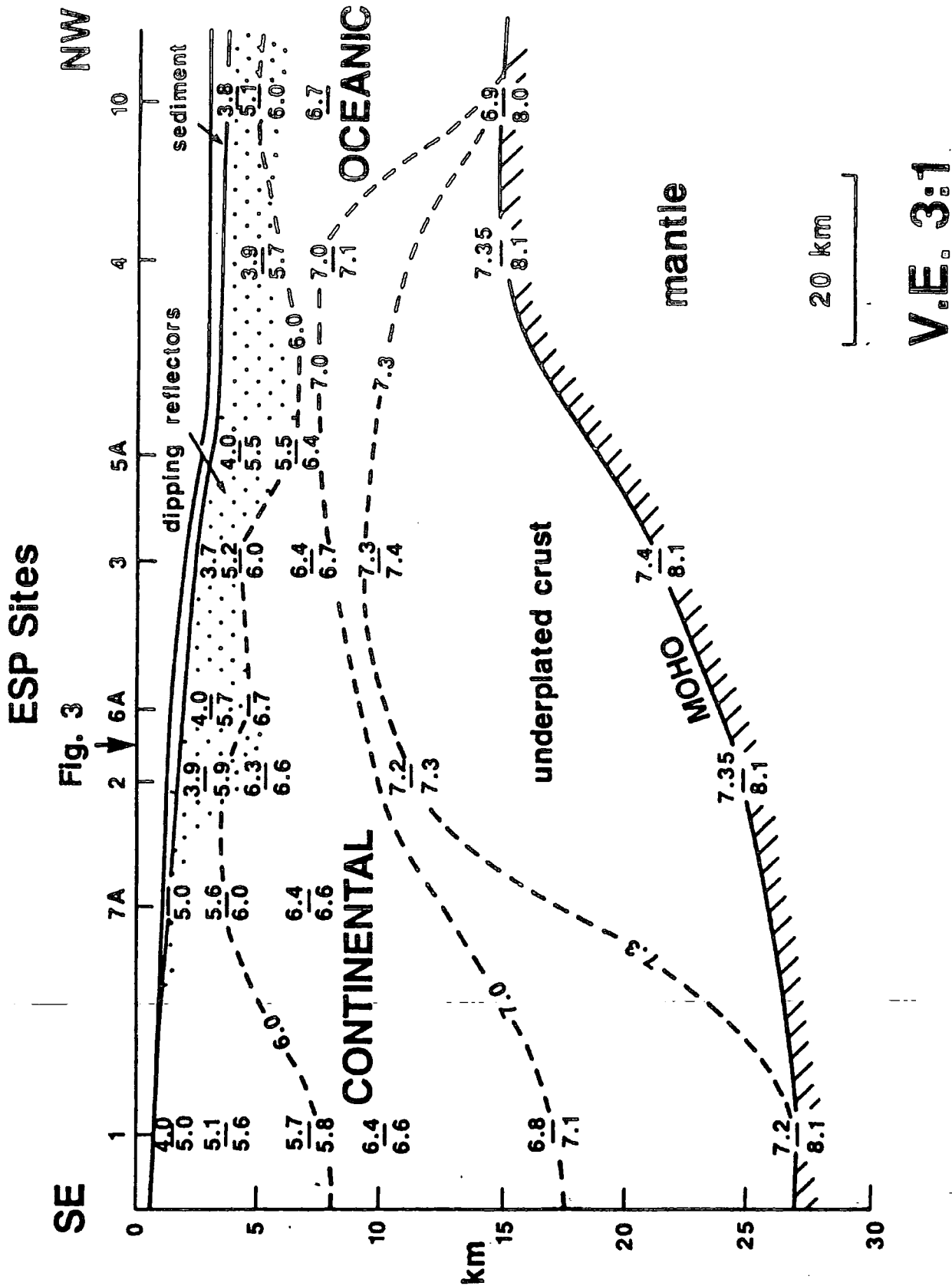


Figure 6.8 Isovelocity contour section across Hatton Bank margin. Velocities in  $\text{km s}^{-1}$ , isovelocity contour levels 6.0, 7.0, 7.3  $\text{km s}^{-1}$ . (Reproduced from White *et al.*, (1986)).

taining few reflectors. However, the detailed structure of zone 2 varies along strike, and consequently is described separately within each SAP.

**SAP 1.** A south-eastern seaward-dipping reflector sequence is well developed in zone 2 of SAP 1 between CMPs 250 and 600. The acoustic basement associated with this sequence is smooth, below a sediment layer thickness of up to 0.7 s TWT. Individual reflectors are planar with seaward dip, and exhibit a general down-dip increase in reflector separation. As a result the unit thickens by up to three times oceanwards and has a consequent wedge or fan shape. There is no clearly observed horizon defining the base of the sequence. Individual reflectors instead become weaker and impersistent with depth in the section, finally merging with and being obscured by the seafloor multiple train. The wedge has a seaward limit at approximately CMP 600, where it passes into an opaque region exhibiting few reflectors.

Detailed examination of the reflectors within the south-eastern sequence reveals that it can be sub-divided into upper and lower oceanward-dipping reflector sub-series corresponding to the late sequence which overlies the oceanward continuation of the continental sequence of zone 1 respectively. The acoustic basement of zone 1 appears to dip below the late sequence reflectors at CMP 250, with an unconformity separating late and continental sequences. The dip of the unconformity is approximately  $7^{\circ}$  at CMP 350. Individual reflectors within the late sequence appear to onlap gently towards the south-east, and exhibit dips which range up to approximately  $7^{\circ}$  at the underlying unconformity. Reflectors below the unconformity are gently cross-cut, and appear to converge gradually up-dip, where they form the volcanic basement of zone 1. These reflectors have dips which range from about  $7^{\circ}$  at the overlying unconfor-

mity, to a maximum of  $20^{\circ}$  at their deepest point of observation. Near their seaward termination, the late sequence appears to up-turn towards the west, becoming more confused and discontinuous, and finally being lost in the opaque region. In contrast, the continental sequence reflectors show no sign of up-turning at their oceanward limit. These continue as planar reflectors, finally being obscured at depth in the section by the relatively strong seafloor multiple train, or fading into the opaque region at their seaward limit.

The central opaque region of SAP 1 forms an extensive feature between CMPs 650 and 1000. It is characterised by an irregular, "hummocky" acoustic basement beneath which discontinuous reflectors of varying dip are evident at shallow depth, which become less apparent with depth. The opaque region forms an area of up-standing basement relief relative to the regions to the south-east and north-west.

North-west of the central opaque region, extending from CMP 1000 to the oceanward limit of zone 2, lies a region of irregular, diffractive basement with short, discontinuous, sub-horizontal reflectors which extends to a depth in the section of 4 s TWT. Below 4 s TWT, reflectors dip oceanwards, and appear unconformable with those above. There is no clearly visible unconformity on SAP 1 separating the two reflector groups. Individual reflectors within the lower group are also discontinuous in nature, forming short segments which combine to give an overall seaward-dipping aspect, with no clearly observed base. This north-western dipping reflector sequence appears to form the landward continuation of the dipping reflector sequence which extends oceanwards to form the sub-sedimentary oceanic sequence of zone 3.

The magnetic anomaly profile recorded along SAP 1 (figure 5.14a) show a large 800 nT positive peak associated with the transition from the south-eastern dipping

reflector sequence into the opaque central region. Oceanwards this falls to near zero at CMP 950, remaining so until the oceanward limit of zone 2 is reached at CMP 1150. There is no evidence of anomaly 24B at its reconstructed position of CMP 1100 on SAP 1. The large positive anomaly corresponds to the arcuate, high amplitude positive anomaly identified in chapter 5 (figure 5.5), which lies approximately 20 km seaward of the reconstructed anomaly 24B position, and is inferred (chapter 5) to result from post-rift igneous activity rather than from seafloor spreading. Landward of the large positive peak is a negative -300 nT trough which corresponds to the feather-edge of the late sequence dipping reflectors to the south-east of the central opaque zone.

**SAP 2.** The general structure of zone 2 within SAP 2 is similar to that observed on SAP 1, consisting of reflector sequences to the south-east and north-west of an opaque, poorly-reflecting region.

The south-eastern dipping reflector sequence is not as well developed as on SAP 1, with individual reflectors lacking continuity. Basement associated with this sequence is smooth, below a sediment thickness of up to 0.5 s TWT. As on SAP 1 this sequence is divisible into an upper and lower dipping reflector sub-series corresponding to the late and continental sequences respectively, separated by an unconformity corresponding to the basement of zone 1. At CMP 1500 a distinct "hump" in the basement is interpreted as representing the landward limit of the late sequence dipping reflectors. The basement of zone 1 forms an unconformity separating late and continental sequences, which dips oceanward at an angle of about  $7.5^\circ$  at CMP 1350. Reflectors within the late sequence are not as planar as those of SAP1, displaying a gentle downward convexity, and appearing to onlap the unconformity to the south-east. Those within the lower continental sequence are



discontinuous in appearance, consisting of short dipping segments which combine to produce the observed overall dipping structure. They are gently cross-cut by the unconformity separating them from the late sequence reflectors. Reflectors within the sequence have maximum observed dips of up to  $20.5^{\circ}$ . These flatten out landwards, to merge with the sub-parallel reflectors of zone 1.

The south-eastern dipping reflector sequence as a whole is terminated at CMP 1100 by the opaque central zone which extends to CMP 900. This region is less extensive than on SAP 1, and does not form such an elevated basement high relative to the south-eastern dipping reflector sequence. The zone is slightly more reflective than on SAP 1, exhibiting short reflecting segments; however, these are few, and do not correlate with those outside the opaque zone, implying a chaotic internal structure.

The opaque zone is terminated on SAP 2 at CMP 900 by the abrupt appearance of a strong reflector at just over 4 s TWT, which can clearly be followed oceanwards to CMP 600 where it appears to form a continuation of the acoustic basement of zone 3. This is a distinct unconformity, separating the overlying conformable late-sequence lavas from the underlying seaward-dipping reflectors of the oceanic sequence. The strongly reflecting intra-crustal horizon exhibits a gentle *continentwards* dip of approximately  $2^{\circ}$ .

The reflectors which underlie this horizon display the gentle upward convex appearance with down-dip increase in reflector separation and dip described by Mutter *et al.* (1982) as characteristic of formation within a subaerial seafloor spreading environment (chapter 7). The deepest reflectors within the sequence have maximum observed dips of  $23^{\circ}$ , and flatten continentwards to conform with the strong over-

lying reflector which marks their top surface. Later overlying reflectors offlap to form a seaward prograding sequence. Their upper surface is therefore an unconformity represented by the strong intra-crustal horizon. As on SAP 1 these dipping reflectors form the continentward continuation of the oceanic basement sequence observed in zone 3.

Overlying the strong intra-crustal horizon is a thick wedge of material extending from CMP 900 to CMP 600 where it is terminated by an abrupt basement step. The wedge exhibits clear internal acoustic stratification. Individual reflectors conform with the strong, intra-crustal horizon at their base, with layers thinning oceanwards to create the observed wedge-shaped structure. The layers within the wedge therefore display a range of dips from a continentward dip of  $2^{\circ}$  at the underlying unconformity, to an oceanward dip of  $1^{\circ}$  at the top of the wedge. Thus the strong intra-crustal horizon forms a distinct unconformity separating the overlying south-eastward thickening late sequence wedge from the underlying dipping reflectors of the oceanic sequence.

Zone 2 on SAP 2 corresponds to the region of arcuate, high amplitude magnetic anomalies described in chapter 5 (figure 5.5). In addition, SAP 2 passes close by the large local anomaly qualitatively interpreted in chapter 5 as originating from two adjacent intrusions having normal and reverse magnetisations. Projection of the position of this anomaly perpendicularly on to SAP 2 indicates that its centre approximately corresponds to CMP 1000, coincident with the centre of the opaque region. This suggests that the abrupt truncation of the strong intra-crustal unconformity at CMP 900, and the formation of the opaque zone, may be a result of the same intrusive igneous activity which was inferred in chapter 5 to have formed the large local anomaly and zone of high amplitude, arcuate anomalies. The recon-

structed anomaly 24B position on SAP 2 lies within zone 2, and corresponds to the position in the section where the deepest horizon within the oceanic dipping reflector sequence underlying the strong intra-crustal unconformity reaches its deepest observable point. No anomaly corresponding to anomaly 24 can be discerned in this vicinity. Magnetic anomaly data recorded along SAP 2 (chapter 5, figure 5.14a) shows a negative -300 nT trough at CMP 1500 corresponding to the landward feather-edge of the late sequence reflectors to the south-east of the opaque zone. This is succeeded oceanward by a positive 500 nT peak at CMP 1175 associated with the transition from the landward late-sequence seaward-dipping reflectors into the central opaque zone. Between CMPs 1100 and 600, an approximately constant magnetic anomaly of 300 nT is observed.

**SAP 3.** The zone 2 structure of SAP 3 is similar, but less well developed to that described on SAPs 1, and 2, with a south-eastern and north-western reflector sequence separated by an intermediate relatively opaque region.

The south-eastern seaward-dipping reflector sequence is divisible into upper late and lower continental sequences by an unconformity which forms the acoustic basement of zone 1. This can be seen to dip below the upper late sequence at CMP 650. Reflectors comprising both sequences appear planar with seaward dip, with the late sequence thickening towards the north-west. The underlying continental sequence displays little sign of thickening, with sub-parallel reflectors forming an oceanward continuation of the continental sequence of zone 1, and displaying dips of up to  $10^\circ$  at CMP 1100. The unconformity separating the two sequences is difficult to locate exactly. However, horizons within the lower continental sequence may be gently cross-cut by the implied unconformity surface, whereas those within the upper sub-series appear to onlap gently towards the south-east in a similar manner to

the structure of SAPs 1 and 2. The base of the sequence is not seen, and reflectors become weaker to fade out with depth in the section.

The opaque zone occurs between CMPs 1150 and 1350. This exhibits a reflective character for 1.5 s below acoustic basement, with individual reflectors in continuity with those of the late sequence to the south-east. In contrast, the lower continental sequence passes into the opaque zone at about CMP 1150. Oceanwards from CMP 1350, the upper reflective region of the opaque zone passes into a region of sub-horizontal reflectors which converge oceanward to CMP 1600, forming a wedge-shaped structure similar to that observed on SAP 2. Underlying this region is a zone of very weak reflectors which are sub-horizontal at their continentward limit of CMP 1400, and which dip increasingly oceanwards, suggesting a structure similar to that observed underlying the intra-crustal unconformity on SAP 2 between CMPs 900 and 600. However, the acoustic basement in this area is highly irregular and diffractive, and the resulting diffraction hyperbolae obscure the details of the underlying structure.

Magnetic anomalies associated with zone 2 of SAP 3 display similar characteristics to those of SAPs 1 and 2. A large positive peak at CMP 950 is flanked landward by a -300 nT trough associated with the landward limit of the upper late sequence dipping reflectors (figure 5.14b). The large positive anomaly corresponds to the arcuate positive anomaly identified from the magnetic contour map (chapter 5, figure 5.5). Reconstructions place the expected anomaly 24B position within zone 2 at CMP 1500; no sign of this is evident in the magnetic anomaly data recorded along SAP 3.

**SAP 4.** Zone 2 is approximately 30 km wide on SAP 4, substantially narrower

than on SAPs 1, 2, and 3, and exhibits the least well-developed structure. At its landward limit, a sequence of weak oceanward-dipping reflectors can be divided into upper late and lower continental reflector sequences by the acoustic basement of zone 1 which dips below the late sequence at CMP 1250. Reflectors within the late sequence are planar at the south-eastern extreme of zone 2, and pass north-westwards into a region of undulating reflectors which are terminated by a basement step at CMP 650 (similar to that observed on SAP 2 at CMP 600). This corresponds to the oceanward limit of zone 2 on SAP 4. The lower continental sequence reflectors are poorly developed, but appear to dip gently oceanwards between CMPs 1400 and 1250. The opaque zone appears to be absent on SAP 4.

The magnetic anomaly pattern within zone 2 of SAP 4 is similar to that observed on SAPs 1, 2, and 3, with a negative -100 nT trough corresponding to the landward termination of the upper late sequence dipping reflectors flanked oceanward by a large 600 nT positive anomaly corresponding to the high amplitude arcuate positive anomaly described for the other SAPs, and in chapter 5 (figure 5.5). An additional -200 nT trough is observed, centred on CMP 900, coinciding with the undulating reflectors of zone 2, which is continuous along strike (figure 5.5). Reconstructions place anomaly 24B coincident with the oceanward limit of zone 2 at CMP 650. A positive peak oceanward of this position may represent part of anomaly 24A not erased by the subsequent igneous activity which does not appear to have been as vigorous on SAP 4 as on other SAPs. However, anomaly 24B cannot be recognised in its reconstructed position.

**Zone 3.** Zone 3 on all SAPs consists of the region of crust beyond the foot of the continental slope which contains the oceanic sequence of seaward-dipping reflectors. Since these reflectors are developed to varying degrees along margin strike, the zone

is briefly described separately for each SAP.

The oceanic dipping reflector sequence of zone 3 is best displayed on SAP 2 where individual reflectors exhibit the arcuate, gentle upward-convex appearance, with down-dip increase in dip and reflector separation observed to be characteristic of formation within a subaerial seafloor spreading environment (Mutter *et al.*, 1982). The oceanic acoustic basement dips gently oceanwards, becoming gradually rougher and more indistinct. Occasional disrupted regions of basement are characterised by diffraction hyperbolae which to some extent obscure the underlying structure. Consequently the oceanic dipping reflector sequence appears to be poorly developed in some areas. Although easily recognised, individual reflectors within the oceanic dipping sequence of zone 3 appear irregular and discontinuous. This is in contrast to their landward continuation into zone 2 between CMPs 600 and 900, where they are relatively smooth and persistent. A similar, but less well developed structure is evident in zone 3 of SAP 3. Reflectors are generally weaker and more impersistent than those of SAP 2, but form a distinct seaward-dipping sequence between CMPs 1750 and 2000. Landward and oceanward of this region, the reflectors are less well developed, possibly due to the presence of diffraction hyperbolae originating from disrupted regions of acoustic basement (eg. between CMPs 1675 and 1750, SAP 3). SAP 1 exhibits a poorly developed seaward-dipping sequence between the landward limit of zone 3 and CMP 1350. Oceanward from CMP 1350, isolated, weak north-westerly dipping reflectors are present. These are discontinuous and difficult to correlate laterally. SAP 4 exhibits the least well-developed zone 3 structure. A weak seaward-dipping sequence is evident between the landward extreme of zone 3 and CMP 525, oceanward of which few consistent coherent reflectors are present. Sub-parallel layering between CMPs 100 and 300 appears to fade laterally, and may

correspond to reverberations within the overlying sediment layer.

On all SAPs the dip of individual reflectors within zone 3 tends to shallow continentwards to become nearly horizontal where they terminate against acoustic basement. The base of the dipping sequences is not seen. Reflectors become progressively more indistinct and discontinuous with depth.

The magnetic anomaly pattern within zone 3 corresponds to the wide positive anomaly observed on the magnetic anomaly map (figure 5.5). Reconstructions place the expected anomaly 23 position within zone 3 coinciding with the oceanward portion of this wide positive anomaly (chapter 5, figure 5.12). The best developed dipping reflector sequences within zone 3 occur on SAPs 2 and 3, where they coincide on the magnetic anomaly map with a 300 nT plateau within the wide positive anomaly (figure 5.12). In contrast, SAPs 1, and 4 exhibit weakly developed dipping reflector sequences within zone 3, which coincides with a region of relatively low amplitude positive magnetic anomalies flanking the 300 nT plateau associated with SAPs 1, and 2. The development of this anomaly may thus correlate with the good development of extensive dipping reflectors within zone 3.

The velocity/depth structure within the crust of zone 3 as determined by synthetic seismogram modelling of ESPs 4 and 10 (figure 6.8) was interpreted as consistent with that of thick oceanic crust (White *et al.*, 1986; 1987). The reconstructed anomaly 24B and 23 positions are consistent with the conclusion that the crust of zone 3 is oceanic.

### 6.3 Basement velocity structure.

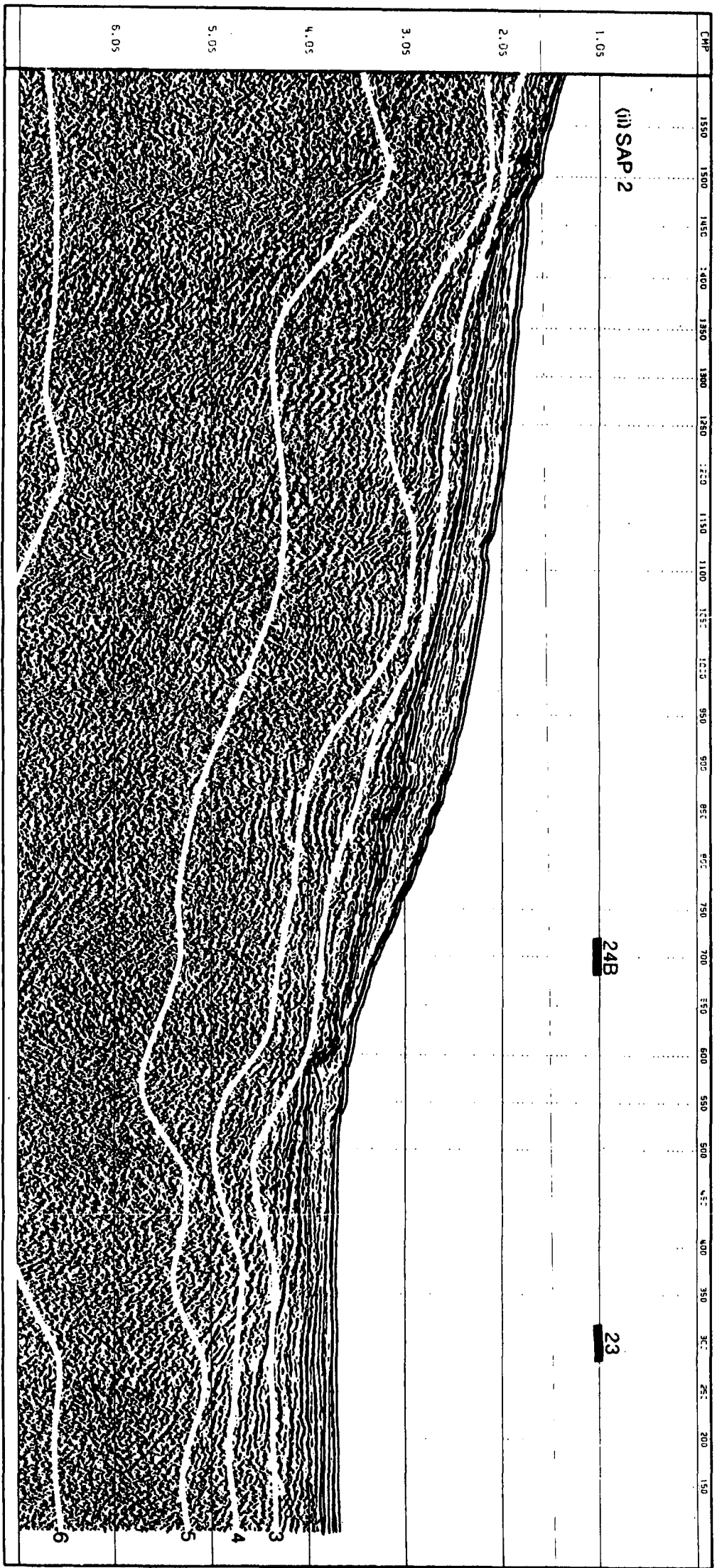
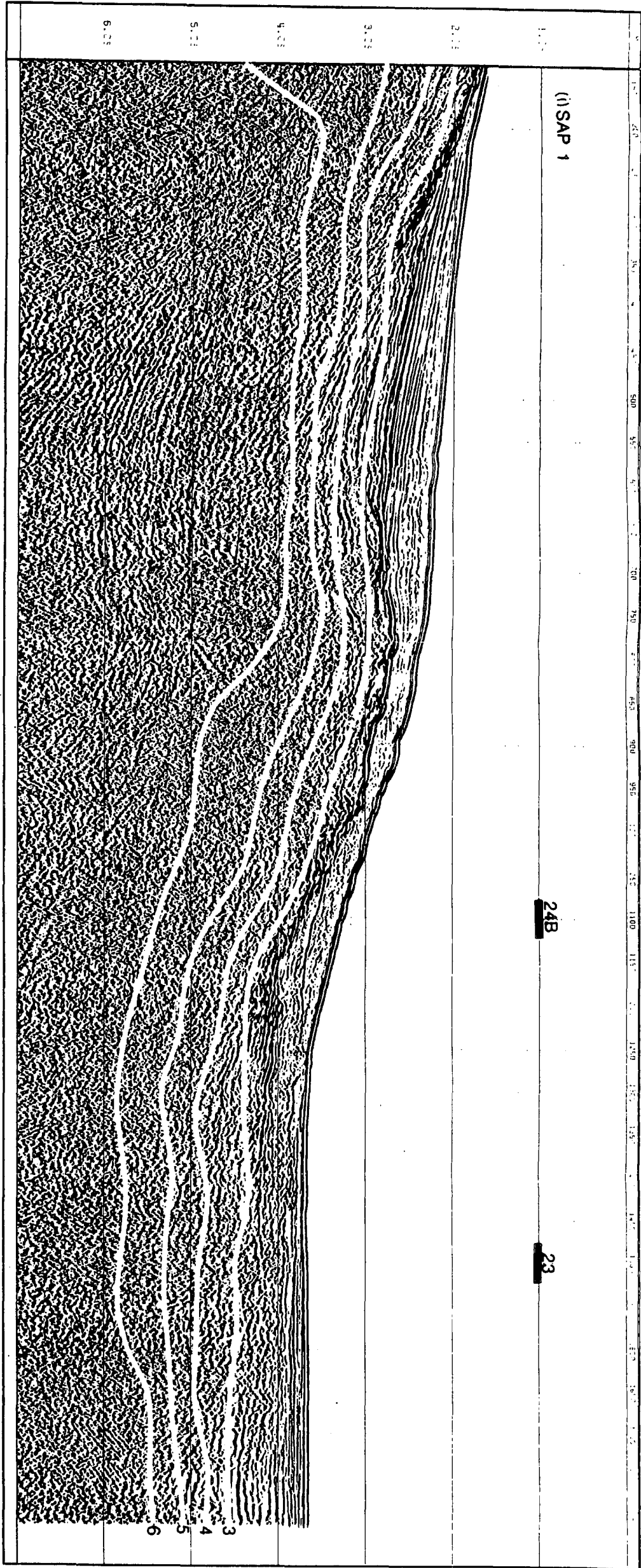
Velocity analysis of the four SAPs provided a suite of stacking velocities as a function of two-way-traveltime (TWT) across the entire margin. These were converted to interval velocity as a function of TWT using the Dix equation (1955) (chapter 3) and, in conjunction with the results from synthetic-seismogram modelling of two-ship ESP data, used to examine the crustal velocity structure of the Hatton Bank continental margin.

The interval velocities were contoured as a function of TWT and CMP position using the SURFACEII contouring package (Sampson, 1975), and the resulting contour plots were superimposed on section plots at the same horizontal and vertical scales (figure 6.9a,b). From this figure it can be seen that the velocities within the dipping reflector sequences generally range from  $3.0 \text{ km s}^{-1}$  at the top, to  $6.0 \text{ km s}^{-1}$  at the base, although some reflectors are seen to penetrate deeper than the  $6.0 \text{ km s}^{-1}$  contour. The isovelocity contours do not follow individual reflectors, but approximately conform with acoustic basement. Velocities increase fairly sharply with TWT to  $6.0 \text{ km s}^{-1}$ , below which the velocity gradient is less steep. The sharp increase in velocity with depth is attributed to the closing of pores and microcracks as confining pressures increase with depth. These results are in agreement with the ESP-defined velocity structure (figure 6.10) which indicates velocities increasing from  $3.5 \text{ km s}^{-1}$  to  $6.0 \text{ km s}^{-1}$  within the dipping reflector sequences (White *et al.*, 1986; in press). Interpretation of the ESP velocity structure additionally showed that the upper portion can be modelled by alternate high and low velocity 100 m thick layers (figure 6.10), which may represent individual lava flows intercalated with layers of volcanic debris and rubble. The layers of alternating velocity were not resolved by SAP velocity analysis.



Figure 6.9(a) Crustal interval velocity structure derived from SAP velocity analysis stacking velocities.

- (i ) SAP1.
- (ii ) SAP2.



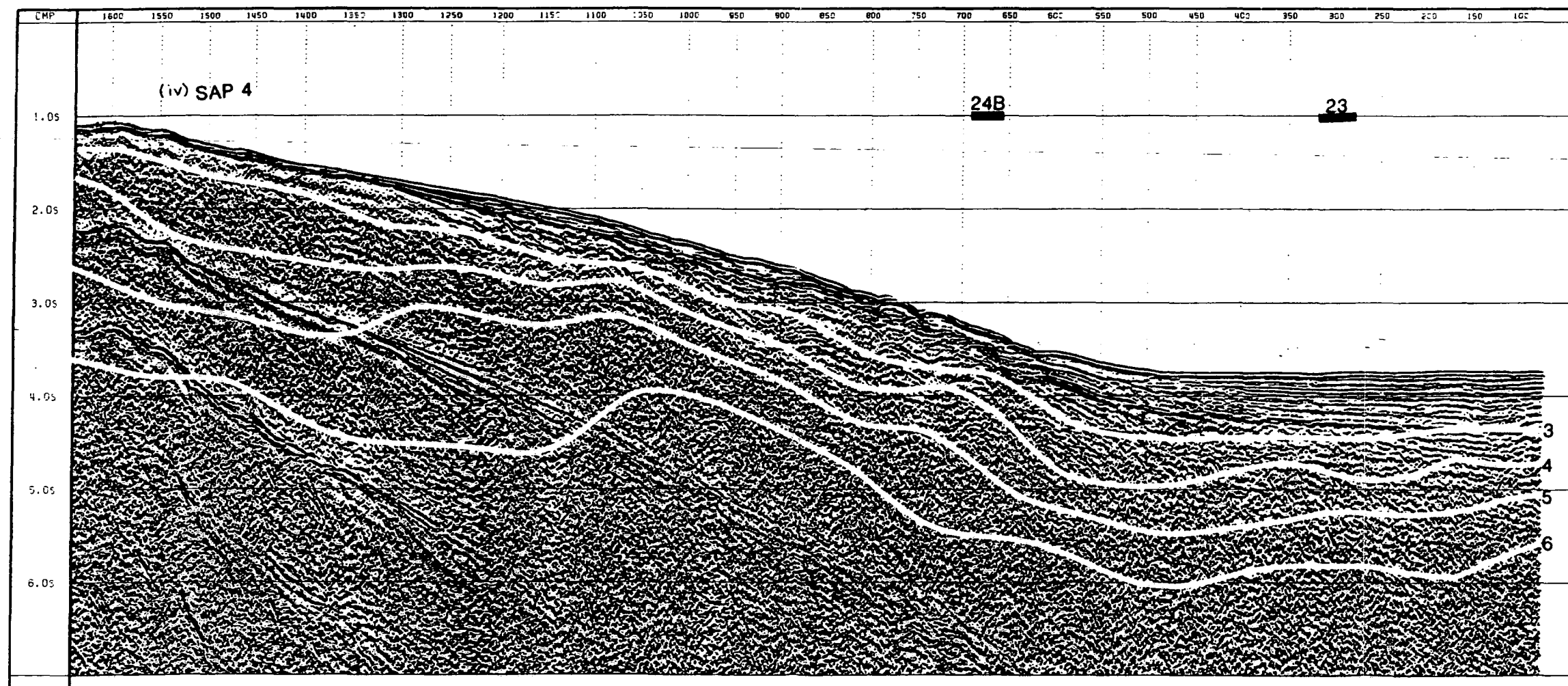
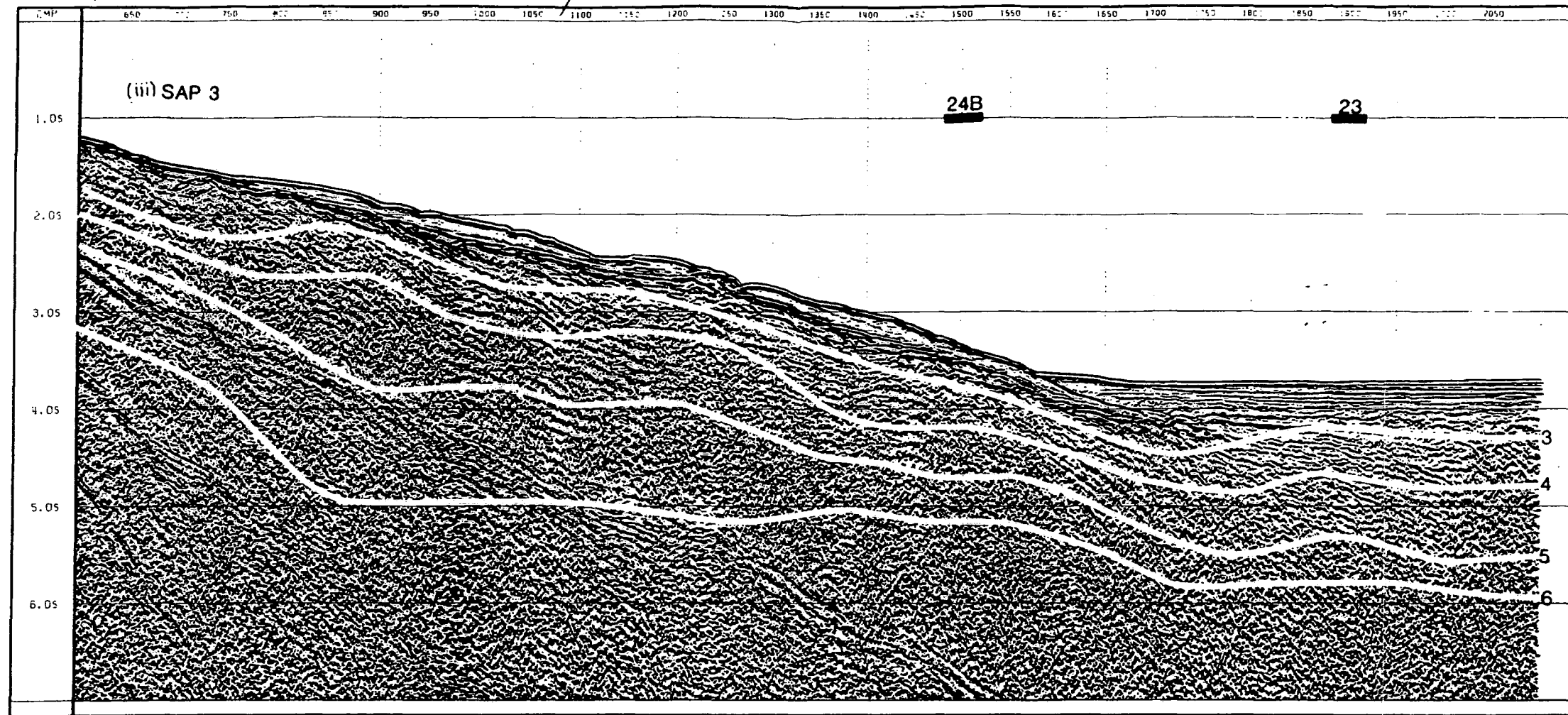


Figure 6.9(b) Crustal interval velocity structure derived from SAP velocity analysis stacking velocities.

(iii) SAP3.

(iv) SAP4.

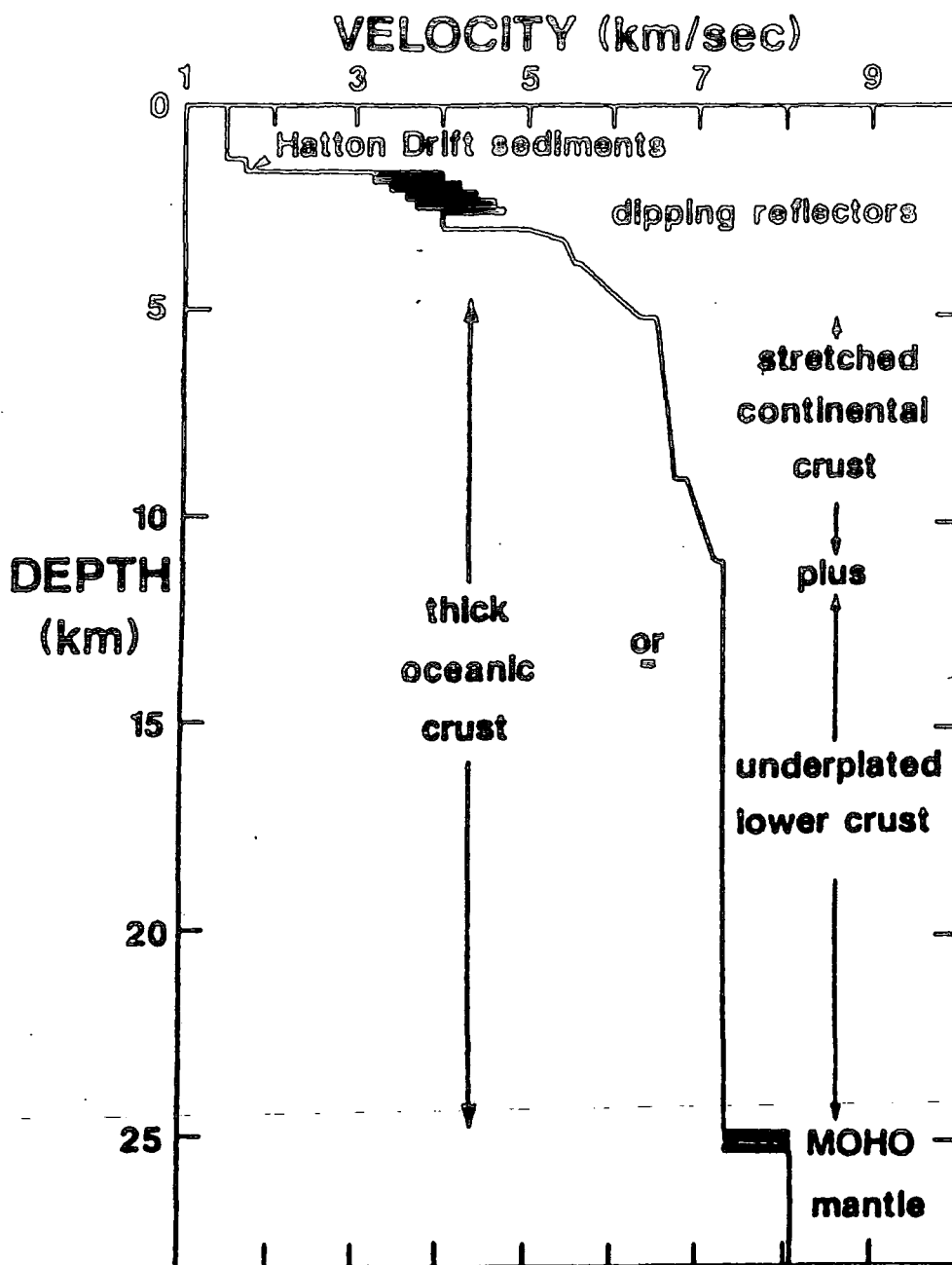


Figure 6.10 Generalised ESP velocity structure reproduced from White *et al.*, (1986). Location shown in figure 6.8. Upper structure from ESP6a, deep structure from ESP2.

The velocities within the late/continental and oceanic dipping reflector sequences were compared to determine whether these could be distinguished on the basis of their velocity structure. A program (CMPENV\_FOR, appendix A) was written which searched velocity files for CMPs within a specified range. These were stacked on a single plot of interval velocity as a function of sub-basement TWT, yielding a velocity envelope representing the sub-basement velocity function variation within the CMP search range. CMP ranges were defined to span approximately comparable regions on SAP sections exhibiting dipping reflectors. An additional option incorporated into the program was the facility to superimpose an appropriate ESP velocity function for further comparison (e.g. figure 6.11). The velocity envelopes from late/continental and oceanic dipping reflector sequences were superimposed to enable their direct comparison.

Figures 6.12-6.13 indicate no consistent differences in the velocity structures the two dipping reflector sequences. Velocities within the sequences appear to increase with depth in a similar fashion down to approximately  $6.0 \text{ km s}^{-1}$ . This separation of the velocity envelopes at  $6.0 \text{ km s}^{-1}$  is due to differences in the underlying crustal type resolved by ESP velocity determinations described in chapter 4, section 4.3.2.

Along-strike comparisons reveal a similar uniformity of velocity structure within the oceanic sequence of dipping reflectors (figure 6.14b). This result is consistent with the interpretation of normal incidence seismic reflection profile NI3 along margin strike (figure 6.15) which exhibits a corresponding lateral continuity within the oceanic dipping reflector sequences (White *et al.*, 1987). The location of NI3 is shown on SAPs 1, 2, and 3. The velocity envelope representing the oceanic sequence dipping reflectors is in agreement with the ESP4 velocity model obtained at a comparable location on all four SAPs.

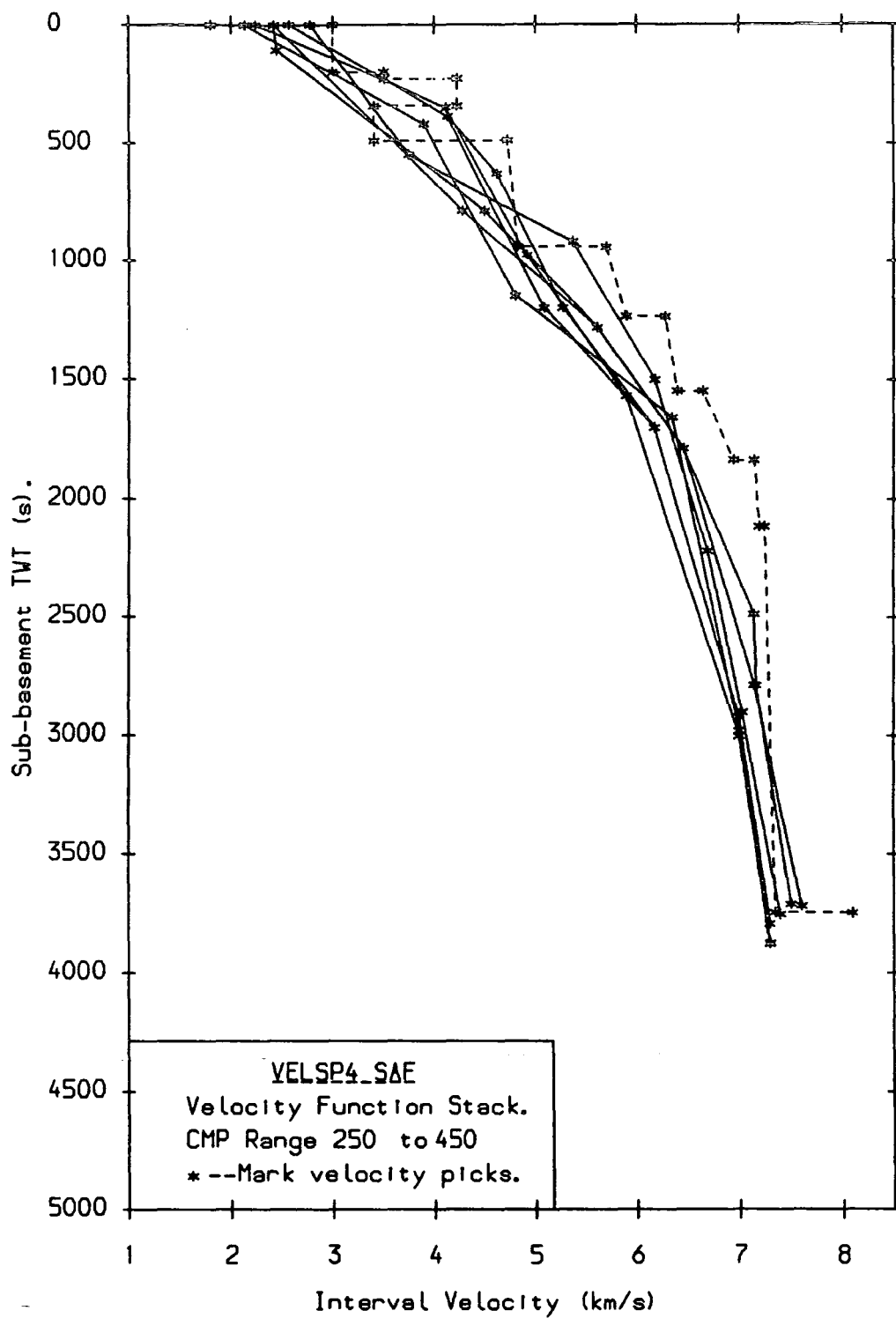
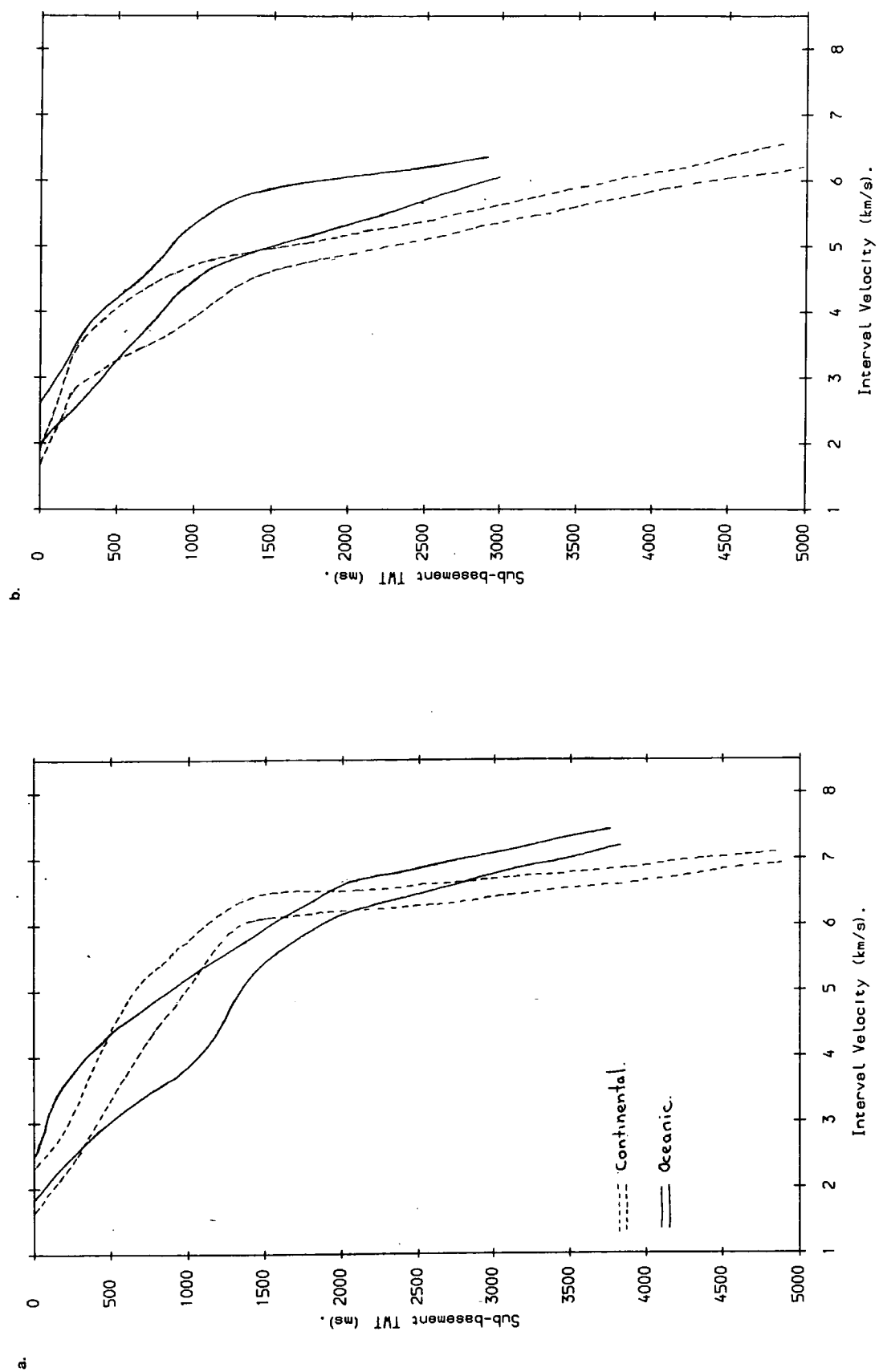
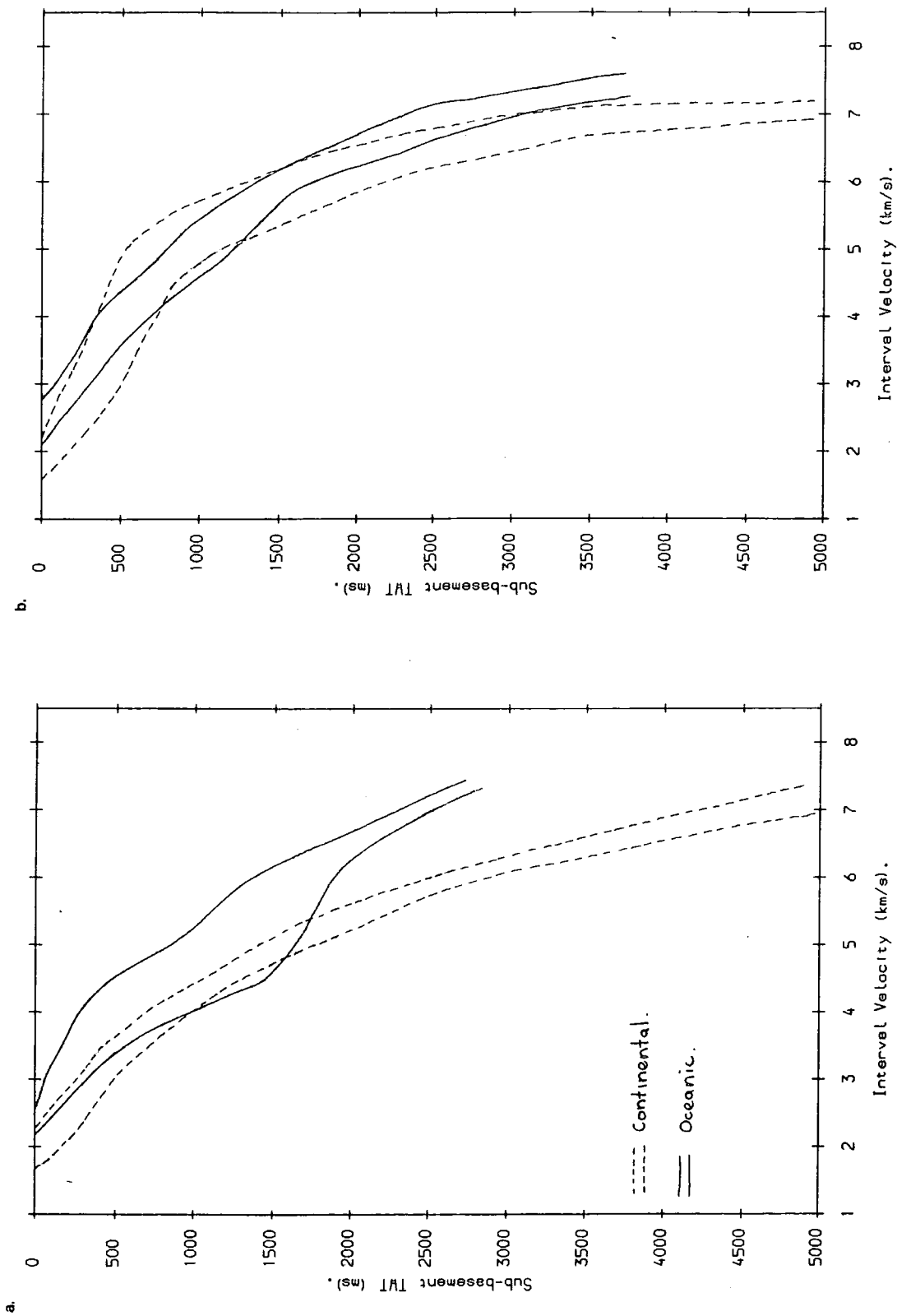


Figure 6.11 Example plot of interval velocity as function of sub-basement two-way-traveltime (ms). Location SAP4, CMPs 250-450. ESP4 velocity function superimposed.



**Figure 6.12** Cross-strike dipping reflector velocity function comparison. Superimposed interval velocity envelopes from continental and oceanic dipping reflector sequences:

- (a) SAP1
- (b) SAP2.



**Figure 6.13** Cross-strike dipping reflector velocity function comparison. Superimposed interval velocity envelopes from continental and oceanic dipping reflector sequences:

(a) SAP3

(b) SAP4.

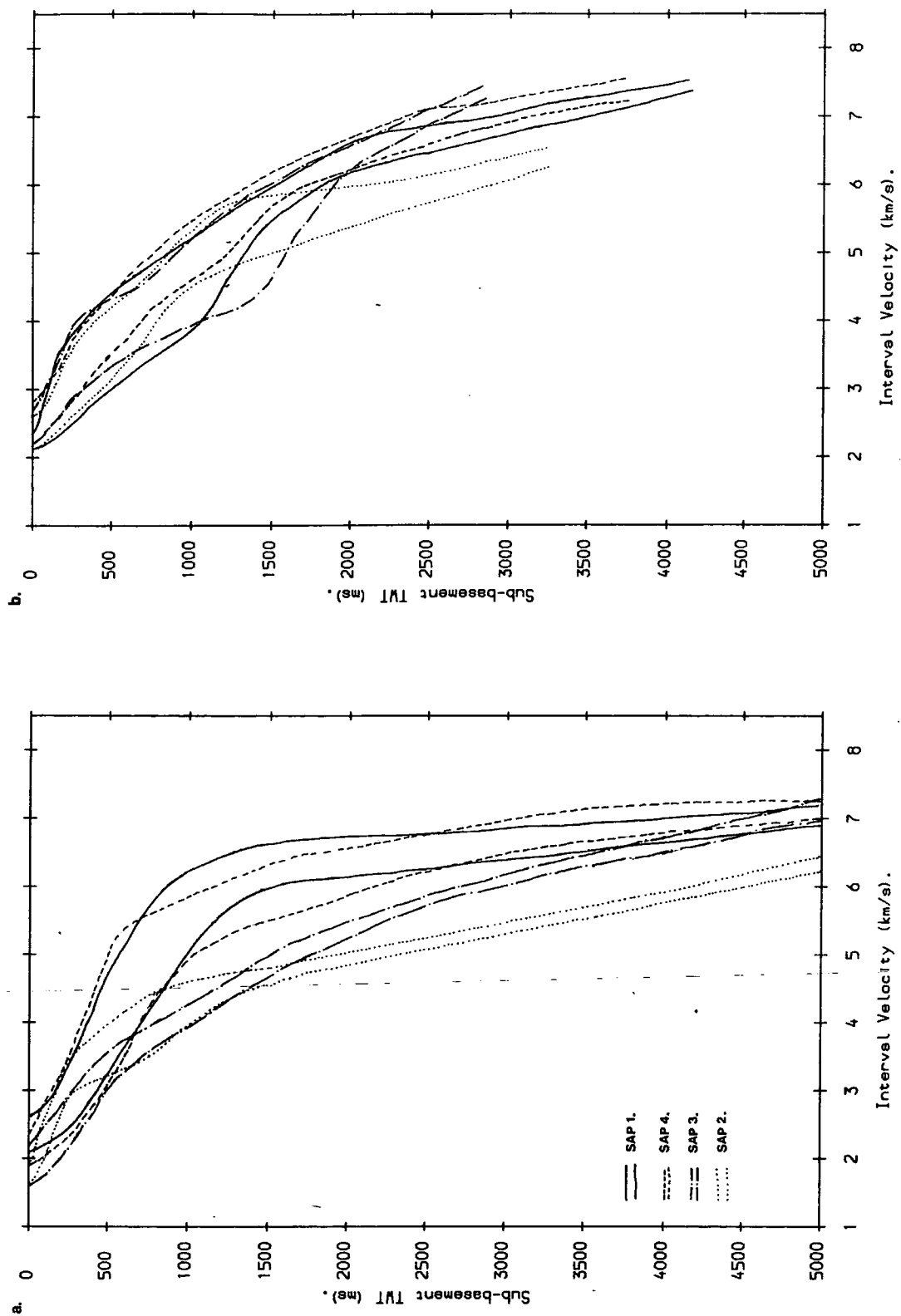
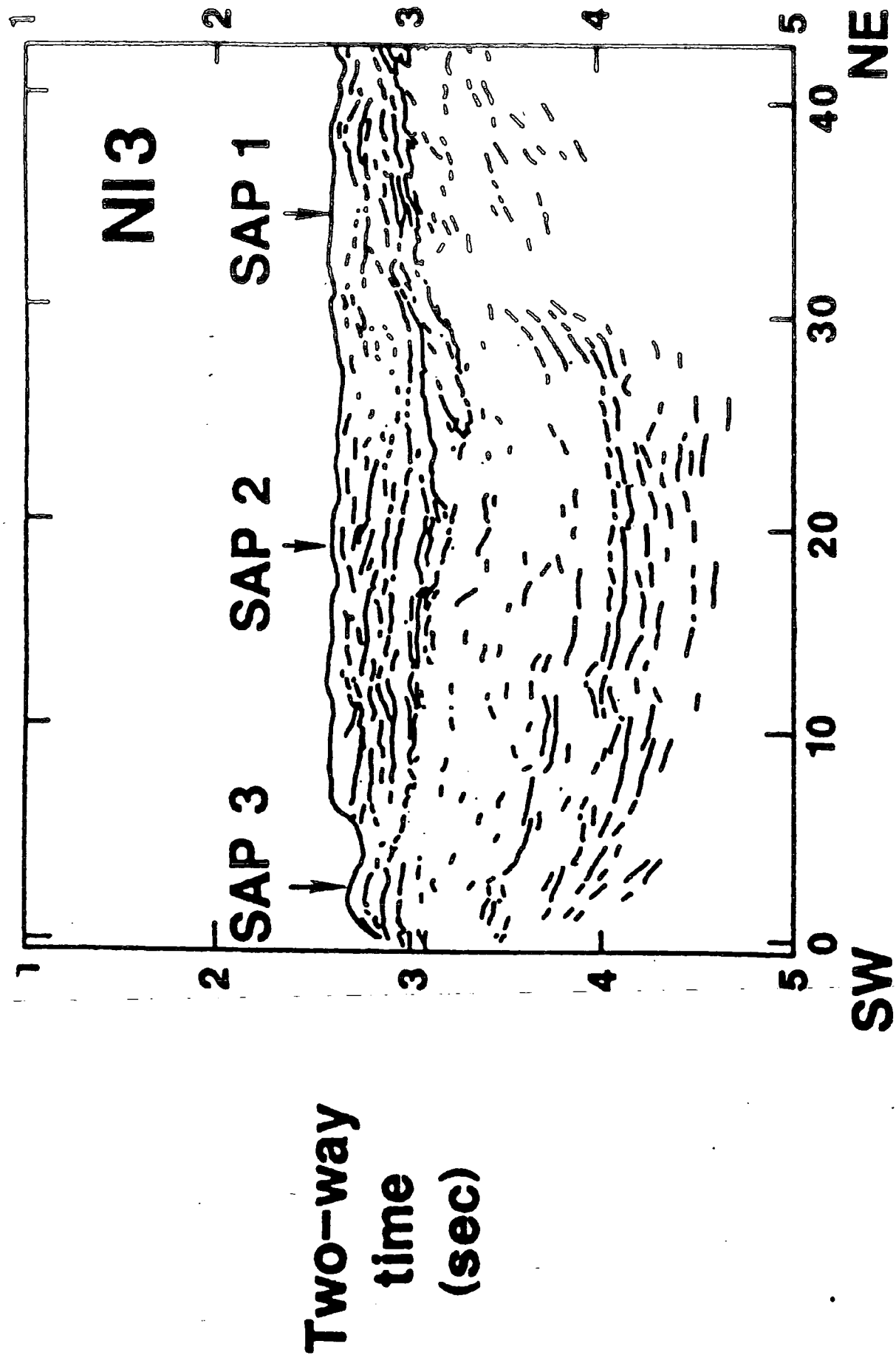


Figure 6.14 Along-strike dipping reflector velocity function comparison. Superimposed velocity envelopes from SAPs 1, 2, 3, & 4.

(a) Continental dipping reflector sequence.

(b) Oceanic dipping reflector sequence.





**Figure 6.15** Line drawing interpretation of normal-incidence MCS line NI3. Illustration of along-strike continuity of oceanic sequence dipping reflectors. Locations shown in figure 1.13. (Reproduced from White *et al.*, (1987)).

Similar comparisons of the late/continental sequence dipping reflectors (figure 6.14a) reveal an apparent along-strike variation in velocity structure. SAPs 1 and 4 exhibit velocities consistent with ESP2 velocity structure, whereas the two inner SAPs 2 and 3 display consistently lower velocities on picks greater than 1.0 s sub-basement TWT. This was presumed due to the 3-dimensional nature of the margin and the associated difficulties in choosing comparable regions on adjacent SAPs for lateral comparison. Additionally, the absence of ESP data to constrain velocity picks in the lower parts of the sections at these levels during velocity analysis may have contributed to the effect. The effect is absent on oceanic sequence comparisons due to the relative along-strike uniformity of the oceanic basin structure.

The opaque region identified as due to late-stage igneous activity is characterised by an absence of reflectors and low signal:noise ratio. Consequently semblance velocity picks within this region below approximately 1 s sub-basement TWT were guided by available ESP results on SAPs 1 and 4, and by other published velocity data on SAPs 2 and 3 (Scrutton, 1972 ; Ewing & Ewing, 1959) relevant to the Hatton Bank margin, and Iceland Basin. The velocity structure (figure 6.16) within the late-stage lavas appears to indicate slightly higher velocity gradients than within the dipping reflector sequences, an effect which manifests itself by a "pulling up" of isovelocity contours within the late-stage lava pile (figure 6.9). The slightly higher velocities within the late-stage lavas was interpreted as due to its apparent homogeneity illustrated by the lack of internal acoustic stratification.

The deeper structure of the ocean-continent transition was determined using full-wave reflectivity synthetic seismogram modelling of the two-ship ESP data. This work was carried out at the University of Cambridge by Dr R. S. White, Dr G. Spence, and Ms S. Fowler, and is described in chapter 4, section 4.3.2.

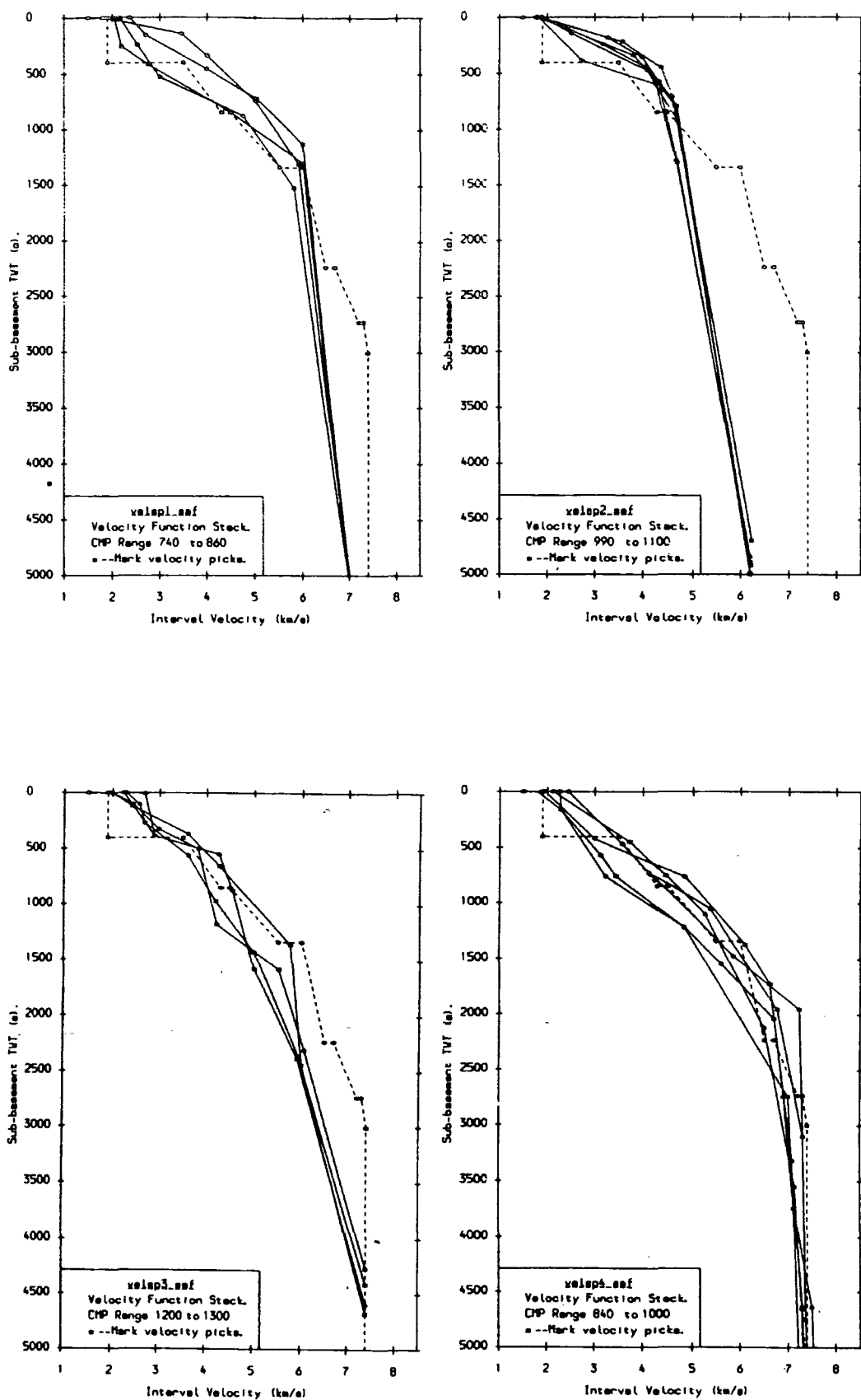


**Figure 6.16** Along-strike velocity function comparison within late sequence volcanic pile. ESP 3 velocity function superimposed.

## 6.4 Interpretation.

In this section an interpretation of the sub-basement structures observed in zones 1, 2, and 3 is presented in terms of three structural sequences which were identified on all SAPs, and termed the continental, late, and oceanic sequences.

**6.4.1 Continental Sequence.** The structure of this sequence is best defined on SAP 1 in zone 1 and the landward portion of zone 2. This consists of the region of basement forming the upper continental slope and shelf of Hatton Bank. Sub-parallel layering underlying a smooth acoustic basement in zone 1 passes oceanward into zone 2 where the sequence thickens to form a wedge of seaward-dipping reflectors. Within zone 2 the continental sequence reflectors are overlain by a younger seaward-dipping reflector sequence which forms part of the late sequence. The velocity-depth structure of the crust of zone 1 as determined at ESP 1 was interpreted as consistent with continental crust having a Moho depth of 27 km (White *et al.*, 1986 ; 1987). The sequence is associated with magnetic anomalies whose amplitudes and wavelengths were interpreted as originating from a volcanic basement (chapter 5). The reconstructed position of anomaly 24B, the oldest recognised seafloor spreading anomaly within the Iceland basin adjacent to the western margin of Rockall Plateau, lies well oceanward of the continental sequence. DSDP Leg 81, site 555 was located on the south-western Rockall Plateau in a region equivalent to zone 1, in which strong, flat-lying reflectors were observed on complimentary seismic reflection profiles. These were penetrated and found to correspond to late-Paleocene to early-Eocene tholeiitic basalt flows interbedded with sediments. The underlying basement was deduced from gravity modelling (Scrutton, 1972 ; Roberts & Ginsburg, 1984) to be continental in nature.

On the basis of the evidence summarised above it is concluded that the continental sequence corresponds to a succession of lavas of late-Paleocene to early-Eocene age overlying metamorphic continental basement. These were extruded during a period of intense igneous activity probably accompanying lithospheric stretching and thinning prior to the onset of seafloor spreading in anomaly 24B time. The velocity structure at ESP 1 suggests that the lavas may be between 3.5 and 7 km in thickness (section 6.2.2). The lava sequence thickens to the northwest, implying eruption from an oceanward source. Dips within the thickened portion of the continental sequence <sup>probably</sup> were originally to the south-east. However, rapid subsidence associated with the loading of earlier flows by subsequent eruptions, together with subsidence induced by lithospheric extension and thinning prior to continental break-up has resulted in an inversion of topography and consequent reversal of dips within the continental sequence to the north-west. Later additional subsidence was caused by the load of the overlying late sequence, and differential thermal subsidence across the margin since formation has increased reflector dips within the sequence to their present values of up to  $20^{\circ}$ .

**6.4.2 Oceanic Sequence.** This sequence is defined as the region of crust displaying the seaward-dipping reflectors of zone 3 and their landward continuation into zone 2. The structure of the sequence is best illustrated on SAP 2. At their landward extreme within zone 2, the oceanic sequence reflectors are overlain by a stratified wedge of late sequence material. The unconformity separating the two sequences dips continentwards at an angle of  $2^{\circ}$ . The underlying reflectors conform with this, and are smoothly continuous, exhibiting the classic upward-convexity with down-dip increase in reflector separation and dip suggested by Mutter *et al.* (1982) as diagnostic of formation by subaerial seafloor spreading. The reconstructed

position of anomaly 24B is associated with these reflectors at the point on SAP 2 where the deepest reflector dips most steeply into the section. Normal incidence line NI3 shot along the strike of the margin indicate that the unconformity and underlying reflectors are remarkably uniform along strike (figure 6.15), confirming their presence on SAPs 1 and 3 as suggested in section 6.2.2, although these are not as obvious as on SAP 2. Oceanward from the foot of the continental slope of SAPs 1-3, the oceanic sequence reflectors become increasingly irregular, although they still display the upward-convex aspect of those underlying the late sequence of zone 2. On SAP 4 the oceanic sequence reflectors are very poorly developed. The velocity structure at ESPs 10 and 4 within zone 3 was interpreted as consistent with thick oceanic crust (White *et al.*, 1986). The oceanic sequence reflectors, which have velocities typical of oceanic layer 2, extend to approximately 2 s below acoustic basement, which implies a thickness of 5 km. Oceanic basement depths are approximately 3 km, which suggest that the oceanic layer 2/3 boundary lies at a depth of 8 km. This corresponds well with the 6.7 to 6.9 km s<sup>-1</sup> interface on ESP 10 interpreted for the purpose of gravity modelling as corresponding to the oceanic layer 2/3 boundary (figure 6.8). A Moho depth of 14 km at ESP 10 (figure 6.8) implies an oceanic layer 3 thickness of 6 km. This suggests that the oceanic crustal thickening occurs principally within oceanic layer 2, and is associated with the dipping reflectors. Oceanic magnetic anomalies 21 and 22 are well developed to the north-west of the SAPs in positions consistent with earlier work (Vogt & Avery, 1974 ; Voppel *et al.*, 1979). Reconstruction of the position of anomaly 23 coincides with the oceanic sequence reflectors on SAPs 1 - 3.

The evidence summarised above indicates that the seaward-dipping reflectors of the oceanic sequence formed as part of the oceanic crust, and may be of two

distinct types. The first corresponds to the smoothly continuous, upward-convex which have maximum dips of  $28^\circ$ , reflectors/associated with the reconstructed anomaly 24B positions which form a landward continuation of the oceanic sequence into zone 2. These were formed as the first oceanic crust was generated, by lava flowing subaerially onto the adjacent, rapidly subsiding continental crust. These pass oceanward into the second type, having maximum dips of  $25^\circ$ , and which correspond to the more irregular seaward dipping reflectors/which may have formed by subaerial seafloor spreading as envisaged by Mutter *et al.* (1982). An estimate of the subsidence of the crust of zone 3 since its formation can be made using the subsidence term of the empirical subsidence formula of Parsons & Sclater (1977) given by

$$z(t) = 2500 + 350 (t)^{1/2}$$

where  $z$  = depth of ocean at time  $t$ , and  $t$  = age of crust in Ma according to the time scale of Heirtzler *et al.* (1968). This implies a subsidence of 2690 m for oceanic crust of anomaly 23 to 24B age. The present basement depth of the crust of zone 3 corrected for sediment load is approximately 2800 m, which suggests that the dipping reflectors observed in the oceanic crust of this zone were formed under shallow marine conditions, and not in a subaerial environment as envisaged by the Mutter *et al.* (1982) model (chapter 7), assuming no additional subsidence mechanisms have operated since rifting. However it is difficult to envisage how lavas erupted subsequently could have achieved the flow lengths required to produce the observed reflector lengths. A possible additional source of uplift during the early rifting and seafloor spreading history of the margin may have been provided by the ponding of hot, buoyant residual magma at the base of the crust following extraction of the overlying lavas. This has subsequently cooled and underplated the lower crust to form the high velocity lens detected by ESP modelling (White *et al.*, 1986). The buoyancy of the residual magma may have been such as to maintain

a substantial subaerial relief during extrusion of the lavas which form the oceanic sequence dipping reflectors within zone 3.

6.4.3 Late Sequence. The late sequence defines the extent of zone 2, and consists of three characteristic regions. At the south-eastern extreme of zone 2, a sequence of seaward-dipping reflectors forms a north-westward thickening wedge which overlies the continental sequence dipping reflectors. This region is best displayed on SAP 1 between CMPs 250 to 600, and passes north-west into a central opaque zone displaying occasional reflectors which imply a chaotic internal structure. North-west of the opaque zone to the oceanward limit of zone 2, a seaward-thinning wedge overlies the landward extreme of the oceanic sequence seaward-dipping reflectors. This structure is best displayed on SAP 2 between CMPs 600 and 900. The upper surface of the wedge has an oceanward dip of  $1^{\circ}$ , whereas its base dips  $2^{\circ}$  continentward. Layers within the wedge have dips which range between these extremes. Since the wedge overlies interpreted oceanic crust of magnetic anomaly 24B age, the late sequence must post-date the onset of seafloor spreading. Magnetic anomalies associated with the late sequence are arcuate, have high amplitudes, and were interpreted in chapter 5 as originating from igneous activity other than simple seafloor spreading. The velocities within the late sequence material as determined from SAP velocity analysis are consistent with igneous rocks (section 6.3). ESP velocity determinations within zone 2 reveal a velocity structure consistent with either very thick oceanic crust, or with thinned continental crust overlain by extrusives and underplated by residual igneous material (White *et al.*, 1986). The sediments which overlie the late sequence exhibit a distinct horizon which was interpreted as corresponding to R4 (Roberts, 1975a), a regional unconformity of Eocene/Oligocene age. This onlaps the late sequence on SAPs 1,3, and 4, indicating that the sequence was formed



prior to R4. Thus the age of the late sequence lies between the age of anomaly 24B (early-Eocene) and the age of R4 (Eocene/Oligocene).

From the evidence presented above was concluded that the late sequence was formed following continental break-up and the onset of seafloor spreading between Greenland and Rockall Plateau as a result of igneous activity in the Eocene. A large local magnetic anomaly centred close to CMP 1100 on SAP2 was interpreted in chapter 5 as corresponding to two adjacent, oppositely magnetised intrusions. This corresponds to a peak on the gravity contour map which was modelled as an intrusive body (chapter 4), and may have formed a volcanic centre from which the late sequence lavas were extruded. Lavas were erupted subaerially (as evidenced from the extent of lateral flow), flowing landwards onto the continental sequence to form the overlying late sequence seaward-dipping reflector wedge, and oceanwards onto the oceanic sequence to form the overlying late sequence stratified wedge. Flows were limited oceanward by cooling on contact with the young ocean to form the abrupt steps in the acoustic basement observed on SAPs 2 and 4 at CMPs 600 and 650 respectively. Subsidence, induced by the weight of the late sequence pile of lavas and intrusives, caused the underlying oceanic sequence to tilt to the south-east. The seaward dips of the underlying continental sequence dipping reflectors to the south-east were increased by the same effect. Along-strike flow of lavas away from the volcanic centre presumably accounts for the variation in late sequence structure along strike. The undulating reflectors of SAP 4 may have formed by extrusion of lavas onto faulted basement. However, there is no evidence of faulting in similar locations on the other SAPs.

## CHAPTER (7)

### Conclusions and discussion.

#### 7.1 Introduction.

In this chapter, a summary of the main results and conclusions derived from the interpretation of the gravity, magnetic, and seismic data presented in chapters 4,5, and 6 is given, and additional points of relevance arising therefrom are discussed. Based on these observations, a sequence of evolution for the Hatton Bank continental margin is presented. A central problem in understanding the structure of passive continental margins is the observation that some of these exhibit sequences of seaward-dipping reflectors which are thought to lie close to the continent-ocean boundary. A review of the principal models proposed to account for the production of the dipping sequences <sup>in chapter 1,</sup> is presented, and followed by the description of the structure of two well studied examples of volcanic margins, the Outer Voring Plateau, and the south-west Rockall Plateau. This section concludes with a discussion of the dipping reflectors revealed by the SAP profiles across the Hatton Bank margin, which give new insights into the problem of the formation and evolution of dipping reflector sequences on volcanic passive margins.

#### 7.2 Conclusions and general discussion.

##### 7.2.1 Gravity modelling.

Gravity modelling of the continent-ocean transition on the Hatton Bank continental margin shows that a crustal density model constrained by ESP velocity-depth structure alone is insufficient to account for the observed gravity profile. Lateral density gradients within the underlying sub-crustal part of the lithosphere and the

asthenosphere are required. These originate from the non-equilibration of the rift thermal anomaly and from the existence of an unusually hot underlying upper mantle, probably due to the proximity of the Icelandic hot-spot, and they maintain the margin in isostatic equilibrium. This is consistent with the suggestions made by previous workers (Haigh, 1973a,b ; Cochran & Talwani, 1978 ; Bott, 1987b) that the north-Atlantic topographic swell between the Azores and Iceland is maintained by elevated temperatures in the upper mantle. Cochran & Talwani (1978) estimated that a 75 K rise in asthenosphere temperature over 200 km is sufficient to cause the observed uplift. Haigh (1973a) concluded that the temperature at the base of the lithosphere may be up to 150 K above normal. A fuller discussion of the origin of the north Atlantic topographic swell in terms of raised upper mantle temperatures is given in section 4.7.

The late sequence volcanic unit extruded onto the margin slope following continental rifting and the onset of seafloor spreading would be expected to represent a considerable load. If not fully compensated locally, this would result in an associated gravity anomaly of approximately 70 mGal. In fact, a gravity mis-match of 10 mGal was modelled by the inclusion of an intrusive body in the vicinity of the late sequence lava body on SAP 2 (chapter 4). The absence of a major gravity anomaly associated with the late sequence lavas implies that the load has been largely compensated locally by the gradual sagging of the margin since extrusion of the lavas. Lack of time has prevented a full flexural study, but the relatively local sagging indicates a very small flexural rigidity, as might be expected under hot lithospheric conditions.

### 7.2.2 ESP Velocity structure, and lateral variations in the upper crust.

Gravity modelling was carried out in a manner consistent with the interpretation of the ESP defined crustal velocity structure presented by White *et al.* (1986). The resulting model (figure 4.26) supports this interpretation. However, the interpretation of the SAP profiles (chapter 6) indicates that the upper crust of the margin exhibits significant variability along strike, due to the presence of the late sequence volcanic unit, which lies between ESP2 and ESP 5a. This would be expected to disrupt the velocity structure of the upper crust as determined by full-wave reflectivity synthetic seismogram modelling which assumes the absence of lateral variation. The deeper structure, interrogated by rays having larger source-receiver offsets which travel predominantly within the lower crust, would be expected to be affected to a lesser extent by lateral variations in upper crustal structure. Possible revision of the ESP-defined velocity structure may be provided by the results of the modelling, by Joanna Morgan and Penny Barton at the University of Cambridge, of a long dip-line shot through the mid-points of the ESP lines, approximately along the line of SAP2 and the gravity model. Preliminary results (Morgan, pers. comm.) suggest a possible downward revision of velocities within the underplated lens by 0.1 to 0.2 km s<sup>-1</sup>, together with the presence of higher velocities within the upper crust coincident with the intrusive body suggested by gravity modelling. The ESPs shot on the continental slope and ocean basin away from the disrupting influence of the late-stage volcanic unit would be expected to produce more accurate velocity depth information.

### 7.2.3 Magnetic anomalies.

Anomaly 24B is the oldest seafloor spreading lineation identified adjacent to

the passive continental margins east of the Reykjanes ridge (Vogt & Avery, 1974 ; Voppel *et al.*, 1979). In the 1985 survey area anomaly 24B cannot be recognised due to post-rift igneous activity and/or subaerial seafloor spreading. Its identification in earlier Durham University cruise data south of the 1985 survey area, and on the conjugate East-Greenland margin (Featherstone *et al.*, 1977), enabled closure of the Reykjanes basin to anomaly 24B time, and subsequent reconstruction of the position of anomaly 24B within the 1985 survey area, consistent with identifications to the north and south. The postulated position is reinforced by reconstruction of anomalies 20 and 21 to anomaly 24B time using finite-difference poles and angles of rotation given by Bott (1985) and Srivastava & Tapscott (1986). This enabled a relatively precise determination of the line of split between Rockall and Greenland on the assumption that the split occurred just prior to anomaly 24B (chapter 5). The position of the continent-ocean boundary can thus be located accurately west of Hatton Bank. Within the 1985 survey area this is associated with the landward limit of an oceanic sequence of seaward-dipping reflectors, as seen on SAP 2 between CMPs 900 and 600. Anomalies 21 and 22 are clearly developed in the north-west of the 1985 survey area.

The magnetic anomaly pattern within the 1985 survey area also facilitates the identification of the late sequence volcanic unit, which is associated with relatively high amplitude, arcuate anomalies, and a large local double-polarity anomaly. Analysis of the wavelengths characteristic of magnetic anomalies found on the upper continental slope indicates that the basement is probably volcanic, consistent with DSDP Leg 81 results which penetrated flat-lying Tertiary basalts at site 555. These observations provide powerful constraints on the interpretation of the SAP profiles presented in chapter 6.

#### 7.2.4 The Hatton Bank volcanic margin.

The interpretation of four SAP profiles shot across the continent-ocean transition is described in chapter 6, where it is shown that the sub-sedimentary basement rocks of the margin can be broadly sub-divided into three distinct volcanic sequences. The continental sequence forms the acoustic basement of the upper continental slope and shelf of Hatton Bank. The reflectors forming this sequence thicken toward their oceanward limit on SAPs 1, 2, and 3, where they form the continental sequence of seaward-dipping reflectors. The magnetic anomalies within this area indicate that the sequence is highly magnetic and thus volcanic (chapter 5). The velocity structure of the underlying crust, as determined from synthetic seismogram modelling of ESP data (White *et al.*, 1986 ; 1987), together with the absence of seafloor spreading magnetic anomalies and the reconstructed position of anomaly 24B which lies well oceanward of the continental sequence, is interpreted as consistent with underlying crust of continental affinity. The continental sequence is interpreted as corresponding to Paleocene lavas extruded from a north-westward source prior to the onset of seafloor spreading between Rockall and Greenland.

The oceanic sequence is defined as the region of crust to the north-west which exhibits the classic upward-convex seaward-dipping reflectors described by Mutter *et al.* (1982) as forming in oceanic crust by the process of subaerial seafloor spreading. These become more impersistent at some distance oceanwards from the foot of the continental slope, and are overlain unconformably at their landward limit by a later volcanic unit corresponding to the late sequence, where they coincide with the reconstructed position of anomaly 24B. The velocity-depth structure, and the reconstructed position of anomaly 24B imply that the crust of the oceanic sequence is oceanic (White *et al.*, 1986 ; 1987). Consequently the sequence is interpreted

as oceanic crust formed during the earliest stages of seafloor spreading, partly in a subaerial environment within which dipping reflectors were able to develop.

The late sequence exists mid-way down the continental slope, separating and overlying part of the continental and oceanic sequences. This consists of a central, relatively opaque zone which exhibits few reflectors, flanked to the south-east by the late dipping reflector sequence, and to the north-west by the acoustically stratified wedge overlying the landward portion of the oceanic sequence. The late sequence is associated with the arcuate, high amplitude magnetic anomalies interpreted in chapter 5 as originating from igneous activity other than seafloor spreading. The presence of a large local double-polarity anomaly centred close to SAP 2, CMP 1100 suggests localised intrusion. The ESP determined velocity-depth structure is consistent with either thick oceanic crust or a layer of stretched continental crust overlain by extrusives and underplated by igneous residue (White *et al.*, 1986 ; 1987). The late sequence overlies, and is consequently younger than oceanic crust of anomaly 24B age. The sedimentary horizon identified as corresponding to the regional Eocene/Oligocene unconformity R4 (Roberts, 1975a), pinches out against the late sequence lavas on SAPs 1,3, and 4. This implies that the late sequence was extruded prior to the formation of R4, and is therefore Eocene in age. The late sequence is thus interpreted as representing a pulse of Eocene volcanic activity occurring shortly after seafloor spreading had become established.

These observations have been used to define a sequence of formation for the Hatton Bank continental margin. As discussed in chapter 5, it is assumed that the split between Rockall Plateau and East Greenland occurred just before the onset of anomaly 24B. The evolutionary history of the margin is divided into five phases (figure 7.1).

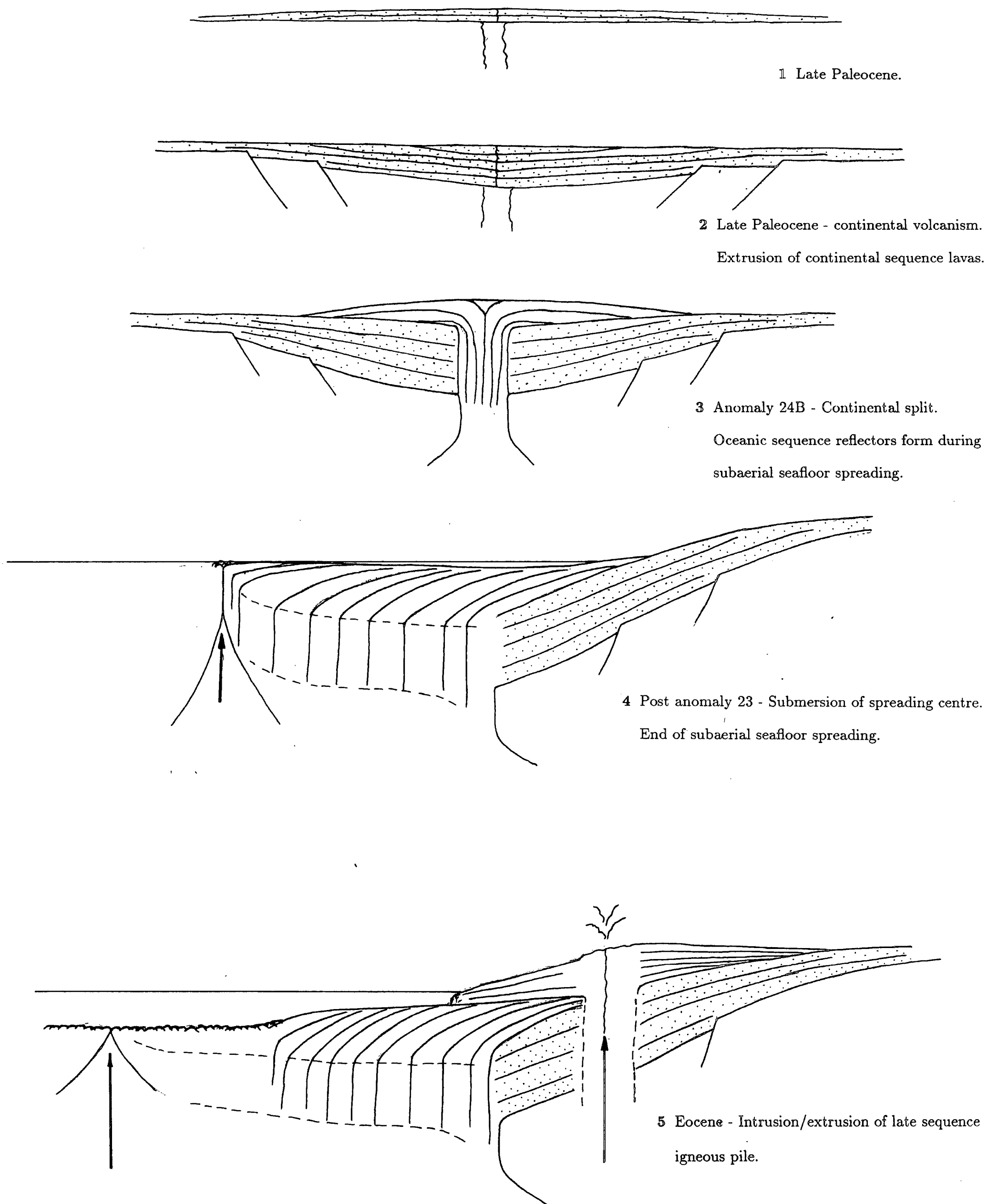
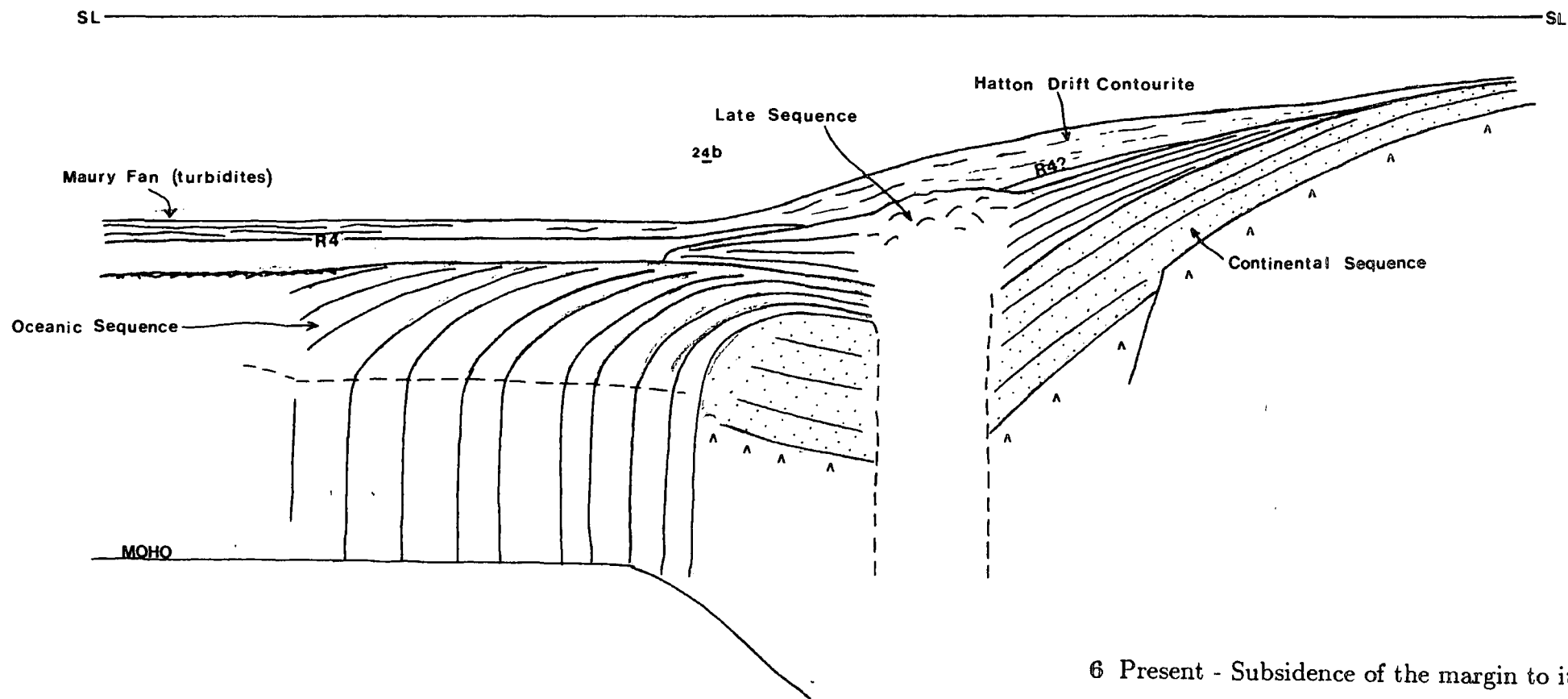


**Figure 7.1** Schematic illustration of the sequence of evolution of the Hatton Bank continental margin. SL = sealevel, R4 = regional unconformity (Roberts, 1975a).





6 Present - Subsidence of the margin to its present configuration.

Phase (1). Voluminous continental volcanism associated with the extrusion of lavas formed the continental sequence. These are possibly between 4 km and 7 km in thickness, and thicken oceanwards on SAPs 1, 2, and 3, implying eruption from a source to the north-west. Dips were presumably originally gently to the south-east, but subsidence during and/or after extrusion has resulted in a reversal of dip to the north-west. Subsidence was possibly associated with crustal thinning and extension just prior to continental break-up. The continental sequence lavas are interpreted as analogous to the flat-lying lavas of zone 4 on the south-west Rockall Plateau (Roberts *et al.*, 1984). These were drilled during DSDP Leg 81, and found to have been erupted entirely within the anomaly 25/24B reverse polarity interval. They are therefore of late Paleocene age. Roberts *et al.* (1984) considered that the lavas of zones 3 and 4 are equivalent to the thick subaerially exposed plateau basalts of the Faeroes and East Greenland, which were also probably erupted within the same reverse polarity interval preceding anomaly 24B (Bott, 1987a).

Phase (2). Continental splitting immediately prior to anomaly 24B was associated with the formation of the first oceanic crust. The south-easternmost seaward-dipping reflectors of the oceanic sequence were formed during this phase as a result of the voluminous extrusion of lavas onto rapidly subsiding continental basement during the earliest stages of continental break-up. This structure is best developed on SAP 2 between CMPs 600 and 900, and less obviously so on SAPs 1, 3, and 4. The lavas were extruded subaerially as indicated by the continuity of the reflectors. The subaerial relief of the margin may have been increased during this phase by the buoyant effect of the ponding of hot magmatic residue at the base of the crust following extraction of the overlying extrusives (chapter 6).

Phase (3). Following the initial split between Rockall Plateau and East Green-

land, early seafloor spreading resulted in the formation of the less regular seaward-dipping reflectors observed within the oceanic sequence on SAPs 1,2, and 3 oceanward from the foot of the continental slope which adjoin the initial oceanic sequence reflectors. The extent of these reflectors implies that seafloor spreading was subaerial in a manner akin to that described by Mutter *et al.* (1982). Although the subsidence term of the empirical subsidence formula of Parsons & Sclater (1977) implies that crust of this age would have been formed in shallow marine conditions, additional uplift due to the buoyant residual magma at the base of the crust may have affected the margin during this phase, and maintained a subaerial relief (chapter 6).

Phase (4). As eruption rates fell, the spreading centre gradually submerged. The reduced outflow lengths of the now subaqueously extruded lavas resulted in the formation of a more chaotic upper oceanic crustal structure, typical of normal oceanic crust. Seafloor spreading has continued uninterrupted in this manner about the Reykjanes Ridge to the present.

Phase (5). Shortly after seafloor-spreading had become established a pulse of igneous activity on the margin, possibly at the old volcanic centre from which the continental sequence was extruded, resulted in the formation of the late sequence volcanic pile. Its relationship to the underlying oceanic sequence crust of anomaly 24B age, and to the overlying sedimentary horizon R4, implies that the late sequence activity occurred sometime in the Eocene. Eruption was probably subaerial as indicated by the lateral extent of the reflector sequences flanking the central opaque zone on SAPs 1 and 2. Flow limits may have been constrained oceanward by chilling on contact with the young ocean to form abrupt basement steps (eg SAP2, CMP 600). The late sequence lava pile caused loading and subsidence of the margin, with

the underlying continental sequence reflector dips increasing to the north-west, and the underlying oceanic sequence reflectors tilting to the south-east to reverse their former dip. Lack of a major gravity anomaly associated with the late sequence indicates subsidence in response to the loading of the margin with a small flexural rigidity characteristic of the still hot margin. The late sequence lavas blanket and obscure the details of the transition from continental to oceanic sequence, and may have resulted in the erasure of anomaly 24B.

### 7.3 Dipping reflectors and the continent-ocean boundary.

The different sequences of dipping reflectors observed on the Hatton Bank continental margin exhibit varying characteristics depending upon their mode of emplacement and subsequent evolutionary history.

(1) **The continental sequence reflectors** are most clearly seen on SAP 1 between CMPs 250 and 600. Characteristically, these reflectors are planar with seaward-dip, and the sequence thickens towards the north-west. Continentwards they pass into the lavas overlying the uppermost continental slope. The sequence overlies continental crust which may be faulted as a result of stretching(?), as evidenced by the undulating reflectors of the overlying late sequence on SAP 4. These originate from continental volcanism, possibly associated with crustal thinning and extension preceding continental splitting. Oceanward reflector dips <sup>of up to 20°</sup> were acquired by subsidence associated with stretching, subsequent loading by late sequence lavas, and thermal subsidence of the margin since rift. These characteristics may typify formation within a continental setting during the rifting stage of passive margin development.

(2) **The oceanic sequence reflectors** are best seen on SAP 2. These are

different in structure to those of the continental sequence, displaying an upward-  
from near horizontal to  $25^\circ$ , and increase in  
concavity, a down-dip increase in dip  $\angle$  thickness. They form an extended seaward  
prograding sequence within oceanic crust. They may be subdivided into two forms:-  
(a) the continuous, smooth reflectors corresponding to those formed immediately  
after continental splitting by lavas flowing onto rapidly subsiding continental crust,  
and (b) those which subsequently formed entirely within oceanic crust, possibly  
subaerially, which comprise the less regular dipping reflectors of the oceanic sequence  
oceanwards from the foot of the continental slope. The model of Smythe (1983)  
appears to best describe the formation of the oceanic sequence.

**(3) Late sequence reflectors.** Individual reflectors within the late sequence  
lavas exhibit structures and dips which vary from the planar, seaward-dipping re-  
flectors of SAP2 (CMPs 250 to 600), through the undulating reflectors of SAP 4,  
to the gently continentward-dipping reflectors of SAP 2 (CMPs 600 to 900). The  
sequence originates from post-rift subaerial igneous activity. Original dips were pre-  
sumably gently away from the active centre. Subsequent sagging of the igneous pile  
has reversed these dips towards the centre, and thermal subsidence of the margin  
has rotated the entire unit to the north-west to its present configuration.

From geophysical descriptions of other volcanic margins (chapter 1) and the  
foregoing discussion, it is obvious that, although possessing an underlying validity,  
current models do not provide a general description of the formation of the dipping  
sequences observed on volcanic passive margins. It is suggested that such attempts  
are unlikely to succeed, since their formation depends on the conditions prevalent  
during continental rifting and early seafloor spreading, which vary with location.  
The definition of certain conditions which may combine in various situations to  
produce dipping reflector sequences appears to be a more valid approach. These

conditions are three-fold. The first is that the rate of eruption of lavas during the production of the dipping reflectors should be high enough to produce the thick igneous sections observed. Secondly, subaerial eruption of the lavas is required in order to attain the lateral extent of flow which appears to be necessary for full development of the dipping sequences. The third condition is the operation of a syn- or post-emplacement tectonic mechanism by which the lavas forming the dipping reflectors acquire their oceanward dip, and thus can occur in a continental or subaerial oceanic environment, or at the newly accreting spreading centre.

The position of the continent-ocean boundary with respect to the seaward-dipping sequences is therefore dependent on the tectonic setting of the igneous activity which results in their formation. Detailed examination of the structure of observed sequences allied with other relevant geophysical observations such as the crustal velocity-depth structure, identification of the oldest adjacent seafloor spreading magnetic anomaly, DSDP results, and gravity modelling is necessary, in order to determine a consistent model of formation of individual dipping sequences, from which the continent-ocean boundary position can be deduced.

#### **7.4 Concluding comments.**

The unambiguous determination of the position of the continent-ocean boundary at passive continental margins has significant implications for the timing of continental separation, the accuracy of plate-tectonic reconstructions, and the testing of the predictions made by models of the evolution of passive margins. Its definition by seismic reflection and refraction techniques has proved difficult since attenuated continental crust can appear similar to adjacent oceanic crust on seismic reflection profiles. Thus the realisation that the sequences of seaward-dipping

reflectors observed on some passive continental margins are related to the processes of continental rifting and the onset of seafloor spreading lead to the development of models for their formation. These made specific predictions concerning the position of the continent-ocean boundary with respect to the position of the seaward-dipping sequences (Hinz, 1981 ; Mutter *et al.*, 1982 ; chapter 1). It was believed that if a model could be substantiated, it would provide a means of precisely locating the continent-ocean boundary at passive margins which exhibit the characteristic dipping reflectors.

However, subsequent detailed geophysical surveys of various volcanic margins, allied with the results of DSDP operations (section 7.3), have revealed that the situation is not as straightforward as originally hoped. This is well illustrated by the present work. It is clear that dipping reflectors display a range of structural styles which are related to, and therefore provide a valuable indication of, the tectonic setting of the igneous activity which resulted in their formation. When combined with other geophysical observations, such as the location of the oldest oceanic magnetic anomaly lineation adjacent to the margin, crustal velocity structure, gravity modelling and deep-sea-drilling, this information can aid in increasing the accuracy of determinations of the position of the continent-ocean boundary at volcanic passive continental margins.

## References.

1. Al-Chalabi, M., (1974). An analysis of stacking, rms, average, and interval velocities of a horizontally layered ground. *Geophys. Prosp.*, **22**, 458-475.
2. Armstrong, T. L., (1981). A marine geophysical investigation of the continental margin of East Greenland (63N to 69N)., Ph.D. thesis, University of Durham.
3. Barton P. J., (1986). The relationship between seismic velocity and density in the continental crust - a useful constraint? *Geophys. J. R. astr. Soc.*, **87**, 195-208.
4. Beaumont, C., Keen, C. E., & Boutilier, R., (1982). On the evolution of rifted continental margins: comparison of models and observations for the Nova Scotia margin. *Geophys. J. R. astr. Soc.*, **70**, 667-715.
5. Bodvarson, G., & Walker, G. P. L., (1964). Crustal drift in Iceland. *Geophys. J. R. astr. Soc.*, **8**, 285-300.
6. Bott, M.H.P., (1985). Plate tectonic evolution of the Iceland transverse ridge and adjacent regions. *J. Geophys. Res.*, **90**, 9953-9960.
7. Bott, M.H.P., (1987). The continental margin of central East Greenland in relation to North Atlantic plate tectonic evolution. *J. Geol. Soc. Lond.*, **144**, 561-568.
8. Bott, M.H.P., (1988). A new look at the causes and consequences of the Iceland hot spot. (in press)
9. Bowen, A. N., (1987a). The reflection processing laboratory. User manual, Seismic Reflection Processing Laboratory, Department of Geological Sciences, University of Durham, 11 pages.
10. Bowen, A. N., (1987b). The SEG-B demultiplex program-DEMUXB. User manual, Seismic Reflection Processing Laboratory, Department of Geological Sciences, University of Durham, 4 pages.
11. Bowen, A. N., (1987c). The absolute-location sort suite. User manual, Seismic Reflection Processing Laboratory, Department of Geological Sciences, University of Durham, 15 pages.
12. Bowen, A. N., (1987d). The processing program. User manual, Seismic Reflection Processing Laboratory, Department of Geological Sciences, University of Durham, 67 pages.
13. Buhl, P., Diebold, J. B., & Stoffa, P. L., (1982). Array length magnification through the use of multiple sources and receiving arrays. *Geophys.*, **47**, 311-315.
14. Bullard, E. C., Everett, J. E., & Smith, A. G., (1965). The fit of the continents around the Atlantic. *Phil. Trans. R. Soc. London*, **A258**, 41-51.



15. Cann, J. R., (1970). New model for the structure of oceanic crust. *Nature*, **226**, 928-930.
16. Cann, J. R., (1974). A model for oceanic structure developed. *Geophys. J. R. astr. Soc.*, **39**, 169-187.
17. Carslaw, H. S., & Jaeger, J. C., (1959). *Conduction of heat in solids*. Oxford, Clarendon Press, 510 pages.
18. Christensen, N. I., & Fountain, D. M., (1975). Constitution of the lower continental crust based on experimental studies of seismic velocities in granulite. *Geol. Soc. Am. Bull.*, **86**, 227-236.
19. Christensen, N. I., & Salisbury, M. H., (1975). Structure and constitution of the lower oceanic crust. *Rev. Geophys. Space Phys.*, **13**, 57-86.
20. Christensen, N. I., & Smewing, J. D., (1981). Geology and seismic structure of the northern section of the Oman ophiolite. *J. Geophys. Res.*, **86**, 2545-2555.
21. Clark, S. P. Jr.(editor), (1966). *Handbook of physical constants*, revised edition. *Mem. Geol. Soc Am.*, **97**, 587 pages.
22. Clark, S. P. Jr., & Ringwood A. E., (1964). Density distribution and constitution of the mantle. *Rev. Geophys. Space Phys.*, **2**, 35-88.
23. Cox, K. G., (1980). A model for flood basalt volcanism. *J. of Petrol.* **21**, 629-650.
24. Cochran, J. R., & Talwani, M., (1978). Gravity anomalies, regional elevation, and the deep structure of the North Atlantic. *J. Geophys. Res.*, **83**, 4907-4924.
25. Dix, C. H., (1955). Seismic velocities from surface measurements. *Geophys.*, **20**, 68-86.
26. Eldholm, O., & Sundvor, E., (1980). The continental margins of the Norwegian-Greenland Sea : recent results and outstanding problems. *Phil. Trans. R. Soc. London*, **A294**, 77-86.
27. Ewing, M., & Ewing, J., (1959). Seismic refraction measurements in the Atlantic Ocean, in the Mediterranean Sea, on the Mid-Atlantic Ridge, and in the Norwegian Sea. *Bull. Geol. Soc. Am.*, **70**, 291-317.
28. Featherstone, P. S., (1976). A geophysical investigation of the Southeast Greenland continental margin. Ph.D. thesis, University of Durham.
29. Featherstone, P. S., Bott, M. H. P., & Peacock, J. H., (1977). Structure of the continental margin of Southeast Greenland. *Geophys. J. R. astr. Soc.*, **48**, 15-25.

30. Fountain, D. M., (1976). Seismic velocities of rocks from the Ivrea-Verbano and Strona-Ceneri zones, Northern Italy: a cross section of the continental crust - new evidence from the seismic velocities of rock samples. *Tectonophysics*, **33**, 145-165.
31. Fountain D. M., & Salisbury, M. H., (1981) Exposed cross-sections through the continental crust: implications for crustal structure, petrology, and evolution. *Earth Planet. Sci. Lett.*, **56**, 263-277.
32. Fowler, S. R., (1986). Flexural studies of the Exmouth and Rockall Plateaux using SEASAT altimetry. *in* Ph.D. thesis, University of Cambridge.
33. Fowler, S. R., White, R. S., Spence, G. D., & Westbrook, G. K., (1988). The Hatton Bank continental margin II : deep structure from two-ship expanding spread seismic profiles. *Geophys. J. R. astr. Soc.*, (in press).
34. Furlong, K. D., & Fountain, D. M., (1986). Continental crustal underplating: thermal considerations and seismic-petrologic consequences. *J. Geophys. Res.*, **91**, 8285-8294.
35. Haigh, B. I. R., (1973a). Crustal and upper mantle structures in oceanic regions. Ph.D. thesis, University of Durham.
36. Haigh, B. I. R., (1973b). North Atlantic oceanic topography and lateral variations in the upper mantle. *Geophys. J. R. astr. Soc.*, **33**, 405-420.
37. Hailwood, E. A., Bock, W., Costa, L., Dupeuble, D. A., Muller, C., Schnitker, D., (1979). Chronology and biostratigraphy of northeast Atlantic sediments, DSDP Leg 48, *in*: Montadert, L., & Roberts, D. G., (1979). *Init. Repts. DSDP.*, **48**, Washington (U. S. Govt. Printing Office), pp 1119-1141.
38. Hall, J., & Simmons, G., (1979). Seismic velocities of Lewisian metamorphic rocks at pressures to 8 kbar: relationship to crustal layering in North Britain. *Geophys. J. R. astr. Soc.*, **58**, 337-347.
39. Heirtzler, J. R., Dickson, G. O., Herron, E. M., Pitman, W. C., & Le Pichon, X., (1968). Marine magnetic anomalies, geomagnetic field reversals, and motion of the ocean floor and its continents. *J. Geophys. Res.*, **73**, 2119-2136.
40. Hinz, K., (1981). A hypothesis on terrestrial catastrophes. Wedges of very thick oceanward dipping reflectors beneath passive continental margins - their origin and paleoenvironmental significance. *geologisches Jahrbuch, Reihe E, Geophysik*, **22**, 3-28.
41. Hobbs, R. W., (1985). Processing of a multichannel reflection survey in the Hebridean region with special emphasis on improvements in velocity analysis. Ph.D. Thesis, volumes 1 & 2, University of Durham.
42. Hyndman, R. D., & Drury, M. J., (1976). The physical properties of oceanic basement rocks from deep drilling on the Mid-Atlantic Ridge. *J. Geophys. Res.*, **81**, 4042-4052.

43. Jones, M. T., & Roberts, D. G., (1975). Magnetic anomalies in the north-east Atlantic, north sheet. Institute of Oceanographic Sciences, U. K.
44. Kharin, G. N., (1967). The petrology of magmatic rocks. DSDP Leg 38. in Talwani, M., Udintsev, G., *et al.*, (1976). Init. Repts. DSDP, 38, Washington (U.S. Govt. Printing Office), 685-716.
45. Kidd, R. G. W., (1977). A model for the process of formation of the upper oceanic crust. Geophys. J. R. astr. Soc., 50, 149-183.
46. Kristofferson, Y., (1978). Seafloor spreading and the early opening of the north Atlantic. Earth. Plan. Sci. Lett., 38, 237-290.
47. LaBrecque, J. L., Kent, D. V., & Cande, S. C., (1977). Revised magnetic polarity timescale for Late Cretaceous and Cenozoic time. Geology, 5, 330-335.
48. Lacoste, L. J. B., (1967). Measurement of gravity at sea and in the air. Rev. Geophys. Space. Phys., 5, 477-526.
49. Larson, H. C., (1984). Geology of the East Greenland shelf, in: Spencer, A. M., *et al.* (eds), Petroleum geology of the north European margin. Graham & Trotman, London, 329-339.
50. Laughton, A. S., Berggren, W. A., *et al.*, (1972). Init. Repts. DSDP, 12, Washington (U.S. Govt. Printing Office).
51. Lewis, B. T. R., (1978). Evolution of oceanic crust seismic velocities. Ann. Rev. Earth & Planet. Sci., 6, 627-645.
52. Leg 81 Scientific Party, (1982). Leg 81 drills west margin, Rockall Plateau. Geotimes, September, 1982, 21-23.
53. Leg-104 Scientific Party, (1986). Dipping reflectors in the Norwegian Sea - ODP leg 104 drilling results. J. Geol. Soc. London, 143, 911-912.
54. Livermore, R. A., (1980). A gravity-derived model of the western margin of Rockall microcontinent. M.Sc. thesis, University of Durham.
55. Ludwig, J. W., Nafe, J. E., & Drake, C. L., (1970). Seismic refraction, in The Sea, 4, 53-84, ed. Maxwell, A. E., Wiley, New York.
56. Matthews, D. J., (1939). Tables of the velocity of sound in pure water and seawater for use in echo sounding and echo ranging. Admiralty Hydrographic Dept., London, 52 pages.
57. Mayne, W. H., (1962). Common-reflection point horizontal stacking techniques. Geophys., 27, 927-938.
58. McKenzie, D. P., (1978). Some remarks on the development of sedimentary basins. Earth Planet. Sci. Lett., 40, 25-32.

59. Meiners, E. P., Lenz, L. L., Dalby, A. E., & Hornsby, J. M., (1972). Recommended standards for digital tape formats. *Geophys.*, **37**, 45-58. (Digital format C).
60. Meissner, R., (1986). *The continental crust : a geophysical approach*. Academic Press, Inc.
61. Miller, J. A., Roberts, D. G., & Matthews, D. H., (1973). Rocks of Grenville age from Rockall Bank. *Nature: Phys. Sci.*, **246**, 61.
62. Montadert, L., & Roberts, D. G., (1979). Init. Repts. DSDP., **48**, Washington (U.S. Govt. Printing Office).
63. Montadert, L., Roberts, D. G., De Charpal, O., & Guennoc, P., (1979). Rifting and subsidence of the northern Bay of Biscay. *In*, Montadert, L., Roberts, D. G., *et al.*, Init. Repts. DSDP, **48**; Washington (U.S. Govt. Printing Office), 1025-1060.
64. Morton, A. C., & Taylor, P. N., (1987). Lead Isotope evidence for the structure of the Rockall dipping-reflector passive margin. *Nature*, **326**, 381-383.
65. Mutter, J. C., Talwani, M., & Stoffa, P. L., (1982). Origin of seaward-dipping reflectors in oceanic crust off the Norwegian margin by "subaerial seafloor spreading". *Geology*, **10**, 353-357.
66. Mutter, J. C., Talwani, M., & Stoffa, P. L., (1984). Evidence for a thick oceanic crust adjacent to the Norwegian margin. *J. Geophys. Res.*, **89(b)** , 483-502.
67. Mutter, J. C., (1985). Seaward-dipping reflectors and the continent-ocean boundary at passive continental margins. *Tectonophysics*, **114**, 117-131.
68. Ness, G., Levi, S., & Crouch, R., (1980). Marine magnetic anomaly timescales for the Cenozoic and Late Cretaceous: a precis, critique, and synthesis. *Rev. Geophys. Space. Phys.*, **18**, 753-770.
69. Næide, N. S., & Taner, M. T., (1971). Semblance and other coherency measures for multichannel data. *Geophys.*, **36**, 482-497.
70. Northwood, E. J., Weisinger, R. C., & Bradley, J. J., (1967). Recommended standard for digital tape formats. *Geophys.*, **32**, 1073-1084. (Digital formats A and B).
71. Nunns, A. G., (1980). *Marine geophysical investigations in the Norwegian-Greenland Sea between the latitudes of 62° N and 74° N*. Ph.D. thesis, University of Durham.
72. Parsons, B., & Sclater, J. G., (1977). An analysis of the variation of ocean floor bathymetry and heatflow with age. *J. Geophys. Res.*, **82**, 803-827.
73. Peacock, K. L., & Treitel, S., (1969). Predictive deconvolution : theory and practice. *Geophys.*, **34**, 155-169.

74. Pollack, H. N., & Chapman, D. S., (1977). On the regional variation of heat flow, geotherms, and lithospheric thickness. *Tectonophysics*, **38**, 279-296.
75. Poulter, M. J., (1982). The design and implementation of the Durham University seismic processing system. Ph.D. Thesis, University of Durham.
76. Press, W. H., Flannery, B. P., Teukolsky, S. A., & Vetterling, W. T., (1986). *Numerical recipes : the art of scientific computing*. Cambridge University Press, Cambridge, 818 pages.
77. Rabinowitz, P. D., & LaBrecque, J. L., (1977). The isostatic gravity anomaly: Key to the evolution of the ocean-continent boundary at passive continental margins. *Earth Planet. Sci. Lett.*, **35**, 145-150.
78. Raitt, R. W., (1963). The crustal rocks, *in* *The Sea*, **3**, Wiley-Interscience, New York, 85-102.
79. Ringwood, A. E., (1969). Composition and evolution of the upper mantle. *Am. Geophys. Un. Geophys. Mono.*, **13**, 1-17.
80. Ringwood, A. E., (1975). *Composition and petrology of the Earth's mantle*. McGraw-Hill book company, New York, 618 pages.
81. Ringwood, A. E., & Green, D. H., (1966). An experimental investigation of the gabbro-eclogite transformation and some geophysical consequences. *Tectonophysics*, **3**, 383-427.
82. Roberts, D. G., Matthews, D. H., & Eden, R. A., (1972). Metamorphic rocks from the southern end of the Rockall Bank. *J. Geol. Soc. London*, **128**, 501-506.
83. Roberts, D. G., Ardur, D. A., & Dearnley, R., (1973). Precambrian rocks drilled on Rockall Bank. *Nature Phys. Sci.*, **244**, 21-23.
84. Roberts, D. G., (1975a). Marine geology of the Rockall Plateau and Trough. *Phil. Trans. R. Soc. London*, **A278**, 447-509.
85. Roberts, D. G., (1975b). Structural development of the British Isles, the continental margin, and Rockall Plateau, *in*: Burke, C. A., & Drake, C. L. (eds), *The geology of continental margins*. Springer Verlag, New York, pp 343-359,
86. Roberts, D. G., Montadert, L., & Searle, R. C., (1979). The western Rockall Plateau: stratigraphy and structural evolution. *in* Montadert, L., Roberts, D. G., et al., *Init. Repts. DSDP, 48*: Washington (US Govt. Printing Office), 1061-1088.
87. Roberts, D. G., Masson, D. G., & Miles, P. R., (1981). Age and structure of the southern Rockall Trough: new evidence. *Earth Planet. Sci. Lett.*, **52**, 115-128.

88. Roberts, D. G., Backman, J., Morton, A. C., Murray, J. W., & Keene, J. B., (1984). Evolution of volcanic rifted continental margins : synthesis of Leg 81 results on the west margin of Rockall Plateau, *in*; Init. Repts. DSDP, 81; Washington (U.S. Govt. Printing Office), 883-911.
89. Roberts, D. G., & Ginzburg, A., (1984). Deep crustal structure of the southeast Rockall Plateau. *Nature*, **308**, 435-439.
90. Roberts, D. G., Schnitker, D., *et al.*, (1984). Init. Repts. DSDP, 81, Washington (U.S. Govt. Printing Office).
91. Roots, W. D., & Srivastava, S. P., (1984) Origin of the marine magnetic quiet zones in the Labrador and Greenland Seas. *Mar. Geophys. Res.*, **6**, 395-408.
92. Ruddiman, W. F., (1972). Sediment redistribution on the Reykjanes Ridge : seismic evidence. *Geol. Soc. Am. Bull.*, **83**, 2039-2062.
93. Ryu, J. V., (1982). Decomposition (DECOM) approach applied to wavefield analysis with seismic reflection records. *Geophys.*, **47**, 869-884.
94. Sampson, R. J., (1975). The surface II graphics system. User manual, University of Durham Computer Centre, 239 pages.
95. Schuepbach, M. A., & Vail, P. R., (1980). Evolution of outer highs on divergent continental margins. *in* : Studies in geophysics ; continental tectonics : Washington, D.C., Natl. Acad. Sci., 50-61.
96. Salisbury, M. H., & Christensen, N. I., (1978). The seismic velocity structure of a traverse through the Bay of Islands ophiolite complex, Newfoundland, an exposure of oceanic crust and upper mantle. *J. Geophys. Res.*, **83**, 805-817.
97. Scrutton, R. A., (1970). Results of a seismic refraction experiment on Rockall Bank. *Nature*, **227**, 826-827.
98. Scrutton, R. A., (1972). The crustal structure of Rockall Plateau Microcontinent. *Geophys. J. R. astr. Soc.*, **27**, 259-275.
99. Scrutton, R. A., & Roberts, D. G., (1971). Structure of the Rockall Plateau and Trough, north-east Atlantic, *in*; ICSU/SCORNG31 Symposium Cambridge 1970 : The geology of the north-east Atlantic continental margin, *Inst. Geol. Sci., Rept. 70/14*, **2**, 77-87.
100. Skogseid, J., & Eldholm, O., (1987). Early Cenozoic crust at the Norwegian continental margin, and the conjugate Jan Mayen Ridge. *J. Geophys. Res.*, **92**, 11471-11491.
101. Smith, P. J., & Bott, M. H. P., (1975). Structure of the crust beneath the Caledonian foreland and Caledonian belt of the north Scottish shelf region. *Geophys. J., R. astr. Soc.*, **40**, 187-205.

102. Smythe, D. K., (1983). Faeroe-Shetland Escarpment and continental margin north of the Faeroes, *in*; Bott, M. H. P., Saxov, S., Talwani, M., & Theide, J., (editors), Structure and development of the Greenland-Scotland Ridge : New methods and concepts. Plenum, New York, 121-132.
103. Spence, G. D., White, R. S., Westbrook, G. K., & Fowler, S. R., (1988). The Hatton Bank continental margin I : shallow structure from two-ship expanding spread seismic profiles. Geophys. J. R. astr. Soc., (in press).
104. Spudich, D., & Orcutt, J., (1980). A new look at the seismic velocity structure of the oceanic crust. Rev. Geophys. Space. Phys., **18**, 627-645.
105. Srivastava, S. P., & Tapscott, C. R., (1986). Plate kinematics of the north Atlantic, *in*: Vogt, P. R., & Tucholke, D. E., (eds): The geology of north America, Volume M, , The western north Atlantic region. Geological society of America, pp 379-404.
106. Srivastava, S. P., (1978). Evolution of the Labrador Sea and its bearing on the early evolution of the north Atlantic. Geophys. J. R. astr. Soc., **52**, 313-357.
107. Stansell, T. A., (1978). The TRANSIT navigation satellite system: status, theory, performance, applications. Magnavox Government and Industrial Electronics Co., Advanced Products Division, 2829, Maricopa Street, Torrance, Calif. 90503, U.S.A., 83 pages.
108. Stoffa, P. L., & Buhl, P., (1979). Two-ship multichannel seismic experiments for deep crustal studies: expanded spread and constant offset profiles. J. Geophys. Res., **84**, 7645-7660.
109. Stow, D. A. V., & Holbrook, J. A., (1984). Hatton Drift contourites, north-east Atlantic, Deep Sea Drilling Project Leg 81, *in*; Roberts, D. G., Schnitker, D., *et al.*, Init. Repts. DSDP, **81**, Washington (U.S. Govt. Printing Office).
110. Talwani, M., & Eldholm, O., (1977). Evolution of the Norwegian-Greenland Sea. Geol. Soc. Am. Bull., **88**, 969-999.
111. Talwani, M., Mutter, J. C., & Eldholm, O., (1981). The initiation of opening of the Norwegian Sea. Oceanologica Acta, N° SP, 123-30.
112. Talwani, M., Mutter, J. C., & Hinz, K., (1983). Ocean continent boundary under the Norwegian continental margin, *in*; Bott, M. H. P., Saxov, S., Talwani, M., & Theide, J., (editors), Structure and development of the Greenland-Scotland Ridge : New methods and concepts. Plenum, New York, 121-132.
113. Talwani, M., Udentsev, G., *et al.*, (1976). Init. Repts. DSDP, **38**, Washington (U.S. Govt. Printing Office), 1256 pages.
114. Taner, M. J., & Koehler, F., (1969). Velocity spectra - digital computer derivation and applications of velocity functions. Geophys., **34**, 859-881.

115. Tiley, G. J., (1984). A ray tracing study of the seismic structure of the Lesser Antilles accretionary complex. M.Sc. Thesis, University of Durham.
116. Uruski, C. I., & Parson, L. M., (1985). A compilation of geophysical data on the east Greenland continental margin, and its use in gravity modelling across the continent-ocean transition. I.O.S. Report No. 214, 53 pages.
117. Vogt, P. R., & Avery, O. E., (1974). detailed magnetic surveys in the northeast Atlantic and Labrador Sea. *J. Geophys. Res.*, **79**, 363-389.
118. Voppel, D.; & Rudloff, R., (1980). On the evolution of the Reykjanes Ridge south of 60° N between 40 and 12 million years before present. *J. Geophys.*, **47**, 61-66.
119. Voppel, D., Srivastava, S. P., & Fleischer, U., (1979). Detailed magnetic measurements south of the Iceland-Faeroe Ridge. *Dt. hydrogr. z.*, **32**, H. 4., 154-172.
120. White, R. S., Spence, G. D., Fowler, S. R., McKenzie, D. P., Westbrook, G. K., & Bowen, A. N., (1987). Magmatism at rifted continental margins. *Nature*, **330**, pp. 439-444.
121. White, R. S., Westbrook, G. K., Fowler, S. R., Spence, G. D., Barton, P. J., Joppen, M., Morgan, J., Bowen, A. N., Prescott, C. N., & Bott, M. H. P., (1986). Hatton-Bank (north-west U. K.) continental margin structure. *Geophys. J. R. astr. Soc.*, **89**, 265-272.
122. Whitmarsh, R. B., Avedik, F., & Saunders, M. F., (1986). The seismic structure of thinned continental crust in the northern Bay of Biscay. *Geophys. J. R. astr. Soc.*, **86**, 589-602.
123. Wigginton, G. M., (1984). Seismic reflection, gravity and magnetic studies over the Outer Banks, south-west of the Faeroes islands. M.Sc. thesis, University of Durham.
124. Woollard, G. P., 1970. Evolution of the isostatic mechanism, and the role of mineralogical transformations from seismic and gravity data. *Phys. Earth & Plan. Interiors*, **3**, 484-498.
125. Worzel, J. I., (1974). Standard oceanic and continental structure. *in* Burk, C. A., & Drake, C. L., (eds). *The geology of continental margins*, Springer-Verlag, New York, 59-66.



## Appendix A.

### Listings of computer programs.

Appendix A contains listings of the program source codes referenced in the text of this thesis. All program are written in FORTRAN 77, and were compiled using the FORTRANVS compiler on the University of Durham Computer Centre AM-DAHL 470V8 mainframe computer. Each program listing comprises an introductory comment block which explains briefly the program function and gives details of input/output channels used. This is followed by the main program which is fully commented. Subroutines called by the main routine contain their own explanatory header, and are also fully commented. Programs or subroutines written by persons other than the author are given appropriate references.

The programs which appear in this appendix are:-

**MERGE, PROCESS, XDIST, GRAV, UDDERSTK,**

**DEPTH, HEAT, MAGTRK, CMPENV.**

# PROGRAM MERGE

```

* Program merges RRS Charles Darwin dead-reckoning (DR) navigation files
* with geophysical data files (gravity and magnetic anomaly, and
* bathymetry) on the basis of recorded time.
* Set check index...
* INPUT
* Read on unit 4 : DR navigation file.
* Read on unit 5 : Geophysical data.
* OUTPUT
* Written to unit 7 : Merged data and associated time.
  N=0
* Read first navigation point...
  READ(4,1000)IDAYN,IIIRN,IMINN,ISECN,DLAT,DLON
* Read first data point...
10  READ(5,1000,END=996)IDAYD,IIIRD,IMIND,ISECD,DATA,ANOM
  N=N+1
* Perform required checks.
* Start of data cannot be before start of
* navigation data. Step forward in data file
* until condition is satisfied...
  IF(IDAYD.LT.IDAYN)GOTO 10
  IF(IDAYD.EQ.IDAYN.AND.IIIRD.LT.IIIRN)GOTO 10
  IF(IDAYD.EQ.IDAYN.AND.IIIRD.EQ.IIIRN.AND.IMIND.LT.IMINN)GOTO 10
  IF(IDAYD.EQ.IDAYN.AND.IIIRD.EQ.IIIRN.AND.IMIND.EQ.IMINN.AND.ISECD
&.LT.ISECN)GOTO 10
  N=N-1
  WRITE(6,FMT='(//,"***No. of data points before start of nav file='
&','I5,','")N
* Start merge search.
* Read first data point & navigation fixes...
  N=0
  READ(5,1000)IDAYD,IIIRD,IMIND,ISECD,DLAT,DLON
20  READ(4,1000,END=997)IDAYN,IIIRN,IMINN,ISECN,DATA,ANOM
  IF(IDAYN.EQ.IDAYD.AND.IIIRD.EQ.IIIRN.AND.IMIND.EQ.IMINN.AND.ISECD
&.EQ.ISECN)THEN
    WRITE(7,2000)IDAYN,IIIRN,IMINN,ISECN,DLAT,DLON,DATA,ANOM
    N=N+1
    READ(5,1000,END=998)IDAYD,IIIRD,IMIND,ISECD,DLAT,DLON
    GO TO 20
  ELSE
    GO TO 20
  ENDIF
1000 FORMAT(3X,I3,1X,I2,1X,I2,1X,I2,1X,E14.6,3X,E14.6)
2000 FORMAT(3X,I3,1X,I2,1X,I2,1X,I2,1X,I2,1X,F12.4,3X,F12.4,3X,F12.4,3X,F12
&.4)
996  WRITE(6,FMT='(//,"**Unable to match first Navigation fix**")')
  WRITE(6,FMT='(***with data points:Termination of run. ***./)')
  GOTO 999
997  WRITE(6,FMT='(//,"**EOF on Navigation data (unit 5):***")')
  WRITE(6,FMT='(*** Normal Termination. ***./)')
  GOTO 999
998  WRITE(6,FMT='(//,"**EOF on Geophysics data (unit 4):***")')
  WRITE(6,FMT='(*** Normal Termination. ***./)')
999  WRITE(6,FMT='(***No of data points written out=" ,I4)'N
  STOP
  END

```

# PROGRAM PROCES

- \* CN Prescott, 1986.
- \* Program to Window, interpolate, and smooth gravity, magnetic or bathymetric data. Input data must be formatted as on tape GMDCPY (appendix B). Output format depends in detail on the exit point chosen, but is in general the same for all data. Differences are in the flagging of data at the various stages of processing. If required, the program can be exited after each process.
- \* OUTPUT
  - \* Unit 7 : Discovery windowed data, or concatenated Discovery/Darwin windowed data.
  - \* Unit 8 : Darwin windowed data.
  - \* Unit 9 : Interpolated output.
  - \* Unit 10 : Smoothed output.
- \* INPUT
  - \* Unit 2 : Darwin raw data.
  - \* Unit 3 : Discovery raw data.
  - \* Unit 4 : Windowed data (input to interpolation stage).
  - \* Unit 5 : Interpolated (input to smoothing stage).
- \* Output at all stages uses the same basic format for ship,day,hr,min,sec,anom,lat,lon. This is...(A4,I4,3I3,3F13.4). It is only sensible to carry on to interpolation and smoothing if there is a single windowed output data file. This is defaulted to -WIND7.DAT when a single output file is indicated. Thus if smoothing and interpolation is required for separate files, the program must be run twice.
- \*

```

      CHARACTER*4 DATG,DAT1,DATN
      CHARACTER*4 IDSHIP,ANS,FLAG2(500)
      CHARACTER*4 REPLY
      INTEGER*4 OUNIT,LUNIT
      INTEGER DSEC,IDY,ITIM1,ITIM2,ITIM3,FLAG(500)
      INTEGER DELTAT,DELT,DELSEC,IFLG
      REAL ARRAY,LAT,LON,TIME,MIN,INDEX,LLIM
      DIMENSION ARRAY(500),LAT(500),LON(500),TIME(500)
      DIMENSION IDY(500),ITIM1(500),ITIM2(500),ITIM3(500)
      DIMENSION WEIGHT(500)
* Statement function to get time diff in secs between readings...
      INSECT(IDAY,IHR,IMIN,ISEC,IDAY2,IHR2,IMIN2,ISEC2)=
&1ABS(
& (ISEC2-ISEC)+
& 60 * (IMIN2-IMIN)+
& 3600 * (IHR2 - IHR)+
&86400 * (IDAY2-IDAY))
      N=1
      IFLG2=0
      ISRCH=0
      WRITE(6,(/, '*** WINDOWING ROUTINE **',/))
      WRITE(6,FMT='(" & **Data write out to same (S/s) file?")')
      READ(6,FMT='(A4)')REPLY
      IF(REPLY.EQ.'S'.OR.REPLY.EQ.'s')THEN
        WRITE(6,(/, '***All data written to -WIND7.DAT."'))
      ELSE
        WRITE(6,(/, '***Discovery data written to -WIND7.DAT."'))
        WRITE(6,(/, '***Darwin data written to -WIND8.DAT."'))
      ENDIF
10  WRITE(6,FMT='(/, ' & **Discovery or Darwin window(DI/DA)?")')
      READ (6,FMT='(A4)')IDSHIP
      IF(IDSHIP.EQ.'DI'.OR.IDSHIP.EQ.'di')THEN
        LUNIT=3
        OUNIT=7
      ELSE
        LUNIT=2
        IF(REPLY.EQ.'S'.OR.REPLY.EQ.'s')THEN
          QUNIT=7
        ELSE
          OUNIT=8
        ENDIF
      ENDIF
* Start windowing loop....read windowing parameters:-
      LLIM=-5000.0
      ULIM= 5000.0

```

```

        WRITE(6,FMT='(/,"&"**Enter start/finish day and times:-")')
        READ(6,*)IDAYST,IDAYFN,TIMST,TIMFN
        IF(IDAYST.LT.1)GOTO 99
* Find first valid data point.
1    READ(LUNIT,FMT=2000,END=97)IDAY,ITIME1,ITIME2,ITIME3,ANOM
        &,DLAT,DLON
        TIM=TYME(ITIME1,ITIME2,ITIME3)
        IF (IDAY.LT.IDAYST)GOTO 1
        IF (IDAY.EQ.IDAYST.AND.TIM.LT.TIMST)GOTO 1
        IF (IDAY.EQ.IDAYFN.AND.TIM.GT.TIMFN)GOTO 97
        IF (IDAY.GT.IDAYFN)GOTO 97
* Window data...
        WRITE(6,'(/,"!!First valid data point found..."')
        WRITE(6,'("Time=" ,A4)')IDAY,ITIME1,ITIME2,ITIME3
        IFLG2=IFLG2+1
        ISRCH=0
2    READ(LUNIT,FMT=2000,END=99)IDAY,ITIME1,ITIME2,ITIME3,ANOM
        &,DLAT,DLON
        TIM=TYME(ITIME1,ITIME2,ITIME3)
        IF (IDAY.EQ.IDAYFN.AND.TIM.GT.TIMFN.OR.IDAY.GT.IDAYFN)GO TO 98
        IF(ANOM.GT.ULIM)GOTO 2
        IF(ANOM.LT.LLIM)GOTO 2
        WRITE(OUNIT,FMT=2020)IDSHIP,IDAY,ITIME1,ITIME2,ITIME3,ANOM,DLAT,
        &DLON,IFLG2
        N=N+1
        GO TO 2
* Window out of data range:try again?
97    WRITE(6,FMT='(/,"!!Window out of data range!!")')
        IF(ISRCH.EQ.0)THEN
            WRITE(6,FMT='(" &??Rewinding and searching again..."')
            REWIND LUNIT
            ISRCH=1
            GOTO 1
        ELSE
            WRITE(6,'("!!Unable to find data within window range!!")')
            WRITE(6,'(" &??Define new window?"')
            READ(6,'(A4)')ANS
            IF(ANS.EQ.'Y'.OR.ANS.EQ.'y')THEN
                ISRCH=0
                GOTO 10
            ELSE
                GOTO 99
            ENDIF
        ENDIF
* End of windowing to current data set?
98    WRITE(6,FMT='(/,"&"**Repeat window? (Y/N)"')
        READ (6,FMT='(A4)')ANS
        IF(ANS.EQ.'Y'.OR.ANS.EQ.'y')GO TO 10
* Exit section.
99    N=N-1
        WRITE(6,FMT='(/,"**Data windowing ends.**")')
        WRITE(6,FMT='(/,"**No of data points=",I5)')N
        IF(REPLY.NE.'S'.AND.REPLY.NE.'s')GOTO 9997
        WRITE(6,'(/,"&??Chain to interpolation routine? (Y/N)"')
        READ(6,'(A4)')ANS
        IF(ANS.EQ.'N'.OR.ANS.EQ.'n')GOTO 9997
* Read in first windowed data point and set up
* mandatory paramters...
        WRITE(6,'(/,"** INTERPOLATION ROUTINE **")')
        PI=3.141593
        DATG='G'
        DATN='N'
        DATI='I'
        LUNIT=4
        OUNIT=9
* Read first data point...
        READ(LUNIT,2020)IDSHIP,IDAY2,IHR2,IMIN2,ISEC2,ANOM2,DLAT2,DLON2
        &,IFLG2
* Read in rest of data point by point...
3    READ(LUNIT,2020,END=910,ERR=700)IDSHIP,IDAY,IHR,IMIN,ISEC,ANOM,
        &DLAT,DLON,IFLG

```

```

IF(IDSHIP.EQ.'DA'.OR.IDSHIP.EQ.'da')THEN
DELSEC=30
ELSE
DELSEC=120
ENDIF
IF(IFLG.NE.IFLG2)THEN
WRITE(6,('/',,'!!New section started!!'))
WRITE(OUNIT,200)IDSHIP,IDAY2,IIR2,IMIN2,ISEC2,ANOM2,DLAT2,DLON2
&,IFLG2,DATN
IDAY2=IDAY
IIR2=IIR
IMIN2=IMIN
ISEC2=ISEC
ANOM2=ANOM
DLAT2=DLAT
DLON2=DLON
TIMOLD=TIM
IFLG2=IFLG
GOTO 3
ENDIF
DELTAT=INSECT(IDAY,IIR,IMIN,ISEC,IDAY2,IIR2,IMIN2,ISEC2)
DELT=IABS(DELSEC-DELTAT)
* For data gap i 1hr flag with "G" and carry on...
IF(DELTAT.GT.3600)THEN
WRITE(OUNIT,200)IDSHIP,IDAY,IIR,IMIN,ISEC,ANOM,DLAT,DLON,IFLG
&,DATG
IDAY2=IDAY
IIR2=IIR
IMIN2=IMIN
ISEC2=ISEC
ANOM2=ANOM
DLAT2=DLAT
DLON2=DLON
TIMOLD=TIM
IFLG2=IFLG
GOTO 3
* Gaps i 1hr, Interpolate...
ELSE IF(DELT.GT.0.AND.DELTAT.LT.3600)THEN
WRITE(6,('/',,'!!Data gap found-interpolating...'))
* Determine no. of data values missing
* and calculate subsequent missing times...
IF(IDSHIP.EQ.'DA'.OR.IDSHIP.EQ.'da')THEN
DSEC=ISEC2-ISEC
IF(DSEC.LT.0)THEN
NGAP=(IMIN-IMIN2)*2+1
ELSE IF(DSEC.EQ.0)THEN
NGAP=(IMIN-IMIN2)*2
ELSE
NGAP=(IMIN-IMIN2)*2-1
ENDIF
ELSE
NGAP=INSECT(IDAY,IIR,IMIN,ISEC,IDAY2,IIR2,IMIN2,ISEC2)/120
ENDIF
* Save old times and data...
ISO=ISEC
IMO=IMIN
IIO=IIR
IDO=IDAY
ISEC=ISEC2
IMIN=IMIN2
IIR=IIR2
IDAY=IDAY2
N=NGAP-1
* Interpolate...
DO 20 J=1,N
IF(IDSHIP.EQ.'DA'.OR.IDSHIP.EQ.'da')THEN
ISEC=ISEC+30
IF(ISEC.EQ.60)THEN
ISEC=0
IMIN=IMIN+1
ENDIF

```

```

ELSE
ISEC=0
IMIN=IMIN+2
ENDIF
IF(IMIN.EQ.60)THEN
IMIN=0
IIIR=IIIR+1
ELSE
ENDIF
ANOM1=(FLOAT(J)*(ANOM-ANOM2)/FLOAT(NGAP))+ANOM2
DLAT1=(FLOAT(J)*(DLAT-DLAT2)/FLOAT(NGAP))+DLAT2
DLON1=(FLOAT(J)*(DLON-DLON2)/FLOAT(NGAP))+DLON2
WRITE(OUNIT,200)IDSHIP,IDAY,IIIR,IMIN,ISEC,ANOM1,DLAT1,DLON1,IFLG
&,DATI
20 CONTINUE
WRITE(OUNIT,200)IDSHIP,IDO,IIIO,IMO,ISO,ANOM,DLAT,DLON,IFLG,DATN
* Reset times...
IDAY2=IDO
IIIR2=IIIO
IMIN2=IMO
ISEC2=ISO
ANOM2=ANOM
DLAT2=DLAT
DLON2=DLON
TIMOLD=TIM
IFLG2=IFLG
GOTO 3
ELSE
WRITE(OUNIT,200)IDSHIP,IDAY,IIIR,IMIN,ISEC,ANOM,DLAT,DLON,IFLG,DATN
* Set old times...
IDAY2=IDAY
IIIR2=IIIR
IMIN2=IMIN
ISEC2=ISEC
ANOM2=ANOM
DLAT2=DLAT
DLON2=DLON
TIMOLD=TIM
IFLG2=IFLG
GOTO 3
ENDIF
* End of interpolation routine...chain to smoothing routine...
910 WRITE(6,/,,"**End of interpolation...")
WRITE(6,/, "&??Chain to smoothing routine? (Y/N)")
READ(6,/(A4))ANS
IF(ANS.EQ.'N'.OR.ANS.EQ.'n')GOTO 9998
WRITE(6,/,,"** SMOOTHING ROUTINE **")
LUNIT=5
OUNIT=10
6 READ(LUNIT,200,ERR=710,END=9999)IDSHIP
BACKSPACE LUNIT
IF(IDSHIP.EQ.'DA'.OR.IDSHIP.EQ.'da')THEN
NLEN=61
ELSE
NLEN=21
ENDIF
WRITE(6,/,,"**Operator length =",I5)NLEN
KLEN=NLEN-1
* Calculate sinc weighting coefficients...
WRITE(6,/,,"**Calculating weighting coefficients...")
AINC=2.0*PI/FLOAT(NLEN)
DO 210 J=1,NLEN
K=J-1
ANGLE=FLOAT(K)*AINC-PI
WEIGHT(J)=(COS(ANGLE)+1.0)/2.0
210 CONTINUE
* Read in NLEN data values.
DO 101 J=1,NLEN
READ(LUNIT,200,ERR=710,END=9999)IDSHIP,IDY(J),ITIM1(J),ITIM2(J),
&ITIM3(J),ARRAY(J),LAT(J),LON(J),FLAG(J),FLAG2(J)
101 CONTINUE

```

```

* Averaging section.
  K=NLEN/2+1
5  SUM=0.0
  WTSUM=0.0
  DO 30 J=1,NLEN
    WTSUM=WTSUM+WEIGHT(J)
    SUM=SUM+ARRAY(J)*WEIGHT(J)
30  CONTINUE
  AV=SUM/WTSUM
  WRITE(OUNIT,200,ERR=710,END=9999)IDSHIP,IDY(K),ITIM1(K),ITIM2(K),
    &ITIM3(K),AV,LAT(K),LON(K),FLAG(K),FLAG2(K)
* Move array elements back one place.
  DO 40 J=1,KLEN
    L=J+1
    IDY(J)=IDY(L)
    ITIM1(J)=ITIM1(L)
    ITIM2(J)=ITIM2(L)
    ITIM3(J)=ITIM3(L)
    TIME(J)=TIME(L)
    ARRAY(J)=ARRAY(L)
    LAT(J)=LAT(L)
    LON(J)=LON(L)
    FLAG(J)=FLAG(L)
    FLAG2(J)=FLAG2(L)
40  CONTINUE
* Read in next data point.
  READ(LUNIT,200,ERR=710,END=9999)IDSHIP,IDY(NLEN),ITIM1(NLEN),
    &ITIM2(NLEN),ITIM3(NLEN),ARRAY(NLEN),LAT(NLEN),LON(NLEN),FLAG(NLEN)
    &FLAG2(NLEN)
* Check for new track section and restart
* smoothing process if detected...
  IF(FLAG(NLEN).NE.FLAG(NLEN-1))THEN
    WRITE(6,/,",!!New section!!")
    GOTO 6
  ENDIF
  MIN=FLOAT(ITIM2(NLEN))+FLOAT(ITIM3(NLEN))/60.0
  TIME(NLEN)=FLOAT(ITIM1(NLEN))+MIN/60.0
  GOTO 5
200  FORMAT(A4,I4,3I3,3F13.4,2X,I2,A4)
2020  FORMAT(A4,I4,3I3,3F13.4,2X,I2,A4)
2000  FORMAT(3X,I3,1X,I2,1X,I2,1X,I2,16X,3F15.4)
* Program termination/error diagnostics.
700  WRITE(6,/,",!!Error in input/output...")
  WRITE(6,/,",!!Condition occurred in routine INTERP.")
  WRITE(6,/,",!!Execution terminated.")
  STOP
720  WRITE(6,/,",!!Error,invalid operator length.")
  WRITE(6,/,",!!Operator length nlen: (500 < NLEN < 3).")
  WRITE(6,/,",!!Operator should be odd.")
  WRITE(6,/,",&*(C)ontinue or (S)top?")
  READ(6,(A4))ANS
  IF(ANS.EQ.'C'.OR.ANS.EQ.'c')THEN
    GOTO 6
  ENDIF
710  WRITE(6,/,",!!Error in input/output...")
  WRITE(6,/,",!!Condition occurred in routine SMOOTH.")
  WRITE(6,/,",!!Execution terminated.")
  STOP
* Normal exit conditions...
9997  WRITE(6,/,",*** NORMAL TERMINATION. ***")
  WRITE(6,/,",***Processing:-")
  WRITE(6,/,",-----")
  WRITE(6,/,",*** (1)Window from: ",I4,2X,F5.2)IDAYST,TIMST
  WRITE(6,/,",*** To: ",I4,2X,F5.2)IDAYFN,TIMFN
  WRITE(OUNIT,/,",***Processing:-")
  WRITE(OUNIT,/,",-----")
  WRITE(OUNIT,/,",*** (1)Window from: ",I4,2X,F5.2)IDAYST,TIMST
  WRITE(OUNIT,/,",*** To: ",I4,2X,F5.2)IDAYFN,TIMFN
  STOP
9998  WRITE(6,/,",*** NORMAL TERMINATION. ***")
  WRITE(6,/,",***Processing:-")

```

```

WRITE(6,(' —————'))
WRITE(6,('*** (1) Window from: ',I4,2X,F5.2))IDAYST,TIMST
WRITE(6,('*** To: ',I4,2X,F5.2))IDAYFN,TIMFN
WRITE(6,('*** (2) Interpolation of data gaps. '))
WRITE(OUNIT,('/', '*** Processing: '))
WRITE(OUNIT,(' —————'))
WRITE(OUNIT,('*** (1) Window from: ',I4,2X,F5.2))IDAYST,TIMST
WRITE(OUNIT,('*** To: ',I4,2X,F5.2))IDAYFN,TIMFN
WRITE(OUNIT,('*** (2) Interpolation of data gaps. '))
STOP
9999 WRITE(6,('/', '*** NORMAL TERMINATION. ***'))
WRITE(6,('/', '*** Processing: '))
WRITE(6,(' —————'))
WRITE(6,('*** (1) Window from: ',I4,2X,F5.2))IDAYST,TIMST
WRITE(6,('*** To: ',I4,2X,F5.2))IDAYFN,TIMFN
WRITE(6,('/', '*** (2) Interpolation. '))
WRITE(6,('/', '*** (3) Smoothing. '))
WRITE(6,('*** Operator length ',I3, ' samples. '))NLEN
WRITE(OUNIT,('/', '*** Processing: '))
WRITE(OUNIT,(' —————'))
WRITE(OUNIT,('*** (1) Window from: ',I4,2X,F5.2))IDAYST,TIMST
WRITE(OUNIT,('*** To: ',I4,2X,F5.2))IDAYFN,TIMFN
WRITE(OUNIT,('/', '*** (2) Interpolation. '))
WRITE(OUNIT,('/', '*** (3) Smoothing. '))
WRITE(OUNIT,('*** Operator length ',I3, ' samples. '))NLEN
STOP
END

*
FUNCTION TYME(HIR,IMIN,ISEC)
* Function to decimalise time...
TYME=FLOAT(HIR)+FLOAT(IMIN)/60.0+FLOAT(ISEC)/3600.0
RETURN
END

*
SUBROUTINE DISTAZ(AL,OL,BL,CL,DIST,DAZ)
* G.K. WESTBROOK.
DOUBLE PRECISION DL,IIL,ERQ,PRQ,A,B,SS,VS,S1,V,CO,S,SDL,CDL,DIF,S1,
IC1,G,GA,EC,EL,TA,GS,FL,GL
DOUBLE PRECISION DIST
DIMENSION NL(50),A(2,50),NS(500),B(2,500),SI(50),CO(50),V(50),VS(5
100),SS(500),GA(50),TA(500),GS(500),TITLE(20),NT(500)
DTR=0.01745329
ER=6378.160
PR=6356.775
ERQ=ER**2
PRQ=PR**2
EC=(ERQ-PRQ)/ERQ
EL=(ERQ-PRQ)/PRQ
DL=AL*DTR
IIL=OL*DTR
SS(1)=DSIN(DL)
TA(1)=SS(1)/DCOS(DL)
VS(1)=ER/DSQRT(1-EC*SS(1)**2)
GS(1)=DSQRT(EL*SS(1)**2)
FL=BL*DTR
GL=CL*DTR
B(1,2)=FL
B(2,2)=GL
S1=DSIN(FL)
C1=DCOS(FL)
V1=ER/DSQRT(1-EC*S1**2)
DIF=IIL-GL
CDL=DCOS(DIF)
SDL=DSIN(DIF)
SS(2)=S1
VS(2)=V1
TA(2)=S1/C1
GS(2)=DSQRT(EL*S1**2)
G=GS(2)
T=(1.0-EC+EC*V1*S1/(VS(1)*SS(1)))*TA(1)
AT=ATAN(T)

```



```

PAZ=C1°T-S1°CDL
SL=SDL
AZ=ATAN2(SL,PAZ)
HQ=EL°C1°2°COS(AZ)°2
H=SQRT(HQ)
BAZ=ABS(AZ)-3.14159
IF(BAZ.GT.-1.0.OR.BAZ.LT.-2.14159) GO TO 57
FD=SDL°COS(AT)/SIN(AZ)
D=ARSIN(FD)
GO TO 58
57 D=ARSIN(COS(AT)*PAZ/COS(AZ))
58 DIST=V1*D*(1.0-D°2°HQ°(1.0-HQ))/6.0+D°3°G°H°(1.0-2.0°HQ)/8.0+D°4
1*(HQ°(4.0-7.0°HQ)-3.0°G°2°(1.0-7.0°HQ))/120.0-D°5°G°H/48.0)
DAZ=AZ/DTR
RETURN
END

```

# PROGRAM XDIST

```

*
*
* Program XDIST projects latitude, longitude, and geophysical (gravity
* and magnetic anomaly, and bathymetry) data perpendicularly onto a
* pre-defined line of section (LOS). The distance of the projected
* positions along the LOS are calculated and are plotted along with
* original positions to check on correct program function. The
* projected positions, distances along LOS, and associated geophysical
* data are written out for subsequent use by other programs (eg GRAV).
* INPUT
* Interactive input of LOS definition, plot title.
* Read on unit 5 : Position and geophysical data.
* OUTPUT
* Written to unit 8 : Projected data.
* Written to unit 9 : Auxiliary check plotfile.
*
      IMPLICIT DOUBLE PRECISION (A-H, O-Z)
      PARAMETER (DEGRAD=0.714532925199432946D-01)
      COMMON /ORIGIN/OLAT, OLON
      REAL UMPMX, UMPMN, VMPMX, VMPMN
      REAL XLAB, YLAB, ULAB, VLAB
      INTEGER IQUAD
      CHARACTER SP*4, TITLE*40
* Statement function to get time diff in secs between readings...
      INSECT(IDAY,IHR,IMIN,ISEC,IDAY2,IHR2,IMIN2,ISEC2)=
      &IABS(
      &(ISEC2-ISEC)+
      &60*(IMIN2-IMIN)+
      &3600*(IHR2-IHR)+
      &86400*(IDAY2-IDAY))
      Z=0.0D0
* Read in line of section (los) definition...
* Define viewing rectangle...
      WRITE(6,('/',," Line of section definition."))
      WRITE(6,('/',,"& ??Line of section origin lat/Lon..."'))
      READ(6,*)OLAT,OLON
      WRITE(6,('/',,"& ??Line of section end lat/Lon..."'))
      READ(6,*)BLAT,BLON
* Calculate LOS length...
      CALL DISTAZ(OLAT,OLON,BLAT,BLON,XLOS,DUMM)
      WRITE(6,('/',,"& ??Enter title(A40) or ;ret;..."'))
      READ(6,*(A40))TITLE
* calculate box dimensions and draw...
      IF(OLAT.GT.BLAT)THEN
        BXLTMX=OLAT
        BXLTMN=BLAT
      ELSE
        BXLTMX=BLAT
        BXLTMN=OLAT
      ENDIF
      IF(OLON.GT.BLON)THEN
        BXLNMX=OLON
        BXLNMN=BLON
      ELSE
        BXLNMX=BLON
        BXLNMN=OLON
      ENDIF
* Top left, bottom right...
      CALL MERCE(BXLTMX, BXLNMN, UMN, VMX, SF)
      CALL MERCE(BXLTMN, BXLNMX, UMX, VMN, SF)
* Vector to nd space mapping parameters...
      UMPMX=UMX
      UMPMN=UMN
      VMPMX=VMX
      VMPMN=VMN
      URANGE=UMPMX-UMPMN
      VRANGE=VMPMX-VMPMN
      WRITE(6,('/',,"Latitude range....",F10.4,/,
      &"Longitude range....",F10.4))VRANGE,URANGE
      IF(URANGE.GT.VRANGE)THEN

```

```

UMAP =0.9
VMAP =0.8*(VRANGE/URANGE)+0.1
ELSE
UMAP =0.8*(URANGE/VRANGE)+0.1
VMAP =0.9
ENDIF
CALL PAPER (1)
CALL PSPACE ( 0.1, UMAP, 0.1, VMAP)
CALL CSPACE ( 0.0, 1.0, 0.0, 1.0)
CALL MAP (UMPMN, UPMX, VMPMN, VMPMX)
CALL CTRMAG (5)
* Draw box...
CALL POSITN (UMPMN, VMPMX)
CALL JOIN (UMPMX, VMPMX)
CALL JOIN (UMPMX, VMPMN)
CALL JOIN (UMPMN, VMPMN)
CALL JOIN (UMPMN, VMPMX)
* Draw lines of lon/lat at 0.25deg intervals.
UINC=URANGE/50.0D0
VINC=VRANGE/50.0D0
CALL CTRMAG (10)
A =0.0D0
XMIN =DINT(OLON)-1.0D0
2  XDEG =XMIN+A*0.25D0
   XLAB =XDEG
   IF(XDEG.LT.OLON)THEN
     A =A+1.0D0
     GOTO 2
   ELSE IF(XDEG.GT.BLON)THEN
     GOTO 3
   ELSE
     CALL MERCE (BXLTMX, XDEG, UDEG, VDUM, SF)
     CALL PLOTNF (UDEG, VMX+VINC, XLAB, 2)
     CALL POSITN (UDEG,VMX)
     CALL JOIN (UDEG,VMN)
     A =A+1.0D0
     GOTO 2
   ENDIF
3  A =0.0D0
   YMIN =DINT(BLAT)
4  YDEG =YMIN+A*0.25D0
   YLAB =YDEG
   IF(YDEG.LT.BLAT)THEN
     A =A+1.0D0
     GOTO 4
   ELSE IF(YDEG.GT.OLAT)THEN
     GOTO 5
   ELSE
     CALL MERCE (YDEG, BXLNMN, UDUM, VDEG, SF)
     CALL PLOTNF (UMN-UINC, VDEG, YLAB, 2)
     CALL POSITN (UMN,VDEG)
     CALL JOIN (UMX,VDEG)
     A =A+1.0D0
     GOTO 4
   ENDIF
5  ULAB =UMPMN+UINC
   VLAB =VMPMN+VINC
   CALL BLUPEN
   CALL POSITN(ULAB, VLAB)
   CALL PLOTCS(ULAB, VLAB, TITLE)
* Calculate length & azimuth of line of section.
* First transform to (u,v) space...
CALL MERCE (OLAT, OLON, U0, V0, SF)
CALL MERCE (BLAT, BLON, U1, V1, SF)
CALL GRNPEN
CALL POINT (U0,V0)
CALL JOIN (U1,V1)
CALL REDPEN
* Set up line of section vector coefficients.
* AABS=Line of section magnitude...
AU =U1-U0

```

```

      AV = V1-V0
      AABS=DSQRT(AU**2+AV**2)
* Azimuth of Line of section, THETA.
* Do this by checking the sign of
* sin & cos in all four quadrants...
      SINTHT=AV/AABS
      COSTHT=AU/AABS
      CALL ANGL(SINTHT, COSTHT, DEGRAD, THETA, IQUAD)
      THETA1=THETA/DEGRAD
      WRITE(6,('Sintht.....',F10.4))SINTHT
      WRITE(6,('Costht.....',F10.4))COSTHT
      WRITE(6,('Theta(rad)',F10.4))THETA
      WRITE(6,('Theta(deg)',F10.4))THETA1
      WRITE(6,('Quadrant...',I10))IQUAD
* Set up small value to add to lat/lon if
* it coincides with a los definition point...
      SMALL=1.0D-06
* Loop for data...
      IFLG=1
      INDEX=1
1     READ (5,100,END=998,ERR=999)ID2,III2,IM2,IS2,ANOM,XLAT,XLON
* Check for line change...
      IF(INDEX.EQ.1)THEN
        IDT=0
        INDEX=INDEX+1
        ID=ID2
        III=III2
        IM=IM2
        IS=IS2
        GOTO 202
      ELSE
        IDT =INSECT(ID, III, IM, IS, ID2, III2, IM2, IS2)
        ID=ID2
        III=III2
        IM=IM2
        IS=IS2
        IF(IDT.GT.3600)IFLG=IFLG+1
      ENDIF
202  SIGN=1.0D0
      IF(XLAT.EQ.OLAT.OR.XLAT.EQ.BLAT)THEN
        WRITE(6,('/', '!!Data and los latitude-point coincidence!!'))
        WRITE(6,('!!Adjusting.....'))
        XLAT=XLAT+SMALL
        IF(XLON.EQ.OLON.OR.XLON.EQ.BLON)XLON=XLON+SMALL
        WRITE(6,('/', '!!Data and los longitude-point coincidence!!'))
        WRITE(6,('!!Adjusting.....'))
        XLON=XLON+SMALL
      ENDIF
* Transform to (u,v)...
      CALL MERCE(XLAT, XLON, U, V, SF)
* Set up data point vector coefficients.
* BABS=data point vector magnitude...
      BU =U-U0
      BV =V-V0
      BABS=DSQRT(BU**2+BV**2)
* Calculate alpha.
* Use scalar product of line of section and
* data point vectors...
      ALPIA=DACOS((AU*BU+AV*BV)/(AABS*BABS))
* Now project aabs onto babs to get
* projection length x...
      X=AABS*DCOS(ALPIA)
* Calculate azimuth of data point...
      SINGAM=BV/BABS
      COSGAM=BU/BABS
      CALL ANGL(SINGAM, COSGAM, DEGRAD, GAMMA, IDUMMY)
* Calculate from theta and gamma the sign of alpha...
      ALPSIN=THETA-GAMMA
      IF(ALPSIN.LT.0.0D0)SIGN=SIGN*(-1.0D0)
* Calculate x, the projection length of
* the point on the line of section.....

```

```

      X=BABS*DCOS(ALPHA)
* Calculate delta using pythag...
      DELTA=DSQRT(BABS**2-X**2)
* Using IQUAD and SIGN calculate udash, vdash...
* Quadrant 1...
      IF(IQUAD.EQ.1)THEN
        DU=DELTA*DSIN(THETA)
        DV=DELTA*DCOS(THETA)
        IF(SIGN.GT.0.0D0)THEN
          UDASH=U-DU
          VDASH=V+DV
        ELSE IF(SIGN.LT.0.0D0)THEN
          UDASH=U+DU
          VDASH=V-DV
        ENDIF
* Quadrant 2...
      ELSE IF(IQUAD.EQ.2)THEN
        FI=180.0D0*DEGRAD-THETA
        DU=DELTA*DSIN(FI)
        DV=DELTA*DCOS(FI)
        IF(SIGN.GT.0.0D0)THEN
          UDASH=U-DU
          VDASH=V-DV
        ELSE IF(SIGN.LT.0.0D0)THEN
          UDASH=U+DU
          VDASH=V+DV
        ENDIF
* Quadrant 3...
      ELSE IF(IQUAD.EQ.3)THEN
        FI=270.0D0*DEGRAD-THETA
        DU=DELTA*DCOS(FI)
        DV=DELTA*DSIN(FI)
        IF(SIGN.GT.0.0D0)THEN
          UDASH=U+DU
          VDASH=V-DV
        ELSE IF(SIGN.LT.0.0D0)THEN
          UDASH=U-DU
          VDASH=V+DV
        ENDIF
* Quadrant 4...
      ELSE IF(IQUAD.EQ.4)THEN
        FI=360.0D0*DEGRAD-THETA
        DU=DELTA*DSIN(FI)
        DV=DELTA*DCOS(FI)
        IF(SIGN.GT.0.0D0)THEN
          UDASH=U+DU
          VDASH=V+DV
        ELSE IF(SIGN.LT.0.0D0)THEN
          UDASH=U-DU
          VDASH=V-DV
        ENDIF
      ENDIF
      ENDIF
* Unless point lies outside defined grid,
* plot original and projected points...
      IF (U.GT.UMPMX.OR.U.LT.UMPMN
&.OR.V.GT.VMPMX.OR.V.LT.VMPMN)THEN
        CALL POSITN (U, V)
        CALL JOIN (UDASH, VDASH)
      ELSE
        CALL POSITN (U, V)
        CALL PLOTNC (U, V, 233)
        CALL JOIN (UDASH, VDASH)
      ENDIF
* Transform back to lat/lon...
      CALL MERCEI (UDASH, VDASH, XLATP, XLONP)
* Xdist along los...
      CALL DISTAZ (OLAT, OLON, XLATP, XLONP, DIST, AZ)
      IF(DIST.GT.XLOS)THEN
        GOTO 1
      ELSE
        WRITE(8,200)DIST,Z,ANOM,XLATP,XLONP,IFLG

```

```

      GOTO 1
    ENDIF
100  FORMAT(4X,14,3I3,3F13.4)
200  FORMAT(5F13.4,14)
998  CALL GREND
      STOP
999  WRITE(6,(' !!!ERROR!!! - Input Terminated. '))
      CALL GREND
      STOP
      END

```

---

```

      SUBROUTINE MERCE ( XLAT, XLON, X, Y, SF )
* M.J.Smith August 1986
* Mercator projection from the ellipsoid
* If true scale lat. other than equator, multiply
* rhs by
*  $\cos(\text{OLAT}) / \sqrt{1 - \text{ECC}^2 \sin^2(\text{OLAT})}$ 
* For inverse equations, divide X and Y by these.
      IMPLICIT DOUBLE PRECISION ( A-H, O-Z )
      LOGICAL INITC
      PARAMETER ( PI = 3.14159265358979312D0 )
      PARAMETER ( DEGRAD = 0.174532925199432946D-01 )
      PARAMETER ( EQRAD = 6378.16D0 )
      PARAMETER ( ECC = 0.081819643D0 )
      COMMON / ORIGIN / OLAT,OLON
      DATA INITC / .TRUE. /
      IF ( INITC ) THEN
        OLATR = OLAT * DEGRAD
        OLONR = OLON * DEGRAD
        SCAFAC =  $\cos(\text{OLATR}) / \sqrt{1.0D0 - (\text{ECC} * \sin(\text{OLATR}))^2}$ 
        PIB4 = PI / 4.0D0
        INITC = .FALSE.
      ENDIF
      PLAT = XLAT * DEGRAD
      PLON = XLON * DEGRAD
      X = SCAFAC * EQRAD * ( PLON - OLONR )
      ECSUM =  $(1.0D0 - \text{ECC} * \sin(\text{PLAT})) / (1.0D0 + \text{ECC} * \sin(\text{PLAT}))$ 
      Y = SCAFAC * EQRAD *  $\log(\tan(\text{PIB4} + \text{PLAT} / 2.0D0))$ 
      ECSUM ** ( ECC / 2.0D0 )
      SFM = SCAFAC *  $\sqrt{1.0D0 - (\text{ECC} * \sin(\text{PLAT}))^2} / \cos(\text{PLAT})$ 
      SF = SFM
      END

```

---

```

      SUBROUTINE MERCEI ( X, Y, XLAT, XLON )
* M.J.Smith August 1986
* Mercator projection from the ellipsoid - inverse
      IMPLICIT DOUBLE PRECISION ( A-H, O-Z )
      LOGICAL INITC
      PARAMETER ( PI = 3.14159265358979312D0 )
      PARAMETER ( DEGRAD = 0.174532925199432946D-01 )
      PARAMETER ( EQRAD = 6378.16D0 )
      PARAMETER ( ECC = 0.081819643D0 )
      COMMON / ORIGIN / OLAT,OLON
      DATA INITC / .TRUE. /
      IF ( INITC ) THEN
        OLATR = OLAT * DEGRAD
        OLONR = OLON * DEGRAD
        SCAFAC =  $\sqrt{1.0D0 - (\text{ECC} * \sin(\text{OLATR}))^2} / \cos(\text{OLATR})$ 
        PIB2 = PI / 2.0D0
        INITC = .FALSE.
      ENDIF
      XSCA = X * SCAFAC
      YSCA = Y * SCAFAC
      PLON = XSCA / EQRAD + OLONR
* Closed form:- For finding PLAT using iteration
      T =  $\exp(-\text{YSCA} / \text{EQRAD})$ 
      PLAT = PIB2 - 2.0D0 *  $\text{ATAN}(T)$ 
100  PLOLD = PLAT

```

```

ES = FES( ECC, PLAT )
PLAT = PIB2 - 2.0D0 * ATAN( T * ES )
PLDIFF = PLAT - PLOLD
IF( PLDIFF .GT. 1.0D-09 ) GO TO 100
XLAT = PLAT / DEGRAD
XLON = PLON / DEGRAD
END

```

---

```

SUBROUTINE DISTAZ(AL,OL,BL,CL,DIST,DAZ)
* Distance calculator accurate to 1 in 10**7 at 1600 km.
* Calculates distance between shot and station from decimal degrees.
* AL:lat1
* OL:lon1
* BL:lat2
* CL:lon2
* ORIGINAL VERSION G.K.WESTBROOK
  DOUBLE PRECISION DL,IIL,ERQ,PRQ,A,B,SS,VS,S1,V,CO,S,SDL,CDL,DIF,S1,
&C1,G,GA,EC,EL,TA,GS,FL,GL
  DOUBLE PRECISION DIST
  DIMENSION NL(50),A(2,50),NS(500),B(2,500),SI(50),CO(50),V(50),VS(5
&00),SS(500),GA(50),TA(500),GS(500),TITLE(20),NT(500)
  DTR=0.01745329
  ER=6378.160
  PR=6356.775
  ERQ=ER**2
  PRQ=PR**2
  EC=(ERQ-PRQ)/ERQ
  EL=(ERQ-PRQ)/PRQ
  DL=AL*DTR
  IIL=OL*DTR
  SS(1)=DSIN(DL)
  TA(1)=SS(1)/DCOS(DL)
  VS(1)=ER/DSQRT(1-EC*SS(1)**2)
  GS(1)=DSQRT(EL*SS(1)**2)
  FL=BL*DTR
  GL=CL*DTR
  B(1,2)=FL
  B(2,2)=GL
  S1=DSIN(FL)
  C1=DCOS(FL)
  V1=ER/DSQRT(1-EC*S1**2)
  DIF=IIL-GL
  CDL=DCOS(DIF)
  SDL=DSIN(DIF)
  SS(2)=S1
  VS(2)=V1
  TA(2)=S1/C1
  GS(2)=DSQRT(EL*S1**2)
  G=GS(2)
  T=(1.0-EC+EC*V1*S1/(VS(1)*SS(1)))*TA(1)
  AT=ATAN(T)
  PAZ=C1*T-S1*CDL
  SL=SDL
  AZ=ATAN2(SL,PAZ)
  IIQ=EL*C1**2*COS(AZ)**2
  II=SQRT(IIQ)
  BAZ=ABS(AZ)-3.14159
  IF(BAZ.GT.-1.0.OR.BAZ.LT.-2.14159) GO TO 57
  FD=SDL*COS(AT)/SIN(AZ)
  D=ARSIN(FD)
  GO TO 58
57 D=ARSIN(COS(AT)*PAZ/COS(AZ))
58 DIST=V1*D*(1.0-D**2*IIQ*(1.0-IIQ)/6.0+D**3*G*II*(1.0-2.0*IIQ)/8.0+D**4
&*(IIQ*(4.0-7.0*IIQ)-3.0*G**2*(1.0-7.0*IIQ))/120.0-D**5*G*II/48.0)
  DAZ=AZ/DTR
  RETURN
  END

```

---

```

DOUBLE PRECISION FUNCTION FES ( ECC, PLAT )
* M.J.Smith August 1986
* Function used in numerous subroutines

```

```

      IMPLICIT DOUBLE PRECISION ( A-H, O-Z )
      T1 = 1.0D0 - ECC * SIN( PLAT )
      T2 = 1.0D0 + ECC * SIN( PLAT )
      FES = SQRT( ( T1 / T2 )**ECC )
      END
*-----
      SUBROUTINE ANGL(SINANG, COSANG, DEGRAD, ANGLE, IQAD)
*
      IMPLICIT DOUBLE PRECISION (A-H, O-Z)
      INTEGER IQAD
* Quadrant 1...
      IF(SINANG.GT.0.0D0.AND.COSANG.GT.0.0D0)THEN
        ANGLE=DASIN(SINANG)
        IQAD=1
* Quadrant 2...
      ELSE IF(SINANG.GT.0.0D0.AND.COSANG.LT.0.0D0)THEN
        ANGLE=DASIN(SINANG)
        IQAD=2
* Quadrant 3...
      ELSE IF(SINANG.LT.0.0D0.AND.COSANG.LT.0.0D0)THEN
        ANGLE=360.0D0*DEGRAD-DACOS(COSANG)
        IQAD=3
* Quadrant 4...
      ELSE IF(SINANG.LT.0.0D0.AND.COSANG.GT.0.0D0)THEN
        ANGLE=360.0D0*DEGRAD-DACOS(COSANG)
        IQAD=4
      ENDIF
      RETURN
      END

```



# PROGRAM GRAV

```

* Author : M. H. P. Bott.
* Modified for two-ship requirements C. Prescott (1986).
* The program calculates the gravity anomaly at specified field points due
* to arbitrary two-dimensional bodies consisting of NB polygonal bodies
* and/or layers.
* Input from unit 5.
* Output to unit 6.
* Plot to unit 9.
* INPUT:
* Free format
* NS - No of station points.
* NB - No of polygonal bodies/layers.
* Polygonal bodies should be defined clockwise with the first
* point repeated to close the body.
* PLOT OPTIONS:
* IG=0 No plot required.
* IG=1 Plot required-automatic axes,vertical exaggeration x1.
* IG=2 Plot required-vertical exaggeration supplied.
* IG=3 Plot required-vertical exaggeration and axes supplied.
* RG - Regional background (MGAL).
* RGG - Regional gradient (MGAL/KM).
* TITLE - Using i 32 characters in single quotation marks.
* BODY-POINT DATA:
* N,RHO(I) - No of body points, layer density contrast (kg/m3).
* XP(J),ZP(J) - Body point (x,z) data, j=1,N
* FIELD-POINT DATA:
* VE Vertical exaggeration.
* XMIN,XMAX,FMIN,FMAX
* XS(K), ZS(K), FO(K), K=1,NS
  DIMENSION XS(1024),ZS(1024),FO(1024),FC(1024),RES(1024),NP(25),
  &RHO(25),SN(200),CN(200),XB(25,200),ZB(25,200)
  CHARACTER*32 LIST
  CHARACTER*4 ESP
* Read input parameters:-
  READ (5,*)NS,NB,IG,RG,RGG,LIST
  ISTA=NS
* densities...
  DO 10 I=1,NB
    READ(5,*)N,RHO(I)
    NP(I)=N
* body points...
  DO 41 J=1,N
    READ(5,'(2F13.4)')XB(I,J),ZB(I,J)
41  CONTINUE
10  CONTINUE
    VE=1.0
    IF (IG.LE.1) GOTO 11
    READ(5,*)VE
    IF (IG.EQ.2) GOTO 11
    READ(5,*)XMIN,XMAX,FMIN,FMAX
11  IF (NS.GT.1) GOTO 13
    READ(5,*)XSTART,XSTEP,ZSTA,NS
    DO 12 K=1,NS
      XS(K)=XSTART+XSTEP*(K-1)
      ZS(K)=ZSTA
12  FO(K)=0.0
    GOTO 14
13  READ(5,'(3F13.4)')(XS(K),ZS(K),FO(K),K=1,NS)
14  DO 15 K=1,NS
15  FC(K)=RG+RGG*(XS(K)-XS(1))
* Main calculation (checked against GRAV2D 5/10/84 MHPB)
  DO 50 I=1,NB
    N=NP(I)
    DO 51 J=2,N
      R=SQRT((XB(I,J)-XB(I,J-1))**2+(ZB(I,J)-ZB(I,J-1))**2)
      IF (R.GT.0.001) GOTO 48
      SN(J)=0.0
      CN(J)=1.0
      GOTO 49
48  SN(J)=(ZB(I,J)-ZB(I,J-1))/R

```

```

      CN(J)=(XB(I,J-1)-XB(I,J))/R
49  CONTINUE
51  CONTINUE
      DO 50 K=1,NS
      DO 50 J=1,N
      X2=XB(I,J)-XS(K)
      Z2=ZB(I,J)-ZS(K)
      R2=X2*X2+Z2*Z2
      P2=0.0
      IF (R2.LE.0.0001) GOTO 52
      P2=ATAN2(Z2,X2)
52  IF (J.EQ.1) GOTO 53
      F=X1*SN(J)+Z1*CN(J)
      G=Z2*P2-Z1*P1
      IF (R1.LE.0.0001) GOTO 54
      IF (R2.LE.0.0001) GOTO 54
      G=G+F*((P1-P2)*CN(J)+0.5*SN(J)*ALOG(R1/R2))
54  FC(K)=FC(K)+0.01334*G*RIIO(I)
53  X1=X2
      Z1=Z2
      R1=R2
50  P1=P2
      SUM=0
      FOM=0.0
      FCM=0.0
      FOV=0.0
      FCV=0.0
      FCO=0.0
      DO 55 K=1,NS
      FOM=FOM+FO(K)
      FCM=FCM+FC(K)
      FOV=FOV+FO(K)**2
      FCV=FCV+FC(K)**2
      FCO=FCO+FC(K)*FO(K)
      RES(K)=FO(K)-FC(K)
55  SUM=SUM+RES(K)**2
      RMS=SQRT(SUM/NS)
      FOV=FOV-FOM**2/NS
      CC=0.0
      IF (FOV.LE.0.01) GOTO 56
      CC=(FCO-FOM*FCM/NS)/SQRT(FOV*(FCV-FCM**2/NS))
56  CONTINUE
* Printed output...
      WRITE(6,2)LIST,RG,RGG
2   FORMAT(10X,A//,'UNITS: KM, KG/M3, MGAL',4X,'REGIONAL =' ,F6.2,
$' MGAL REGIONAL GRADIENT = ' ,F4.2, ' MGAL/KM')
      DO 70 I=1,NB
      WRITE(6,3)I,RIIO(I)
3   FORMAT(//,'BODY NO ',I2,6X,'DENSITY CONTRAST =' ,F7.1, ' KG/M3',
$//6X,'X',9X,'Z')
      N=NP(I)
      WRITE(6,4)(XB(I,J),ZB(I,J),J=1,N)
4   FORMAT(2F10.2)
70  CONTINUE
      IF (ISTA.EQ.1) GOTO 71
      WRITE(6,5)
5   FORMAT(///'RESULTS',//7X,'X',9X,'Z',7X,'OBSERVED',1X,'CALCULATED',
$1X,'RESIDUAL')
      WRITE(6,6)(XS(K),ZS(K),FO(K),FC(K),RES(K),K=1,NS)
6   FORMAT(5F10.2)
      WRITE(6,7)RMS,CC
7   FORMAT('RMS RESIDUAL =' ,F5.2,'MGAL CORRELATION COEFF =' ,F6.4)
      GOTO 61
71  WRITE(6,8)
8   FORMAT(///'RESULTS',//7X,'X',9X,'Z',7X,'ANOMALY')
      WRITE(6,9)(XS(K),ZS(K),FC(K),K=1,NS)
9   FORMAT(3F10.2)
* Plotfile...
61  IF (IG.EQ.0) GOTO 62
      IF (IG.GE.3) GOTO 63
      FMAX=FO(1)

```

```

      FMIN=FO(1)
      DO 60 K=1,NS
      FMIN=AMIN1(FMIN,FO(K),FC(K))
60    FMAX=AMAX1(FMAX,FO(K),FC(K))
      D=(FMAX-FMIN)/10.0
      FMAX=FMAX+D
      FMIN=FMIN-D
      XMIN=XS(1)
      XMAX=XS(NS)
63    YP=4.0*(XMAX-XMIN)/(8.5*VE)
      CALL PAPER(1)
      CALL MAP (XMIN,XMAX,FMIN,FMAX)
      CALL PSPACE(0.10,0.95,0.5,0.9)
      CALL CSPACE(0.0,1.0,0.0,1.0)
      CALL BORDER
      CALL CTRMAG(8)
      CALL SCALES
      CALL CTRFNT(1)
      IF (ISTA.EQ.1) GOTO 64
      CALL GRNPEN
      CALL CURVEO(XS,FO,1,NS)
      DO 115 K=1,NS
      CALL BROKEN(6,6,6,6)
      IF(K.EQ.1)THEN
      CALL PLOTNC(XS(K),FO(K),224)
      CALL FULL
      ELSE IF((K/20)*20.EQ.K)THEN
      CALL PLOTNC(XS(K),FO(K),224)
      ENDIF
115  CONTINUE
64    CALL REDPEN
      CALL BROKEN(6,6,6,6)
      CALL CURVEO(XS,FC,1,NS)
      CALL FULL
      DO 116 K=1,NS
      IF(K.EQ.1)THEN
      CALL PLOTNC(XS(K),FC(K),227)
      ELSE IF((K/20)*20.EQ.K)THEN
      CALL PLOTNC(XS(K),FC(K),227)
      ENDIF
116  CONTINUE
* Plot CMP positions...
      NCMP=1
      INDEX=1
      CALL BLUPEN
      CALL CTRMAG(3)
      CALL CTROI(90.0)
1003 READ(3,'(2F13.4)',END=1004)XCMP,ZCMP
      IF(INDEX.EQ.1)THEN
      CALL PLOTNC(XCMP,RG,42)
      CALL PLOTNI(XCMP,RG,NCMP)
      INDEX=INDEX+1
      NCMP=NCMP+1
      GOTO 1003
      ELSE IF((NCMP/100)*100.EQ.NCMP)THEN
      CALL PLOTNC(XCMP,RG,42)
      CALL PLOTNI(XCMP,RG,NCMP)
      NCMP=NCMP+1
      GOTO 1003
      ELSE
      NCMP=NCMP+1
      GOTO 1003
      ENDIF
1004 CALL CTRMAG(15)
      CALL BLKPEN
      CALL CTROI(0.0)
      CALL BROKEN(3,3,3,3)
      CALL POSITN(XS(1),RG)
      R=RG+RGG*(XS(NS)-XS(1))
      CALL JOIN (XS(NS),R)
      CALL FULL

```

```

      CALL MAP (XMIN,XMAX,YP,0.0)
      CALL PSPACE(0.10,0.95,0.01,0.41)
      CALL BORDER
      CALL YSCALE
      DO 80 I=1,NB
      N=NP(I)
      CALL POSITN(XB(I,1),ZB(I,1))
      DO 80 J=2,N
      CALL JOIN (XB(I,J),ZB(I,J))
80    CONTINUE
* Read & plot esp positions...
      NESP=1
      CALL CTRMAG(10)
      CALL BLUPEN
      CALL BROKEN(3,3,3,3)
1001  READ(4,'(2F13.4,A4)',END=1002)XESP,ZESP,ESP
      CALL PLOTNC(XESP,ZESP,187)
      CALL PLOTCS(XESP,ZESP-1.0,ESP)
      CALL JOIN (XESP,45.0)
      GOTO 1001
1002  CALL POSITN(XMIN,0.0)
      CALL FULL
      CALL BLKPEN
      CALL CTRMAG(15)
      CALL JOIN (XMAX,0.0)
      CALL MAP (0.0,1.0,0.0,1.0)
      CALL CSPACE(0.0,1.0,0.0,1.0)
      CALL PSPACE(0.0,1.0,0.0,1.0)
      CALL CTRFNT(1)
      CALL PLOTCS(0.15,0.95,LIST)
      CALL GRNPEN
      CALL PLOTNC(0.6,0.95,224)
      CALL PLOTCS(0.63,0.95,'OBS')
      CALL REDPEN
      CALL PLOTNC(0.8,0.95,227)
      CALL PLOTCS(0.83,0.95,'CALC')
      CALL BLKPEN
      CALL PLOTCS(0.44,0.44,'DISTANCE (KM)')
      CALL CTRMAG(5)
      CALL PLACE(31,132)
      CALL TYPECS('VERTICAL EXAGGERATION X')
      CALL TYPENF(VE,2)
      IF (ISTA.EQ.1) GOTO 65
      CALL CRLNFD(2)
      CALL SPACE (30)
      CALL TYPECS('RMS RESIDUAL =')
      CALL TYPENF(RMS,2)
      CALL TYPECS(' MGAL')
      CALL CRLNFD(2)
      CALL SPACE (30)
      CALL TYPECS('CORRELATION COEFFICIENT =')
      CALL TYPENF(CC,4)
65    CALL CTRORI(90.0)
      CALL CTRMAG(15)
      CALL PLOTCS(0.04,0.60,'ANOMALY (MGAL)')
      CALL PLOTCS(0.04,0.15,'DEPTH (KM)')
      CALL GREND
62    CONTINUE
      STOP
      END

```

```

* Subroutine UDDERSTK
* C.N.Prescott, July 1987.
* User-defined data entry routine for use with MJS program HYPLOT.
* This version will read position and anomaly(grav/mag) data from
* file in PROCESS o/p format, window out data within a given perpendicular
* distance from a defined line of section, calculate the x-distances
* of the projection of the data on the LOS, sort the resultant file
* into ascending order, then finally bin and low pass filter the data.
* INPUT
* Read on unit 2 : Discovery data.
* Read on unit 3 : Darwin data.
* Read on unit 5 : Accepted data written to unit 4.
* OUTPUT
* written to unit 4 : accepted data.
* written to unit 8 : unsmoothed binned and stacked data.
* written to unit 21 : Final low-pass filtered data.
      SUBROUTINE UDDER(CURPLT,IPNEWF)
      IMPLICIT DOUBLE PRECISION (A-H, O-Z)
      DIMENSION X(25000), XANOM(25000)
      CHARACTER CURPLT*4
      INTEGER IPNEWF,IOFLG
      PARAMETER (IPIN=1,ISOUT=13)
      IF(IPNEWF.NE.0)CALL NEWPLT(CURPLT,IPNEWF)
* User code...
* Do over ships
      N=0
      WRITE(6,/, "Windowing...")
      DO 1 ISHIP=1,2
      IF(ISHIP.EQ.1)THEN
      WRITE(6,/, "Discov...")
      ELSE
      WRITE(6,/, "Darwin...")
      ENDIF
* Set parameters according to ship type
      LUNIT=ISHIP+1
* Window data...
100  READ(LUNIT,200,ERR=900,END=1)PVAL,PLAT,PLON
      CALL USERPT(CURPLT,PLAT,PLON,PVAL,X,Y,IOFLG)
      IF(IOFLG.NE.0)THEN
      GOTO 100
      ELSE
      WRITE(4,201)PVAL,PLAT,PLON
      N=N+1
      GOTO 100
      ENDIF
1  CONTINUE
*Projection...
      WRITE(6,/, "Projection...")
      CALL XDIST (N, X, XANOM)
*Sort...
      WRITE(6,/, "Sort...")
      CALL SORT (N, X, XANOM)
*Bin...
      WRITE(6,/, "Bin...")
      CALL BIN (N, X, XANOM)
      RETURN
200  FORMAT(28X,3F15.4)
201  FORMAT(3F13.4)
900  WRITE(6,/, "!! Error in input/output.")
      STOP
      END
*
      SUBROUTINE XDIST (N, X1, XANOM)
* See XDIST.
      IMPLICIT DOUBLE PRECISION (A-H, O-Z)
      PARAMETER (DEGRAD=0.714532925199432946D-01)
      DIMENSION X1(N), XANOM(N)
      COMMON / ORIGIN / OLAT,OLON
      REAL UMPMX,UMPMN,VMPMX,VMPMN
      REAL XLAB,YLAB,ULAB,VLAB
      INTEGER IQUAD

```

```

CHARACTER SP*4
* Statement function to get time diff in secs between readings...
INSECT(IDAY,IHR,IMIN,ISEC,IDAY2,IHR2,IMIN2,ISEC2)=
&IABS(
&(ISEC2-ISEC)+
&60*(IMIN2-IMIN)+
&3600*(IHR2-IHR)+
&86400*(IDAY2-IDAY))
Z=0.0D0
* Define Line of Section...
OLON=-19.9542
OLAT= 59.8410
BLON=-17.0582
BLAT= 58.2303
* Calculate los length...
CALL DISTAZ(OLAT,OLON,BLAT,BLON,XLOS,DUMM)
* Calculate length & azimuth of line of section.
* First transform to (u,v) space...
CALL MERCE(OLAT,OLON,U0,V0,SF)
CALL MERCE(BLAT,BLON,U1,V1,SF)
* Set up line of section vector coefficients.
* AABS=Line of section magnitude...
AU=U1-U0
AV=V1-V0
AABS=DSQRT(AU**2+AV**2)
* Azimuth of Line of section, THETA.
* Do this by checking the sign of
* sin & cos in all four quadrants...
SINTHT=AV/AABS
COSTHT=AU/AABS
CALL ANGL(SINTHT,COSTHT,DEGRAD,THETA,IQUAD)
THETA1=THETA/DEGRAD
WRITE(6,('Quadrant...',I10))IQUAD
* Set up small value to add to lat/lon if
* it coincides with a los definition point...
SMALL=1.0D-06
* Loop for data...
K=1
1 READ(5,100,END=998,ERR=999)ANOM,XLAT,XLON
SIGN=1.0D0
* Check for coincidental points...
IF(XLAT.EQ.OLAT.OR.XLAT.EQ.BLAT)THEN
WRITE(6,('/', '!!Data and los latitude-point coincidence!!'))
WRITE(6,('/', '!!Adjusting....'))
XLAT=XLAT+SMALL
IF(XLON.EQ.OLON.OR.XLON.EQ.BLON)XLON=XLON+SMALL
WRITE(6,('/', '!!Data and los longitude-point coincidence!!'))
WRITE(6,('/', '!!Adjusting....'))
XLON=XLON+SMALL
ENDIF
* Transform to (u,v)...
CALL MERCE(XLAT,XLON,U,V,SF)
* Set up data point vector coefficients.
* BABS=data point vector magnitude...
BU=U-U0
BV=V-V0
BABS=DSQRT(BU**2+BV**2)
* Calculate alpha.
* Use scalar product of line of section and
* data point vectors...
ALPIA=DACOS((AU*BU+AV*BV)/(AABS*BABS))
* Now project aabs onto babs to get
* projection length x...
X=AABS*DCOS(ALPIA)
* Calculate azimuth of data point...
SINGAM=BV/BABS
COSGAM=BU/BABS
CALL ANGL(SINGAM,COSGAM,DEGRAD,GAMMA,IDUMMY)
* Calculate from theta and gamma the sign of alpha...
ALPSIN=THETA-GAMMA
IF(ALPSIN.LT.0.0D0)SIGN=SIGN*(-1.0D0)

```

```

* Calculate x, the projection length of
* the point on the line of section.....
  X=BABS*DCOS(ALPHA)
* Calculate delta using pythag...
  DELTA=DSQRT(BABS**2-X**2)
* Using IQUAD and SIGN calculate udash, vdash...
  IF(IQUAD.NE.4)THEN
    WRITE(6,('Iquad ne 4.'))
    WRITE(6,('STOP-Redefine LOS.'))
    GOTO 999
  ELSE
    FI=360.0D0*DEGRAD-THETA
    DU=DELTA*DSIN(FI)
    DV=DELTA*DCOS(FI)
    IF(SIGN.GT.0.0D0)THEN
      UDASH=U+DU
      VDASH=V+DV
    ELSE IF(SIGN.LT.0.0D0)THEN
      UDASH=U-DU
      VDASH=V-DV
    ENDIF
  ENDIF
* Transform back to lat/lon...
  CALL MERCEI (UDASH, VDASH, XLATP, XLONP)
* Xdist along los...
  CALL DISTAZ (OLAT, OLON, XLATP, XLONP, DIST, AZ)
  X1(K)=DIST
  XANOM(K)=ANOM
  K=K+1
  GOTO 1
998 RETURN
100 FORMAT(3F13.4)
999 WRITE(6,('!!!ERROR!!! - Input Terminated.'))
  STOP
  END

*
  SUBROUTINE MERCE ( XLAT, XLON, X, Y, SF )
* M.J.Smith, August 1986.
* Mercator projection from the ellipsoid
* If true scale lat. other than equator, multiply
* rhs by
* COS( OLAT ) / SQRT( 1 - ECC2 * SIN( OLAT ) **2 )
  IMPLICIT DOUBLE PRECISION ( A-H, O-Z )
  LOGICAL INITC
  PARAMETER ( PI = 3.14159265358979312D0 )
  PARAMETER ( DEGRAD = 0.174532925199432946D-01 )
  PARAMETER ( EQRAD = 6378.16D0 )
  PARAMETER ( ECC = 0.081819643D0 )
  COMMON / ORIGIN / OLAT,OLON
  DATA INITC / .TRUE. /
  IF ( INITC ) THEN
    OLATR = OLAT * DEGRAD
    OLONR = OLON * DEGRAD
    SCAFAC = COS( OLATR ) /
    &SQRT( 1.0D0 - ( ECC * SIN( OLATR ) )**2 )
    PIB4 = PI / 4.0D0
    INITC = .FALSE.
  ENDIF
  PLAT = XLAT * DEGRAD
  PLON = XLON * DEGRAD
  X = SCAFAC * EQRAD * ( PLON - OLONR )
  ECSUM = ( 1.0D0 - ECC * SIN( PLAT ) ) /
  &( 1.0D0 + ECC * SIN( PLAT ) )
  Y = SCAFAC * EQRAD * LOG( TAN( PIB4 + PLAT / 2.0D0 ) *
  &ECSUM ** ( ECC / 2.0D0 ) )
  SFM = SCAFAC * SQRT(1.0D0 - (ECC * SIN(PLAT))**2) / COS(PLAT)
  SF = SFM
  END

*
  SUBROUTINE MERCEI ( X, Y, XLAT, XLON )
* M.J.Smith, August 1986.

```

\* Mercator projection from the ellipsoid - inverse.

```

IMPLICIT DOUBLE PRECISION ( A-H, O-Z )
LOGICAL INITC
PARAMETER ( PI = 3.14159265358979312D0 )
PARAMETER ( DEGRAD = 0.174532925199432946D-01 )
PARAMETER ( EQRAD = 6378.16D0 )
PARAMETER ( ECC = 0.081819643D0 )
COMMON / ORIGIN / OLAT,OLON
DATA INITC / .TRUE. /
IF ( INITC ) THEN
  OLATR = OLAT * DEGRAD
  OLONR = OLON * DEGRAD
  SCAFAC = SQRT( 1.0D0 - ( ECC * SIN( OLATR ) )**2 ) /
    &COS( OLATR )
  PIB2 = PI / 2.0D0
  INITC = .FALSE.
ENDIF
XSCA = X * SCAFAC
YSCA = Y * SCAFAC
PLON = XSCA / EQRAD + OLONR

```

\* Closed form:- For finding PLAT using iteration

```

T = EXP( -YSCA / EQRAD )
PLAT = PIB2 - 2.0D0 * ATAN( T )
100 PLOLD = PLAT
ES = FES( ECC, PLAT )
PLAT = PIB2 - 2.0D0 * ATAN( T * ES )
PLDIFF = PLAT - PLOLD
IF( PLDIFF .GT. 1.0D-09 ) GO TO 100
XLAT = PLAT / DEGRAD
XLON = PLON / DEGRAD
END

```

---

\* SUBROUTINE DISTAZ(AL,OL,BL,CL,DIST,DAZ)

\* G K Westbrook.

\* Distance calculator accurate to 1 in 10\*\*7 at 1600 km.

\* Calculates distance between shot and station from decimal degrees.

```

*
DOUBLE PRECISION DL,IIL,ERQ,PRQ,A,B,SS,VS,S1,V,CO,S,SDL,CDL,DIF,S1,
&C1,G,GA,EC,EL,TA,GS,FL,GL
DOUBLE PRECISION DIST
DIMENSION NL(50),A(2,50),NS(500),B(2,500),SI(50),CO(50),V(50),VS(5
&00),SS(500),GA(50),TA(500),GS(500),TITLE(20),NT(500)
DTR=0.01745329
ER=6378.160
PR=6356.775
ERQ=ER**2
PRQ=PR**2
EC=(ERQ-PRQ)/ERQ
EL=(ERQ-PRQ)/PRQ
DL=AL*DTR
IIL=OL*DTR
SS(1)=DSIN(DL)
TA(1)=SS(1)/DCOS(DL)
VS(1)=ER/DSQRT(1-EC*SS(1)**2)
GS(1)=DSQRT(EL*SS(1)**2)
FL=BL*DTR
GL=CL*DTR
B(1,2)=FL
B(2,2)=GL
S1=DSIN(FL)
C1=DCOS(FL)
V1=ER/DSQRT(1-EC*S1**2)
DIF=IIL-GL
CDL=DCOS(DIF)
SDL=DSIN(DIF)
SS(2)=S1
VS(2)=V1
TA(2)=S1/C1
GS(2)=DSQRT(EL*S1**2)
G=GS(2)
T=(1.0-EC+EC*V1*S1/(VS(1)*SS(1)))*TA(1)

```



```

    AT=ATAN(T)
    PAZ=C1*T-S1*CDL
    SL=SDL
    AZ=ATAN2(SL,PAZ)
    IIQ=EL*C1**2*COS(AZ)**2
    II=SQRT(IIQ)
    BAZ=ABS(AZ)-3.14159
    IF(BAZ.GT.-1.0.OR.BAZ.LT.-2.14159) GO TO 57
    FD=SDL*COS(AT)/SIN(AZ)
    D=ARSIN(FD)
    GO TO 58
57  D=ARSIN(COS(AT)*PAZ/COS(AZ))
58  DIST=V1*D*(1.0-D**2*IIQ*(1.0-IIQ))/6.0+D**3*G*II*(1.0-2.0*IIQ)/8.0+D**4
    &*(IIQ*(4.0-7.0*IIQ)-3.0*G**2*(1.0-7.0*IIQ))/120.0-D**5*G*II/48.0)
    DAZ=AZ/DTR
    RETURN
    END

```

---

```

    DOUBLE PRECISION FUNCTION FES ( ECC, PLAT )

```

\* M.J.Smith, August 1986.

\* Function used in numerous subroutines

```

    IMPLICIT DOUBLE PRECISION ( A-II, O-Z )

```

```

    T1 = 1.0D0 - ECC * SIN( PLAT )

```

```

    T2 = 1.0D0 + ECC * SIN( PLAT )

```

```

    FES = SQRT( ( T1 / T2 )**ECC )

```

```

    END

```

---

```

    SUBROUTINE ANGL(SINANG, COSANG, DEGRAD, ANGLE, IQUAD)
    IMPLICIT DOUBLE PRECISION (A-II, O-Z)
    INTEGER IQUAD

```

\* Quadrant 1...

```

    IF(SINANG.GT.0.0D0.AND.COSANG.GT.0.0D0)THEN

```

```

        ANGLE=DASIN(SINANG)

```

```

        IQUAD=1

```

\* Quadrant 2...

```

    ELSE IF(SINANG.GT.0.0D0.AND.COSANG.LT.0.0D0)THEN

```

```

        ANGLE=DASIN(SINANG)

```

```

        IQUAD=2

```

\* Quadrant 3...

```

    ELSE IF(SINANG.LT.0.0D0.AND.COSANG.LT.0.0D0)THEN

```

```

        ANGLE=360.0D0*DEGRAD-DACOS(COSANG)

```

```

        IQUAD=3

```

\* Quadrant 4...

```

    ELSE IF(SINANG.LT.0.0D0.AND.COSANG.GT.0.0D0)THEN

```

```

        ANGLE=360.0D0*DEGRAD-DACOS(COSANG)

```

```

        IQUAD=4

```

```

    ENDIF

```

```

    RETURN

```

```

    END

```

---

```

    SUBROUTINE SORT ( N, RA, RB )

```

\* Subroutine to perform heap sort on projected data.

\* Ref: Press *et al.*, (1986).

\* N - no of data points.

\* RA - X array.

\* RB - Data array

```

    IMPLICIT DOUBLE PRECISION (A-II, O-Z)

```

```

    DIMENSION RA(N), RB(N)

```

```

    L=N/2+1

```

```

    IR=N

```

10 CONTINUE

```

    IF(L.GT.1)THEN

```

```

        L=L-1

```

```

        RRA=RA(L)

```

```

        RRB=RB(L)

```

```

        ELSE

```

```

            RRA=RA(IR)

```

```

            RRB=RB(IR)

```

```

            RA(IR)=RA(1)

```

```

            RB(IR)=RB(1)

```

```

            IR=IR-1

```

```

        IF(IR.EQ.1)THEN
          RA(1)=RRA
          RB(1)=RRB
          RETURN
        ENDIF
        ENDIF
        I=L
        J=L+L
20      IF(J.LE.IR)THEN
        IF(J.LT.IR)THEN
          IF(RA(J).LT.RA(J+1))J=J+1
        ENDIF
        IF(RRA.LT.RA(J))THEN
          RA(I)=RA(J)
          RB(I)=RB(J)
          I=J
          J=J+J
        ELSE
          J=IR+1
        ENDIF
        GOTO 20
      ENDIF
      RA(I)=RRA
      RB(I)=RRB
      GOTO 10
    END

```

---

```

SUBROUTINE BIN(N, X, XANOM)
* Bin the sorted data into prescribed bin-sizes, then call
* low-pass filter LOPASS. Data is binned into NN equal-sized
* bins where NN is defined in PARAMETER statement, and should
* be a power of 2 for compatabilty with the fast-fourier
* transform routine.
* Binned and filtered data are written to Bin.dat (unit 7).
  IMPLICIT DOUBLE PRECISION (A-H, O-Z)
  DIMENSION X(N), XANOM(N), XBN(1024), BN(1024), DATA(2048)
  PARAMETER (NN=1024, FCUT=1.8D-01)
  LOGICAL EXIT
*Set up binning parameters...
  K=1
  NBIN=1
  ZBIN=0.0D0
  BINDIM=X(N)/1024.0D0
* Upper/Lower bin limits...
1  XBINU=BINDIM*DFLOAT(NBIN)
  XBINL=XBINU-BINDIM
* Check XBINU < X(N)...
  IF(NBIN.EQ.NN)THEN
    EXIT=.TRUE.
  ELSE
    EXIT=.FALSE.
  ENDIF
* Bin coordinates...
  XBN(NBIN)=XBINL+(XBINU-XBINL)/2.0
* Average anomaly...
  IBNCNT=0
  SUM=0.0
2  IF(X(K).LE.XBINU.AND.X(K).GT.XBINL)THEN
    SUM=SUM+XANOM(K)
    IBNCNT=IBNCNT+1
    K=K+1
    GOTO 2
  ENDIF
  IF(IBNCNT.NE.0)THEN
    BN(NBIN)=SUM/DFLOAT(IBNCNT)
  ELSE
    BN(NBIN)=9999.0D0
  ENDIF
* Exit or continuac...
  IF(EXIT)THEN
* Write unsmoothed bin data...

```

```

        WRITE(7,'(3F13.4)')(XDN(K),ZBIN,BN(K),K=1,NN)
* Smooth binned data.
* Remove linear trends from gravity data...
    DTRND=(BN(1)-BN(NN))/DFLOAT(NN)
    DO 10 K=1,NN
        BN(K)=BN(K)+DTRND*DFLOAT(K)
10    CONTINUE
* Set up complimentary complex array DATA(2*NN)...
    N2=2*NN
    DO 20 J=2,N2,2
        DATA(J)=0.0
        DATA(J-1)=BN(J/2)
20    CONTINUE
* Evaluate cut-off index...
    FINC=1.0D0/(DFLOAT(NN)*BINDIM)
    NCUT=1
3    F=FINC*DFLOAT(NCUT)
    IF(F.GT.FCUT)THEN
        GOTO 4
    ELSE
        NCUT=NCUT+1
        GOTO 3
    ENDIF
4    INDCT=NCUT
* Call low pass filter routine...
    CALL LOPASS(DATA, NN, BINDIM, INDCT)
* Replace linear trend...
    DO 30 J=1,NN
        BN(J)=(DATA(2*J-1)/1024.0)-DTRND*DFLOAT(J)
30    CONTINUE
* Write final binned data set...
    WRITE(8,'(3F13.4)')(XDN(I),ZBIN,BN(I),I=1,NN)
    RETURN
    ELSE
        NBIN=NBIN+1
        GOTO 1
    ENDIF
END

```

---

```

SUBROUTINE LOPASS(DATA, NN, BINDIM, INDCT)
* Low pass digital filtering routine.
    IMPLICIT REAL*8 (A-H, O-Z)
    DIMENSION DATA(2*NN)
    N2=2*NN
* Transform array DATA...
    ISIGN=1
    CALL FFT(DATA, NN, ISIGN)
    WRITE(21,'(F13.4)')BINDIM
    WRITE(21,'(F13.4)')(DATA(K),K=1,N2)
* Apply low pass function to transformed data...
    DO 30 K=1,N2
        IF(K.LT.INDCT.OR.K.GT.(N2-INDCT-2))THEN
            FACT=1.0D0
        ELSE
            FACT=0.0D0
        ENDIF
        DATA(K)=DATA(K)*FACT
30    CONTINUE
* Apply inverse transform...
    ISIGN=-1
    CALL FFT(DATA, NN, ISIGN)
    RETURN
    END

```

---

```

SUBROUTINE FFT(DATA, NN, ISIGN)
* Ref: Press et al., (1986).
* Fast Fourier Transform of input complex array DATA(2*NN)
* ISIGN= 1 : Discrete Fourier Transform,
* =-1 : Inverse Discrete Fourier Transform.
* For complex array, arrange real and imaginary components
* of input series in alternate array locations.

```

° For real input series, set imaginary components to zero.

° NN = complex array length.(must be power of 2).

```

      IMPLICIT REAL*8 (A-H, O-Z)
      DIMENSION DATA(2*NN)
      N=2*NN
      J=1
      DO 11 I=1,N,2
      IF(J.GT.I)THEN
        TEMPR=DATA(J)
        TEMPI=DATA(J+1)
        DATA(J)=DATA(I)
        DATA(J+1)=DATA(I+1)
        DATA(I)=TEMPR
        DATA(I+1)=TEMPI
      ENDIF
      M=N/2
1    IF((M.GE.2).AND.(J.GT.M))THEN
      J=J-M
      M=M/2
      GOTO 1
    ENDIF
      J=J+M
11   CONTINUE
      MMAX=2
2    IF(N.GT.MMAX)THEN
      ISTEP=2*MMAX
      THETA=6.28318530717959D0/(ISIGN*MMAX)
      WPR=-2.D0*DSIN(0.5D0*THETA)**2
      WPI=DSIN(THETA)
      WR=1.0D0
      WI=0.0D0
      DO 13 M=1,MMAX,2
      DO 12 I=M,N,ISTEP
      J=I+MMAX
      TEMPR=SNGL(WR)*DATA(J)-SNGL(WI)*DATA(J+1)
      TEMPI=SNGL(WR)*DATA(J+1)+SNGL(WI)*DATA(J)
      DATA(J)=DATA(I)-TEMPR
      DATA(J+1)=DATA(I+1)-TEMPI
      DATA(I)=DATA(I)+TEMPR
      DATA(I+1)=DATA(I+1)+TEMPI
12   CONTINUE
      WTEMP=WR
      WR=WR*WPR-WI*WPI+WR
      WI=WI*WPR+WTEMP*WPI+WI
13   CONTINUE
      MMAX=ISTEP
      GOTO 2
    ENDIF
      RETURN
      END

```

# PROGRAM DEPTII

```

*
* Program corrects observed sea depths for the effects of sediment load,
* abnormal crustal thickness, and anomalously low density upper mantle.
* Corrected depths are then compared to those predicted by the
* empirical age/depth relationship of Parsons & Sclater (1977).
* INPUT
* Read on 5 : Crustal, upper mantle parameters, and oceanic crustal model
* OUTPUT
* Written to 9 : Plotfile.
    DIMENSION B(200), S(200), C(200)
    DIMENSION XB(200), BSED(200), BCRST(200), BMNTLE(200)
    COMMON /DATA/ RIOM, RIOM1, RIOCI, RIOS, RIOW, RIOA, RIOA1
    CHARACTER SWITCH*1
* Read :No of data points, asthenosphere switch...
    READ (5,'(I3;A1)')NB,SWITCH
* Read : normal oceanic depth,
* :normal crustal thickness,
* : Depths of compenstion...
    READ (5,*)DNORM,CNORM,DCOMP,DASTII
    DAST=DASTII-DCOMP
* Read : normal,actual U.M. densities,
* :average crustal, sediment, water densities...
    READ (5,*)RIOM, RIOM1, RIOCI, RIOS, RIOW, RIOA, RIOA1
* Read sea-floor, basement & moho depths...
    DO 10 J=1,NB
        READ (5,'(4F13.4)')XB(J),B(J),S(J),C(J)
        IF(J.EQ.1)THEN
            XMX=XB(J)
            XMN=XB(J)
        ELSE
            IF(XB(J).GT.XMX)XMX=XB(J)
            IF(XB(J).LT.XMN)XMN=XB(J)
        ENDIF
10    CONTINUE
* Correct for sediment layer...
    CALL SEDCOR(NB, B, S, BSED)
* Correct for abnormal crustal thickness...
    CALL CSTCOR(NB, CNORM, BSED, S, C, BCRST)
* Correct for anomalous upper mantle density...
    CALL MNTCOR(NB, DCOMP, CNORM, BCRST, BMNTLE)
* If required, correct for anomalous asthenosphere density...
    IF(SWITCH.EQ.'Y'.OR.SWITCH.EQ.'y')THEN
        CALL ASTCOR(NB, BMNTLE, DAST)
    ENDIF
* Plot corrected/uncorrected depths...
    CALL PAPER (1)
    CALL PSPACE (0.1,0.9,0.1,0.4)
    CALL CSPACE (0.0,1.0,0.0,1.0)
    CALL MAP (XMN,XMX,8.0,0.0)
    CALL BORDER
    CALL XSCALE
    CALL YSCALE
*Expected ridge-model depth...
    CALL GRNPEN
    CALL POSITN (XMN,DNORM)
    CALL JOIN (XMX,DNORM)
*Data points...
    DO 190 J=1,NB
190    CALL PLOTNC (XB(J), DNORM, 224)
*Observed depths...
    CALL BLUPEN
    CALL CURVEO (XB,B,1,NB)
*Corrected depths...
    CALL BROKEN (5,5,5,5)
    CALL CURVEO (XB,BMNTLE,1,NB)
    CALL FULL
*Data points...
    DO 200 K=1,NB
    CALL PLOTNC (XB(K), B(K), 245)
    CALL PLOTNC (XB(K), BMNTLE(K), 227)

```

```

200 CONTINUE
* Write annotation.
  XX = XMN+(XMX-XMN)/2.0
  XY = 9.5
  YX = -2.0
  YY = 4.0
  CALL BLKPEN
  CALL PCSCEN (XX,XY,'X-Distance (km).')
  CALL CTRORI (90.0)
  CALL PCSCEN (YX,YY,'Depth (km).')
  CALL CTRORI ( 0.0)
* Legend...
  CALL PSPACE (0.5,0.9,0.4,0.5)
  CALL CSPACE (0.5,0.9,0.4,0.5)
  CALL MAP (0.0,1.0,0.0,1.0)
  CALL BORDER
  CALL POSITN (0.05,0.8)
  CALL TYPECS ('DEPTH CORRECTION.')
  CALL POSITN (0.05,0.8)
  CALL TYPECS ('_____')
  CALL BLUPEN
*Corrected original depth...
  CALL PLOTNC (0.15, 0.20, 227)
  CALL POSITN (0.05, 0.20)
  CALL BROKEN (5,5,5,5)
  CALL JOIN (0.25, 0.20)
  CALL FULL
  CALL BLKPEN
  CALL TYPECS (': Corrected Depth.')
*Original depth...
  CALL BLUPEN
  CALL PLOTNC (0.15, 0.40, 245)
  CALL POSITN (0.05, 0.40)
  CALL JOIN (0.25, 0.40)
  CALL BLKPEN
  CALL TYPECS (': Original Depth.')
*Theoretically expected depth...
  CALL GRNPEN
  CALL PLOTNC (0.15, 0.60, 224)
  CALL POSITN (0.05, 0.60)
  CALL JOIN (0.25, 0.60)
  CALL BLKPEN
  CALL TYPECS (': Expected Depth.')
  CALL GREND
  STOP
  END
*
  SUBROUTINE SEDCOR(NB, B, S, BSED)
* Correct for sediment layer...
  DIMENSION B(200), S(200), BSED(200)
  COMMON /DATA/ RIOM, RIOM1, RHOC, RHOS, RHOW, RHOA, RHOA1
  DO 10 K=1,NB
    STHK=S(K)-B(K)
    DELW=STHK*(RIOM1-RHOS)/(RIOM1-RHOW)
10  BSED(K)=B(K)+STHK-DELW
  RETURN
  END
*
  SUBROUTINE CSTCOR(NB, CNORM, BSED, S, C, BCRST)
* Correct for abnormal crustal thickness...
  DIMENSION BSED(200), BCRST(200), S(200), C(200)
  COMMON /DATA/ RIOM, RIOM1, RHOC, RHOS, RHOW, RHOA, RHOA1
  DO 10 K=1,NB
    CTHK=C(K)-S(K)
    DELC=CTHK-CNORM
    DELW=DELC*(RIOM1-RHOC)/(RIOM1-RHOW)
10  BCRST(K)=BSED(K)+DELW
  RETURN
  END
*
  SUBROUTINE MNTCOR(NB, DCOMP, CNORM, BCRST, BMNTLE)

```

```

* Correct for anomalous lithosphere density...
  DIMENSION BCRST(200), BMNTLE(200)
  COMMON /DATA/ RHIOM, RHIOM1, RHIOC, RHIOS, RHIOW, RHIOA, RHIOA1
  DRIOM=RHIOM1-RHIOM
  DROMW=RHIOM1-RHIOW
  DO 10 K=1,NB
  IIM=DCOMP-(BCRST(K)+CNORM)
10  BMNTLE(K)=BCRST(K)-IIM*DRIOM/DROMW
  RETURN
  END

*
  SUBROUTINE ASTCOR (NB, BMNTLE, DAST)
* Correct for anomalous asthenosphere density...
  DIMENSION BMNTLE(200)
  COMMON /DATA/ RHIOM, RHIOM1, RHIOC, RHIOS, RHIOW, RHIOA, RHIOA1
  DELRAW=RHIOA-RHIOW
  DELROA=RHIOA-RHIOA1
  DO 10 K=1,NB
10  BMNTLE(K)=BMNTLE(K)+((DAST*DELROA)/DELRAW)
  RETURN
  END

```

```

PROGRAM HEAT
* CN Prescott, 1987.
* Program to do finite-difference modelling of development of
* temperature/depth distribution with time in instantaneously
* stretched continental lithosphere according to McKenzie (1978)
* theory, and calculate the resultant horizontal density gradient.
* INPUT
* Read on unit 5 : Thermal parameters and mesh.
* OUTPUT
* written to unit 7 : New temperature mesh.
* written to unit 8 : New temperature mesh (contour format).
* written to unit 9 : Density gradient Plotfile.
* written to unit 10 : Temperature gradient mesh (contour format).
* written to unit 11 : Density gradient listing.
  DIMENSION T(320,80), T2(320,80), T3(320,80)
  CHARACTER FMT*20
  REAL M
* Read : Input/output format definition...
  READ (5, '(A20)') FMT
* : Thermal parameters...
  READ (5, *) SPIIT, DEN, TCOND
* : Dimensional parameters...
  READ (5, *) TRAN, TINC, EX, EZ, NI, NJ
* Check stability criterion satisfied...
  STAB = TINC * TCOND / (DEN * SPIIT * EZ ** 2.0)
  M = TINC * TCOND / (DEN * SPIIT * EX ** 2.0 * EZ ** 2.0)
  IF (STAB.GT.0.5) THEN
    WRITE(6, ('-Warning!!'))
    WRITE(6, ('-Solution Unstable...'))
  ENDIF
* Calculate # of passes required...
  NPASS = TRAN / TINC
* Read temperature grid...
  READ (5, FMT) ((T(I,J), I=1,NI), J=1,NJ)
* Start finite-differencing...
  DO 900 NP=1, NPASS
    IF ((NP/100)*100.EQ.NP) THEN
      WRITE(6, ('Pass #', I5)) NP
    ENDIF
    CALL FINITE(EX, EZ, NI, NJ, M, T, T2)
900  CONTINUE
* Calculate horizontal temperature gradients...
  CALL HTGRAD(NI, NJ, T, T3)
* Write temperature array...
  WRITE(7, FMT) ((T(I,J), I=1,NI), J=1,NJ)
* Write contour mesh:-
* Temperature mesh unit 8,
* Gradient mesh unit 9...
  DO 50 J=1, NJ
    Z = EZ * (FLOAT(J)-0.5) / 1000.0
    DO 50 I=1, NI
      X = EX * (FLOAT(I)-0.5) / 1000.0
      WRITE(8, '(3F13.4)') X, Z, T(I,J)
      WRITE(10, '(3F13.4)') X, Z, T3(I,J)
50  CONTINUE
* Calculate predicted density distribution...
  CALL DENSTY(EX, NI, NJ, T)
  STOP
  END

*
  SUBROUTINE FINITE(EX, EZ, NI, NJ, M, T, T2)
*
  DIMENSION T(320,80), T2(320,80)
  REAL M
  DO 20 J=1, NJ
    DO 20 I=1, NI
* Top surface T=0.0 ...
    IF (J.EQ.1.AND.I.GE.1.AND.I.LE.NI) THEN
      T2(I,J)=0.0
      GOTO 20
* Oceanic end, linear temp gradient...

```



```

ELSE IF(I.EQ.1.AND.J.GT.1.AND.J.LT.NJ)THEN
  T1=T(I,J)+(T(I,J)-T(I+1,J))
  AX=M*EZ**2.0*(T1+T(I+1,J))
* Lower surface T=1300.0...
ELSE IF(J.EQ.NJ.AND.I.GE.1.AND.I.LE.NI)THEN
  T2(I,J)=1300.0
  GOTO 20
* Right surface, no heat flow...
ELSE IF(I.EQ.NI.AND.J.GT.1.AND.J.LT.NJ)THEN
  T2(I,J)=T(I,J)
  GOTO 20
* main body, normal finite difference...
ELSE IF(I.GT.1.AND.I.LT.NI.AND.J.GT.1.AND.J.LT.NJ)THEN
  AX=M*EZ**2.0*(T(I-1,J)+T(I+1,J))
  ENDIF
  AZ=M*EX**2.0*(T(I,J-1)+T(I,J+1))
  T2(I,J)=AX+AZ-T(I,J)*(2.0*M*(EX**2.0+EZ**2.0)-1.0)
20 CONTINUE
* Reset temperature array, and initialise auxillary array...
DO 40 J=1,NJ
DO 40 I=1,NI
40 T(I,J)=T2(I,J)
RETURN
END

```

---

```

* SUBROUTINE HTGRAD(NI,NJ,T,T3)
*
  DIMENSION T(320,80), T3(320,80)
  CHARACTER GRAD*4
  WRITE(6,(/,
+ "& Temperature Gradient (h,v,c, def h)?"'))
  READ (6,('A4'))GRAD
  DO 10 J=1,NJ
  DO 10 I=1,NI
* I...
  IF(I.EQ.1)THEN
    TI=T(I,J)-T(I+1,J)
  ELSE IF(I.EQ.NI)THEN
    TI=T(I-1,J)-T(I,J)
  ELSE
    TI=(T(I-1,J)-T(I+1,J))/2.0
  ENDIF
* J...
  IF(J.EQ.1)THEN
    TJ=T(I,J+1)-T(I,J)
  ELSE IF(J.EQ.NJ)THEN
    TJ=T(I,J)-T(I,J-1)
  ELSE
    TJ=(T(I,J+1)-T(I,J-1))/2.0
  ENDIF
* Horizontal, vertical or composite temperature gradient...
  IF(GRAD.EQ.'C')THEN
    T3(I,J)=(TI+TJ)/2.0
  ELSE IF(GRAD.EQ.'V')THEN
    T3(I,J)=TJ
  ELSE
    T3(I,J)=TI
  ENDIF
10 CONTINUE
RETURN
END

```

---

```

* SUBROUTINE DENSITY(EX,NI,NJ,T)
* Convert temperature variations into average density variations...
  DIMENSION X(320), RHO(320), T(320,80), TAV(320)
  PARAMETER (TEXP=2.5E-05)
  CHARACTER TITLE*20
* Calculate average column temperatures...
DO 10 I=1,NI
  TSUM=0.0
DO 20 J=1,NJ

```

```

20  TSUM=TSUM+T(I,J)
    TAV(I)=TSUM/FLOAT(NJ)
    X(I)=EX*(FLOAT(I)-0.5)/1000.0
10  CONTINUE
* Calculate resultant densities...
    RHIO(NI)=3330.0
    RIIMAX=RHIO(NI)
    RIIMIN=RHIO(NI)
    DO 30 I=1,NI-1
        DELT=TAV(NI)-TAV(I)
        RHIO(I)=RHIO(NI)+TEXP*RHIO(NI)*DELT
        IF(RHIO(I).LT.RIIMIN)RIIMIN=RHIO(I)
30  CONTINUE
* Print average densities...
    WRITE(11,('      X(km)      Tav(c)      Density (kg/m*3)'))
    WRITE(11,('      _____'))
    DO 31 I=1,NI
31  WRITE(11,('3(2X,F13.4)'))X(I),TAV(I),RHIO(I)
* Plot density distribution...
    RIIMAX=RIIMAX+1.0
    RIIMIN=RIIMIN-1.0
    WRITE(6,('/', ' Density distribution. '))
    WRITE(6,(' & Title?...''))
    READ (6,('A20'))TITLE
    CALL PAPER (1)
    CALL PSPACE(0.1,0.9,0.1,0.5)
    CALL MAP (X(1),X(NI),RIIMIN,RIIMAX)
    CALL BORDER
    CALL SCALES
    DO 40 I=1,NI
        IF(I.EQ.1)THEN
            CALL POSITN(X(I),RHIO(I))
        ELSE
            CALL JOIN (X(I),RHIO(I))
        ENDIF
40  CONTINUE
*Label axes...
    XXLAB=X(1)+(X(NI)-X(1))/2.0
    XYLAB=RIIMIN-(RIIMAX-RIIMIN)/5.0
    YXLAB=X(1)-30.0
    YYLAB=RIIMIN+(RIIMAX-RIIMIN)/2.0
    CALL PCSCEN (XXLAB,XYLAB,'Distance (km).')
    CALL CTRORI (90.0)
    CALL PCSCEN (YXLAB,YYLAB,'Density (kg/m*3).')
    CALL CTRORI ( 0.0)
*Label plot...
    CALL PLOTCS (X(2),RIIMAX-1.0,'Modelled U.M Density Variation.')
    CALL PLOTCS (X(2),RIIMAX-1.0,'_____')
    CALL PLOTCS (X(2),RIIMAX-2.0,TITLE)
    CALL GREND
    RETURN
    END

```

# SUBROUTINE UDDER(CURPLT,IPNEWF)

```

* User defined data entry program for use with HYPOPLOT(M. J. Smith).
* Program plots magnetic anomaly data perpendicular to ships tracks.
* Digitised bathymetry, coastlines, and magnetic anomaly lineations can
* be plotted if required. Track data is read in and plotted point by
* point in unformatted format if within the defined map limits.
* Accepted data is re-read and magnetic anomalies are plotted
* perpendicular to ships tracks in variable-area form.
* INPUT
* Read on unit 3 : Digitised coast/bathymetry/anomaly lineations. (optional)
* Read on unit 4 : SAP CMP positions. (optional)
* Read on unit 5 : Magnetic anomaly data (unformatted).
* Read on unit 7 : Accepted magnetic anomaly data (unformatted).
* OUTPUT
* Written to unit 7 : Accepted magnetic anomaly data (unformatted).
* Written to unit 9 : Plotfile.

      DIMENSION XLAT(10000), XLON(10000)
      DOUBLE PRECISION DLAT,DLON,PVAL,SCLON1,SCLON2,ALAT
      DOUBLE PRECISION DLON1,DLON2,XLAT,XLON
      CHARACTER CURPLT*4,TITLE*13,BLANK*40,IDSHIP*4,ANS*4
      PARAMETER (IPIN=1,ISOUT=13)
      INTEGER IPNEWF,IOFLG

* Statement function to get time in secs between readings...
      INSECT(LD1,LH1,LM1,LS1,LD2,LH2,LM2,LS2)=
      & IABS((LS2-LS1)+
      & 60*(LM2-LM1)+
      & 3600*(LH2-LH1)+
      & 86400*(LD2-LD1))
      IF(IPNEWF.NE.0)CALL NEWPLT(CURPLT,IPNEWF)

* Read in and plot ships tracks.
* Open input/output files...
      OPEN (UNIT=5,FORM='UNFORMATTED',ERR=998)
      OPEN (UNIT=7,FORM='UNFORMATTED',ERR=996)

* Acceptance headings...
      A1= 0.0
      A2= 90.0
      A3=180.0
      A4=270.0

* Find and position pen at first point...
      ISTAT=0
      READ(5,END=3)IDSHIP,LD1,LH1,LM1,LS1,ANOM,DLAT,DLON,IFLAG
      ANOMAX=ANOM
      ANOMIN=ANOM
      WRITE(6,('/',," Plotting Track."))
      WRITE(6,('" _____",/'))
600  READ(5,END=3)IDSHIP,LD1,LH1,LM1,LS1,ANOM,DLAT,DLON,IFLAG
      PVAL=ANOM
      CALL USERPT(CURPLT,DLAT,DLON,PVAL,X,Y,IOFLG)
      IF(IOFLG.NE.0)GOTO 600
      ISTAT=1
      CALL POSITN(X,Y)
      XOLD=X
      YOLD=Y

* Plot subsequent points point by point...
2    READ(5,END=3)IDSHIP,LD2,LH2,LM2,LS2,ANOM,DLAT,DLON
      &,IFLAG

* Check for new track section...
      IF(INSECT(LD1,LH1,LM1,LS1,LD2,LH2,LM2,LS2).GT.1800)THEN
      WRITE(6,('!!!New track section.'))
      CALL USERPT(CURPLT,DLAT,DLON,PVAL,X,Y,IOFLG)
      CALL POINT (X,Y)
      XOLD=X
      YOLD=Y
      LD1=LD2
      LH1=LH2
      LM1=LM2
      LS1=LS2
      GOTO 2
      ENDIF

```

```

*accepted data...
  WRITE(7)IDSHIP,LD1,LH1,LM1,LS1,ANOM,DLAT,DLON,IFLAG
  LD1=LD2
  LH1=LH2
  LM1=LM2
  LS1=LS2
  PVAL=ANOM
  CALL USERPT(CURPLT,DLAT,DLON,PVAL,X,Y,IOFLG)
  IF(IOFLG.NE.0)GOTO 600
  DELX=X-XOLD
  DELY=Y-YOLD
  XOLD=X
  YOLD=Y
  HEAD=VECTOR(DE LX,DELY)
  IF(HEAD.GT.A1.AND.HEAD.LT.A2.OR.HEAD.GT.A3.AND.HEAD.LT.A4)THEN
*Plot track...
  IF(IDSHIP.EQ.'DA'.OR.IDSHIP.EQ.'da')THEN
    CALL BLUPEN
  ELSE IF(IDSHIP.EQ.'DI'.OR.IDSHIP.EQ.'di')THEN
    CALL REDPEN
  ELSE
    CALL GRNPEN
  ENDIF
  CALL JOIN(X,Y)
  IF(ANOM.LT.ANOMIN)ANOMIN=ANOM
  IF(ANOM.GT.ANOMAX)ANOMAX=ANOM
  GOTO 2
  ELSE
    CALL POSITN (X,Y)
    GOTO 2
  ENDIF
* End of track plotting section.
* Plot magnetic data at 90deg to track...
3  IF(ISTAT.EQ.1)THEN
  WRITE(6,FMT=('/'," **Tracks Plotted."))
  WRITE(6,FMT=('/'," -----"))
  WRITE(6,FMT=('/'," **Plotting magnetics along tracks."))
  WRITE(6,FMT=('/'," -----"))
  ELSE
    WRITE(6,FMT=('/'," !!WARNING!!"))
    WRITE(6,FMT=('/'," No Data in Map Area..."))
    WRITE(6,FMT=('/'," Skipping mag plot section. "))
    GOTO 700
  ENDIF
* Map area contains data...Rewind input file...
  REWIND 5
* Calculate anomaly scale-factor in vector-space.
* Scale anomaly data so that maximum anomaly is plotted
* 1.0 deg of longitude in amplitude...
  AMPLIT=ANOMAX-ANOMIN
  READ (IPIN,100)SCLON1, SCLON2
  ALAT =60.0
  PVAL =0.0
  CALL USERPT(CURPLT,ALAT,SCLON1,PVAL,X1,Y1,IOFLG)
  CALL USERPT(CURPLT,ALAT,SCLON2,PVAL,X2,Y2,IOFLG)
  DIFLAT=ABS(X2-X1)
  SCFAC=DIFLAT/AMPLIT
* Position pen at first mag point, and set pen colour to black...
  REWIND 7
  CALL BLKPEN
700 READ(7,END=5)IDSHIP,LD1,LH1,LM1,LS1,ANOM,DLAT,DLON,IFLAG
  ANOM=ANOM*SCFAC
  PVAL=ANOM
  CALL USERPT(CURPLT,DLAT,DLON,PVAL,X,Y,IOFLG)
  IF(IOFLG.NE.0)GOTO 700
  XOLD=X
  YOLD=Y
* Calculate anomaly co-ordinates...
  CALL MAGPOS(ANOM,X,Y,XMAG,YMAG)
  CALL POSITN(XMAG,YMAG)
* Read in navigation and anomaly data, calculate

```

```

* anomaly co-ordinates and plot...
4  READ(7,END=5)IDSIIIP,LD2,LII2,LM2,LS2,ANOM,DLAT,DLON,IFLAG
   ANOM=ANOM*SCFAC
* Check for new track section...
   IF(INSECT(LD1,LII1,LM1,LS1,LD2,LII2,LM2,LS2).GT.1800)THEN
     CALL USERPT(CURPLT,DLAT,DLON,PVAL,X,Y,IOFLG)
     IF(IOFLG.NE.0)GOTO 4
     WRITE(6,('!!New Track Section.'))
     CALL MAGPOS (ANOM,X,Y,XMAG,YMAG)
     CALL POSITN (XMAG,YMAG)
     LD1=LD2
     LII1=LII2
     LM1=LM2
     LS1=LS2
     XOLD=X
     YOLD=Y
     GOTO 4
   ENDIF
   LD1=LD2
   LII1=LII2
   LM1=LM2
   LS1=LS2
   PVAL=ANOM
   CALL USERPT(CURPLT,DLAT,DLON,PVAL,X,Y,IOFLG)
   IF(IOFLG.NE.0)GOTO 4
   DELX=X-XOLD
   DELY=Y-YOLD
   HEAD=VECTOR (DELX,DELY)
   IF(HEAD.GT.A1.AND.HEAD.LT.A2.OR.HEAD.GT.A3.AND.HEAD.LT.A4)THEN
     CALL MAGPOS (ANOM,X,Y,XMAG,YMAG)
     IF(ANOM.GT.0.0)THEN
       CALL JOIN (XMAG,YMAG)
       CALL JOIN (X,Y)
       CALL JOIN (XMAG,YMAG)
     ELSE
       CALL JOIN (XMAG,YMAG)
     ENDIF
     ELSE
       CALL MAGPOS (ANOM,X,Y,XMAG,YMAG)
       CALL POSITN (XMAG,YMAG)
       ENDIF
       XOLD=X
       YOLD=Y
       GOTO 4
5  WRITE(6,FMT=('/'," **Magnetics plotted."))
   WRITE(6,FMT=('/'," _____"))
1000 WRITE(6,FMT=('/'," **Plotting SAP CMP positions..."))
* Read in first set of cmp data, and set pen colour to blue...
   CALL BLUPEN
   NCMP=0
   INDANG=1
10  K=1
   INDANG=INDANG+1
   NPOINT=1
   NCMP=NCMP+1
   WRITE(6,FMT=('/'," **Plotting Sap ",II))NCMP
   ICMPOL=0
   PVAL=0.0
   ANGLE=3.1415925/4.0
20  READ(4,FMT= '(I8,2F20.8)',END=991,ERR=999)ICMP,DLAT,DLON
   IF(NPOINT.EQ.1)THEN
     CALL USERPT(CURPLT,DLAT,DLON,PVAL,X,Y,IOFLG)
     XOLD=X
     YOLD=Y
     NPOINT=NPOINT+1
   ELSE
     ENDIF
   IF(ICMP.LT.ICMPOL)THEN
     GOTO 10
   ELSE
     IF(((ICMP/200)*200).NE.ICMP)GOTO 20

```

```

      CALL USERPT(CURPLT,DLAT,DLOX,PVAL,X,Y,IOFLG)
* Get heading vector and set character orientation...
      DELX=X-XOLD
      DELY=Y-YOLD
      XOLD=X
      YOLD=Y
      IF(((INDANG/2)*2).EQ.INDANG)THEN
        ANGLE=VECTOR(DELX,DELY)
      ELSE
        ANGLE=VECTOR(DELX,DELY)+180.0
      ENDIF
      CALL CTRORI(ANGLE)
* Calculate and set character size in vector space units...
      DELPOS=SQRT(DELX**2+DELY**2)
      CHRSIZ=DELPOS/5.0
      CALL CTRSIZ(CHRSIZ)
      CALL PLOTNC(X,Y,42)
      CALL PLOTNI(X,Y,ICMP)
      ICMPOL=ICMP
      K=K+1
      GOTO 20
    ENDIF
991  WRITE(6,FMT=('/'," **CMP positions plotted."'))
      WRITE(6,FMT=('/'," -----"))
* Plot coastline/bathymetry...
990  CALL BLKPEN
      CALL CTRMAG (10)
      CALL FULL
5000 READ (3,'(15,I2)',END=6000)NCOAST,ILNTYP
      IF(ILNTYP.LT.1)THEN
        CALL BROKEN (3,3,3,3)
      ELSE IF(ILNTYP.GT.1)THEN
*m24..
        IF(ILNTYP.EQ.2)THEN
          ISYMBL=245
*m23..
        ELSE IF(ILNTYP.EQ.3)THEN
          ISYMBL=244
*m22..
        ELSE IF(ILNTYP.EQ.4)THEN
          ISYMBL=241
*m21..
        ELSE IF(ILNTYP.EQ.5)THEN
          ISYMBL=250
*m20..
        ELSE IF(ILNTYP.EQ.6)THEN
          ISYMBL=253
        ENDIF
*Plot anomalies...
        DO 6 J=1,NCOAST
          READ(3,'(2F8.4)')ALAT,ALON
          CALL USERPT (CURPLT,ALAT,ALON,PVAL,X,Y,IOFLG)
          IF(IOFLG.NE.0)GOTO 6
          CALL PLOTNC (X,Y,ISYMBL)
6      CONTINUE
          CALL FULL
          CALL BLKPEN
          GOTO 5000
        ELSE
          CALL FULL
        ENDIF
* Read and plot data points in section...
        READ(3,'(2F8.4)')(XLAT(I),XLON(I),I=1,NCOAST)
        ICHK=0
        DO 11 J=1,NCOAST
          CALL USERPT(CURPLT,XLAT(J),XLON(J),PVAL,X,Y,IOFLG)
          IF(IOFLG.NE.0)THEN
            ICHK=0
            GOTO 11
          ELSE
            IF(ICHK.EQ.0)THEN

```

```

        CALL POSITN(X,Y)
        ICHK=1
        ELSE
        CALL JOIN (X,Y)
        ENDIF
        ENDIF
11  CONTINUE
* Go for next section...
    GOTO 5000
*Plot scale if mag data present, otherwise skip...
6000 PVAL =100.0
    CALL FULL
    IF(ISTAT.EQ.0)GOTO 997
    READ (IPIN, 100) DLAT, FAC
    READ (IPIN, 100)DLON1, DLON2
    TOP =1000.0
    CALL USERPT (CURPLT,DLAT,DLON1,PVAL,X1,Y1,IOFLG)
    CALL USERPT (CURPLT,DLAT,DLON2,PVAL,X2,Y2,IOFLG)
    Y3=Y1+TOP*SCFAC
    Y4=Y1-TOP*SCFAC
    XRANG=X2-X1
    XLAB=X1-XRANG/5.0
    XINC =XRANG/256.0
    AINC =3.141593/128.0
*Plot axes...
    CALL BLKPEN
    CALL CTRSI(0.025)
    CALL POSITN (X1,Y1)
    CALL JOIN (X2,Y2)
    CALL POSITN (X1,Y3)
    CALL JOIN (X1,Y4)
    CALL PLOTNC (X1,Y3,45)
    CALL PLOTNC (X1,Y4,45)
    CALL PCSCEN (X1-FAC*XINC,Y3,' 1000.0')
    CALL PCSCEN (X1-FAC*XINC,Y1,' 0.0')
    CALL PCSCEN (X1-FAC*XINC,Y4,'-1000.0')
    CALL CTRORI (90.0)
    CALL PCSCEN (XLAB,Y1,'Gamma')
    CALL CTRORI (00.0)
*Plot sinc-curve...
    DO 111 K=0,256
    X=X1+XINC*FLOAT(K)
    SINE=Y1+SIN(AINC*FLOAT(K))*TOP*SCFAC
    IF(K.EQ.0)THEN
    CALL POSITN (X,SINE)
    ELSE
    IF(SINE.GT.Y1)THEN
    CALL JOIN(X,SINE)
    CALL JOIN(X, Y1)
    CALL JOIN(X,SINE)
    ELSE
    CALL JOIN(X,SINE)
    ENDIF
    ENDIF
111  CONTINUE
997  CALL GREND
100  FORMAT(21X, F5.2, 28X, F5.2)
    STOP
* Error exit...
998  WRITE(6,FMT=('"!!Unable to open input file."'))
    STOP
996  WRITE(6,FMT=('"!!Unable to open output file."'))
    STOP
999  WRITE(6,FMT=('"!!Error in 1/P"'))
    STOP
    END

```

---

```

* Subroutine MAGPOS.
* Subroutine to calculate magnetic anomaly co-ordinates
* from ships position at right-angles to the ships track.
SUBROUTINE MAGPOS(ANOM,X,Y,XMAG,YMAG)

```

```

      THETA=3.1415927/4.0
      DELX=ANOM*SIN(THETA)
      DELY=ANOM*COS(THETA)
      XMAG=X+DELX
      YMAG=Y+DELY
      RETURN
      END

```

---

```

* Function VECTOR.
* (Taken from Ray Jackson's TRAK program.)
* Determines current heading from change in position, thereby enabling
* annotation to be drawn at right angles to the ship track.
      FUNCTION VECTOR (DELTAX, DELTAY)
      REAL DELTAX,DELTAY
* The returned value of VECTOR is the ship's heading, measured in
* degrees anticlockwise from north.
      PARAMETER (SX=-1.0E-6, SY=1.0E-6, HALFPI=1.570795, DTR=.01745329)
* Check for stationary ship
      IF(ABS(DELTAX).GT.SX.OR.ABS(DELTAY).GT.SY) GO TO 100
      VECTOR = 0.0
      RETURN
* Determine quadrant
100  N=1
      IF(DELTAX.GT.0.0)N=N+2
      IF(DELTAY.GT.0.0)N=N+1
* Find angle
      ANGLE=ATAN((DELTAY+SY)/(DELTAX+SX))
* Adjust for quadrant
      GO TO (200,200,300,300), N
200  VECTOR=(HALFPI+ANGLE)/DTR
      RETURN
300  VECTOR=(3.0*HALFPI+ANGLE)/DTR
      RETURN
      END

```



```

PROGRAM CMPENV
* Program to produce velocity function envelope from SAP velocity model.
* The program reads data from a specified TWT/Vrms velocity file,
* converts these if required to TWT/Vint, or DEPTH/Vint. The velocity
* file is then searched for CMPs within a user defined CMP range, which
* are reduced to a defined baseline TWT/Depth, and plotted on a single
* frame, thus defining a velocity envelope for the specified area of the
* model.
* INPUT/OUTPUT
* Program is fully interactive. Specified velocity file is read from unit 1,
* plotfile is written to unit 9 connected to CMP-ENV.
      DIMENSION V(2,11,200), V2(2,11,200), VPLT(2,11,200), KCMP(2)
      CHARACTER DATYP*2, ANS*2, INPUT*10
* Open and read data file...
      NPLT=0
      NVEL=0
      WRITE(6,('/', '& Velocity file name...'))
      READ(6, (A10)) INPUT
      OPEN (UNIT=1, FILE=INPUT, STATUS='OLD', ERR=9998)
10    READ(1, (2I6)) END=30) NCMP, NLYR
      NVEL=NVEL+1
      V(1,1,NVEL)=FLOAT(NCMP)
      V(2,1,NVEL)=FLOAT(NLYR)
      DO 20 K=1, NLYR
        READ(1, (2F10.0)) V(1,K+1,NVEL), V(2,K+1,NVEL)
20    CONTINUE
      GOTO 10
* End data...
30    CLOSE(UNIT=1)
      WRITE(6,('/', A10, " velocity file read,")) INPUT
      WRITE(6, (I4, " picks in file. ")) NVEL
* Determine data output type...
40    WRITE(6,('/', " Give data o/p required. "))
      WRITE(6, ( " TWT/VRMS (TR/tr,)" ))
      WRITE(6, ( " TWT/VINT (TI/ti,)" ))
      WRITE(6, ( " & DEP/VINT (DI/di,)" ))
      READ(6, (A2)) DATYP
* Transform...
      IF(DATYP.EQ.'TR'.OR.DATYP.EQ.'tr') THEN
        CALL TWTRMS(V,V2,NVEL)
      ELSE IF(DATYP.EQ.'TI'.OR.DATYP.EQ.'ti') THEN
        CALL TWTINT(V,V2,NVEL)
      ELSE IF(DATYP.EQ.'DI'.OR.DATYP.EQ.'di') THEN
        CALL DEPINT(V,V2,NVEL)
      ELSE
        WRITE(6,('/', "!! Invalid choice, try again. "))
        GOTO 40
      ENDIF
* Find and plot given CMP velocity function range...
50    WRITE(6,('/', " Give: "))
      WRITE(6, ( " & First CMP... "))
      READ(6, *) KCMP(1)
      WRITE(6, ( " & Last CMP... "))
      READ(6, *) KCMP(2)
* Check for CMP within data range...
      IF(KCMP(1).LT.IFIX(V2(1,1,1)).OR.
& KCMP(2).GT.IFIX(V2(1,1,NVEL))) THEN
        WRITE(6, ( " Invalid CMP range...try again. "))
        GOTO 50
      ENDIF
* Loop to find first CMP...
      I=1
60    IF(IFIX(V(1,1,I)).GE.KCMP(1)) THEN
      NPLT=1
      GOTO 65
    ELSE
      I=I+1
      GOTO 60
    ENDIF
* First CMP found...plot range...
65    IF(IFIX(V2(1,1,I)).GT.KCMP(2)) THEN

```

```

      GOTO 70
    ELSE
      NCMP=IFIX(V2(1,1,I))
      NLYR=IFIX(V2(2,1,I))
      WRITE(6,(/," CMP ",I4," found.")'')NCMP
      WRITE(6,(/," & Give basement TWT..")'')
      READ (6,*)BASE
      VPLT(1,1,NPLT)=V2(1,1,I)
      VPLT(2,1,NPLT)=V2(2,1,I)
      DO 80 K=1,NLYR
        VPLT(1,K+1,NPLT)=V2(1,K+1,I)-BASE
        VPLT(2,K+1,NPLT)=V2(2,K+1,I)
80    CONTINUE
      NPLT=NPLT+1
      I=I+1
      ENDIF
      GOTO 65
70    WRITE(6,(/," CMP range plotted.")'')
      NPLT=NPLT-1
* Plot & Exit...
      CALL CMPPLT(VPLT,NPLT,INPUT,KCMP)
      WRITE(6,(/," CMPs plotted.")'')
9999 STOP
9998 WRITE(6,(/," Error opening input velocity file.")'')
      STOP
      END
*
      SUBROUTINE TWTINT(V,V2,NVEL)
* TWT/VRMS to TWT/VINT conversion.
      DIMENSION V(2,11,200), V2(2,11,200)
      WRITE(6,(/," TWT/VRMS to TWT/VINT conversion..." ,/))
      DO 10 I=1,NVEL
        NLYR=INT(V(2,1,I))
        NCMP=INT(V(1,1,I))
        V2(1,1,I)=V(1,1,I)
        V2(2,1,I)=V(2,1,I)
        DO 20 K=1,NLYR
* for k=1, interval=rms...
          IF(K.EQ.1)THEN
            V2(1,K+1,I)=V(1,K+1,I)
            V2(2,K+1,I)=V(2,K+1,I)
          ELSE
*else...
            V2(1,K+1,I)=V(1,K+1,I)
            VL=V(1,K+1,I)*(V(2,K+1,I)**2.0)
            VU=V(1,K,I)*(V(2,K,I)**2.0)
            T = V(1,K+1,I)-V(1,K,I)
            VINT=(VL-VU)/T
            V2(2,K+1,I)=SQRT(VINT)
          ENDIF
20    CONTINUE
10    CONTINUE
      RETURN
      END
*
      SUBROUTINE DEPINT(V,V2,NVEL)
* Subroutine converts from twt/vrms to depth/vint.
      DIMENSION V(2,11,200), V2(2,11,200)
      WRITE(6,(/," TWT/VRMS to DEP/INT conversion..." ,/))
      DO 10 I=1,NVEL
        NLYR=INT(V(2,1,I))
        NCMP=INT(V(1,1,I))
        V2(1,1,I)=V(1,1,I)
        V2(2,1,I)=V(2,1,I)
        DO 20 K=1,NLYR
* for k=1, interval=rms...
          IF(K.EQ.1)THEN
            V2(1,K+1,I)=(V(2,K+1,I)*V(1,K+1,I))/2.0
            V2(2,K+1,I)=V(2,K+1,I)
          ELSE
*else...

```

```

      DELT=(V(1,K+1,I)-V(1,K,I))/2.0
      VL=V(1,K+1,I)*(V(2,K+1,I)**2.0)
      VU=V(1,K,I)*(V(2,K,I)**2.0)
      T =V(1,K+1,I)-V(1,K,I)
      VINT=(VL-VU)/T
      V2(2,K+1,I)=SQRT(VINT)
      V2(1,K+1,I)=V2(1,K,I)+DELT*V2(2,K+1,I)
      ENDIF
20  CONTINUE
10  CONTINUE
      RETURN
      END
*
      SUBROUTINE TWTRMS(V,V2,NVEL)
* Subroutine writes out twt/vrms.
      DIMENSION V(2,11,200),V2(2,11,200)
      WRITE(6,(/,"Write out TWT/VRMS..."//))
      DO 10 I=1,NVEL
      V2(1,1,I)=V(1,1,I)
      V2(2,1,I)=V(2,1,I)
      NLYR=INT(V(2,1,I))
      NCMP=INT(V(1,1,I))
      DO 20 K=1,NLYR
      V2(1,K+1,I)=V(1,K+1,I)
      V2(2,K+1,I)=V(2,K+1,I)
20  CONTINUE
10  CONTINUE
      RETURN
      END
*
      SUBROUTINE CMPPLT(VPLT,NPLT,INPUT,KCMP)
* Plot required CMPS.
      DIMENSION VPLT(2,11,200), KCMP(2)
      CHARACTER DATYP*2,YLAB*22,XLAB*24,INPUT*10,PFILE*7
* Open plotfile...
      PFILE='CMP_PLT'
      WRITE(6,(/,"Plotting CMPS..."//))
      WRITE(6,(/,"Plotfile written to CMP_PLT."//))
      OPEN (UNIT=9,FILE=PFILE,STATUS='NEW',ERR=9998)
* Labels...
      IF(DATYP.EQ.'DI'.OR.DATYP.EQ.'di')THEN
      YLAB='Sub-basement depth (m).'

```

```

      CALL TCSCEN (YLAB)
      CALL CTRORI (0.0)
      CALL CTRMAG (10)
*Loop to plot...
      DO 20 I=1,NPLT
        NLYR=IFIX(VPLT(2,1,I))
        NCMP=IFIX(VPLT(1,1,I))
        DO 10 K=1,NLYR
          IF(VPLT(1,K+1,I).LT.0.0)THEN
            CALL POSITN (VPLT(2,K+1,I),VPLT(1,K+1,I))
            GOTO 10
          ELSE IF(K.EQ.1.)THEN
            CALL POSITN (VPLT(2,K+1,I),VPLT(1,K+1,I))
            CALL PLOTNC (VPLT(2,K+1,I),VPLT(1,K+1,I),161)
          ELSE
            CALL JOIN (VPLT(2,K+1,I),VPLT(1,K+1,I))
            CALL PLOTNC (VPLT(2,K+1,I),VPLT(1,K+1,I),161)
          ENDIF
        10 CONTINUE
      20 CONTINUE
      CALL PSPACE (0.25,0.50,0.15,0.25)
      CALL MAP (0.0,1.0,0.0,1.0)
      CALL BORDER
      CALL PLOTCS (0.35,0.8,INPUT)
      CALL PLOTCS (0.35,0.8,'_____ ')
      CALL PLOTCS (0.15,0.6,'Velocity Function Stack.')
      CALL PLOTCS (0.15,0.4,'CMP Range')
      CALL TYPENI (KCMP(1))
      CALL PLOTCS (0.65,0.4,'to')
      CALL POSITN (0.70,0.4)
      CALL TYPENI (KCMP(2))
      CALL PLOTNC (0.15,0.2,161)
      CALL PLOTCS (0.2,0.2,'-Mark velocity picks.')
      CALL GREND
      CLOSE (UNIT=9)
      RETURN
9998 WRITE(6,('/',," Error opening plotfile."))
      STOP
      END

```

## Appendix B.

### Details of data available on magnetic tape at Durham.

This appendix gives details of the magnetic data tapes from the Discovery 155/85 and Charles Darwin 4/85 cruises to the Hatton Bank continental margin. The tapes are archived in the computing centre at the University of Durham, under the ownership of GPM3, and are permitted READ GPT9. Details concerning mounting the tapes, and reading the data contained therein are given. Tapes containing magnetic data recorded during earlier Durham University cruises aboard the RRS Shackleton are also described. ASCII tape data should be translated to EBCDIC prior to use by mounting the appropriate tape as described, and issuing the following command:-

```
$RUN DURH:ATOEB 1=*T* 2=-FILE
```

#### Discovery.

**(a) Tape Name : GPDI85 (ASCII 1600 bpi).**

Tape contains Dead-Reckoning (DR) navigation and associated geophysical and course data.

Mount command : \$MOUNT GPDI85 \*T\* NV FMT=FB(80,80)

**(b) Tape Name : LODI85 (ASCII 1600 bpi).**

Tape contains Loran navigation and associated geophysical and course data.

Mount command : \$MOUNT LODI85 \*T\* NV FMT=FB(114,114)

**Charles Darwin.**

**(a) Tape Name : GDA485 (ASCII 1600 bpi).**

Tape contains two files: Time data at 30 s interval plus

(i) Final DR navigation data (137 19:45 - 160 13:51).

(ii) Final cmg, smg data (137 19:45 - 160 13:51).

Mount command : \$MOUNT GDA485 \*T\* NV FMT=FB(800,80)

NOTE: files are not separated by EOF, and tape is not terminated by LEOT.

**(b) Tape Name : LDA485 (ASCII 1600 bpi)**

Tape contains single file of Loran navigation data.

Mount command : \$MOUNT GDA485 \*T\* NV FMT=FB(800,80)

**(c) Tape Name : GPDA85 (ASCII 1600 bpi)**

Tape contains 3 files of magnetic, gravity, and bathymetry data.

Mount command : \$MOUNT GPDA85 \*T\* NV FMT=FB(800,80)

The data on this tape contains repeated sections which should be manually edited, prior to merging with navigation data (Darwin tapes (a) or (b)) using program MERGE (appendix A).

**(d) Tape Name : TRI185 (ASCII 1600 bpi).**

Tape contains 14 files of Trisponder range data (141 08:50 - 159 14:08).

Mount command : \$MOUNT TRI185 \*T\* NV FMT=FB(800,80)

**(e) Tape Name : TRI285 (ASCII 1600 bpi).**

Tape contains 1 file of Trisponder range data (154 06:34:00 - 156 17:29:38).

Mount command : \$MOUNT TRI285 \*T\* NV FMT=FB(800,80)

**(f) Tape Name : TRI285 (ASCII 1600 bpi).**

Tape contains 1 file of Trisponder range data (156 17:29:39 - 158 22:30:00).

Mount command : \$MOUNT TRI385 \*T\* NV FMT=FB(800,80)

**(g) Tape Name : LOGP85 (EBCDC 6250 bpi).**

Tape contains translations and copies of (i) DR Navigation, (ii) Loran Navigation data (Darwin Tapes (a) & (b))

Mount command : \$MOUNT LOGP85 \*T\* VOL=LOGP85 FMT=FB(8000,80)

**(h) Tape Name : TCPY85 (EBCDC 6250 bpi).**

Tape contains translations and copies of 3 trisponder tapes (d), (e), (f).

Mount command : \$MOUNT TCPY85 \*T\* VOL=TCPY85 FMT=FB(8000,80)

**Final working tape.**

**(a) Tape Name : GDACPY (EBCDC 6250 bpi).**

Tape contains Discovery/Darwin data in final working format. Files 1-4 are Darwin free-air gravity and magnetic anomaly, bathymetry, and corrected bathymetry

merged with DR navigation. Files 5-7 contain Discovery free-air gravity and magnetic anomaly, and bathymetry data, with associated DR navigation data. Files 8 & 9 contain drift-corrected Darwin and Discovery free-air gravity anomaly data respectively.

Mount command : \$MOUNT TCPY85 \*T\* VOL=TCPY85 FMT=FB(8000,80)

### **Shackleton data tapes.**

All Shackleton data tapes are 1600 bpi ASCII format tapes, and should be translated to EBCDIC prior to use.

(a) Shackleton 1973. Tape name DGP457 (owner GPT9).

(b) Shackleton 1974. Tape name DGP482 (owner GPT9).

(c) Shackleton 1977. Tape name GPO401 (owner GPT9).

Mount command : \$MOUNT GPO401 \*T\* NV FMT=FB(800,80)





60

21

22

23

24B

22

23

24B

59

58

20

19

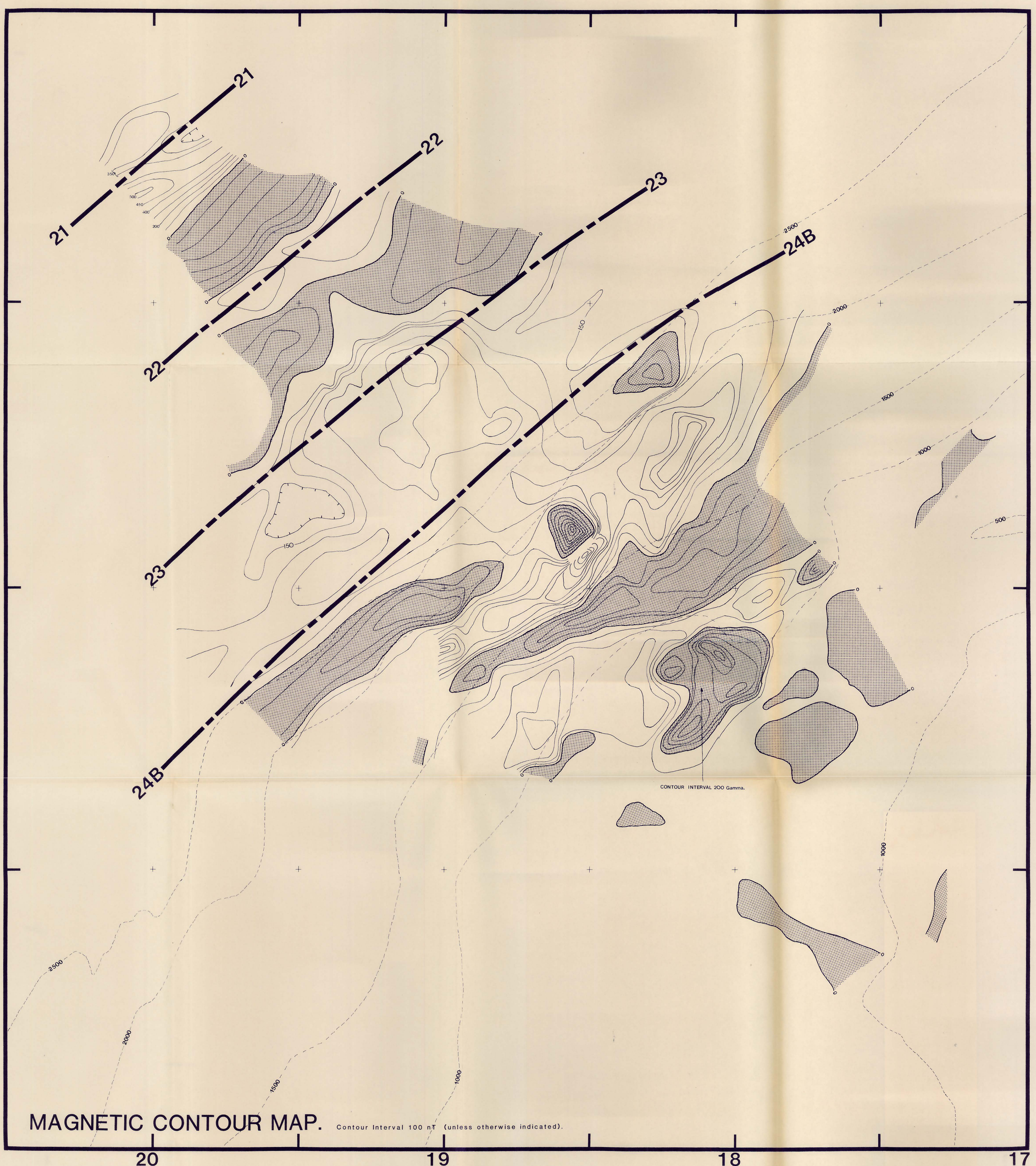
18

17

# MAGNETIC CONTOUR MAP.

Contour Interval 100 nT (unless otherwise indicated).

CONTOUR INTERVAL 200 Gamma.





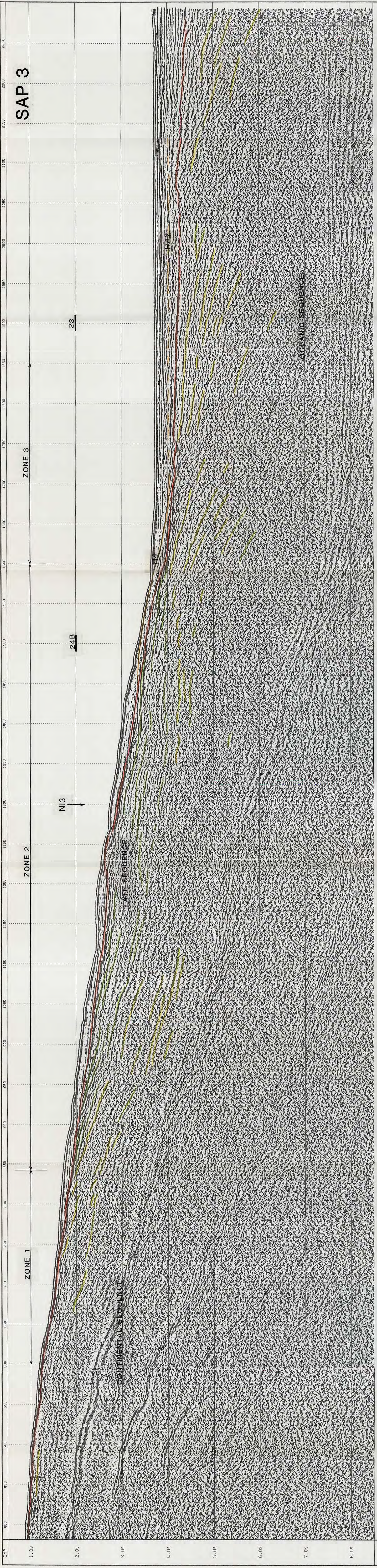




DISPLAY PARAMETERS:

CMP GATHERS  
AGC WINDOW LENGTH 200 MS  
INTENSITY FACTOR 0.90  
CLIP FACTOR 0.50  
TRACE WIDTH 0.1500 INCHES  
TRACE DATUM 0.0000  
POSITIVE LOBE SHADED

SAP3.

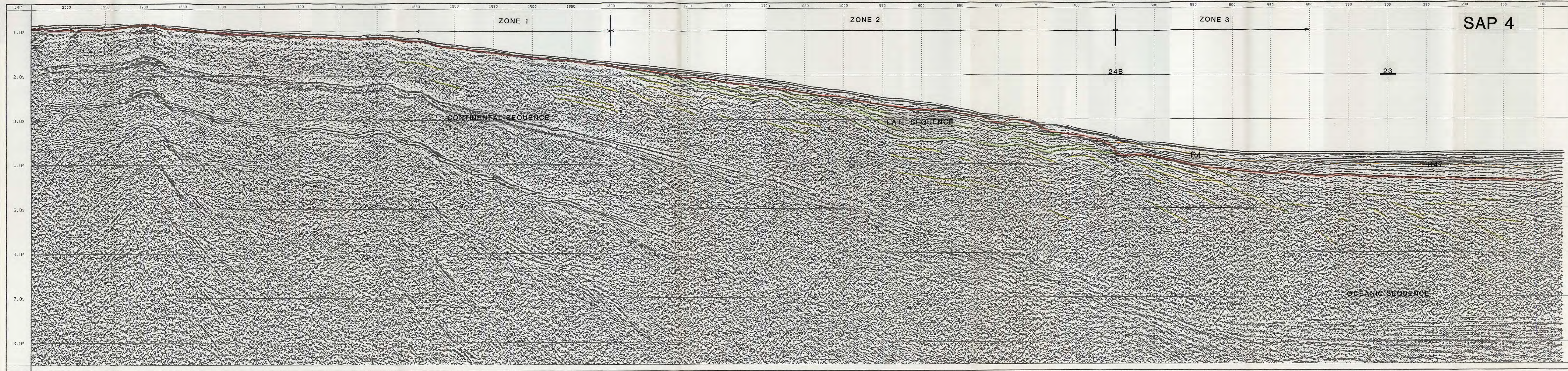




DISPLAY PARAMETERS:

CMP GATHERS  
AGC WINDOW LENGTH 200 MS  
INTENSITY FACTOR 0.90  
CLIP FACTOR 0.50  
TRACE WIDTH 0.1500 INCHES  
TRACE DATUM 0.0000  
POSITIVE LOBE SHADED  
REVERSE PLOT

SAP4.

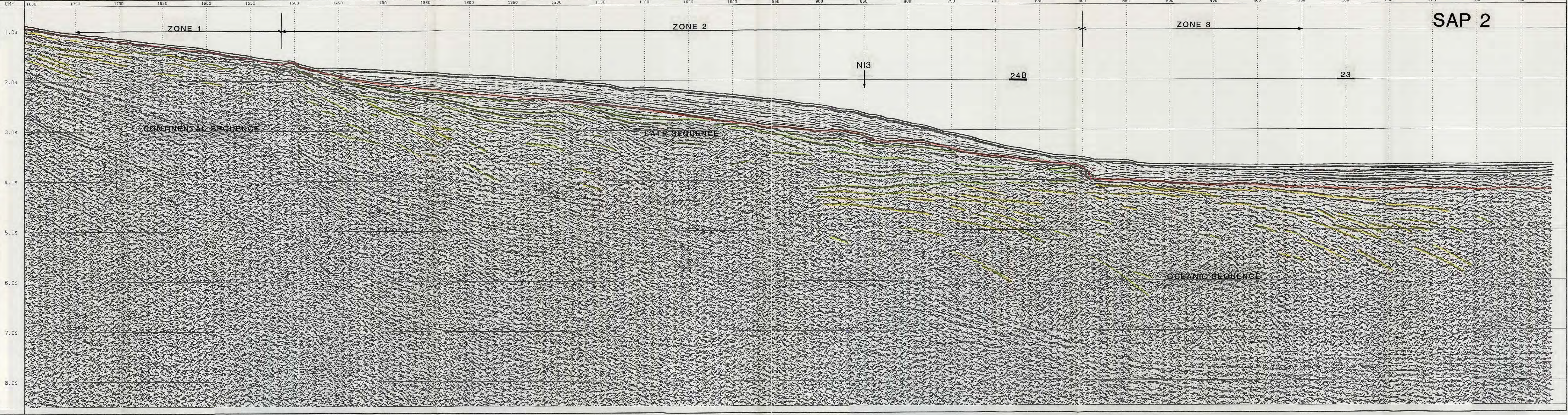




DISPLAY PARAMETERS:

CMP GATHERS  
AGC WINDOW LENGTH 200 MS  
INTENSITY FACTOR 0.90  
CLIP FACTOR 0.50  
TRACE WIDTH 0.1500 INCHES  
TRACE DATUM 0.0000  
POSITIVE LOBE SHADED  
REVERSE PLOT

SAP2.

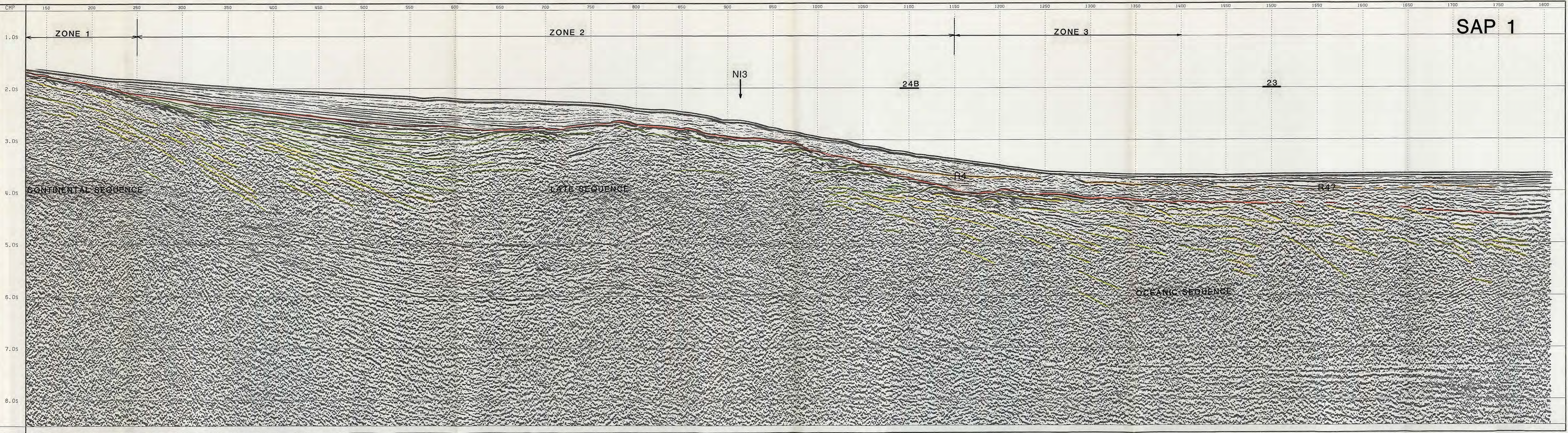




DISPLAY PARAMETERS:

CMP GATHERS  
AGC WINDOW LENGTH 200 MS  
INTENSITY FACTOR 0.90  
CLIP FACTOR 0.50  
TRACE WIDTH 0.1500 INCHES  
TRACE DATUM 0.0000  
POSITIVE LOBE SHADED

SAP1.





60

59

58

20

19

18

17

GRAVITY CONTOUR MAP.

